Titre: Title:	Engineered Photophysical Properties via Rational Molecular Design
Auteur: Author:	Orlando Ortiz Rodriguez
Date:	2026
Type:	Mémoire ou thèse / Dissertation or Thesis
Référence: Citation:	Ortiz Rodriguez, O. (2026). Engineered Photophysical Properties via Rational Molecular Design [Thèse de doctorat, Polytechnique Montréal]. PolyPublie. https://publications.polymtl.ca/74650/

URL de PolyPublie: PolyPublie URL:	https://publications.polymtl.ca/74650/
Directeurs de recherche: Advisors:	Stéphane Kéna-Cohen, & William Skene
Programme: Program:	Génie des matériaux

POLYTECHNIQUE MONTRÉAL

affiliée à l'Université de Montréal

Engineered Photophysical Properties via Rational Molecular Design

ORLANDO ORTIZ RODRIGUEZ

Département de génie physique

Thèse présentée en vue de l'obtention du diplôme de *Philosophiæ Doctor*

Génie des matériaux

Février 2026

POLYTECHNIQUE MONTRÉAL

affiliée à l'Université de Montréal

Cette thèse intitulée :

Engineered Photophysical Properties via Rational Molecular Design

présentée par **Orlando ORTIZ RODRIGUEZ**

en vue de l'obtention du diplôme de *Philosophiæ Doctor*

a été dûment acceptée par le jury d'examen constitué de :

Clara SANTATO, présidente
Stéphane KÉNA-COHEN, membre et directeur de recherche
William SKENE, membre et codirecteur de recherche
Daria Camilla BOFFITO, membre
Mihaela CIBIAN, membre externe

DEDICATION

Ad Maiorem Dei Gloriam.

ACKNOWLEDGEMENTS

I would like to express my sincere gratitude to my supervisor Prof. Stéphane Kéna-Cohen and my co-supervisor Prof. William Skene, first for giving me the opportunity to be part of your research groups, and for your advice and support throughout these years. I would also like to thank both of you for allowing me independence in my research; thanks to both, I have developed and improved my skills as a researcher.

I would also like to thank the members of my thesis jury, Prof. Mihaela Cibian, Prof. Clara Santato, and Prof. Daria Camilla Boffito, for kindly agreeing to examine my thesis.

I'm deeply grateful to Prof. Jian Mao, whose several advice in the early years of my PhD were, are, and will continue to be vital to my life as a researcher. Similarly, I would like to express my sincere gratitude to Prof. Tomohiro Ishii, for his teachings and invaluable help, which was vital for the photostability measurements, as well as to Dr. Mohan Raj Anthony Raj for all his support and teachings, which have contributed to the development of my skills as a researcher.

I would also like to thank my lab colleagues, especially Alex, and my dear friend Rupinder, for your advice and support.

Last but certainly not least, I would like to thank my family and friends, and especially my beloved parents, who have always believed in me and whose love and encouragement have been instrumental in the completion of my PhD.

RÉSUMÉ

La conception moléculaire rationnelle constitue une stratégie puissante pour contrôler les propriétés photophysiques des matériaux à couche fermée et à couche ouverte. Ainsi, il est essentiel de comprendre la relation entre la structure et les propriétés pour concevoir des matériaux efficaces, stables et ajustables. Pour relever ce défi, deux stratégies de conception complémentaires ont donc été mises en œuvre.

Dans la première stratégie, la modulation de l'empilement cristallin dans un système à couche fermée a été évaluée. À cet égard, deux polymorphes cristallins d'un fluorophore benzothiadiazole conjugué ont été obtenus par des voies de synthèse distinctes, révélant comment des changements subtils dans les motifs d'empilement dictent l'émission à l'état solide. Les différences dans les interactions C-H···N/S et π-π ont entraîné des variations dans le rendement quantique absolu de l'émission et la dynamique de l'état excité, démontrant que le polymorphisme peut être utilisé comme un outil de conception supramoléculaire pour ajuster la luminescence sans modification chimique.

La deuxième stratégie consiste à lier de manière covalente des substituants donneurs d'électrons sur des radicaux à base de trityle afin d'améliorer la photostabilité et d'obtenir une émission dans le proche infrarouge. Ainsi, l'introduction de donneurs de carbazole et de triphénylamine a entraîné une augmentation de > 1 000 fois de la photostabilité et des transitions optiques décalées vers le rouge par rapport au radical trityle non substitué. Enfin, les radicaux trityle synthétisés ont été étudiés en tant que matériaux électrochromiques. En ce sens, leur comportement électrochromique réversible a produit une modulation de transmittance importante (< 80 %) et une efficacité de coloration dans la région NIR s'étendant de 425 à 590 cm^2/C. De plus, un électrochromisme réversible a également été observé dans la région visible, ce qui en fait des matériaux électrochromiques ambipolaires, les positionnant comme des candidats prometteurs pour les écrans optiques et les fenêtres intelligentes.

Dans l'ensemble, cette thèse établit des relations fondamentales entre la structure et les propriétés qui relient la conception moléculaire et l'organisation supramoléculaire à la fonction photophysique dans les matériaux à couche fermée et ouverte. Elle fournit également un cadre pour la conception de systèmes organiques avec une photostabilité, une émission et des performances électrochromiques sur mesure, contribuant ainsi à l'avancement de la science des matériaux.

ABSTRACT

Rational molecular design constitutes a powerful strategy to control the photophysical properties of both closed- and open-shell materials. Thus, understanding the structure-property relationship is essential to engineer efficient, stable, and tunable materials. Hence, to address this challenge two complementary design strategies were pursued,

In the first strategy the modulation of crystal packing in a closed-shell system was evaluated. In this regard, two crystalline polymorphs of a conjugated benzothiadiazole fluorophore were obtained through distinct synthetic routes, revealing how subtle changes in packing motifs dictate solid-state emission. Differences in C-H···N/S and π-π interactions led to variations in emission, absolute quantum yield, and excited-state dynamics, demonstrating that polymorphism can be used as a supramolecular design tool to tune luminescence without chemical modification.

The second strategy consist in covalently link electron-donor substituents on trityl-based radicals to improve photostability and achieve near-infrared emission. Thus, the introduction of carbazole and triphenylamine donors resulted in more than 1000-fold increase in photostability and red-shifted optical transitions compared to the unsubstituted trityl radical. Finally, the synthesized trityl radicals were investigated as electrochromic materials. In this sense, their reversible electrochromic behaviour produced large transmittance modulation (< 80%) and coloration efficiency across the NIR region that span from 425 to 590 cm^2/C. Also, reversible electrochromism was also found in the visible region which makes them ambipolar electrochromic materials, positioning them as promising candidates for optical displays and smart windows.

Overall, this thesis establishes fundamental structure-property relationships that link molecular design and supramolecular organization to photophysical function in both closed- and open-shell materials. Also, it provides a framework for engineering organic systems with tailored photostability, emission, and electrochromic performance, contributing to the advancement of materials science.

TABLE OF CONTENTS

LIST OF TABLES

LIST OF FIGURES

LIST OF SYMBOLS AND ABBREVIATIONS

BZT	2,1,3-benthotiadiazole
CE	Coloration efficiency
CT	Charge-transfer
D_0	Doublet ground state
D_1	Lowest-energy doublet excited state
D-A	Donor- acceptor
DET	Triplet-triplet energy transfer
DSC	Differential Scanning Calorimetry
ECD	Electrochromic device
EPR	Electron Paramagnetic Resonance
Φ_{fl}	Fluorescence quantum yield
HPLC	High-Performance Liquid Cromatography
HOMO	Highest Occupied Molecular Orbital
IC	Internal convertion
ISC	Intersystem crossing
k_{nr}	Non-radiative rate constant
k_r	Radiative rate constant
LC	Liquid chromatography
LE	Locally excited states
LUMO	Lowest Unoccupied Molecular Orbital
M	Multiplicity
MCF	Mechanochromic fluorophores
NIR	Near-infrared

OLED	Organic Light Emitting Diode
PMMA	Polymethyl methacrylate
PTM	Perchlorotriphenylmethyl radical
Q	Quartet state
RISC	Reverse intersystem crossing
S_0	Singlet ground state
S_1	Lower-energy singlet excited state
S_n	Excited state of higher energy
SCXRD	Single-crystal X-ray Diffraction
SOMO	Singly Occupied Molecular Orbital
SUMO	Singly Unoccupied Molecular Orbital
SPR	Structure-property relationship
T1	Lowest-energy triplet excited states
TADF	Thermally activated delayed fluorescence
TDM	Transition dipole moment
TGA	Thermogravimetric Analysis
TPA	Triphenylamine
TRES	Time-Resolved Emission Spectra
TTA	Triplet-triplet annihilation
TTM	Tris(2,4,6-trichlorophenyl)methyl radical
τ	Excited-state lifetime
VR	Vibrational relaxation

LIST OF APPENDICES

CHAPTER 1 INTRODUCTION

This chapter gives a succinct introduction to the doctoral thesis, including the motivation of the work described, the objectives, and the structure.

1.1 Motivation

The current climate challenges demand the development of novel, durable, and energy-efficient materials. At the core of this effort lies a fundamental principle in Materials Science, the structure–property relationship (SPR). This principle states that any modification at the molecular or chemical level of a material directly influences its resulting physical, chemical, and photophysical properties, ultimately determining its potential application.

In this context, this thesis investigates SPR across two distinct organic molecular systems: emissive crystalline polymorphs and photostable electroactive radicals. In both cases, molecular design serves as a strategy to modulate solid-state emission, enhance photostability, and enable electrochromic behavior relevant to optical and energy-related technologies. Therefore, the objectives of this thesis are formulated to systematically explore how rational molecular design can control photophysical behavior across closed-shell and open-shell fluorophores.

1.2 Objectives

The objective of this thesis is to investigate how rational molecular design can be used to control the photophysical behaviour of organic materials through different, yet complementary approaches. Thus, the first approach is focus on closed-shell crystalline emitters where variations in crystal packing are used to correlate supramolecular organization with emission. The second approach examines open-shell electroactive materials where molecular structure and redox properties are tuned to enhance photostability and reversible electrochromism. Considering these approaches, the research objectives of the thesis are:

1. Understanding the influence of crystal packing on emission quantum yield by comparing two crystalline polymorphs of a conjugated benzothiadiazole fluorophore obtained through independent synthetic routes.

2. Enhancing the photostability and red-shift the emission towards the near-infrared of functionalized trityl-based radicals via an electron-donating substituent strategy, using the unsubstituted trityl radical as reference molecule.
3. Demonstrating that carbon-centered organic radicals can be use as electrochromic materials through reversible redox-driven optical modulation in solution.

1.3 Outline of the Thesis

This thesis is organized into six chapters that collectively explore how rational molecular design can be employed to control the photophysical behavior of organic materials, spanning from closed-shell crystalline emitters to open-shell electroactive radicals.

In Chapter 2 we provide the theoretical background necessary to frame the research presented in this thesis. We first introduce fundamental concepts of molecular photophysics that are relevant to the systems investigated in the following chapters. This is followed by an overview of the electronic structure and photophysical behavior of organic radicals. Finally, a short literature review is presented on several fundamental topics that support the research in this thesis, including the stability of polychlorinated trityl radicals, near-infrared trityl open-shell materials, electrochromic organic radicals, and polymorphism in benzothiadiazole derivatives.

In Chapter 3, we investigate how crystal packing influences the emissive properties of benzothiadiazole-based fluorophores. In this regard, two crystalline polymorphs of a conjugated benzothiadiazole derivative were obtained and structurally characterized. By comparing their supramolecular organization, we establish how differences in intermolecular interactions and π–π stacking affect the solid-state photophysical behavior. The results illustrate how subtle variations in molecular packing can modulate emission efficiency and spectral position, highlighting polymorphism as an effective strategy for tuning the optical properties of organic materials.

In Chapter 4, we examine how an electron-donating substituent strategy influences the photophysical properties and photostability of functionalized trityl-based radicals. Thus, through photophysical characterization and photostability studies, we determine how donor substitution modifies the optical behavior of the radicals, shifts their emission toward the near-infrared region, and improves their resistance to photodegradation, using the unsubstituted trityl radical as a reference. These results highlight the role of molecular design in controlling emission and photostability in open-shell fluorophores.

In Chapter 5, we investigate the electrochromic properties of the synthesized trityl radicals showed in the previous chapter. Thus, through electrochemical and spectroelectrochemical characterization, we determine how molecular structure, and redox processes govern reversible optical switching in the near-infrared region. In particular, we show that these open-shell radicals exhibit ambipolar electrochromic behavior, enabling selective modulation of visible and NIR absorption with applied bias. The electrochromic response of these radicals is discussed in comparison with classical viologen-based electrochromes, which typically operate in the visible region. These results highlight the potential of trityl-based radicals as electrochromic materials and illustrate how rational molecular design can be used to achieve tunable NIR electrochromic responses.

In Chapter 6, the conclusions of the previous experimental chapters are presented. Moreover, the limitations of each chapter are discussed, and the directions for future research are outlined.

CHAPTER 2 THEORETICAL BACKGROUND AND LITERATURE REVIEW

2.1. Light-induced photophysical processes in molecular systems

The first principle of photochemistry dictates that any chemical change is triggered by an absorption of light.[1] In this regard, a chromophore is the structural unit of a molecule that due to its delocalized π-system is responsible for absorbing light in the UV-visible region.[2] Thus, the interaction between light and matter promotes electrons from the ground state to excited states, triggering the photophysical processes that govern the optical behavior of the material.

In conjugated organic systems, these transitions are typically of $\pi \rightarrow \pi^*$ or $n \rightarrow \pi^*$ character, and their energy depends on the degree of π-conjugation and the presence of electron-donating or electron-withdrawing substituents.[3] Hence, if the absorbed energy is released radiatively, the molecule acts as a luminophore, whereas nonradiative pathways lead to quenching.[4] Understanding the competition between radiative and nonradiative decay channels is therefore essential for the rational design of organic compounds with tailored photoactive properties.

2.1.1. Return to the ground state: the Franck-Condon principle

A key concept to understand the spin configuration of a molecular excited states is the concept of multiplicity (M).[3] In this sense, each electron possesses a spin, which is defined by the spin quantum number ($m_s = \pm {}^1\!/_2$). Thus, the overall spin configuration of a system is determined by the sum of all individual spins, called the total spin quantum number (S). Therefore, the corresponding multiplicity ($M = 2S + 1$) indicates the number of degenerate spin states associated with an electronic configuration. In this regard, when all electrons are paired with opposite spins ($S = 0$), the system adopts a singlet state ($M = 1$). On the contrary, if two electrons possess parallel spins ($S = 1$), the system exhibits a triplet state ($M = 3$), characterized by three spin-degenerate sublevels. Furthermore, in open-shell molecules containing an unpaired electron ($S = {}^1\!/_2$), the resulting configuration corresponds to a doublet state ($M = 2$), which is typical of many organic radicals.[5] Hence, the distinction between singlet, triplet and doublet states governs the probability of photophysical transitions, as changes in spin multiplicity are generally spin-forbidden according to selection rules.[6]

According to the spin selection rule, electronic transitions that preserve spin multiplicity are significantly more probable than those involving a change in spin state. Therefore, in a closed-shell molecule once a chromophore absorbs a photon an electron is promoted from a singlet ground state (S_0) to an electronically excited state of higher energy (S_n), if the absorbed light has the same frequency that the energy difference between two electronic states.[7] Moreover, it is worth noting that a transition between two electronic states is accompanied by simultaneous changes in vibrational and rotational states. Thus, within each electronic state, there exists a manifold of closely spaced vibrational sub-levels, forming what can be regarded as a quasi-continuum of states, whose population follows a Boltzmann distribution favoring the lowest-energy states.[8]

The distribution of the intensity of an electronic transition among its vibrational components is interpreted based on the Franck-Condon principle. The physical foundation of this principle lies in the large difference in mass between nuclei and electrons, which makes electronic transitions much faster processes (10^{-14} - 10^{-15} s) than nuclear vibrational motions (10^{-10} - 10^{-12} s).[9] This principle, states that the geometry of a molecule remains the same immediately before and after an electronic transition. Consequently, the electronic transition must occur at constant molecular geometry and constant nuclear kinetic energy.[10-12]

This process is depicted in figure 2.1, where anharmonic potential energy curves are used to describe the vibrational dynamics of the molecule. Thus, upon excitation, an electron is vertically promoted from a bonding to an antibonding molecular orbital, altering the electronic distribution and consequently shifting the equilibrium nuclear position. This change in geometry is accompanied by molecular vibrations that enable the electron to relax rapidly to the lowest vibrational level of the new potential energy surface. Hence, such vibrational relaxation (VR) takes place on an ultrafast timescale, typically between 10^{-14} and 10^{-15} s,[9, 13] which means that during the electronic transition the molecules involve are conformationally frozen.[14]

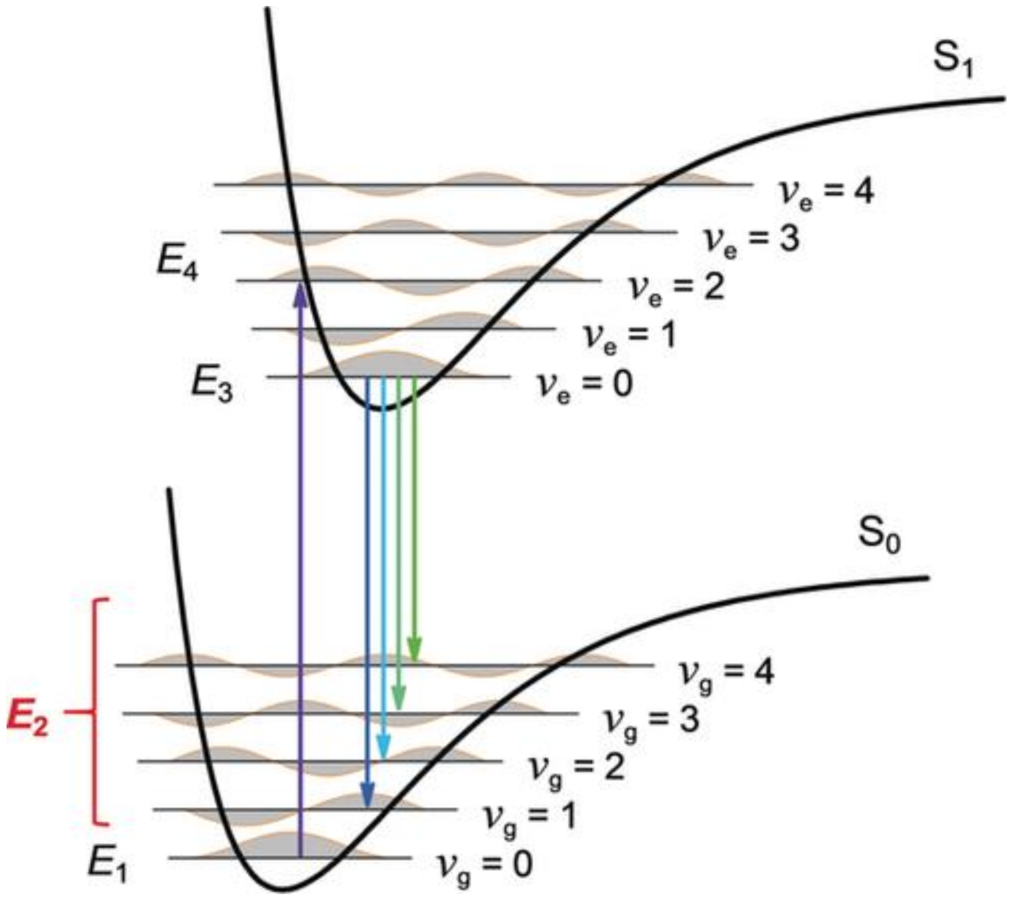

Figure 2.1. Franck–Condon principle energy diagram. The scheme depicts excitation from the lowest vibrational level of the ground state (E_1) to higher vibrational levels of the first singlet excited state (E_4), followed by relaxation to the lowest level of that state (E_3), and subsequent radiative and nonradiative transitions toward vibrationally excited levels of the ground state (E_2) and finally back to E_1.[15]

After VR, the molecule resides in the lowest vibrational level of the excited electronic state, from which, according to Kasha's rule, the emission of a photon will occur exclusively, regardless of which level was initially populated after absorption.[16] At this point, comprehending the mechanism by which an excited molecule returns to its ground state forms the foundation for understanding the radiative and nonradiative transitions that regulate molecular photophysics.

2.1.2. Radiative and non-radiative transitions between electronic states

Electronically excited molecules have several possible de-excitation pathways, among them the re-emission of photons, referred to as luminescence, a term first introduced by Wiedemann in 1888 to describe all those light phenomena which are not conditioned exclusively by an increase in temperature.[17]

There are different types of luminescence, classified according to the mode of excitation. When the excitation mode is the absorption of a photon that promotes the absorbing species to an electronically excited state, the subsequent photon emission accompanying de-excitation is called photoluminescence, a term that includes fluorescence, phosphorescence, and delayed fluorescence.[1]

A molecule excited by photon absorption can return to the ground state through different pathways, which constitute the molecule's intrinsic de-excitation mechanisms, such as internal conversion (IC), intersystem crossing (ISC), fluorescence, and phosphorescence, as illustrated in figure 2.2. Furthermore, de-excitation can also occur through interactions between the excited molecules and other molecules, a process known as quenching, which includes photochemical reactions, spin interactions, energy transfer, and electron transfer.[14, 18]

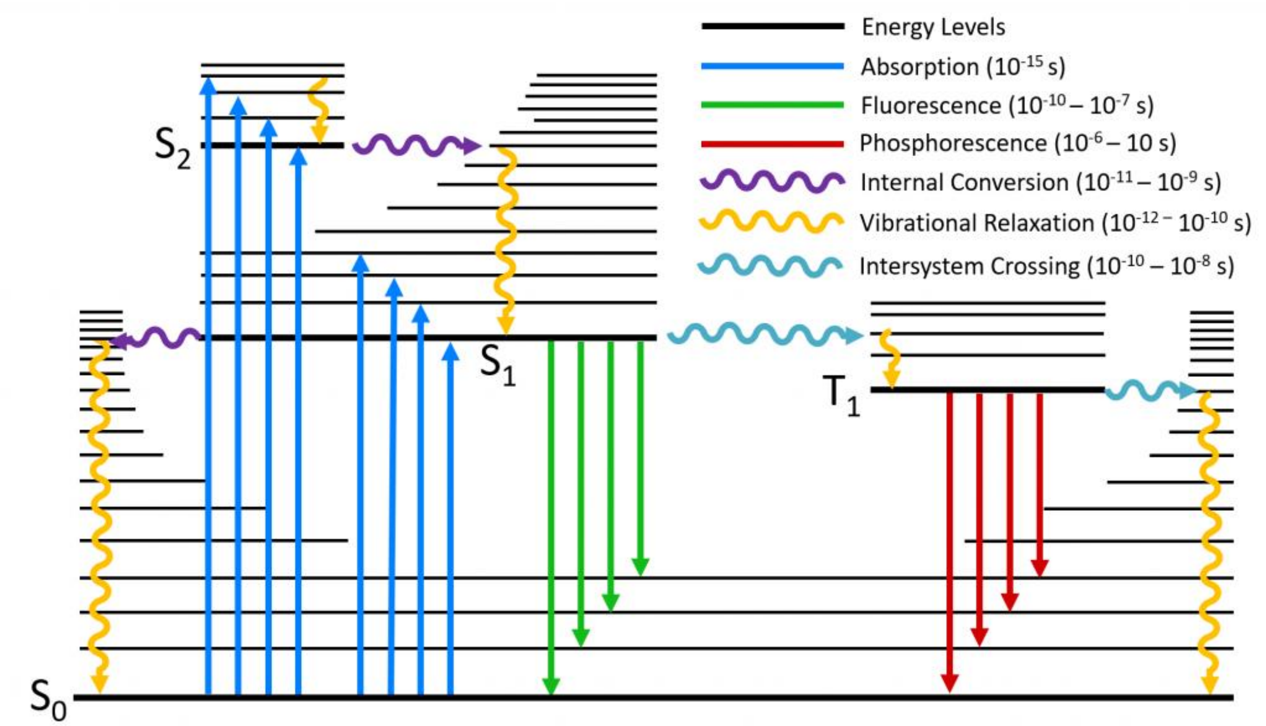

Figure 2.2. Perrin–Jablonsky diagram illustrating the radiative and non-radiative transitions.[19]

The Perrin-Jablonski diagram is a convenient tool for visualizing possible intrinsic de-excitation processes for closed-shell molecules. In this regard, the singlet electronic states are denoted as S_0

(ground state), S_1, S_2, and the triplet states as T_1, T_2. The vibrational levels associated with each electronic state are also represented. It is important to recall that radiation absorption is extremely fast (~ 10^{-15} s); therefore, according to the Franck–Condon principle, no displacement of the nuclei occurs during absorption. The vertical lines corresponding to absorptions originate from the lowest vibrational energy level 0 of S_0, since most molecules occupy this level at room temperature. This allows for the analysis of the subsequent de-excitation processes following absorption.

The photon emission associated with the radiatively de-excitation from S_1 to S_0 is called fluorescence. This is a spin-allowed process that takes places between 10^{-7} – 10^{-10} s. Moreover, the spacing between the maximum of the first absorption band and the fluorescence maximum is known as the Stokes shift . This parameter can provide information about the excited states, and from a practical standpoint, the detection of fluorescent species is easier when the Stokes shift is large. In general, the differences between vibrational levels are similar in the ground and excited states, such that the fine structure of the fluorescence spectrum resembles that of the first absorption band (mirror image rule).[9, 13, 20] In addition, according to the Kasha-Vavilov rule its emission spectrum does not depend on the excitation wavelength.[21] On the other hand, phosphorescence is another radiatively process that arises from the de-excitation $T_1 \rightarrow S_0$, which is a not spin-allowed transition, but it can still be observed due to spin-orbit coupling. Therefore, phosphorescence is usually a slow process, with triplet states lifetimes between 10^{-6} – 10 s, that competes with faster non-radiative transitions.[9] The effects that attenuate phosphorescence can be reduced at low temperatures, however room-temperature phosphorescence can also be observed under rational molecular design.[22-25]

Delayed fluorescence is another radiative process that occurs when triplet excitons are transfer back to singlet excitons. Thus, upon molecular design, a small energy difference between T_1 and S_1 and longer lifetime of T_1 can be achieved, which leads to reverse intersystem crossing (RISC) $T_1 \rightarrow S_1$ to occur. The efficiency of this type of fluorescent emission, known as thermally activated delayed fluorescence (TADF), increases with rising temperature.[26-28] Additionally, another type of delayed fluorescence can be observed in concentrated solutions, where a collision between two molecules in their T_1 states can lead to a return to the S_1 state. This mechanism is known as triplet–triplet annihilation (TTA) and is illustrated in figure 2.3. It is also possible that, after a molecule is excited and reaches the triplet state T_1, it can absorb another photon at a defined wavelength through the $T_1 \rightarrow T_n$ transition. These transitions are spin-allowed and can be observed as long as the population of molecules in the triplet state is sufficiently large.[29, 30]

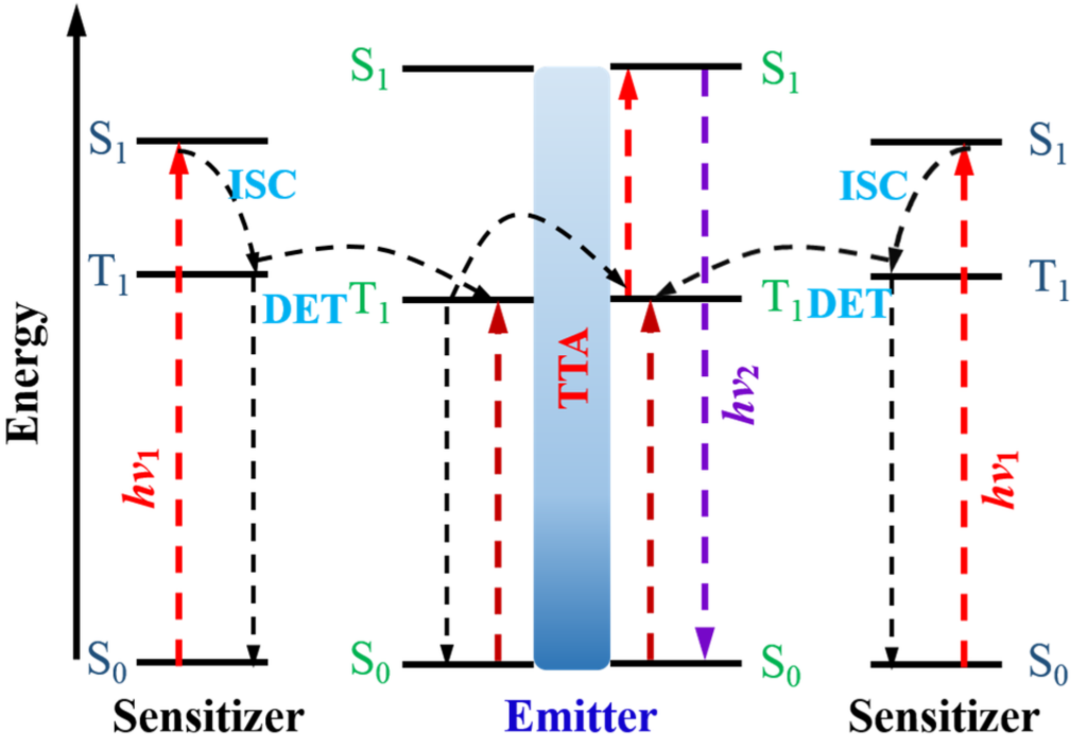

Figure 2.3. Working principle of the triplet-triplet annihilation (TTA) involving a sensitizer and emitter molecule. Upon absorption of incident light, the sensitizer generates a singlet exciton that undergoes intersystem crossing (ISC) to form a triplet state (T_1). Through triplet–triplet energy transfer (DET), this triplet exciton is transferred from the sensitizer to the emitter. When a sufficient population of triplet excitons accumulates on the emitter, two of them interact, one promoting an electron to the singlet excited state of the emitter, while the other relaxes non-radiatively to the ground state. The resulting singlet exciton then decays radiatively, emitting a photon.[31]

In addition to radiative processes, non-radiative channels are essential in the de-excitation dynamics of excited molecules. In this sense, IC is a transition between electronic states of the same spin multiplicity. It usually happens within 10^{-9} - 10^{-11} s when the electron is excited to higher energy excited states. Moreover, this radiationless process includes losing energy through vibrational relaxation, which happens when molecules collide and pass on their extra energy to the solvent around them.[9] On the other hand, ISC is another non-radiative transition between isoenergetic electronic states with different spin multiplicities via spin–orbit coupling. This process takes place within $10^{-8} – 10^{-10}$ s after which vibrational relaxation brings the molecule to the lowest vibrational level of T_1. Furthermore, even though ISC is formally spin-forbidden, it can effectively compete with other de-excitation mechanisms, such as fluorescence and internal conversion fluorescence. Thus, when heavy atoms are present the spin-orbit coupling is increased which make it easier for the triplet manifold to be populated.[9, 13]

Having established the fundamental radiative and non-radiative pathways governing the de-excitation of closed-shell organic molecules, it is now pertinent to extend this discussion to open-shell systems.

2.2. Electronic and photophysical properties of organic radicals

Compared to closed-shell molecules, which possess paired electrons and a singlet ground state with fully occupied molecular orbitals up to the highest occupied molecular orbital (HOMO), open-shell systems contain at least one unpaired electron located on single occupied molecular orbital (SOMO), resulting in a different electronic configuration and spin multiplicity.[32]

Triphenylmethyl organic radicals or most commonly know as trityl radicals, which were first reported by Gomberg,[33] are open-shell molecules with a doublet multiplicity. In this sense, Tonnelé et al have confirmed trough density functional theory calculations the doublet nature of the ground and excited states in trityl radicals.[34] In this regard, for a long time, it was erroneously believed that the excited state (D_1) was originated from a transition from the SOMO to a singly unoccupied molecular orbital (SUMO).[35] Thus, recent studies have proven that this apparent orbital splitting of open-shell molecules is in reality a direct consequence of broken spin symmetry.[36] Hence, as depicted in figure 2.4 and according to the Aufbau principle, the SOMO is usually above the NHOMO and below the NLUMO.[37] However, it is worth noting that upon rational molecular design non-Aufbau organic radicals with SOMO-HOMO inversion have also been reported.[38-40]

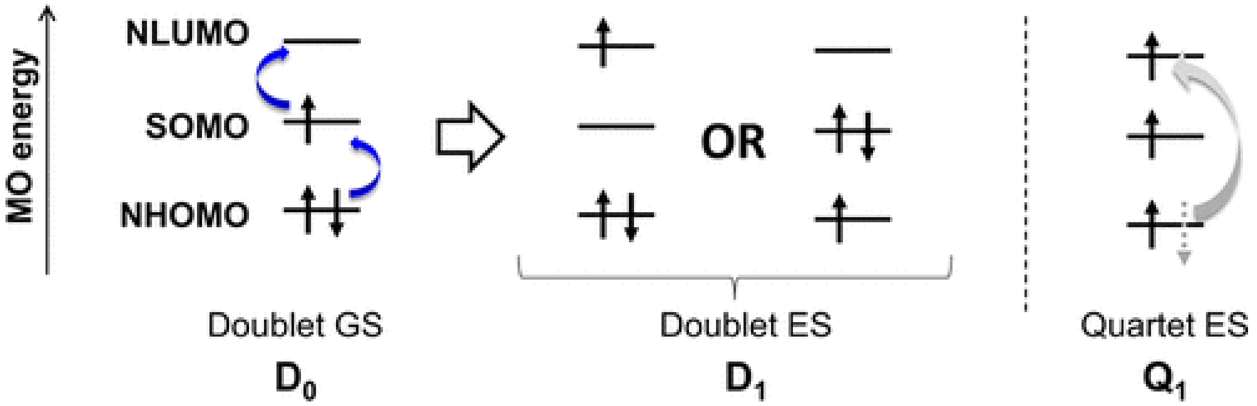

Figure 2.4. Frontier orbital configurations in the ground state (D_0), excited state (D_1), and quartet state (Q_1) states of conventional open-shell molecules. Blue arrows represent one-electron excitations from D_0, while the gray arrow indicates the spin flip excitation leading to Q_1.[37]

As illustrated in the above figure upon excitation the lowest energy electronic transition come from either the NHOMO to the SOMO or from this molecular orbital to the NLUMO, both resulting in the lowest energy doublet excited state (D_1). Furthermore, even though both ground and excited states have doublet multiplicity, and therefore their transition is spin-allowed, quarter states (Q_1) with three unpaired electrons can also been formed upon excitation. Thus, a radiative transition from Q_1 to D_1 is spin-forbidden and requires an increment in the stability of Q_1 via spin flipping to weekly emit. Furthermore, the lowest Q_1 for trityl radical derivatives is located at a higher energy level than D_1, which makes the emission dominant from D_1 to D_0 (figure 2.5).[37, 41] Furthermore, high-energy absorption could also lead to higher energy doublet states (D_n) with larger oscillator strength, and hence with higher probability to occur than D_1 to D_0.[41] Nevertheless, Kasha's rule is also applicable to open-shell molecules, therefore all electrons in D_n will relax via IC to D_1, although some anti-Kasha emission have also been reported.[42, 43]

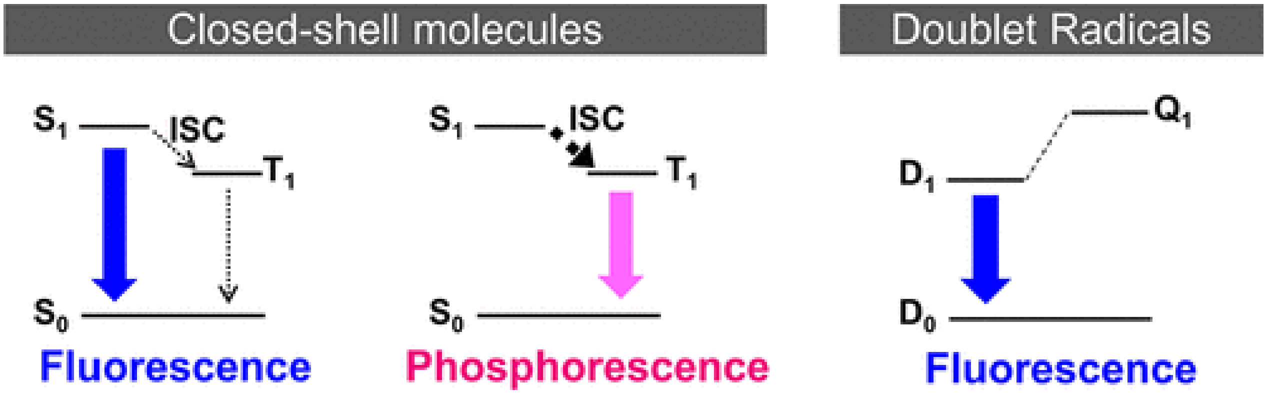

Figure 2.5. Radiative process in closed-shell (left) and open-shell (right) molecules. Dotted arrows represents non-radiative process.[37]

Alternant π-hydrocarbon systems (figure 2.6 a), where atoms in the π-system can be divided into two sets in a way that no two adjacent atoms can be found in the same set, constitutes a drawback that limits the emission of polychlorinated trityl radicals, like tris(2,4,6-trichlorophenyl)methyl (TTM).[44]

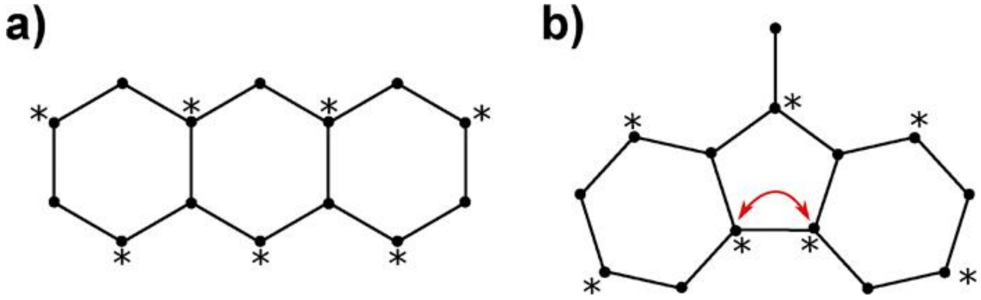

Figure 2.6. Alternant and non-alternant three-membered rings. Example structures of (a) alternant and (b) non-alternant three-membered rings (π-systems omitted for clarity). In alternant systems, with an even-numbered ring the atoms forming the delocalized framework can be divided into two distinct sets (starred and unstarred) such that no two atoms within the same set are directly connected. In contrast, for the non-alternant system containing and odd-numbered rings and also can contain heteroatoms (b), such a separation is impossible; at least two atoms of the same set would be adjacent (see red double-headed arrow).[41]

Alternacy in these open-shell fluorophores leads to a degeneracy of the energies of HOMO-SOMO and SOMO-LUMO transitions as depicted in figure 2.7 a. Thus, as a consequence of the degenerate nature, the transition dipoles moments (TDM) of both transitions are identical and mixed forming an in-phase (|D_2>) and out-of-phase (|D_1>) excitation (figure 2.7 b). Consequently, the latter is found to have a lower oscillator strength (*f*), which measure the probability of an electronic transition to take place. Thus, since *f* is proportional to the square of the TDM, a vanishing TDM for the $D_0 \rightarrow D_1$ absorption leads to a week emission from D_1, whereas ($|D_2>$ has a higher *f* and therefore an intense absorption (figure 2.7c).[44-46]

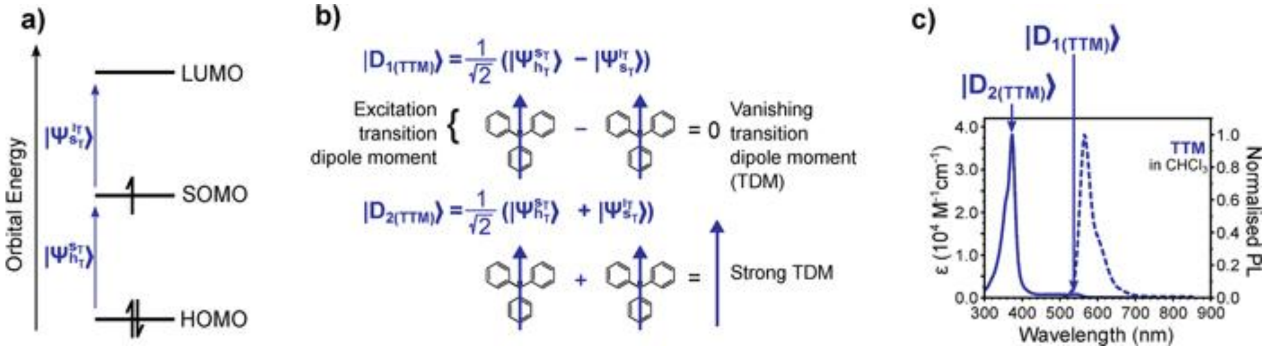

Figure 2.7. Excitation mixing in alternant radical systems. (a) Schematic representation of the frontier molecular orbitals of TTM, showing the HOMO–SOMO and SOMO–LUMO transitions. (b) Illustration of the mixing between these transitions, which gives rise to the dark D_1 (TTM) and bright D_2 (TTM) excited states. (c) absorption spectrum (solid line) and emission spectrum (dashed line) of TTM in $CHCl_3$, with the D_1 and D_2 transitions highlighted on the absorption spectrum.[41]

In non-alternat molecules the symmetry of the π-system is broken, consequently lifting the energies of the HOMO-SOMO and SOMO-LUMO transitions. Thus, the TDM for D_1 increases which leads to a higher oscillator strength of the emission. In this sense, it has been proven that if a non-alternat molecule is incorporated into an alternat moiety, the new molecule will be non-alternant. Moreover, alternacy can be broken by adding a heteroatom to the alternant core or by having conjugated rings with an odd number of atoms.[41, 44]

The addition of a non-alternat molecule trough covalent functionalization to an alternat core has proven to be an efficient strategy to enhance the radiative rates of the functionalized radicals, often leading to donor-acceptor (D-A) type structures, where the HOMO is generally found on the donor moiety while the SOMO localized in the electron acceptor trityl core.[47-50] Furthermore, these D-A structures exhibit a strong charge transfer (CT) character the HOMO to SOMO (figure 2.8 a), which correspond to the D_1 transition.[49, 51, 52] On the other hand, if the molecule is covalently attached to an electron acceptor molecule (figure 2.8 b) the D_1 transition comes from the CT from the SOMO to the LUMO of the electron acceptor molecule. Nevertheless, if the radical is functionalized with an alternant hydrocarbon the resulting radical will maintain the alternacy, and therefore a weak TDM for D_1 transition which hinder the emission leading to a “dark radical”.[41]

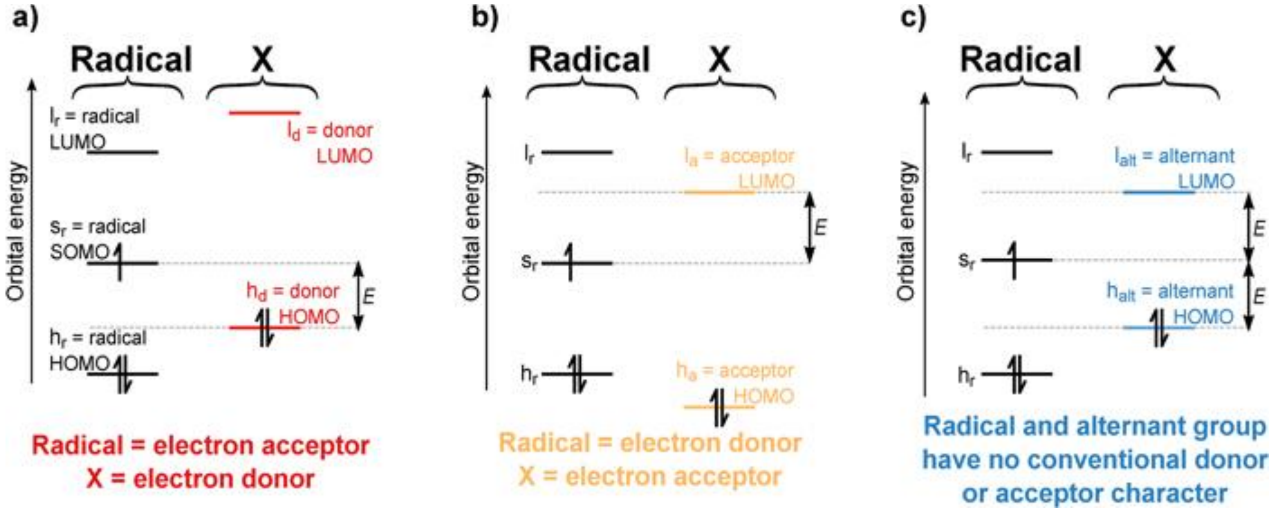

Figure 2.8. Charge-transfer radical excitations. Schematic molecular orbital diagrams illustrating (a) a radical acceptor-electron donor configuration, (b) a radical donor-electron acceptor configuration, and (c) a radical functionalized with an alternant group. E denotes the lowest-energy excitation, neglecting two-electron (Coulomb and exchange) interactions.[41]

Something that is worth to note is that, due to lack orbital overlap, CT transitions have a weak oscillator strength.[53, 54] However, many trityl radicals show a relative high oscillator strength value for the $D_0 \rightarrow D_1$ absorption.[55] In this sense, in trityl radical derivatives upon hybridization between high lying locally excited (LE) states, which exhibit higher TDM, and the CT state, an intense borrowing from the LE states can increases the oscillator strength of the otherwise dark CT-type emission. Thus, in D-A radical structures, intense borrowing of the oscillator strength leads to bright radicals, which is enhanced upon planarization of the open-shell π-system.[44]

In terms of applicability the stability of open-shell fluorophores plays a crucial role. Therefore, in the next section this subject will be addressed.

2.2.1. Stability of polychlorinated trityl radicals: the case of TTM

In contrast to closed-shell molecules, which generally exhibit greater chemical stability, open-shell molecules display higher reactivity and reduced intrinsic chemical stability. This is a direct consequence of their unpaired electron which leads to different reactive pathways such as disproportionation, dimerization and hydrogen subtraction. These undesired reactions are thermodynamically favoured and generally take place with little to no activation barrier.[56] Nevertheless, stable organic radicals have been reported. In this regard, it is worth noting that stable radicals refer to isolated and long-lived species while persistent radicals are those that cannot be isolated but have lifetimes which are long enough to allow spectroscopic characterization.[57]

The increment of radical's lifetime can be achieved mostly by two different routes. The first relies on delocalizing the unpaired electron over the molecular framework, which decreases the spin density at the formally radical-bearing atom and thereby reduces molecular reactivity. In this sense, heteroatoms such as nitrogen and oxygen are particularly effective at carrying spin density, explaining the remarkable stability of verdazyl, nitronyl nitroxide, and nitroxide radicals like TEMPO (figure 2.9), in which the unpaired electron is extensively delocalized over the heteroatoms.[37, 58-62]

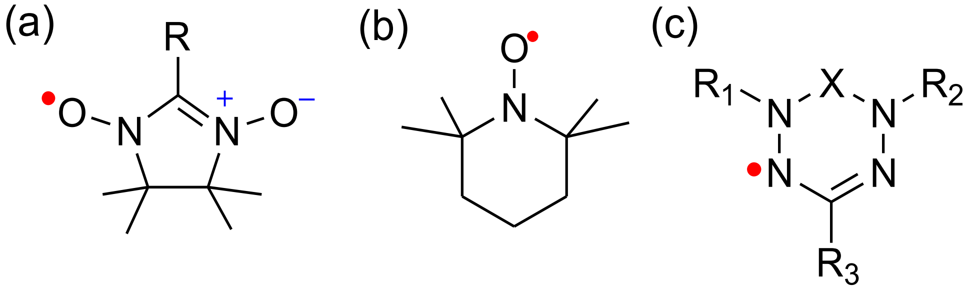

Figure 2.9. Chemical structures of (a) nitronyl nitroxide, (b) TEMPO, and (C) verdazyl radicals. The X represents C=O or C=S bonds, whereas $R_{1\text{-}3}$ are alkyl or aryl substituents. The red dot indicates the radical.

The second route involves steric protection, where bulky substituents shield the radical center from spontaneous reactions. In this sense, the most prominent examples of this type are the trityl radicals, which remain among the most stable neutral organic radicals known so far.[37, 63, 64]

In the case of polychlorinated trityl radicals like TTM the chlorination at the para and ortho positions sterically shield the α-carbon-centered radical (figure 2.10 a) which enhance the chemical stability.[64-66] Thus, the replacement of hydrogen for chlorine atoms increases the dihedral angle between the aryl rings and the SP^2 α-carbon plane to approximately 48^0, which decreases the spin delocalization,[16, 67-69] and hence decreases its chemical stability, being the unpaired electron primarily localized on the central α-carbon, with only minor delocalization onto the ortho and para carbons of the phenyl rings.[69] Another chemically stable trityl open-shell fluorophore is the perchlorotriphenylmethyl (PTM) radical (figure 2.10 b) where the steric protection provided by the chlorine atoms afford kinetic and thermodynamic stability to the α-carbon-centered radical.[70] Furthermore, in PTM compared to TTM the spin is entirely localized at the tertiary α-carbon as a consequence of an increment of the dihedral angle to 50°,[71, 72] making TTM the most chemically stable among them.

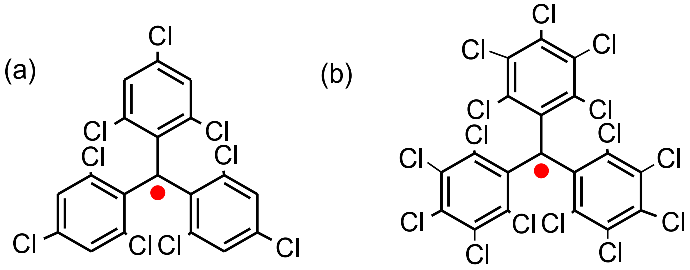

Figure 2.10. Chemical structure of (a) tris(2,4,6-trichlorophenyl)methyl (TTM) radical, and (b) perchlorotriphenylmethyl (PTM) radical. The red dot indicates the α-carbon-centered radical.

Despite its high chemical stability both TTM and PTM photodegrades fast when exposed to light. Therefore, another critical factor to consider for the practical implementation of polychlorinated trityl organic radicals relies on their photostability. Thus, under continuous illumination triarylmethyl radicals undergo photochemical degradation, which constitute a key limitation that prevent their practical usefulness to be fully exploited.[37] For example, TTM photodegrades in < 1 min under pulsed excitation.[49, 73] Although the photostability of trityl radicals can be improved in the absence of both oxygen and solvent, bimolecular degradation dominates at high concentrations.[74-76]

The photodegradation mechanism of TTM is analogous to that of the PTM radical. This involves C–Cl bond cleavage upon photoexcitation, followed by intramolecular cyclization to the perchloro-9-phenylfluornyl radical.[77] It has been proposed that TTM photodegrades similarly.[78] Identifying the photodegradation mechanism has been important for rationally designing subsequent derivatives of TTM with improved photostability.

The molecular design rules that have been established include increasing steric bulkiness at the radical center to prevent radical coupling by further promoting electron delocalization across the π-framework**.** Substituting the chlorines of TTM with other halogens such as bromines[79, 80] and iodines[81] were also successful approaches for improving the photostability. Finally, substituting trityl radical with electron aromatics such as pyridine was used to increasing the photostability while tuning the photophysical properties.[82-85] For example, this allows for both the absorption and emission to be shifted to the visible, opening the possibility of using the radicals as active materials for optical applications such as lasers and emitting devices.[35, 47, 86-88] Spectroscopic tuning has been further possible by varying the electronic richness of the substituting aromatic to include anthracene, carbazole and triphenylamine.[73, 89-93] Their added advantage is improved photostability of the radical, especially when further substituting carbazole with carbazoles.[89]

2.2.2. Near-infrared trityl organic radicals

Given the remarkable chemical stability of polychlorinated trityl radicals, subsequent molecular design efforts have focused on tuning their optical properties.[37, 41] In this sense, shifting their emission toward the near-infrared (NIR) region through molecular design constitute a challenge due to the increment of non-radiative process that decrease or quench the emission. Thus, the enhancement of non-radiative molecular decay can be rationalized by the energy gap law (equation 1), which empirically relates the non-radiative rate constant (k_{nr}) to the energy difference between two electronic states (ΔE).[94, 95]

$$k_{nr} = Ae^{-\gamma \Delta E} \ (\mathbf{1})$$

where, A is a pre-exponential factor, and γ denotes an empirical parameter associated with the strength of vibronic coupling.[94] Hence, according to this law as long as the emission is shifting towards longer wavelengths, the energy gap will decreases and the k_{nr} will therefore increase. However, even though most of reported TTM derivatives which emit in the NIR have fluorescence quantum yield (Φ_{fl}) values between 0.0032 – 6.0 %,[73, 96-98] a remarkable exemption that violates the energy gap law is found in a polychlorinated trityl radical, where a triphenylamine (TPA) moiety is directly attached to the electron acceptor TTM core, has been reported.[99]

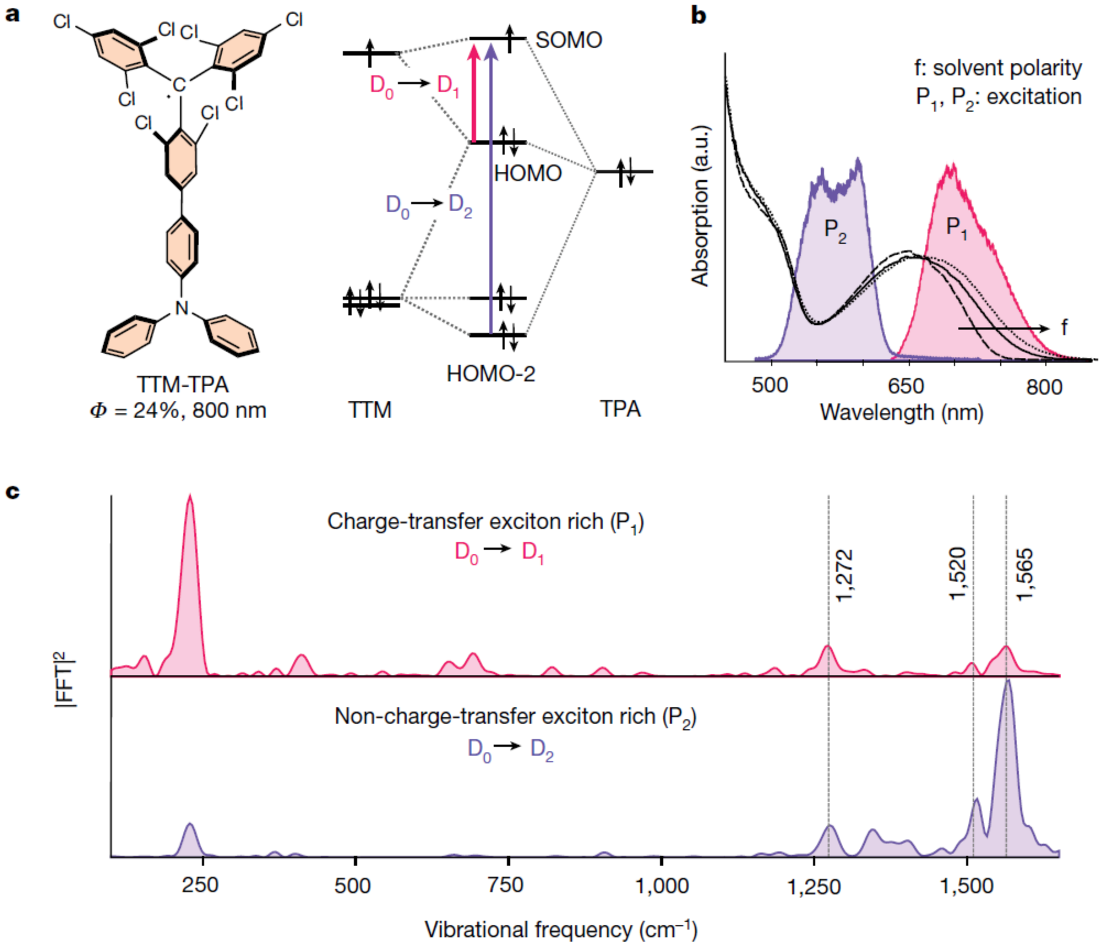

Figure 2.11. (a) Chemical structure of NIR-emissive radical TTM-TPA and its corresponding molecular orbital diagram, illustrating the two lowest energy electronic transitions addressed in the band-selective excitation experiment (indicated by the magenta and purple arrows). Energy levels in the molecular orbital diagram are not drawn to scale. **(b)** Steady-state absorption spectra of TTM-TPA recorded in solvents of increasing polarity (from cyclohexane to chloroform to tetrahydrofuran). The shaded magenta and purple regions denote the spectral profiles of the impulsive pump pulses (P_1 and P_2) used to selectively excite the respective transitions. **(c)** Excited-state vibrational spectra derived from vibrational coherence generated on early femtosecond timescales (100 -1,250 fs) following excitation with the magenta and purple impulsive pumps. This figure was modified from reference [99]

TTM-TPA emits at 800 nm while exhibits a $\Phi_{fl} = 24$ % in toluene (figure 2.11 a), which is unusually high for NIR-radical emitters.[99] In this regard, it has been reported that non-radiative recombination rates in organic molecules are typically accelerated by coupling to high-frequency molecular vibrations, especially C-C stretch modes (1000 – 1600 cm^{-1}).[100, 101] Thus, when TTM-TPA is excited to its CT state ($D_0 \rightarrow D_1$ transition), the excited-state vibrational spectrum is dominated by low-frequency modes below 250 cm^{-1}, with only a minor contribution from high-frequency modes in the 1272-1570 cm^{-1} range (figure 2.11 c). Hence, the reason of this energy gap violation is related to the suppression of non-radiative decay rates by avoiding coupling to the vibrational modes that typically accelerate non-radiative losses. Thus, the decoupling of its lowest energy electronic transition ($D_0 \rightarrow D_1$) from high frequency molecular vibrations effectively suppresses non-radiative channels, increasing its otherwise low Φ_{fl}.[99]

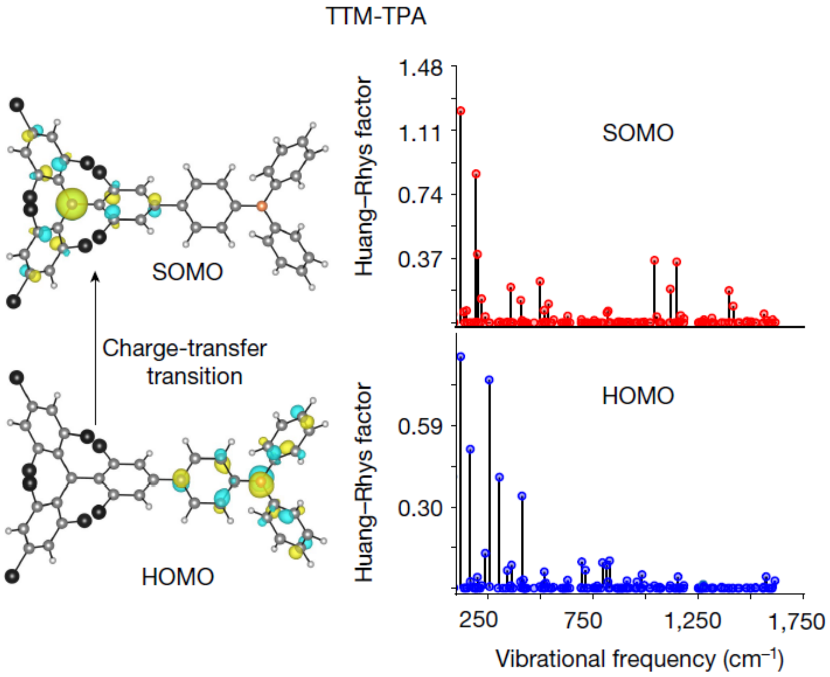

Figure 2.12. (a) Vibrational coupling to the frontier molecular orbitals of TTM-TPA obtained from first principles DFT calculations, where the HOMO is localized on the central nitrogen atom and exhibits a non-bonding character, reflecting a lower coupling to high-frequency phenyl ring stretching modes. Moreover, as depicted in the above figure the SOMO also display a non-bonding character and suppressed high-frequency coupling relative to the HOMO. This figure was modified from reference [99]

As illustrated in figure 2.12 another critical design rule that helps to decouple the exciton from high-frequency vibrational modes relies on the non-bonding character of both HOMO and SOMO levels. In this regard, the TPA donor moiety utilizes a nitrogen p_z-centered non-bonding type

HOMO, which is not strongly coupled to the high-frequency phenyl rings stretching vibrations. Moreover, the SOMO level localized on the TTM moiety also has a non-bonding character.[99] Hence, the presence of non-bonding orbitals in TTM-TPA helps to suppress non-radiative process allowing a moderate Φ_{fl} despite a low energy gap.

In this section the luminescence of polychlorinated NIR-radicals has been briefly discussed. Now the focus will be centered to the electrochromic behaviour of electrochromic radicals.

2.2.3. Electrochromic organic radicals

Developing displays that have reduced blue emission has gained interest during the last decades.[102, 103] This is to prevent eye discomfort to users during prolonged use.[102] Electrochromic devices (ECDs) are a viable solution to ocular discomfort because of their outdoor readability and no blue emission. The advantage of such devices is the color is generated either by reflected or transmitted light in response to an applied electrical stimuli, rather than by emission as with convention displays.[104-106] The operation of ECDs is therefore not reliance on blue emission. Thus, since 1969 when the first electrochromic device was reported several efforts have been made towards developing novel electrochromic materials capable of rapid and reversible optical modulation across a broad spectral range spanning the UV–Vis–NIR region.[104, 107]

ECDs are reliant on electrochromes as the active materials. These undergo reversible transmittance or reflectance change with an applied potential. Electrochromes absorbing in the NIR have gained considerable interest because their change in optical transmission with applied potential that is ideally suited for optical communication (figure 2.13).[108]

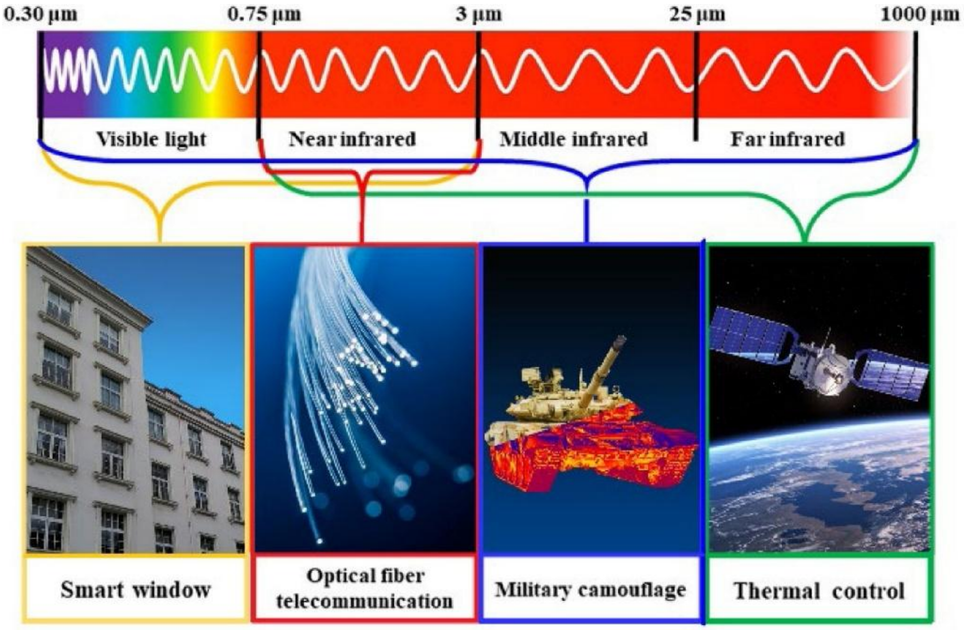

Figure 2.13. Schematic representation of the electromagnetic spectrum from the visible to the far-infrared region and representative technological applications of each range.[108]

Desired visible to NIR color changes with applied potential can be rationally designed.[108-110] Several strategies have been developed toward such reversible color changes such as covalent-organic framework,[111-114] metal complexes,[115-119] conducting polymers,[120-123] inorganic oxides,[124-127] and organic molecules.[128, 129].

Viologens currently stand as the most extensively studied classes of organic electrochromic materials.[110, 130-133] In these systems, the colored species is not the neutral precursor but the electrochemically generated radical cation. Thus, as illustrated in figure 2.14 upon reduction of the dicationic form (V^{2+}), a radical species ($V^{\bullet+}$) is formed, which exhibits a strong absorption band in the visible region, being therefore viologens primarily visible electrochromic materials .[130, 134]

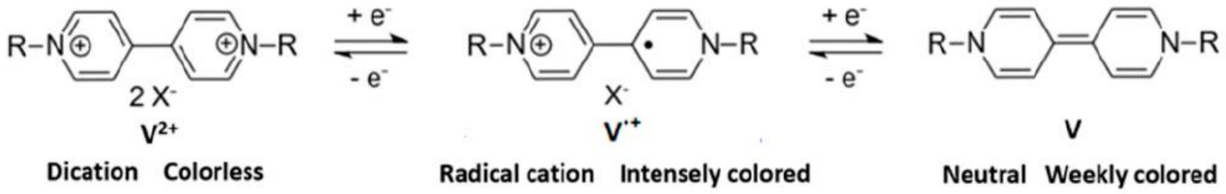

Figure 2.14. Different redox states of viologen.**[130]**

A fundamental limitation of viologen-based electrochromic materials lies in the necessity to continuously generate and stabilize the radical species under applied potential. In this regard, the radical cation is susceptible to side reactions such as dimerization, disproportionation, and degradation under prolonged cycling, which can compromise long-term stability and device durability.[135] Consequently, while viologens demonstrate efficient and reversible electrochromic behavior, their operational stability and limited NIR modulation restrict their applicability in advanced broadband electrochromic technologies. Nevertheless, viologen materials has been widely investigated due to their electrochromic properties can be modulated trough functionalization of the substituents of the pyridyl groups located on the nitrogen positions, or by interconnecting two pyridyl groups.[136] Moreover, it is worth noting that functionalization of viologen constitute an essential step towards enhancement of the stability of viologen radical-cation that form π-dimers in the solid state and undergoes reversible π-dimerization in solution.**[137]**

In the context of NIR electrochromic materials, TPA units play a central role as strong electron donors that can be covalently linked to electron-withdrawing groups to form D-A architectures.[129, 138-142] In this regard, among the different acceptor motifs available, benzothiadiazoles have been used as a versatile and robust heterocycle capable of tuning the optical and electronic properties of organic π-systems. Thus, the incorporation of benzothiadiazole units into conjugated frameworks is an interesting strategy for achieving D-A structures with controlled solid-state packing, and emission modulation. These aspects, which are particularly relevant to understand polymorphism in benzothiadiazoles derivatives are discussed in the following section.

2.3. Polymorphism in benzothiadiazole derivatives

Achieving efficient solid-state luminescence is a long-standing challenge with molecular organic fluorophores. This is owing to efficient deactivation pathways such as rotational and vibrational motions and intermolecular interactions that open efficient non-radiative excited state decay channels of fluorophores. The end result is the otherwise bright and intense emission in solution that becomes weak in the solid state for both crystals and thin films.[143-145]

2,1,3-benzothiadiazole (figure 2.15, left) ring is a strong electron-withdrawing heterocycle system that has been widely explored due to its potential as a suitable molecular building bock for D-A structures in materials science.[146-148] Thus, conjugated benzothiadiazoles consisting of the general framework represented by BZT (figure 2.15, right) stand out as true exceptions to aggregation-induced quenching that plagues the solid-state emission deactivation of conventional fluorophores. Indeed, the rigidity of the benzothiadizole minimizes torsional freedom and lowers the LUMO. This, in turn, results in high Φ_{fl} in the condensed phase.[149, 150] Further locking the central benzothiadiazole of BZT to restrict intermolecular motion courtesy of electronic donor–acceptor (D-A) and even D-A-D frameworks can increase the Φ_{fl} to near unity.[143] Such solid-state emission advantages have made BZT scaffolds choice candidates as active materials in organic light emitting diodes (OLEDs),[151, 152] fluorescence imaging probes,[153] and electrofluorochromic coatings.[129]

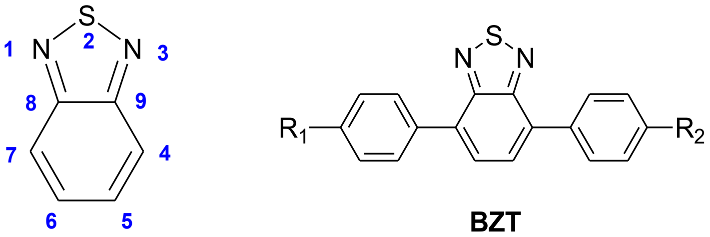

Figure 2.15. Numbering of 2,1,3-benzothiadiazole core [154] (left), and the general structure of conjugated benzothiadiazole fluorophores, BZT (right).

Polymorphism is defined as the ability of a solid compound to exist in different forms or crystallized structures that have same stoichiometry but different stabilities.[155, 156] In this regard, it is worth noting that the tendency of a compound to present polymorphism is related to the accessibility of various stable structures via crystallization,[155] leading to different photophysical behaviour. Thus, polymorphism in BZTs introduces an additional lever to tune solid-state photophysics, and therefore playing a key role in governing the properties of materials.[156, 157] For example, the bioavailability and hence the bioactivity of pharmaceuticals are underpinned by their polymorphism. Polymorphism further enriches the landscape of organic fluorophores by introducing variability in the crystal packing that can significantly influence the photophysical properties and the stimuli responsiveness of constitutionally identical fluorophores.[156] Such property tuning is valuable for mechanochromic fluorophores (MCF) whose emission wavelength can be adjusted with either crystal-to-amorphous or crystal-to-crystal changes.[158] Such phase transitions are ideally suited for applications in security printing, sensors, data storage, and bioimaging.[159] Conductivity, magnetism, fluorescence, and bioactivity are among numerous other properties that can be adjusted via polymorphism.[156] Bearing these in mind, it is of interest to understand polymorphism, in part to shift the perception that is a hindrance rather than a viable means for property modification through controlled transitions of metastable phases.

The conjugation, rigidity, and electronic transitions of BZTs are ideally suited for promoting metastable and stable polymorphs. These are further enabled by its supramolecular contacts such as antiparallel [2+2] N•••S dimers, π-π stacking, and CH•••aryl interactions that are known to direct the crystallization.[160-163] These collective attributes have been exploited to adjust the photophysical properties. For example, the fluorescence of the powder of BZT conjugated with a triphenylamine could be reversibly modified between the perceived orange and deep red emission by mechanical grinding followed by solvent-vapor annealing to change between the ground to the unground powders, respectively.[164, 165] Minor modifications to the molecular structure further cause distinct crystallization that can alter the spectroscopic properties. This was the case with BZT functionalized with electron-withdrawing groups such as -CHO/aldehyde that exhibited multiple fluorescence transitions.[166]

Despite these promising findings of emission wavelength modulation with solid-state phase changes, detailed studies correlating the molecular organization with emission of single-crystals of fluorophores are scarce. In this regard, Echeverri et al. has reported two single crystal BZT-based polymorphs where the different supramolecular organization leads to different emission and Φ_{fl} values (figure 2.16).[167] However, this study focuses mainly on the mechanochromic phase transformation and supramolecular topology of the polymorphs, rather than a systematic correlation between crystal packing and detailed photophysical behavior.

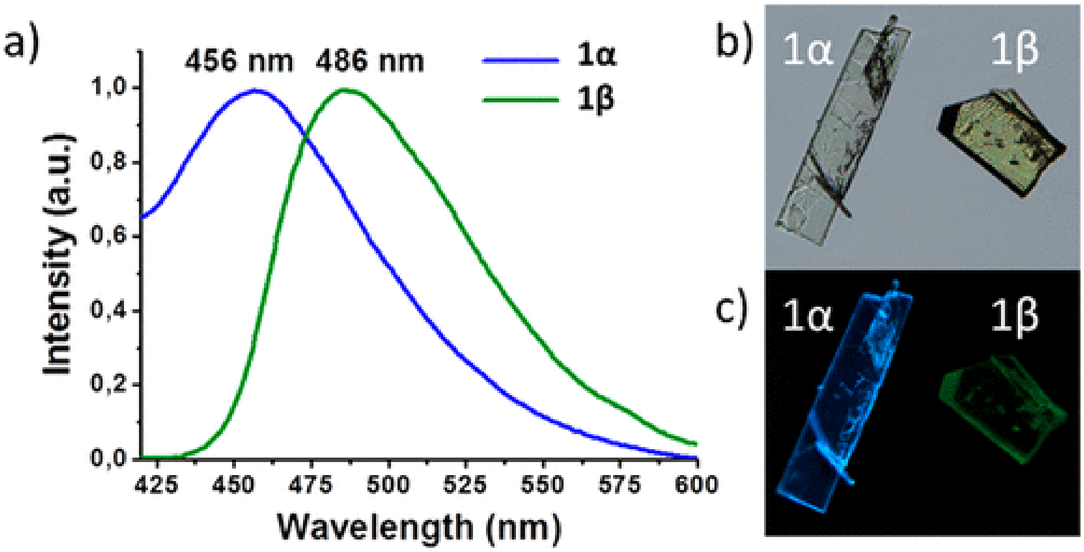

Figure 2.16. (a) Solid-state fluorescence spectra of 1α (ϕ_{fl} = 15 %) and 1β (ϕ_{fl} = 2 %) polymorphs, (b) photograph of crystals under visible light (c) and illuminated with a 365 nm UV lamp.[167]

Toward addressing this gap, the next chapter studies how photophysical properties vary between two distinct single crystal polymorphs of a conjugated D–A benzothiadiazole derivative.

CHAPTER 3 MODULATING SOLID-STATE EMISSION TRHOUGH INTERMOLECULAR INTERACTIONS IN BENZOTHIADIZOLE-BASED POLYMORPH

In this chapter two crystalline polymorphs of a conjugated organic fluorophore (**1**) were obtained through separate synthetic protocols, despite crystallizing under identical conditions.

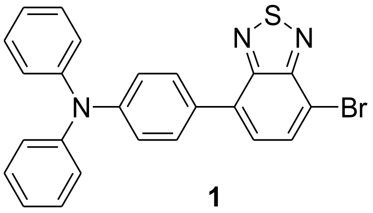

1

Figure 3.1. General structure of the conjugated closed-shell organic fluorophore (**1**).

The unique polymorphs were confirmed by single-crystal X-ray diffraction, observing that both polymorphs had markedly different supramolecular packing. Thus, Polymorph A was stabilized by directional C–H···N/S interactions with limited π overlap, while Polymorph B assembled into extended π–π stacks and a denser network with short contacts. These structural differences resulted in distinct photophysics. Indeed, the Φ_{fl} of Polymorph B was fourfold lower along with multiexponential excited state kinetics compared to Polymorph A in addition to a 38 nm blue shifted in the emission. Additionally, it was observed that the metastable Polymorph B could be converted to the thermodynamically stable Polymorph A by grinding the pristine crystal. Both intra- and supramolecular contacts could be leveraged to guide the crystal packing for modulating the emissive properties of intrinsic fluorophores.

The chapter concludes with a detailed materials and methods section outlining the synthesis, structural elucidation, crystallographic analysis, thermal characterization, and photophysical measurements employed.

To the best of our knowledge, this is one of the few examples that correlate polymorphic transformation of single crystals with their solid-state spectroscopy, especially for benzothiadiazoles such as **1**.

The experiments presented in this chapter were published in Crystal Growth & Design:

Orlando Ortiz, Mohan Raj Anthony Raj, Thierry Maris, Stéphane Kéna-Cohen, William Skene, Leveraging Intermolecular Contacts of Polymorph for Tuning Solid-State Emission, *Cryst. Growth Des.* 2026, 26, 3, 1236–1243.

The author of this thesis performed the synthesis and purification of polymorph A. Furthermore, the author carried out the crystallization, spectroscopic and photophysical characterization, and data analysis for both polymorphs.

The synthesis and purification of polymorph B was done by Mohan Raj Anthony Raj, who also provided guidance for the photophysical characterization. The SCXRD measurements and data curation was carried out by Thierry Maris. The project was supervised by Prof. Stéphane Kéna-Cohen and Prof. William Skene, who also provided conceptual guidance and critical review of the chapter.

3.1. Results and Discussion

3.1.1. Fluorophore Polymorphism

The benzothiadiazole fluorophores (**1**) were obtained via Suzuki-Miyaura cross-coupling reaction using different reaction conditions (figure 3.2). In this regard, Polymorph A was obtained using potassium carbonate, whereas using a phase transfer catalyst and potassium hydroxide as the base gave the Polymorph B, being both synthetic procedures described in detail in the experimental section of this chapter. Then, after been purified by column chromatography the benzothiadiazole derivatives (**1**) were isolated as a red and orange powders for the synthetic procedure A and B respectively (figure 3.2) and further crystallized.

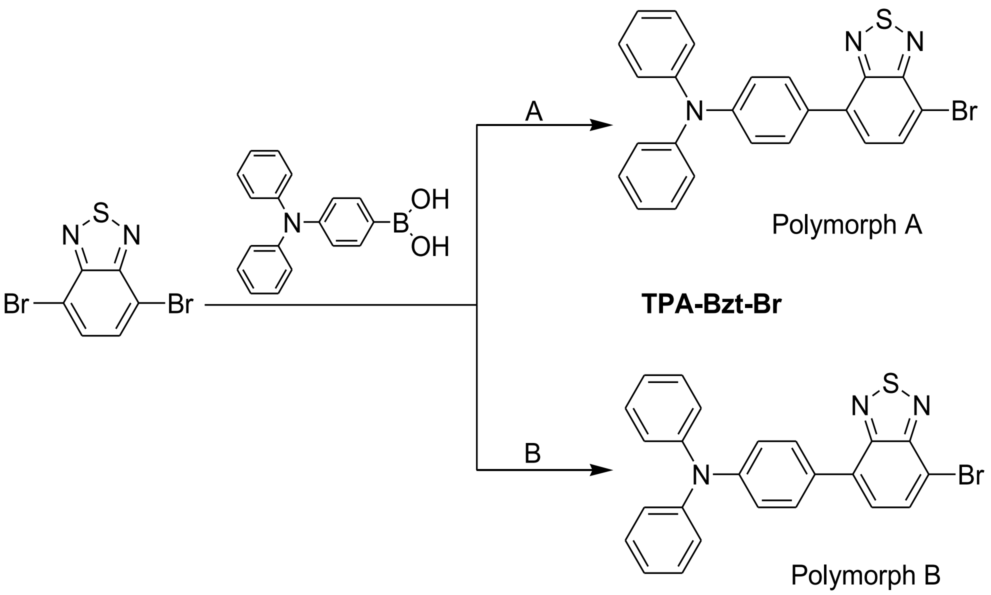

Figure 3.2. General synthetic route for the preparation of polymorphs of 1 via Suzuki-Miyaura coupling: A) K_2CO_3 (2 M) and B) KOH with cat. tetrabutylammonium bromide.

Even though the crystallization protocols were identical for the two routes, each path consistently gave the respective polymorph upon crystallization. To ensure both the product and resulting polymorphs were void of impurities, the degree of purity of the products that were isolated by column chromatography and used for crystallization was confirmed by high-performance liquid chromatography (HPLC) by (<99%, figures A.3.16 – A.3.17) along with differential scanning calorimetry (DSC, vide infra). Moreover, the consistent nuclear magnetic resonance (NMR) data confirm both polymorphs are from the identical **1** (figures A.3.10 – A.3.13) . Also, no other compounds were found in the X-ray diffractograms of the single crystals. Thus, single-crystal X-ray diffraction (SCXRD) revealed that both polymorphs of the crystallized **1** belonged to the orthorhombic system, but with different space groups: *Pbca* (Polymorph A) and $Pna2_1$ (Polymorph B). Furthermore, despite being identical, the two structures of **1** had significantly different unit cell parameters and packing arrangements according to Table 3.1. From the distinct symmetry elements and crystallographic data, the two forms are indeed polymorphs. These unique polymorphs are suitable for investigating the relationship between molecular packing and the solid-state photophysics.

Table 3.1. Crystallographic parameters of the two polymorphs of 1 .

Polymorph	Space group	Crystal system	Unit cell dimensions (Å)			Z	Volume (A^3)
			A	b	c		
A	*Pbca*	Orthorhombic	10.1597	16.55771	23.4674	8	3952.34
B	*Pna*2_1	Orthorhombic	10.9741	73.9324	7.3151	12	5935.00

3.1.2. Polymorph Photophysics

The photophysics of the two polymorphs were investigated to see whether the structure of the crystal affected the Φ_{fl}, excited state lifetime, and the emission wavelength. The two polymorphs of **1** differed markedly due to variations in their supramolecular packing (vide infra), as evidenced by both the steady-state and the time-resolved measurements. The polymorphs fluoresced differently, shifted by 38 nm. Polymorph A emitted at 624 nm while the emission of Polymorph B was relatively hypsochromic, emitting at 586 nm (figure 3.3 A). The different fluorescence of the two polymorphs can readily be discerned as perceived red and yellow emission for Polymorphs A and B, respectively (inset figure 3.3 A). The difference in emission wavelength is a result of different organizations of **1** in the crystals (vide infra).

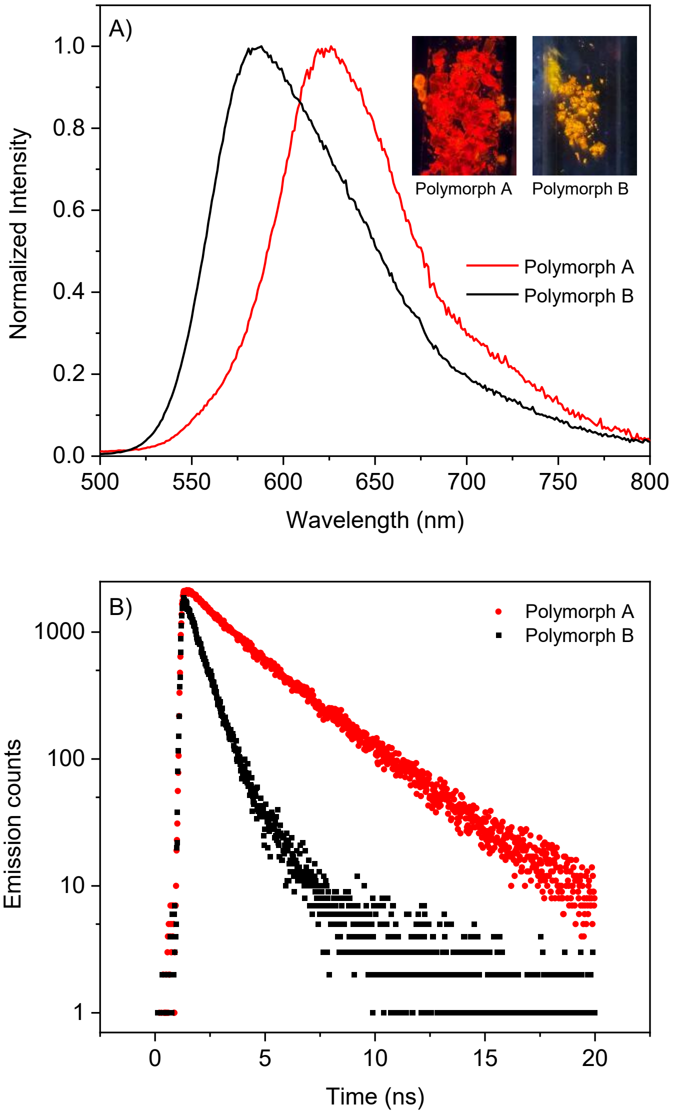

Figure 3.3. Normalized emission spectra (A) and fluorescence emission kinetic (B) of crystals of Polymorphs A (red) and B (black) of benzothiadiazole fluorophore **1**. Inset: photographs of crystals of Polymorphs A (left) and B (right) irradiated with a handheld UV lamp at 365 nm.

The Φ_{fl} and lifetime (τ) are among the most important properties of fluorophores, and were calculated from the following formulas:

$$\Phi_{fl} = \frac{k_r}{k_r + k_{nr}}$$

$$\tau = \frac{1}{k_r + k_{nr}}$$

where k_r represents the radiative rate constant while k_{nr} denotes the non-radiative rate constant.

To directly compare the Φ_{fl} of the two polymorphs and ensure its independence of variables such as excitation wavelength, material amount, crystal size, and unavailable solid-state reference, the absolute Φ_{fl} was measured using an integrating sphere. Like the emission wavelength, the Φ_{fl} of the two polymorphs was significantly different. The Φ_{fl} of Polymorph A was 33 %, whereas the orange emission of Polymorph B was fourfold lower, Φ_{fl} = 8 %. The Φ_{fl} is underpinned by the excited state lifetime, with short-excited state lifetimes and nonradiative decays giving rise to low Φ_{fl}. Bearing this mind, the time-resolved emission spectra (TRES) and excited state kinetics of the two polymorphs were evaluated to corroborate the differences in observed Φ_{fl}. The fluorescence lifetime of Polymorph A was exclusively monoexponential being $\tau = 3.56 \pm 0.02$ ns (figure A.3.3). The lifetime was constant (± 0.6 ns) across the range of emission wavelengths examined by TRES, confirming a single emissive species within a homogeneous environment. The uniform lifetime reflects a highly ordered crystalline phase with minimal conformational or energetic disorder. In contrast, the excited state kinetics of Polymorph B were heterogeneous, dominated by a biexponential decay. These could be deconvoluted into two monoexponential lifetimes of 3.68 ± 0.23 and 0.75 ± 0.01 ns, contributing to 27% and 73% of the decay, respectively. Multi-exponential lifetimes, with up to three decay components depending on the emission wavelength were observed for the TRES of Polymorph B (figure A.3.4). The emission was dominated by a short decay ($\tau_a \approx 0.08$–0.11 ns) at short wavelengths (500–540 nm), contributing upwards to 26 % of the signal. This component arises from a weakly emissive/quenched state having an efficient non-radiative decay. This is due to minor populations with less favorable packing/conformational disorder. This fast kinetic decreased when approaching the maximum emission concomitant with a slower kinetic dominating the lifetime decay ($\tau_b \approx$ 0.63–0.86 ns). This indicates a larger population of moderately emissive species within a more stabilized environment. The emission kinetics of the bathochromic region of the emission spectrum were longer-lived ($\tau_c \approx$ 3.06 – 4.20 ns). Their contribution to the decay kinetics progressively increased when shifting the emission wavelength to longer wavelengths, reaching 66 % of the signal at 700 nm. This evolution indicates spectral diffusion from the initially excited state and less emissive species toward more stabilized emissive states. The lifetime distribution is consistent with a broader distribution of local environments and dynamic relaxation pathways in Polymorph B. The variable lifetimes that are contingent on the emission wavelength confirm the broad distribution of conformers of Polymorph B that organize differently in the crystal. This contrasts with the highly emissive and consistent unimolecular kinetic of polymorph A whose crystal structure should be uniform. These aside, the marked difference in Φ_{fl} of the two polymorphs is supported by the differences in emission lifetimes. The collective steady-state and time-resolved emission underscore the impact of crystal packing on excited-state kinetics and highlight how polymorphism governs the photoemission fluorophores in the solid-state. Drawing analogies of the spectral shifts with *J* and *H* aggregates of amorphous solids,[168] the blue-shifted emission of Polymorph B, taken along with its other marked photophysical properties, suggest aromatic overlapping of **1**, whereas these are expected to be absent for Polymorph A. The 57 nm hypsochromic shift of the excitation spectrum of Polymorph B (figure A.3.2) relative to Polymorph A (figure A.3.1) further suggests face-to-face stacking similar to *H* aggregates. Indeed, overlapping aromatic contacts such π-π stacking are known modes of efficient excited state deactivation. Bearing this mind, the difference in the fluorescence Φ_{fl} can be assigned to a more rigid packing of Polymorph A that restricts non-radiative decay and facilitates radiative relaxation.

Of interest, the emission wavelength of both polymorphs when they were dissolved in dichloromethane was identical at 685 nm (figure 3.4). The lifetime was also monoexponential, albeit longer ($\tau = 6.01$ ns; figure A.3.5). The identical red-shifted emission and lifetimes in solution further illustrate the fluorophore as an in-situ sensor capable of detecting differences in organization. It is evident that the changes in emissive, Φ_{fl}, and excited state lifetime are from distinct packing motifs adopted by each crystalline form.

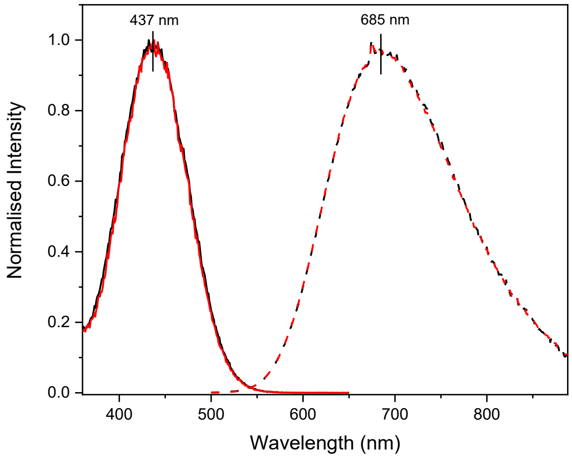

Figure 3.4. Normalized **a**bsorption (solid line) and emission (dashed line) of Polymorphs A (red) and B (black) in CH_2Cl_2.

3.1.3. Structural Origin of the Distinct Photophysical Behavior

SCXRD provided evidence of the solid-state structure that was responsible for the contrasting photophysical of the two polymorphs of **1**. Polymorph A was characterized by Z′ = 1, indicating a single independent molecule in the asymmetric unit cell, whereas polymorph B displayed Z′ = 3, containing three crystallographically independent molecules.

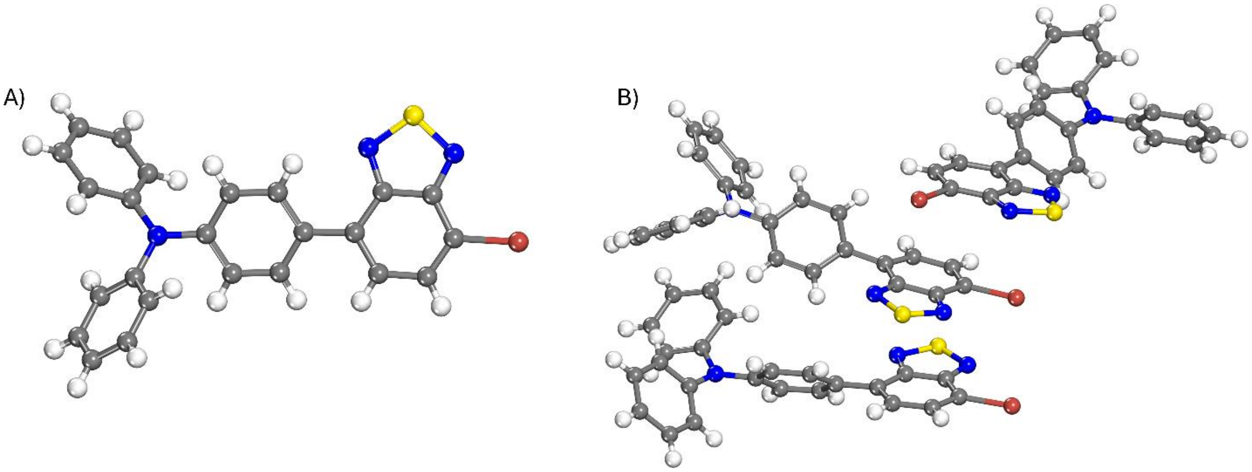

Figure 3.5. Asymmetric unit of Polymorphs A (A) and B (B). Color code of atoms: C = grey, H = white, N = blue, S = yellow, Br = brown.

An overlay of these three molecules revealed modest yet significant variations in torsions around the donor–acceptor bond and for the local intermolecular contacts. Such deviations, though subtle at the molecular level, translate into distinct packing environments within the same crystal. These are responsible for the multiple emissive species and broader lifetime distributions observed by the TRES. DSC further supported this according to the crystal melting temperatures. Polymorph A had a single melting transition that was sharp at 166.8 °C, consistent with a uniform packing motif. This contrasted with Polymorph B that had two distinct melting events . The first was at 150.1 °C and the second at 166.8 °C, coinciding with the melting point of Polymorph A (figure 3.6). The near equal intensity of the two thermal events precludes a contaminant that would have otherwise been evident in the other characterization methods. The lower temperature melting point is consistent with a phase transition from Polymorph B to Polymorph A upon heating. The near equal intensity of the two thermal events precludes a contaminant that would have otherwise been evident in the other characterization methods. The lower temperature melting point is consistent with a phase transition from Polymorph B to Polymorph A upon first heating cycle. The two thermal transitions observed in Polymorph B are consistent with different molecular environments within the polymorph packing, in line with its higher Z' value and the packing heterogeneity. These are responsible in part for the observed differences in the emission wavelength, Φ_{fl}, and excited state lifetimes.

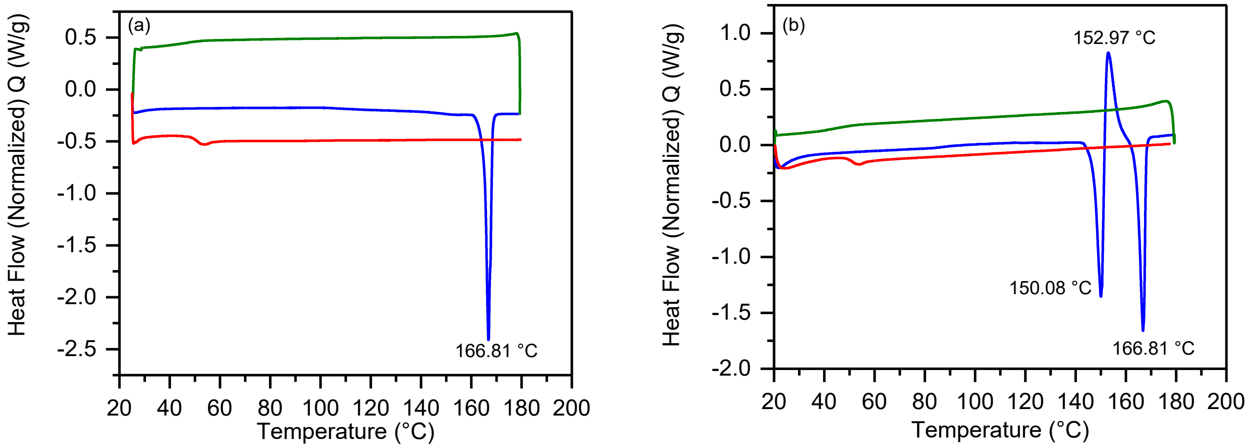

Figure 3.6. Differential scanning calorimetry of Polymorph A (a) and B (b) measured in both cases at 5 ^{o}C/min to 180 ^{0}C (heating 1, blue), followed by cooling process (100c/min to 25 ^{0}C, green), and isothermal of 25 ^{0}C for 1 min (green), and finally a second heating depicted in red (10 ^{0}C/min to 180 ^{0}C).

The Hirshfeld surface analysis (HSA) provides further insight into the asymmetric units and the packing heterogeneity of the two polymorphs. CH···N/S interactions of the benzothiadiazole dominate in Polymorph A. Thus, the 2D fingerprint plot indicate that H···H and C···H interactions dominate in both polymorphs (table A.3.2), which is consistent with previously reported data for a structurally similar compound.[169] These are according to the visible contacts in the d_{norm} map (red spots, figure 3.7 A, C). Spatially limited π–π contacts are also present. These are derived from isolated and discontinuous red/blue triangular pairs in the corresponding shape index map. On the other hand, a denser distribution of short contacts over the aromatic regions takes place in Polymorph B (figure 3.7 B, D). These are complemented with multiple π–π stacking motifs between neighboring aromatics according to the shape index map of complementary red/blue patches. Collective, the HSA indicates that Polymorph A is stabilized mainly by directional C–H···N/S interactions with only a modest π overlap. This contrasts with Polymorph B that has a persistent and heterogeneous sets of π–π contacts. These are responsible for the different solid-state emissions of the two polymorphs. The more rigid and locally fixed π–π contacts in Polymorph A correlate with its higher Φ_{fl} and nearly single-exponential decays. Whereas the rich and extended π-stacking of Polymorph B quenched the fluorescence and their broad distribution is responsible for the multiexponential TRES.

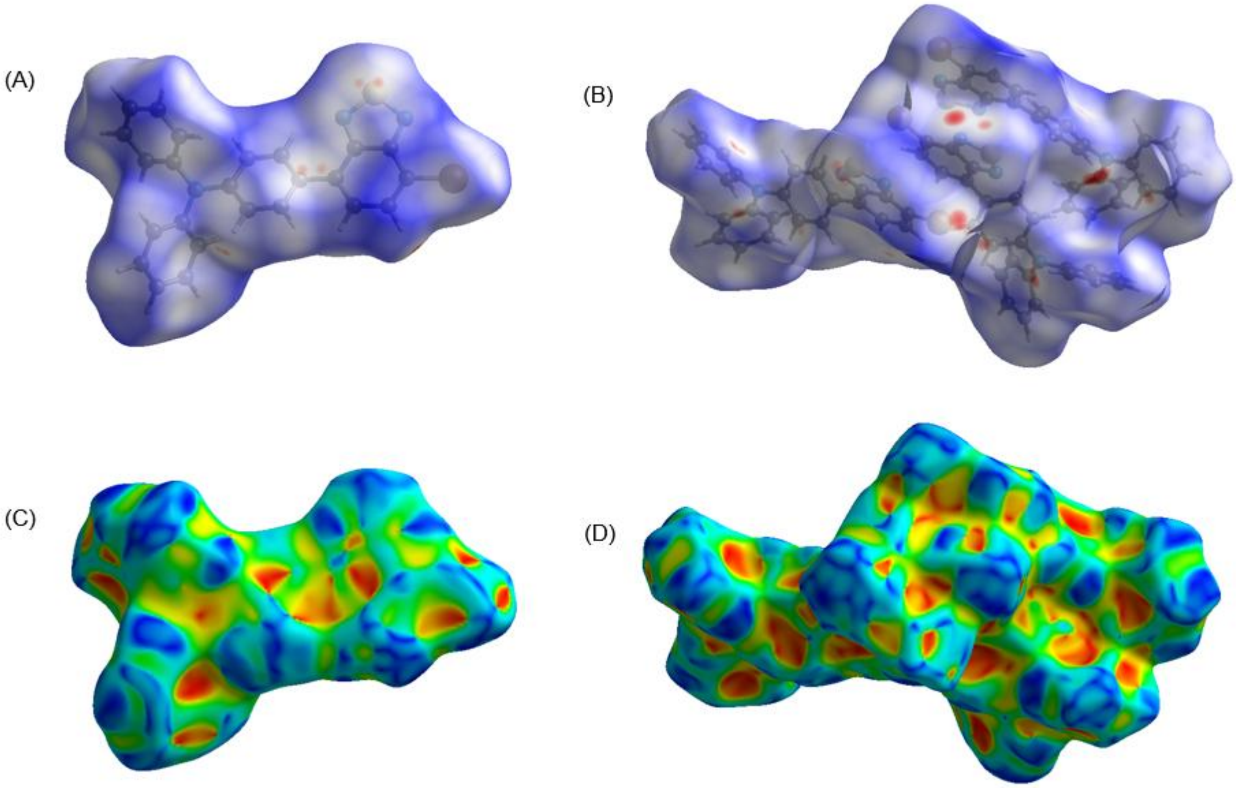

Figure 3.7. Hirshfeld surface analysis of the two polymorphs of **1**. Polymorphs A (left) and B (right) showing d_{norm} (transparent; top) and shape index surfaces (bottom).

The crystal packing provided further evidence of the distinct intermolecular contacts of the two polymorphs. The molecules were tilted in the cell and they were offset with slipped π–π interactions (with centroid-centroid separations in the 4.08-4.38 Å range and slippages of about 2.3 – 2.8 Å) occurring only locally in Polymorph A (figure 3.8 A). Additional C–H···π interactions reinforce the packing with contacts exhibiting H···centroid distances near 2.83 Å and C–H···centroid angles close to 145°, characteristic of moderate dispersive hydrogen contacts. These were complemented with directional C–H···N/S contacts that anchor the benzothiadiazole moiety. This packing motif restricts extended π-overlap, leading to a relatively open framework where interactions were spatially confined. On the contrary, a different supramolecular architecture was adopted by Polymorph B (figure 3.8 B). The molecules assembled into continuous extended face-to-face stacking along the crystallographic b-axis, with centroid-to-centroid separation distances as low as 3.6397(14) Å and 3.6644(1) Å, favoring recurrent π–π contacts between adjacent aromatic units, with small slippage (0.3 - 1.7 Å) and interplanar angles (less than 10°). Several C–H···π interactions complement this stack network and bridge neighbouring columns. These include interaction between ring centroid (Cg) with H16B -C16B (H···Cg = 2.84 Å) and H17B-C17B (H···Cg = 2.83 Å), with C–H···centroid angles in the range 132–155°, consistent with significant edge-to-face dispersive contacts that reinforce the stacking. This extended stacking network is accompanied by a denser distribution of short intermolecular interactions, producing a more compact and heterogeneous packing environment.

A distinctive stabilizing feature of polymorph B is the presence of short coplanar heteroatom contacts between sulfur and nitrogen, with distances N1A···S1B at 3.251 Å and S1A···N2B at 3.135 Å; both distances are shorter than the sum of van der Waals radii (3.35 Å), so indicative of directional chalcogen–nitrogen interactions. The contrast between the localized, directionally fixed packing in Polymorph A and the π-stacking-rich motif of Polymorph B is consistent with their solid-state photophysics: Polymorph A favoring radiative decay and quenched fluorescence of Polymorph B by π-π interactions.

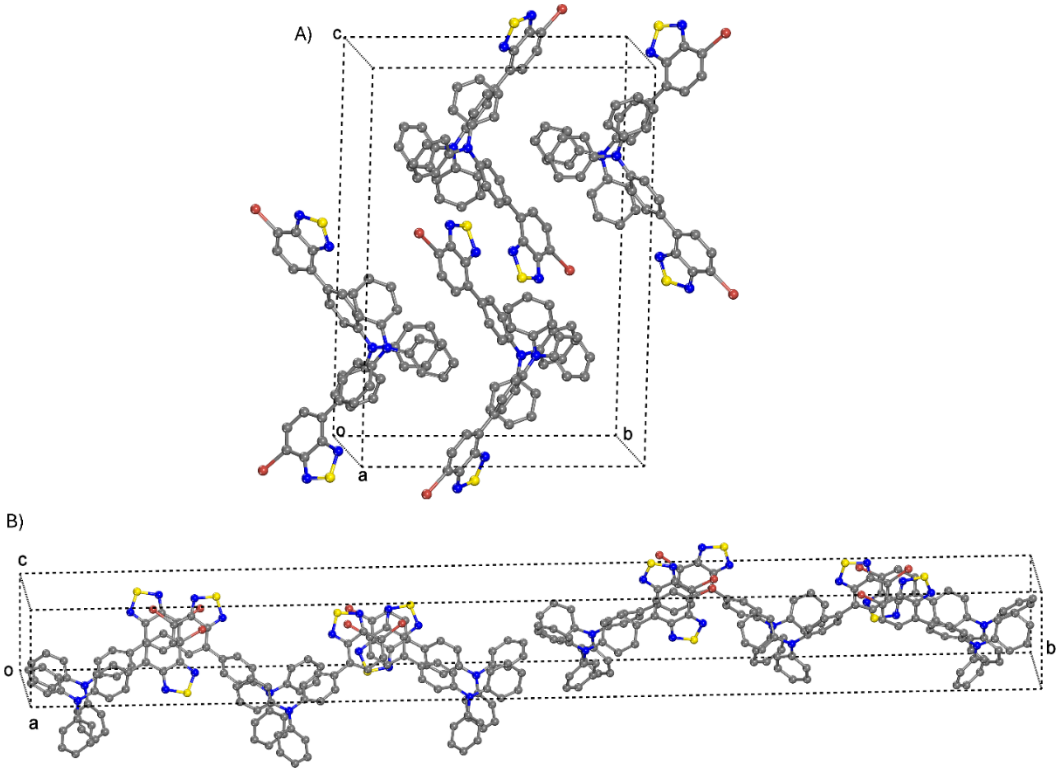

Figure 3.8. Crystal packing of the polymorphs of **1**. A) Polymorph A, viewed to show the inclined, offset orientation of neighboring molecules with limited face-to-face aromatic overlap. B)

Polymorph B, highlighting columns propagating along the *b* axis in which adjacent aromatic motifs engage in recurrent π-stacking contacts.

3.1.4. Polymorph Selection Driven by Crystal Packing

Mechanical grinding of the polymorphs was done to provide insight into their stability. A change in emission would indicate a change in polymorphism. The solid-state emission of the two polymorphs of **1** changed significantly when grinding the crystals (figure 3.9). This further illustrates the sensitivity of the fluorophore for reporting structural perturbations. The initial deep red emission centered at 624 nm of Polymorph A hypsochromically shifted to 608 nm with grinding. Similarly, the orange crystals of Polymorph B bathochromically shift to 611 nm with grinding. The emission of the two polymorphs after grinding was consistent with the emission of the pristine powder of **1**.[164] This suggests that stress from grinding disrupts the ordered packing in both crystals, leading to the energetically more favorable polymorph.

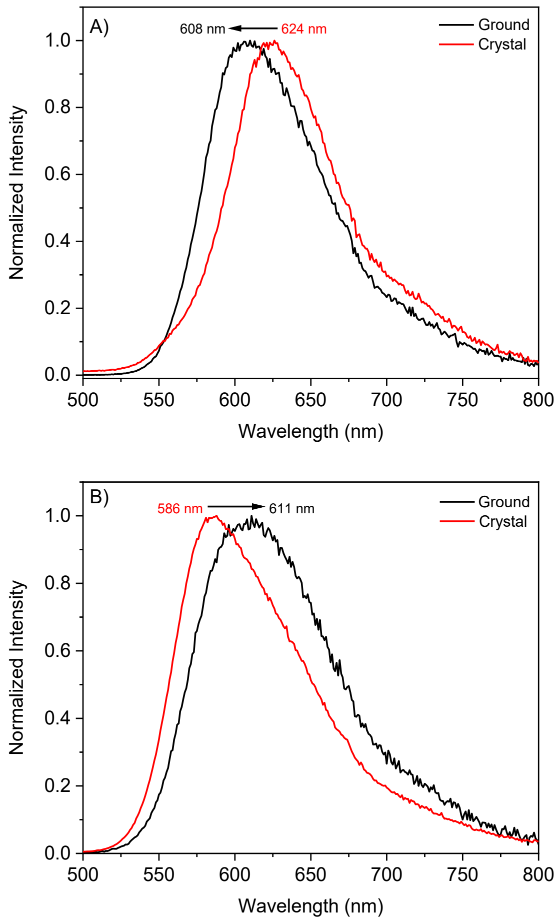

Figure 3.9. Normalized solid-state emission spectra of crystals of Polymorphs A (A) and (B) before (black) and after (red) grinding.

To further explore the reversibility of each polymorph, both grounded powders were redissolved in dichloromethane and then recrystallized with identical conditions. Remarkably, despite being different crystalline polymorphs, both samples yielded crystals whose structures, determined by single-crystal X-ray diffraction, corresponded to Polymorph A (figure A.3.9). This indicates a thermodynamic preference for Polymorph A, being the most thermodynamical stable polymorph, consistent with the DSC measurements. The exclusive formation of Polymorph A further suggests that Polymorph B is a metastable form that reverts to its thermodynamically favored structure after grinding and further recrystallization. This is further consistent with what is known about high-energy Z' structures that relax to their thermodynamically stable structures.[157, 170]

These results clearly show that differences in molecular packing have a direct impact on the persistence of each polymorph under external stimuli. The fact that both forms convert to polymorph A upon grinding indicates that this structure represents the lowest-energy structure under the applied conditions. This observation reinforces the idea that crystal packing not only governs the photophysical behavior but also dictates the relative stability of the solid forms.

3.2. Materials and Methods

Synthesis

Synthesis of 4-(7-bromobenzo[c][1,2,5]thiadiazol-4-yl)-N,N-diphenylaniline (1)

Polymorph A

4,7-Dibromobenzo[c][1,2,5]thiadiazole (2.00 g, 6.8 mmol) and 4-(diphenylamino)phenylboronic acid (1.97 g, 6.8 mmol) were dissolved in THF (50 mL). Then 2 M aqueous K_2CO_3 solution (10.2 mL) was added. The mixture was degassed for 5 min, and tetrakis(triphenylphosphine)palladium(0) ($Pd(PPh_3)_4$; 0.31 g, 0.27 mmol) was added. Afterwards, the solution was degassed for 15 min under nitrogen. The mixture was stirred and heated at 80 °C for 6 h. After cooling the reaction mixture to room temperature, the crude product was extracted with dichloromethane (3 × 60 mL). The organic layer was dried over anhydrous $MgSO_4$ and filtered, and the solvent was evaporated. Then, the crude product was purified by silica gel chromatography using n-hexane/dichloromethane (6:1) as eluent. The product was isolated as a red solid (2.3 g, yield 62%). ^1H NMR ($CDCl_3$, 400 MHz) δ ppm: 7.91 (d, J = 7.6 Hz, 1H), 7.82 (d, J = 8.8 Hz, 2H), 7.56 (d, J = 7.6 Hz, 1H), 7.32-7.28 (m, 4H), 7.20-7.17 (m, 6H), 7.08 (t, J = 7.3 Hz, 2H). ^{13}C NMR ($CDCl_3$, 100 MHz,) δ ppm: 153.9, 153.2, 148.4, 147.3, 133.6, 132.4, 129.9, 129.4, 127.3, 125.0, 123.5, 122.6, 112.2. ESI-MS $[M+H]^+$: m/z calcd for $C_{24}H_{16}BrN_3S$ 458.0321, found 458.0313.

Polymorph B

4,7-Dibromobenzo[c][1,2,5]thiadiazole (2.00 g, 6.8 mmol) and 4-(diphenylamino)-phenylboronic acid (1.97 g, 6.8 mmol) were dissolved in anhydrous and deaerated toluene (50 mL) and an aqueous solution of potassium hydroxide (2 M, 10.2 mL water). A catalytic amount of tetrabutylammonium bromide (TBAB) was then added to the mixture. The reaction mixture was purged with N_2 for 15 mins and a catalytic amount of $Pd(PPh_3)_4$ was added to the mixture under nitrogen. The mixture was heated to 100 ˚C and stirred overnight under nitrogen. After cooling to room temperature, the mixture was washed with water, and it was extracted with dichloromethane. The crude product was purified by silica gel column chromatography using dichloromethane/hexane (v/v = 1:6) as eluent. The title compound was obtained as an orange solid (2.5 g, 68%). ^{1}H NMR ($CDCl_3$, 400 MHz) δ 7.93 (d, J = 7.6 Hz, 1H), 7.84 (d, J = 8.8 Hz, 2H), 7.58 (d, J = 7.6 Hz, 1H), 7.38 – 7.30 (m, 4H), 7.26 – 7.19 (m, 6H), 7.11 (t, J = 7.3 Hz, 2H). ^{13}C NMR ($CDCl_3$, 100 MHz) δ ppm = δ 153.97, 153.16, 148.45, 147.34, 133.57, 132.38, 129.91, 129.84, 129.42, 127.34, 125.05, 123.53, 122.63, 112.19, ESI-MS [M+H]$^+$: m/z calcd for $C_{24}H_{16}BrN_3S$ 458.0321, found 458.0313.

Single-crystal X-ray diffraction

For both polymorphs, SCXRD data were collected at 150 K from shock-cooled crystals mounted on a Bruker Venture diffractometer equipped with a κ-geometry goniometer and a Bruker Photon III CMOS detector. A MetalJet X-ray source with Helios MX mirror optics was used to generate Ga Kα radiation (λ = 1.34139 A). Data collection, integration, and scaling were performed using the SAINT software package (Bruker, 2013),[171]-and a multi-scan absorption correction was applied with SADABS 2016/2.[172] The crystal structures were solved using dual-space methods with *XT*,[173] and refined by full-matrix least-squares on F^2 using *XL,*[174] within the OLEX2 software environment.[175] All non-hydrogen atoms were refined with anisotropic displacement parameters. Hydrogen atoms were positioned geometrically and refined isotropic on calculated positions using a riding model with their U_{iso} values constrained to 1.2 times the U_{eq} of their pivot atoms. CIF files and final reports were generated using FinalCif.[176]

Thermal measurements

DSC measurements were performed on a TA Instruments DSC 500 calorimeter, equipped with a refrigerated cooling system. Samples (~3–5 mg) were placed in aluminum pans and analyzed under a nitrogen flow (50 mL min^{-1}) at a heating rate of 5 °C min^{-1} over the temperature range of 20–180 °C.

Fluorescence measurements

Fluorescence measurements were carried out with a combined steady-state and time-resolved spectrometer (FLSP-920 Edinburgh Instruments). Emission spectra were recorded with two detectors: (1) a standard photomultiplier for the UV–visible range (220–800 nm), and (2) a fast multichannel plate detector for time-resolved measurements, offering picosecond resolution for fluorescence lifetimes. Steady-state emission spectra and absolute quantum yields (Φ_{fl}) were measured using a quartz cuvette with an inner path length of 1 mm, specifically designed for solid-state measurements. The samples were deposited directly onto the inner wall of the cuvette without any dispersing medium. The cuvette was sealed with black tape to prevent light leakage. An identical empty cuvette was used as a blank reference during the Φ_{fl} measurements to correct for background and scattering effects.[177] The Φ_{fl} values were measured with a calibrated integrating sphere.

Lifetime and TRES measurements were made by exciting the given fluorophore crystals with a 405 nm picosecond laser diode. The kinetics were recorded with a time correlated single photon counting system (TCPCS; Edinburgh Instruments). The kinetics were subsequently fitted with commercial software using mono, and biexponential fits, accordingly, to obtain the singlet excited state lifetimes having the best correlations. The instrument response frequency (IRF) was removed from the fast component of the kinetic signal by the reconvolution fitting method, using commercially available software. The IRF was determined using the scattering from a white cardboard card placed at 45° in the cell holder

CHAPTER 4 ENHANCING THE PHOTOSTABILITY OF OPEN-SHELL FLUOROPHORES AND NIR EMISSION VIA ELECTRON DONATING SUBSTITUENTS

As shown in section 2.2.1 the photostability of organic radicals constitutes a significant drawback when it comes to their application. Hence, this chapter focuses on the synthesis of two novel NIR photostable open-shell fluorophores via coupling the electron acceptor trityl moiety to the electron donating carbazole and its functionalized carbazoles analogues. Towards this goal, we synthesized four organic radicals whose chemical structures are illustrated in figure 4.1 being **1** and **2** the unsubstituted and carbazole substituted trityl radicals, respectively. Despite the structural variations of **2** the photostability of such open-shelled chromophore has not yet reached a level that is adequate for their use in tangible applications.

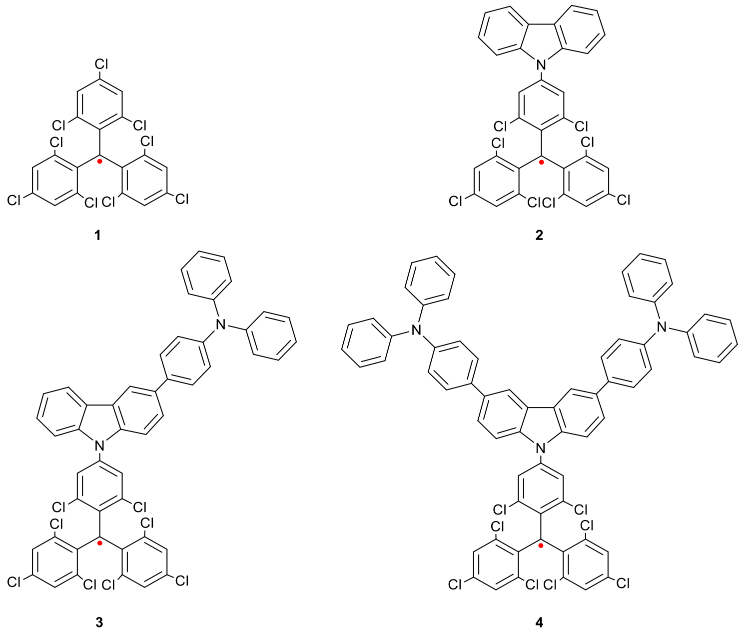

Figure 4.1. Carbon-centered radicals investigated (**3-4**) for improved photostability along with their unsubstituted perchlorotriphenylmethyl (**1**) and carbazole benchmark (**2**) counterparts.

To further study this problem, a series of carbazole-substituted trityl radicals were developed and investigated (**3** and **4**). Strong electron-donating triphenylamines were chosen given that charge transfer character of the radical is known to be an important factor determining photostability,[178, 179] due to an increment of the spin delocalization, which stabilize the radicals and therefore reducing the probabilities of C-Cl photocleavage responsible of photodegradation in trityl radicals.

Furthermore, leveraging intramolecular charge transfer with such donating groups allows the absorption and the emission of the radical should be shifted deep into the visible and NIR regions, respectively. Red-shifting the spectroscopic properties would be useful for quantum technology applications where optically tunable organic radicals are desirable, providing their photostability and efficiency match the application requirements.[93, 180] Triphenylamines are further advantageous because they can readily be functionalized, opening the possibility of integrating chemically stable carbon radical into a broad ensemble of uses such as polymers, functionalized surfaces, and thin films to name but a few.

Herein, we find that the extended π-conjugated framework of the new radicals allows to improve the photostability by more than 1000 fold under continuous irradiation compared to the unsubstituted radical counterpart. Both the absorption and emission are shifted into the red and NIR regions in solution (> 750 m), respectively, due to strong intramolecular charge transfer. Although, low Φ_{fl} in solution (0.5 – 0.6 %) and solid-state (3.0 – 7.0 %) were achieved.

This chapter concludes with a detailed materials and methods section outlining the synthesis, structural elucidation, theoretical calculations, crystallographic analysis, thermal characterization, and photophysical measurements used.

4.1. Results and Discussion

4.1.1. Radical Synthesis

The synthesis of both fluorophores (**3** and **4**) was carried out in a multi-step procedure. In this regard, it starts with the synthesis of compound **6** via the Friedel–Crafts alkylation of 1,3,5-trichlorobenzene with chloroform in the presence of $AlCl_3$. Then, the corresponding **6** radical was generated by a standard deprotonation-oxidation sequence.[35, 78, 90] This stage defines the open-shell core and provides a robust handle for chemical diversification.

The next step was focused on the synthesis of the donor fragments (**7** and **8**), which were prepared independently, through Suzuki-Miyaura coupling of the triphenylamine boronic acid with the corresponding bromo carbazole. Subsequently, the obtained donor moieties were coupled to the trityl framework through a nucleophilic aromatic substitution reaction allowing the obtention of the closed-shell radical-precursors (**9** and **10**). Finally, the targeted open-shell fluorophores (**3** and **4**) were synthesized via the same strategy used for radical **6** (figure 4.2). Moreover, all synthesised organic radicals were chemically stable allowing their purification and isolation by column chromatography.

Detail information regarding the synthetic procedure for both closed-shell intermediates and final open-shell fluorophores is reported in the materials and methods section of this chapter.

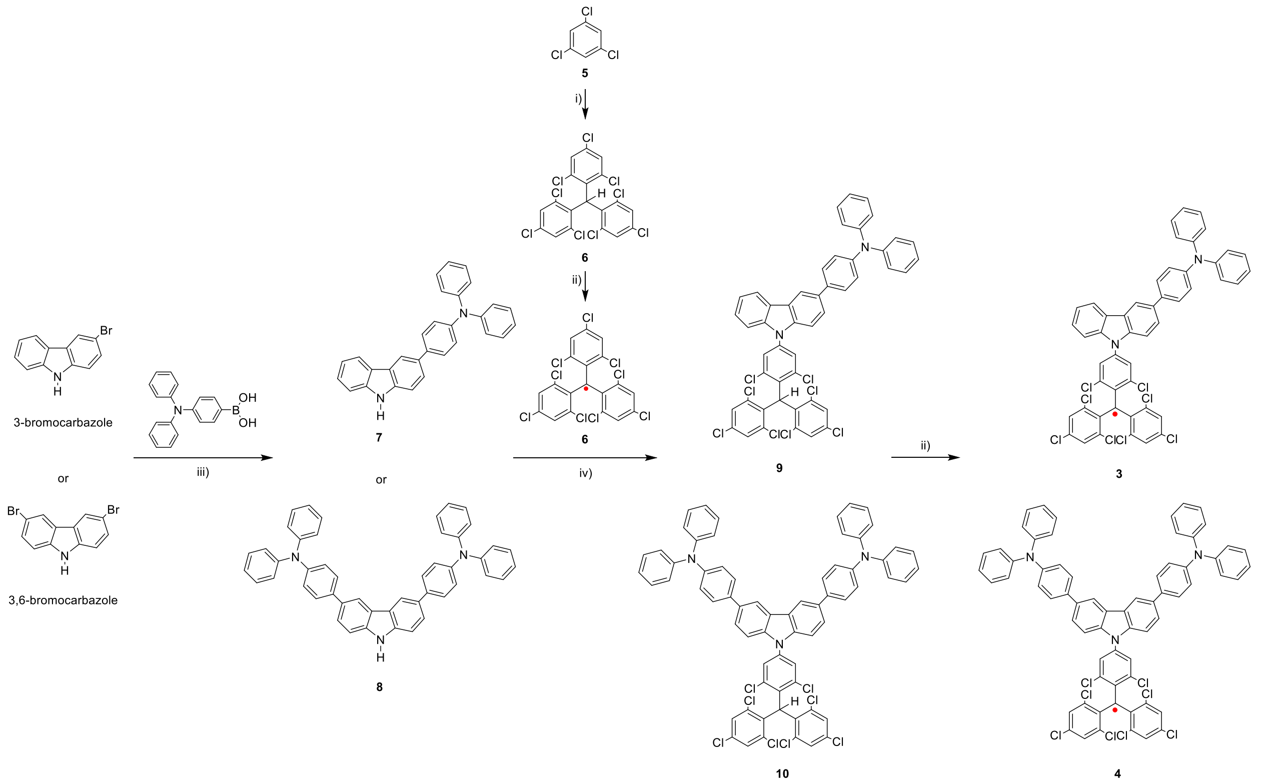

Figure 4.2. Synthetic scheme for the preparation of the substituted tris(2,4,6-trichlorophenyl)methyl radicals. i) CHCl$_3$, AlCl$_3$, 2.5 h, 80 ^{o}C , ii) KO^{t}Bu, p-chloranil, THF, r.t iii) Cs$_2$CO$_3$, Pd(PPh$_3$)$_4$, 1,4-dioxane, 100 ^{o}C iv) Cs$_2$CO$_3$, DMF, 160 ^{o}C

The fluorophores were obtained in sufficiently high purity (< 99%) to meet the requirements for spectroscopic analyses (figures B.4.43 to B.4.47). The structural elucidation of all intermediates were done by NMR (^{1}H and ^{13}C) and mass Spectrometry (figure B.4.21 to B.4.37), while for the radicals Electron Paramagnetic Resonance (EPR, figure B.4.1) along with mass spectrometry (figure B.4.38, B.4.40 and B.4.42) allow to confirm the formation of radicals.

4.1.2. Radicals Photophysics

The new radicals can be unequivocally confirmed spectroscopically according to the characteristic absorption at 373 nm (figure 4.3). This shoulder is absent in the reduced counterparts **9** and **10**) and constitute an optical fingerprint for the formation of these radicals.

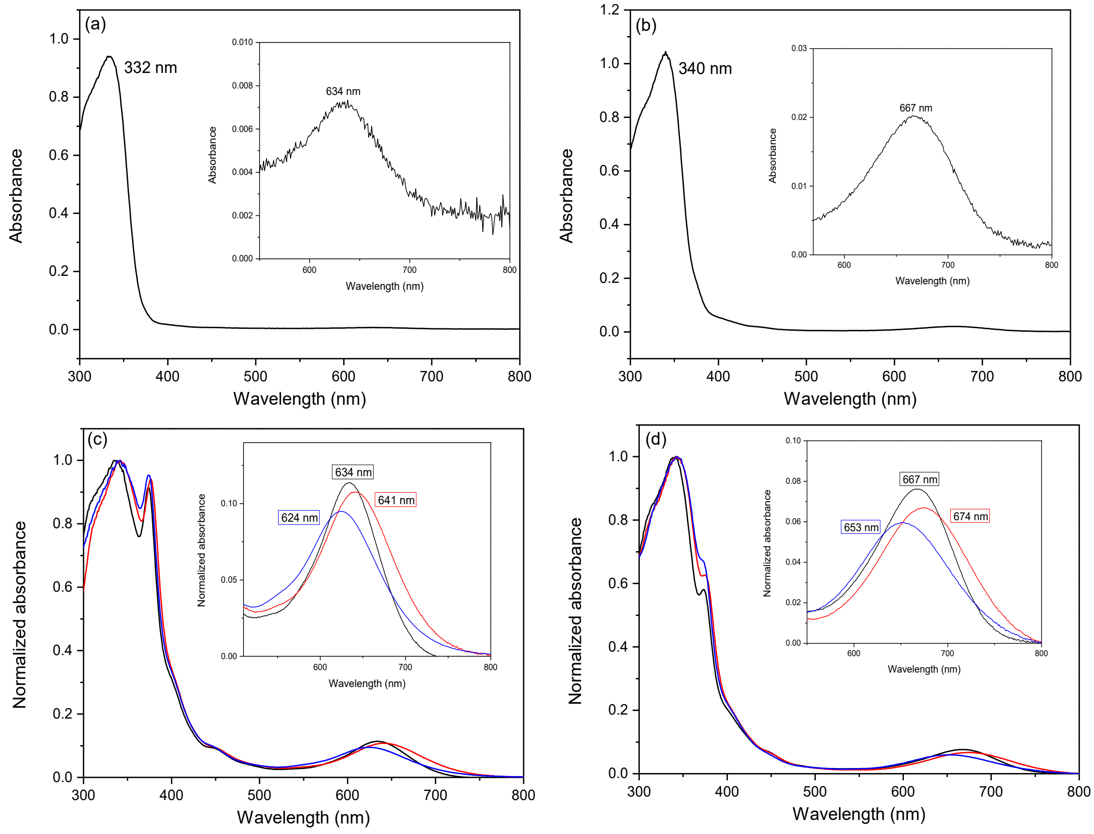

Figure 4.3. a) Absorption spectrum of 9 in cyclohexane, showing an intense π–π* band at 332 nm. Inset: weak long-wavelength band centered at 634 nm. b) Absorption spectrum of 10 in cyclohexane, with the main π–π* band at 340 nm. Inset: weak band at 667 nm. c) Normalized absorption spectra of 3 in cyclohexane (black), toluene (red) and chloroform (blue). Inset: enlarged view of the CT region. d) Normalized absorption spectra of 4 in the same solvents. Inset: enlarged CT region. All spectra were recorded at room temperature (1 cm path length).

The absorption profiles of the synthesized open-shell trityl derivatives are dominated by a broad, yet weak charge-transfer (CT) band typical of triarylmethyl radicals (figure 4.3 c, d). For **3** the maximum appears at 634 nm (cyclohexane), 641 nm (toluene) and 624 nm (chloroform), while for **4** it shifts to 667 nm, 674 nm and 653 nm, respectively. The systematic bathochromic shift observed in toluene respect to cyclohexane for both the mono- to the bis-arylamine donor indicates a stronger stabilization of the CT band with the increased donor number. However, an unexpected hypsochromic shift was observed for both radicals in chloroform. This blue-shifting of the excited states with the increased solvent polarity cannot be explained, and hence further studies are needed.

Integrating the electron donors into the radical framework further shifted the emission upwards of 150 nm relative to the benchmark **2** (figure 4.4). Indeed, the emission is shifted into the NIR and outside the region of visible detection. The Φ_{fl} could be measured in cyclohexane from the charge-transfer doublet manifold, albeit was <1% (table 4.1). This contrasts with the unsubstituted **2** that was 135-fold greater under the same conditions,[181] but, as discussed in section 2.2.2, the measured Φ_{fl} values of both newly synthesized radicals follow the general trend reported for other NIR open-shell fluorophores. The only known exception remains TTM-TPA, which, as far as we know, is the only NIR organic radical reported so far to violate the energy gap law.[99]

The quenched Φ_{fl} of **3** and **4** is related to the increment of the non-radiative rate constant (k_{nr}) that is >150 times faster than the corresponding radiative rate (k_r), which remains similar for all compounds. The dominance of k_{nr} is owing to vibronic coupling according to the energy-gap law. This is complemented with photoinduced electron transfer from the electron-rich arylamine to the trityl acceptor. From the known reduction and oxidation potentials, respectively of the trityl core and triphenylamine, along with the $E_{0,0}$ (figure 4.4), the photoinduced electron transfer is thermodynamically favorable ($\Delta G \approx -1.08$ eV). The resulting charge separation relaxes through fast non-emissive back-electron transfer, further increasing k_{nr}. This is supported by the absence of emission in both chloroform and toluene that otherwise support charge separated species in contrast to cyclohexane. This aside, the increased delocalization of **4** partly damps non-radiative modes, but not enough to overcome the efficient deactivation by vibronic coupling. This is according to its larger k_r/k_{nr} ratio compared to **3**.

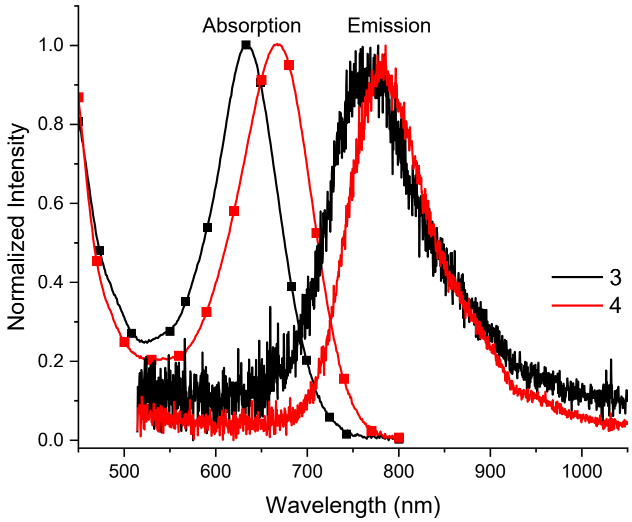

Figure 4.4. Normalized absorption (symbols) and steady-state emission (lines) spectra of **3** (black) and **4** (red) measured in cyclohexane at room temperature.

Table 4.1. Photophysical parameters of synthesized open-shell fluorophores in solution at 298K.

Compound	**Solvent**	λ_{abs} (nm) [a]	λ_{PL} (nm)[a]	Φ_{fl} (%)	**τ (ns)**	k_r (s^{-1}) [b]	k_{nr} (s^{-1}) [c]	$\tau_{degrade}$ (min)[d]
2	Cyclohexane	605	635	82	43.9	1.9 x10^{7}	4.1 x 10^{6}	28.7
3	Cyclohexane	635	767	0.5	0.76	6.6 x 10^{6}	1.3 x 10^{9}	846.7
	Toluene[e]	641	-	-	-	-	-	
	Chloroform[e]	624	-	-	-	-	-	
4	Cyclohexane	667	785	0.6	1.17	5.1 x 10^{6}	8.5 x 10^{8}	1153.3
	Toluene[e]	674	-	-	-	-	-	

	Chloroform[e]	653	-	-	-	-	-	

[a] Longest wavelength transition. [b] Radiative rate constant. [c] Non-radiative rate constant. [d] Photodegradation half-life during 376 nm continuous irradiation. [e] Blank entries were not determined.

When radicals **3** and **4** are doped in a PMMA matrix (1 wt%), their Φ_{fl} in the solid-state increase significantly compared to solution. Thus, in PMMA, **3** exhibits a Φ_{fl} of around 3 % (λ_{PL}= 667 nm, figure 4.5 a), while **4** reaches 7.0 % (λ_{PL} = 700 nm, figure 4.5 b). These values are one order of magnitude higher than those measured in cyclohexane solution. Thus, the enhanced efficiencies in PMMA can be attributed to the rigid host environment, which suppresses nonradiative decay channels by restricting molecular motions, thereby stabilizing the emissive doublet state and facilitating more efficient radiative recombination.

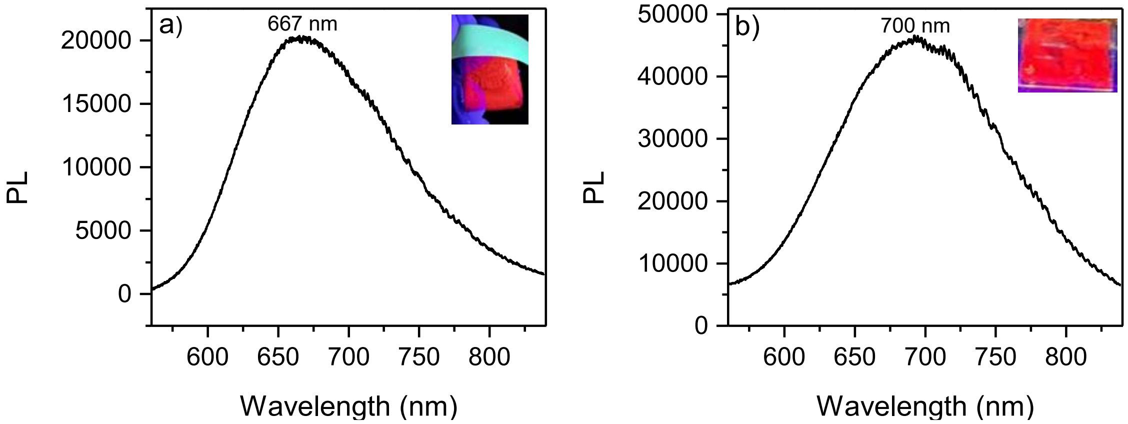

Figure 4.5. PL spectra of (a) 3 and (b) 4 dispersed in PMMA (1 wt%). The solid films were prepared by drop-casting from toluene solutions onto quartz substrates. Insets: photographs of the films under 365 nm UV illumination.

4.1.3. Theoretical Calculations

Leveraging Natural Transition Orbitals that consolidate the combinations of the various transitions involved in electronic excitation into unique orbitals allow us to visualize the lowest energy absorption, which occurs from the HOMO that is delocalized over the carbazole and extended to the triphenylamines (figure 4.6 C) to the LUMO (figure 4.6 D) that is localized on the trityl radical.[182] This contrasts with the small absorption in the UV at ~373 nm that is assigned to the SOMO➞LUMO excitation whose orbitals are located exclusively on the delocalized radical framework. The orbitals involved in the electronic transitions did not differ when using cyclohexane, toluene, and chloroform (figure B.4.8 to B.4.19) as the solvent continuum, although the energies of the electron excitation were perturbed.

The calculations were done with the PBE0 functional because it was the only hybrid functional that captured the low energy charge transfer. High levels of spin contamination plagued the other functionals such as CAM-B3LYP and ω–B97XD, resulting in only high energy transitions. This contrasted with PBE0 that had a low degree of spin contamination ≈ 11%.

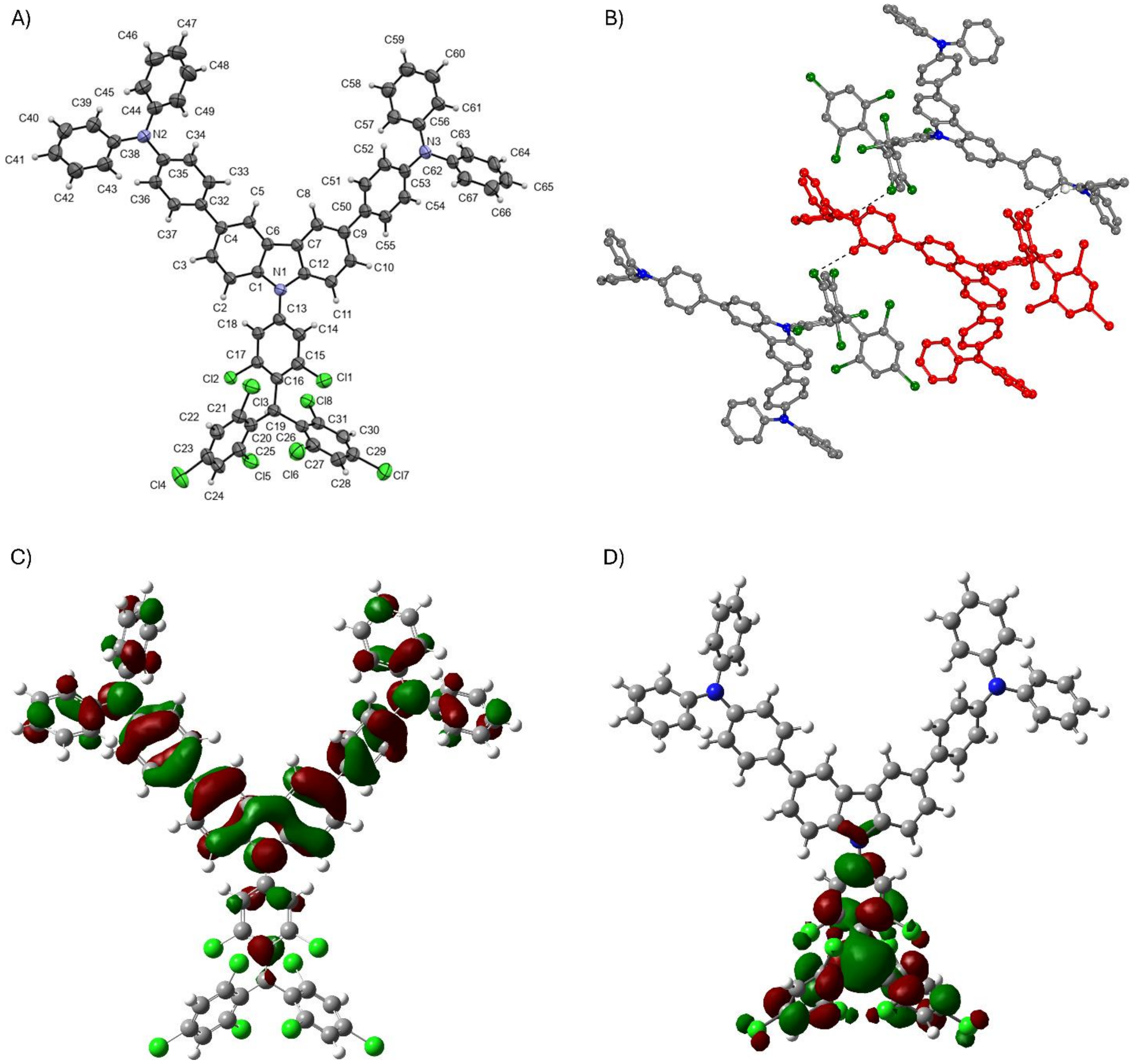

Figure 4.6. A) Thermal displacement ellipsoid plot of the single crystal structure of **10** with ellipsoids drawn at the 50% probability level with hydrogen atoms shown as spheres of arbitrary size. 4 Color code: C (gray), N (blue), Cl (green). B) Three sets of CH···Cl bonds. C and D) Natural Transition Orbitals[182] of **4** calculated in chloroform with PBE0 functional[183] and correlation-consistent polarized valence triple-zeta basis set drawn with density=0.0004 of the lowest electronic energy transition: HOMO (C) and LUMO (D).

4.1.4. Photodegradation Measurements

Photodegradation is a key limitation of carbon centered radicals for replacing their closed-shell counterparts. Indeed, the photostability of open-shelled fluorophores must be improved to match their closed-shell counterparts. The emission intensity of **1 - 4** was monitored under continuous irradiation at 376 nm UV light in air in solution (figure 4.7). The intensity of **2 - 4** decreased by only <7% during 7 min. of irradiation. This contrasted with **1** whose emission decreased by 50% during the same time according to known C–Cl homolytic cleavage followed by irreversible cyclization.[77] Indeed, its emission was nearly quenched within 25 min of exposure to light. The stability of **2** was somewhat better, degrading only after 2 hours of exposure. No subsequent degradation of **3** and **4** was apparent during the same continuation exposure time. Likewise, no degradation of the characteristic radical fingerprint absorption was observed upon exposing the radicals to ambient conditions upwards of 7 days.

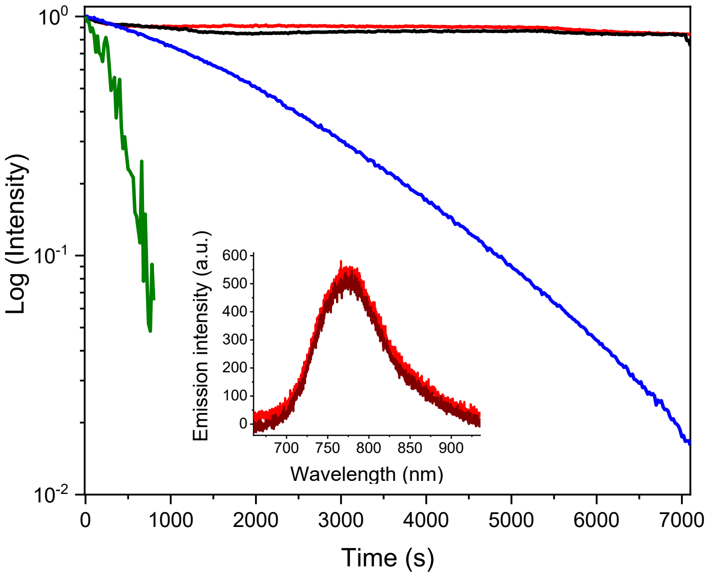

Figure 4.7. Photostability kinetics of **1** (green), **2** (blue), **3** (black), and **4** (red) in cyclohexane monitored at 376 nm under continuous irradiation at 376 nm in air at room temperature. Inset: emission spectra of **4** before (red) and after 2 h (wine) of continuous irradiation.

Integrating the electron donating triphenylamines into the framework increases the photostability 4000-fold and 40-fold relative to **1** and **2**, respectively. Thus, the increased photostability might come from efficient deactivation of the excited state by nonradiative loss courtesy of the extended delocalization of the low-lying HOMO of the CT that acts as an energy sink. Moreover, the absorption spectra of **3** and **4** in dichloromethane were unchanged even after storing the sample for four months under ambient conditions (figure B.4.5). Furthermore, no appreciable degradation of **3** and **4** was observed even after one year when stored as solids under ambient conditions. The increased stability in the solid state arises from the increased steric bulkiness afforded by the triphenylamines (figure 4.6 B) that prevent intramolecular radical formation.

Evidence for the higher photostability of **4** in solid-state was further confirmed by SCXRD (figure 4.6 A) of it reduced counterpart (**10**). The salient features of the crystal are asymmetric rotation (28.3° and 43.3°) between the planes of the carbazole and the aminophenyls. The off-coplanarity of the two aromatics is required to accommodate the *ipso* hydrogens. Of noteworthy is the packing of **10** that is governed by CH···Cl interactions. Indeed, each molecule makes three CH···Cl contacts: two with one molecule (C52–H52···Cl7 and C57–H57···Cl8) and one with another molecule (C57–H57···Cl8) (figure 4.3 B). The three sets of bonds are at <3 Å (table B.4.1). The collective effect is the trityl core being surrounded by triphenylamines and increasing the solid state photostability.

In addition to their photostability, the thermal stability of **3** and **4** was evaluated by thermogravimetric analysis (TGA) under nitrogen atmosphere. As shown in figure 4.8, both radicals exhibited only minor weight loss below 110 °C (ca. 2–4%), which can be attributed to the release of low volatiles such as residual solvents or adsorbed moisture. The main decomposition events, indicative of structural degradation, were observed above 300 °C for both compounds (317 °C for **3** and 320 °C for **4**), confirming their excellent thermal stability. This finding along with previous data confirms that the novel synthesized open-shell fluorophores are chemical, photo- and thermal stable materials.

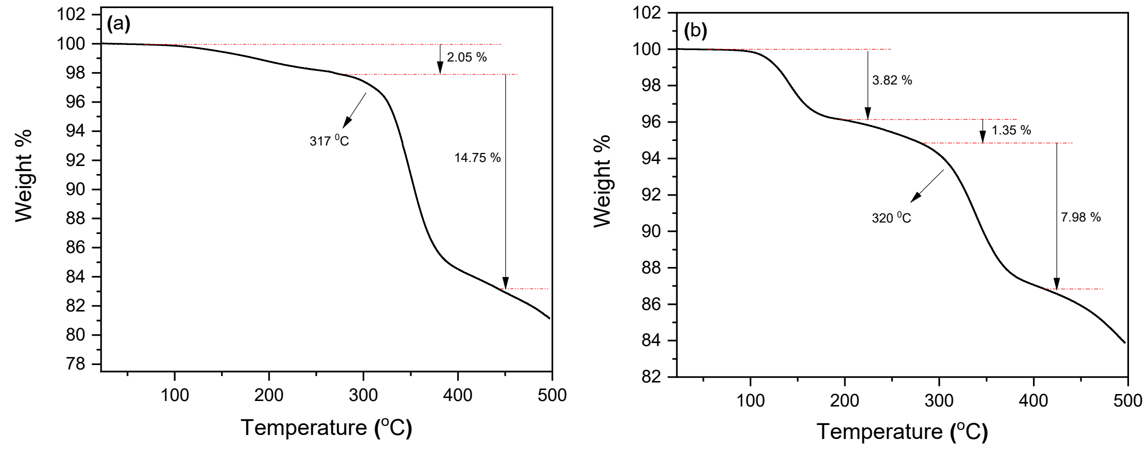

Figure 4.8. Thermogravimograms of 3 (a) and 4 (b) measured under nitrogen at 10 °C/min.

4.2. Materials and Methods

Synthesis

All chemicals used as received from commercial sources. Anhydrous and purged solvents were obtained from an activated aluminum column system.

Tris(2,4,6-trichlorophenyl)methane (1).[184] Synthesized by Friedel-Crafts alkylation according to 1,3,5-trichlorobenzene (10.14 g, 55.9 mmol), anhydrous $CHCl_3$ (0.5 mL, 6.3 mmol), and anhydrous $AlCl_3$ (0.91 g, 6.8 mmol) were sequentially added to a glass pressure vessel under nitrogen. The vessel was then sealed and removed from the glovebox prior to heating. The sealed vessel was heated at 80 °C for 2.5 h. Upon completion of the reaction, the mixture was cooled to room temperature, and the vessel was carefully vented in a well-ventilated fume hood to release the accumulated HCl gas. Afterwards, the solidified reaction mixture was dissolved in $CHCl_3$ and poured over ice/HCl (1 M). The organic phase was separated, washed with water (3 × 200 mL), dried over anhydrous $MgSO_4$, filtered, and concentrated under reduced pressure. The crude mixture was purified by gravity column chromatography over silica gel, using petroleum ether as eluent affording **6** as a white solid (2.78 g, 80 %). ^{1}H NMR (400 MHz, $CDCl_3$, δ): 7.36 (d, $J = 2.2$ Hz, 3H), 7.24 (d, $J = 2.2$ Hz, 3H), 6.68 (s, 1H). ^{13}C NMR ($CDCl_3$, 100 MHz): 137.9, 137.1, 133.8, 130.0, 128.4, 49.8. APCI-MS $[M{-}H]^-$: m/z calcd $C_{19}H_7Cl_9$ 552.7614, found 552.7636.

Tris(2,4,6-trichlorophenyl)methyl radical (1).[78] The radical of the corresponding methane precursor (**6**) was synthesized via two steps deprotonation–oxidation. Under nitrogen and in the dark, **6** (2.47 g, 4.46 mmol) was dissolved in anhydrous THF and then potassium *tert*-butoxide (1.75 g, 15.59 mmol) was added. The mixture was stirred at room temperature for 6 h, followed by the addition of *p*-chloranil (2.96 g, 12.03 mmol). After 1 h of stirring at room temperature, the solvent was evaporated under reduced pressure. The crude product was adsorbed on silica and it was purified by gravity column chromatography using petroleum ether as the mobile phase, yielding **1** as a red powder (2.17 g, 87%). APCI-MS $[M^-]$: m/z calcd $C_{19}H_6Cl_9$ 552.7614, found 552.7604.

General procedure for cross-coupling synthesis of carbazole-triphenylamine derivatives.

The corresponding carbazole-based triphenylamine (TPA) derivatives were synthesized via Suzuki–Miyaura cross-coupling. In an oven-dried round-bottom flask, equipped with a magnetic stir bar, either the mono- or dibrominated carbazole precursor (1 equiv.) and the corresponding arylboronic acid (2.0 - 2.4 equiv., respectively) were dissolved in anhydrous 1,4-dioxane. Afterwards, an aqueous solution of Cs_2CO_3 (2 M) was added. The mixture was purged with nitrogen for 5 minutes. Then, a catalytic amount of *tetrakis*(triphenylphosphine)palladium(0) ($Pd(PPh_3)_4$) was added, followed by an additional purging with nitrogen for 15 minutes. The mixture was stirred under reflux at 100 °C overnight. After cooling to room temperature, the reaction mixture was poured into water and extracted with dichloromethane (3 × 50 mL). The combined organic layers were washed with brine solution, dried over anhydrous $MgSO_4$, filtered, and concentrated under reduced pressure. The crude residues were purified by gravity column chromatography on silica gel using a petroleum ether/dichloromethane mixture (2:1 v/v) as eluent, affording the target carbazole-TPA derivatives as white solids.

3-[4'-(*N*,*N*-Diphenylamino)-1'-phenyl]carbazole (7). As per the general procedure**,** 3-bromocarbazole (650 mg, 2.64 mmol) and 4-(*N*,*N*-diphenylamino)phenylboronic acid (1527.3 mg, 5.28 mmol) were dissolved in anhydrous 1,4-dioxane (15 mL) **i**n an oven-dried round-bottom flask (50 mL). Aftewards, Cs_2CO_3 (5 mL, 2 M) was added. Then, $Pd(PPh_3)_4$ (58.0 mg, 0.05 mmol) was added. The crude residue was purified by gravity column chromatography on silica gel using a petroleum ether/dichloromethane mixture (2:1 v/v) as eluent, affording **7** as a white solid (510.8 mg, 47%). ^{1}H NMR (400 MHz, $CDCl_3$, δ): 8.27 (s, 1H), 8.12 (d, *J* = 7.7 Hz, 1H), 8.05 (s, 1H), 7.66 (d, *J* = 8.1 Hz, 1H), 7.61 (d, *J* = 8.4 Hz, 2H), 7.48–7.44 (m, 3H), 7.30–7.28 (m, 5H), 7.20–7.15 (m, 6H), 7.03 (t, *J* = 7.2 Hz, 2H). ^{13}C NMR ($CDCl_3$, 100 MHz): 147.9, 146.5, 140.0, 138.7, 136.4, 132.6, 129.3, 127.9, 126.0, 125.1, 124.5, 124.2, 123.9, 123.5, 122.7, 120.4, 119.6, 118.4, 110.8. ESI-MS $[M+H]^+$: m/z calcd $C_{30}H_{22}N_2$ 411.1856, found 411.1838.

3,6-*Bis*[4'-(*N*,*N*-diphenylamino)-1'-phenyl]carbazole (8). In an oven-dried round-bottom flask (50 mL), 3,6-dibromocarbazole (650 mg, 2.00 mmol) and 4-(*N*,*N*-diphenylamino)phenylboronic acid (1.388 g, 4.80 mmol) were dissolved in anhydrous THF (30 mL). Then, a freshly prepared solution of Cs_2CO_3 (2 M, 10 mL, 1.303 g, 4.00 mmol) was added, followed by $Pd(PPh_3)_4$ (122.1 mg, 0.10 mmol). The crude residue was purified by gravity column chromatography on silica gel using a petroleum ether/dichloromethane mixture (2:1 v/v) as eluent, affording **8** as a white solid (474.2 mg, 53%). ^{1}H NMR (400 MHz, $CDCl_3$, δ): 8.30 (s, 2H), 8.10 (s, 1H), 7.68 (dd, *J* = 8.4 Hz, 2H), 7.61 (d, *J* = 8.6 Hz, 4H), 7.50 (d, *J* = 8.4 Hz, 2H), 7.30 (t, *J* = 8.4 Hz, 8H), 7.20-7.15 (m,12 H), 7.03 (t, *J* = 7.3 Hz, 4H). ^{13}C NMR ($CDCl_3$, 100 MHz): 147.8, 146.5, 139.2, 136.3, 132.7, 129.2, 127.9, 125.3, 124.5, 124.2, 124.1, 122.7, 118.4, 110.9. APCI-MS $[M+H]^+$: m/z calcd $C_{48}H_{35}N_3$ 654.2904, found 654.2916.

General procedure for functionalized *tris*(2,4,6-trichlorophenyl)methane.

Functionalized *tris*(2,4,6-trichlorophenyl)methane derivatives were synthesized by nucleophilic aromatic substitution of the **1** core with the corresponding carbazole derivatives. In this sense, **1** (1.0 equiv.), the corresponding carbazole-based donor (1.1-4.9 equiv.), and cesium carbonate (3.5 equiv.) were added to an oven-dried round-bottom flask under nitrogen and dissolved in anhydrous

DMF. The reaction mixture was heated at 160 °C in the dark and its progress was monitored by TLC. Then, upon completion, it was cooled to room temperature and poured into an excess of cold aqueous HCl (1 M). The resulting suspension was extracted with dichloromethane (3 × 50 mL), and the combined organic layers were washed with brine, dried over anhydrous Na_2SO_4, and concentrated under reduced pressure. The crude product was purified by column chromatography on silica gel using petroleum ether/dichloromethane mixtures (5:1 v/v) as eluent, affording the corresponding tris(2,4,6-trichlorophenyl)methane derivatives as colored solids.

4-(9H-Carbazol-1-yl)-2,6-dichlorophenylbis(2,4,6-trichlorophenyl)methane (11). A mixture of **1** (1.00 g, 1.81 mmol), carbazole (1.51 g, 9.00 mmol), and anhydrous Cs_2CO_3 (0.94 g, 2.90 mmol) were placed in an oven-dried round-bottom flask (100 mL) under nitrogen. Anhydrous *N*,*N*-dimethylformamide (DMF, 20 mL) was then added, and the reaction mixture was stirred at 160 °C in the dark for 2.5 h. After completion, the mixture was cooled to room temperature and poured into an excess of cold aqueous HCl (1 M). The resulting precipitate was collected by filtration, dissolved and then extracted using dichloromethane. The combined organic layers were washed with a brine solution, dried over anhydrous $MgSO_4$, filtered, and concentrated under reduced pressure. Finally, the crude product was adsorbed onto silica gel and purified by gravity column chromatography using petroleum ether/dichloromethane, 5:1 v/v, as mobile phase, affording **11** as a light brown solid (567.3 mg, 45%). ^{1}H NMR (400 MHz, $CDCl_3$, δ): 8.14 (d, J = 7.7 Hz, 2H), 7.62 (d, J = 2.2 Hz, 1H), 7.48 (d, J = 2.2 Hz, 1H), 7.46–7.43 (m, 5H), 7.41 (d, J = 2.2 Hz, 1H), 7.34 – 7.30 (m, 3H), 7.29 (d, J = 2.2 Hz, 1H), 6.86 (s, 1H). ^{13}C NMR ($CDCl_3$, 100 MHz): 140.1, 138.5, 138.0, 137.6, 137.2, 134.0, 133.9, 133.8, 130.2, 130.1, 128.5, 128.2, 126.6, 126.3, 123.8, 120.8, 120.5, 109.6, 50.1. ESI-MS [M^+]: m/z calcd $C_{31}H_{15}Cl_8N$ 680.8707, found 680.8736.

4-[3-(4-(*N*,*N*-Diphenylamino)phenyl)-9H-carbazol-1-yl]-2,6-dichlorophenylbis(2,4,6-trichlorophenyl)methane (9). Similar to **11** using **1** (400.00 mg, 0.72 mmol), **7** (534.18 mg, 1.30 mmol), and anhydrous Cs_2CO_3 (824.40 mg, 2.53 mmol) in anhydrous DMF (20 mL). The reaction mixture was stirred at 160 °C in the dark for 1.5 h. The mixture was cooled to room temperature and poured into an excess of cold aqueous HCl (1 M). The resulting precipitate was collected by filtration, dissolved in dichloromethane, and extracted with the same solvent. The combined organic layers were washed with brine, dried over anhydrous $MgSO_4$, filtered, and concentrated under reduced pressure. The crude product was adsorbed onto silica gel and purified by gravity column chromatography using a petroleum ether/dichloromethane mixture (5:1 v/v, gradient) as eluent, affording **9** as a green solid (255.40 mg, 38 %). ^{1}H NMR (400 MHz, CDCl$_3$, δ): 8.30 (d, *J* = 1.3 Hz, 1H), 8.17 (d, *J* = 7.7 Hz, 1H), 7.68 (d.d, *J* = 1.6 Hz, 1H), 7.64 (d, *J* = 2.2 Hz, 1H), 7.58 (d, *J* = 8.6 Hz, 2H), 7.51-7.50 (m, 2H), 7.48-7.46 (m, 2H), 7.44 (d, *J* = 2.2 Hz, 1H), 7.41 (d, *J* = 2.2 Hz, 1H), 7.36-7.27 (m, 7H), 7.21-7.16 (m, 6H), 7.04 (t, *J* = 7.3 Hz, 2H), 6.87 (s, 1H). ^{13}C NMR (CDCl$_3$, 100 MHz): 147.9, 146.9, 140.6, 139.4, 138.6, 138.1, 137.8, 137.4, 134.2, 134.2, 134.1, 134.0, 130.3, 130.2, 129.4, 128.7, 128.2, 128.1, 126.6, 126.6, 125.6, 124.4, 124.1, 123.0, 121.1, 120.7, 118.67, 110.0, 109.9, 50.2. ESI-MS [M+H]$^+$: m/z calcd $C_{49}H_{28}Cl_8N_2$ 924.9833, found 924.9841.

4-[3,6-*bis*(4-(*N*,*N*-Diphenylamino)phenyl)-9H-carbazol-1-yl]-2,6-dichlorophenylbis(2,4,6-trichlorophenyl)methane (10). Under a nitrogen atmosphere, in an oven-dried round-bottom flask (100 mL), **1** (200.00 mg, 0.36 mmol), **8** (253.00 mg, 0.30 mmol) and anhydrous Cs_2CO_3 (412.20 mg, 1.26 mmol) were added and dissolved in anhydrous DMF (20 mL). The reaction mixture was stirred at 160 °C in the dark for 1 h. The mixture was cooled to room temperature and poured into an excess of cold aqueous HCl (1 M). The resulting precipitate was collected by filtration, dissolved in dichloromethane, and the organic solution was washed with brine, dried over anhydrous $MgSO_4$, filtered, and concentrated under reduced pressure. The crude product was adsorbed onto silica gel and purified by gravity column chromatography using petroleum ether/dichloromethane (5:1 v/v) as eluent, affording **10** as a green solid (143.8 mg, 34 %). ^{1}H NMR (400 MHz, CDCl$_3$, δ): 8.34 (d, *J* = 1.5 Hz, 2H), 7.66–7.30 (m, 3H), 7.61 (d, *J* = 8.6 Hz, 4H), 7.53–7.49 (m, 3H), 7.44 (d, *J* = 2.2 Hz, 1H), 7.42 (d, *J* = 2.2 Hz, 1H), 7.32–7.29 (m, 9H), 7.21–7.15 (m, 13H), 7.04 (t, *J* = 7.3 Hz, 4H), 6.87 (s, 1H). ^{13}C NMR (CDCl$_3$, 100 MHz): 148.1, 144.8, 146.8, 139.7, 138.5, 138.0, 138.0, 137.9, 137.7, 137.2, 135.7, 134.0, 133.9, 133.9, 130.2, 130.1, 129.3, 129.1, 128.5, 127.9, 126.3, 125.6, 124.5, 124.3, 123.1, 122.8, 118.6, 110.0, 50.1. ESI-MS [M+H]$^+$: *m/z* calcd $C_{67}H_{41}Cl_8N_3$ 1168.0881, found 1168.0857.

General procedure for π-radicals synthesis

The corresponding open-shell derivatives were synthesized similarly to **1**. In a typical reaction, the neutral precursor (tris(2,4,6-trichlorophenyl)methane derivatives, 1 equiv.) was dissolved in anhydrous THF under an inert nitrogen atmosphere and protected from light. Potassium *tert*-butoxide (5.6 equiv.) was added, and the reaction mixture was stirred at room temperature overnight. Subsequently, *p*-chloranil (2.7 equiv.) was introduced and the reaction was stirred for 2

h. The solvent was then removed under reduced pressure, and the crude product was adsorbed onto silica and purified by gravity column chromatography using a petroleum ether/dichloromethane mixture as eluent. The desired radical products were obtained as colored powders.

(4-*N*-Carbazolyl-2,6-dichlorophenyl)*bis*(2,4,6-trichlorophenyl)methyl radical (2). In a dry round-bottom flask (100 mL), **11** (200.0 mg, 0.29 mmol) was dissolved in anhydrous THF (50 mL) under nitrogen in the dark. Then, potassium *tert*-butoxide (183.45 mg, 1.64 mmol, 5.6 equiv.) was added, and the solution was stirred for 5 h. Subsequently, *p*-chloranil (193.81 mg, 0.39 mmol, 2.7 equiv.) was added and the reaction mixture was stirred an additional 2 h. The resulting solution was concentrated and purified by gravity column chromatography using petroleum ether/dichloromethane mixture (2:1 v/v) as mobile phase, affording **2** as a deep red powder (171.1 mg, 86%). APCI-MS [M$^+$]: m/z calcd $C_{31}H_{14}Cl_8N$ 683.8575, found 683.8590.

4-[3-(4-(*N*,*N*-Diphenylamino)phenyl)carbazol-1-yl]-2,6-dichlorophenyl)bis(2,4,6-trichlorophenyl)methyl radical (3). In a dry round-bottom flask (100 mL), **9** (150.0 mg, 0.16 mmol) was dissolved in anhydrous THF (50 mL) under nitrogen and protected from light. Afterwards, potassium *tert*-butoxide (101.5 mg, 0.90 mmol, 5.6 equiv.) was added and the mixture was stirred for 5 h at room temperature. Then, *p*-chloranil (107.3 mg, 0.44 mmol, 2.7 equiv.) was added and the reaction was stirred for 2 h. After removing the solvent under reduced pressure, the crude material was adsorbed onto silica gel and purified by gravity column chromatography using petroleum ether/dichloromethane (2:1 v/v) as eluent. **3** was isolated as a green solid (119.6 mg, 80 %). APCI-MS [M+H]$^+$: m/z calcd $C_{49}H_{27}Cl_8N_2$ 923.9755, found. 923.9745.

(4-[3,6-*bis*(4-(*N*,*N*-Diphenylamino)phenyl)carbazol-1-yl]-2,6-dichlorophenyl)bis(2,4,6-trichlorophenyl)methyl radical (4). In a dry round-bottom flask (100 mL), **10** (113.8 mg, 0.10 mmol) was dissolved in anhydrous THF (50 mL) under nitrogen and in the dark. Then, potassium *tert*-butoxide (61.0 mg, 0.54 mmol, 5.6 equiv.) was added, and the solution was stirred for 5 h at room temperature. Afterwards, *p*-chloranil (64.5 mg, 0.26 mmol, 2.7 equiv.) was added and the reaction was stirred for 2 h. After evaporation of the solvent, the residue was purified by gravity column chromatography using petroleum ether/dichloromethane (2:1 v/v), yielding **4** as a deep green powder (83.7 mg, yield: 73%). ESI-MS [M]$^+$: m/z calcd $C_{67}H_{40}Cl_8N_3$ 1170.0685, found 1170.0690.

Single-crystal X-ray diffraction

The data were collected from a shock-cooled single crystal at 150 K on a Bruker Venture Metaljet k-geometry diffractometer with a Metal Jet using a Helios MX Mirror Optics as monochromator and a Bruker CMOS Photon III detector. The diffractometer was equipped with an Oxford Cryostream 700 low temperature device and used Ga K_α radiation ($\lambda = 1.34139$ Å). All data were integrated with *SAINT* and a multi-scan absorption correction using *SADABS* was applied.[171, 172] The structure was solved by intrinsic phasing methods with *XT* and refined by full-matrix least-squares methods against F^2 using *XL,*[173, 174] within the graphical user interface of *OLEX2*.[185] All non-hydrogen atoms were refined with anisotropic displacement parameters. The hydrogen atoms were refined isotropically on calculated positions using a riding model with their U_{iso} values constrained to 1.2 times the U_{eq} of their pivot atoms. The structure contains a Void volume of 332 A^3 but refinement with the MASK/SQUEEZE option implemented in *OLEX2* returned an empty content (i.e. with no residual electron density detected in these voids). This report and the CIF file were generated using FinalCif.[176]

EPR measurements

Powder EPR spectra were recorded at room temperature on a Bruker Elexsys E500 spectrometer equipped with a 4108 TMH X-band resonator (≈9.5–9.9 GHz). Finely ground samples were loaded into quartz EPR tubes (4 mm OD) and gently packed to a consistent height. Typical acquisition parameters were: field 3495.0 G, power 0.21 mW, quality factor 1600, frequency 9.87 GHz; 2–4 scans were averaged.; 2-4 scans were averaged.

Absorption measurements

Spectra were recorded at room temperature on a UV–visible–NIR spectrophotometer using four-window quartz cuvettes (1 cm pathlength). Measurements (ca. 10^{-5} M) were carried out in anhydrous solvents such as cyclohexane, toluene and chloroform; solvent blanks were recorded under identical conditions and used for baseline correction.

Fluorescence measurements

Emission measurements were performed on a combined steady-state/time-resolved spectrometer (FLSP-920, Edinburgh Instruments). Emission spectra were collected with a photomultiplier tube over 300–800 nm. Absolute quantum yield measurements were carried out using a calibrated integrating sphere in a 1 mm-pathlength quartz cuvette. An identical empty cuvette was used as a blank to correct for background and scattering. Both, the sample and blank were degassed by bubbling with N_2 for over 15 minutes before performing the measurements. Moreover, an absorbance of 0.1 for the charge-transfer band was ensured during measurements to avoid the inner filter effect.[186] Fluorescence lifetimes were acquired by time-correlated single-photon counting (TCSPC, Edinburgh Instruments) upon excitation with a 405 nm picosecond laser diode. Kinetic decay profiles were fitted with mono-exponential function using Origin software. Instrument-response effects were treated by reconvolution, and the instrument response function (IRF) was determined from scattered light using a white card set at 45° in the cell holder.

Photostability and thermal measurement

To evaluate the photostability of the organic radicals a Melles Griot 56RCS007/HV diode laser (CW, power of the laser: 1.2 mW) was used at continuous excitation at 376 nm over 2 h. The samples (ca. 10^{-5} M**)** were prepared in solution using spectrophotometric-grade cyclohexane and deoxygenated by bubbling N_2 and kept under a gentle N_2 flow during acquisition**.** The photoluminescence at the emission maximum was monitored over time at room temperature with a CCD camera (Pixis 400BExcelon) coupled to a monochromator with a 15 μm slit opening (dark conditions).The incident laser power at the cuvette was measured with a calibrated photodiode and adjusted with neutral-density filters to keep the absorbed power constant at P_{abs}=36.36 μW across samples.

Thermogravimetric analysis (TGA) was performed on a TA Instruments TGA 550 using a heating rate of 10 °C min^{-1} from room temperature to 500 °C, under N_2.

Theoretical calculations

Theoretical calculations were done using Gaussian 16, Revision C.01.[187] The geometries were optimized with the PBE0 (PBE1PBE1)[183] functional using a correlation-consistent polarized valence triple-zeta basis basis set. The optimized geometry were calculated with restricted-open Hartree-Fock (ROHF). The electronic excitation energies, corresponding to the absorption spectrum, were calculated with unrestricted Hartree-Fock (UHF) time-dependent DFT (TD-DFT) using the solvent linear response correction.[188] The integral equation formalism polarizable continuum solvent model (IEFPCM) was used for all the calculations using chloroform, toluene and cyclohexane dielectric constants. The Natural Transition Orbitals (NTO)[188] analyses was done for the lowest energy transition (#1) to visualize the principle transitions in the absorption spectrum, typically the beta spin. The orbitals were visualized in GaussView 6.0.16.[189] In all the cases, the first energy transition corresponding to the lowest energy electronic transition.

CHAPTER 5 OPEN-SHELL ELECTROCHROMES AS SUITABLE REPLACEMENTS FOR THEIR VIOLOGEN-BASED COUNTERPARTS

In the previous chapter, the synthesis and photophysical properties of two novel photostable open-shell fluorophores were discussed. Building on these findings, the present chapter investigates a different functional aspect of these organic materials, that is their electrochromic behavior.

As discussed in section 2.2.1, trityl organic radicals are chemical stable open-shell molecules with an unpaired electron in the SOMO. Both the reduced (neutral) and open-shelled redox states are stable,[190, 191] unlike their neutral closed-shell counterparts.[130, 192] Thus, the unique electronic structure of the doublet multiplicity of trityl radicals is ideally poised for tuning the optical properties both by substitution and electrochemically similar to TPAs to meet the need of NIR absorbing electrochromes.[34, 44] In this regard, as stated in section 2.2.3 TPA has emerged as a crucial design element for electrochromes in part owing to its reversible oxidation.[193] Moreover, TPA units can be readily functionalized through well-established synthetic procedures, enabling fine tuning of their oxidation potential and of the optical properties of both the neutral and oxidized states.[108, 194-198]

Electrochromic materials for the NIR must be photostable and reversibly switch between their redox states under applied bias. As previously discussed in section 2.2.3, classical viologen-based electrochromic systems exhibit efficient and reversible electrochromic responses. However, their operational stability and limited modulation in the NIR region restrict their applicability in advanced broadband electrochromic technologies. In this context, open-shell electrochromes based on chemically and photostable organic radicals represent a promising alternative strategy.

To the best of our knowledge, so far, no polychlorinated trityl organic radicals have been reported as electrochromic materials. Therefore, this chapter focuses specifically on exploring the electrochromic potential of such radicals.

Toward demonstrating the suitability of open-shell electrochromes as replacements for traditional viologen-based materials, the electrochromic behavior of two substituted trityl radicals (**2** – **3**; figure 5.1) is investigated.[104] TTM was not considered as a potential electrochromic material due to its poor photostability (figure 4.7).

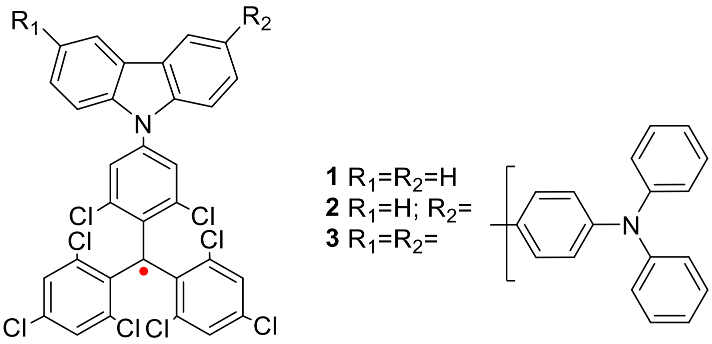

Figure 5.1. Molecular structures of NIR electrochromic open-shell chromophores **1-3**. The red dot marks the trityl radical center.

These molecular electrochromes were rationally designed by integrating critical components to confer higher photostability to the trityl radical core according to our previous findings. Meanwhile, integrating TPA served three roles. On one hand, it increased the photostability of the radical, a desired trait for smart-windows applications. On the other hand, the intrinsic electron donation of the triarylamine promotes intramolecular charge transfer, resulting in a desired broad NIR absorption of the oxidized state. The TPA was further expected to confer a secondary redox activity, enhancing the electrochemically induced colored state. The electrochromism of **2** and **3** are presented and benchmarked against **1** to illustrate the property enhancement with TPA.

5.1. Results and Discussions

5.1.1. Electrochemistry of synthesized organic radicals

As shown in the previous chapter **2** and **3** (previously numbered as **3** and **4**, respectively) exhibited high photostability and did not undergo any degradation of their optical properties during 846.7 and 1153.3 min, respectively under continuous irradiation in solution. Photostability is a key criterion for smart-window applications given their continuous exposure to sun during the lifetime of the material. To other key metric for electrochromic use is reversible redox activity. This was evaluated for the open-shelled electrochromes by cyclic voltammetry.

The cyclic voltammograms revealed three distinct features of the electrochromes (figure 5.2).

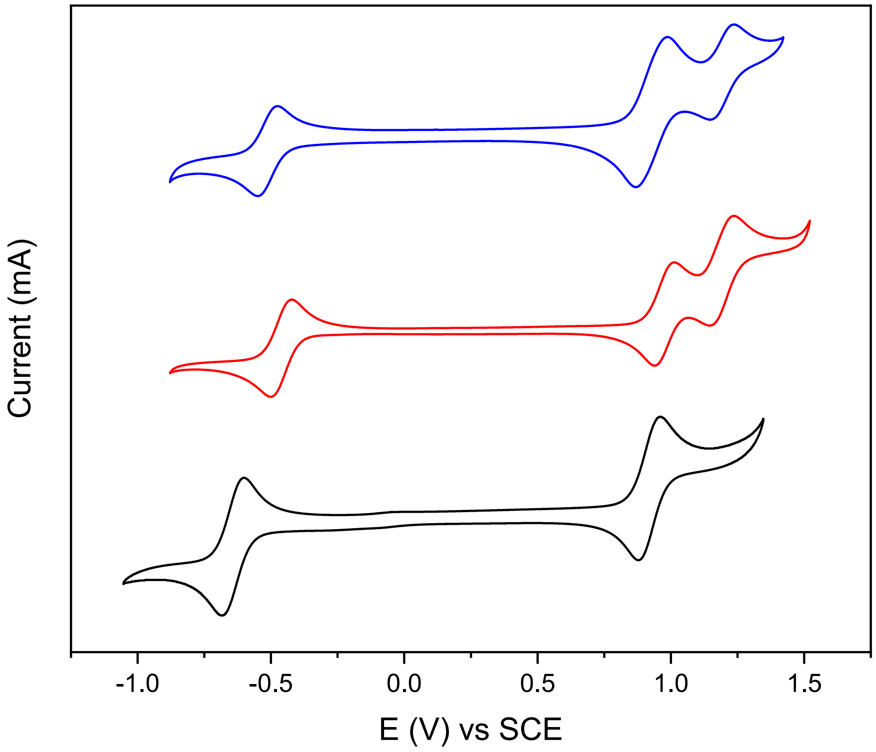

Figure 5.2. Cyclic voltammograms of **1** (black), **2** (red), and **3** (blue) recorded in anhydrous dichloromethane with TBAP (0.1 M) at 20 mV/s.

The number of redox processes was dependent on the substitution of the trityl. For example, the simple carbazole substituent underwent uniquely two one-electron redox processes: oxidation and reduction. The oxidation was assigned to the carbazole oxidation resulting in the radical cation. In contrast, the reduction was assigned to the reduction of the radical. The one-electron oxidation was assigned according to the similar peak currents of the two redox processes along with similar peak current with equimolar ferrocene that was added for internal calibration. Both **2** and **3** had similar oxidation and reduction comparable to **1**. Their reduction potential was less negative than that **1** owing to their increased degree of conjugation (table C.5.1). While the first oxidation of **2** and **3** occurred at similar potentials to **1**, this reversible process was assigned to the radical cation formation of the TPA substituent. This is according to the first wave of **3** being twice as intense of the similar oxidation wave of **2**. The increased current is a result of simultaneously oxidation of the second TPA, resulting in a bis(radical cation) radical. The simultaneous double oxidation, as opposed to the sequential two step one-electron oxidation, is further corroborated by the oxidation peak not splitting into two resolvable oxidation processes as different scan rates. Subsequent oxidation of **2** and **3** gives rise to the trityl radical oxidation. The proposed redox pathway for electroactive radicals **1 - 3** is illustrated in figure 5.3.

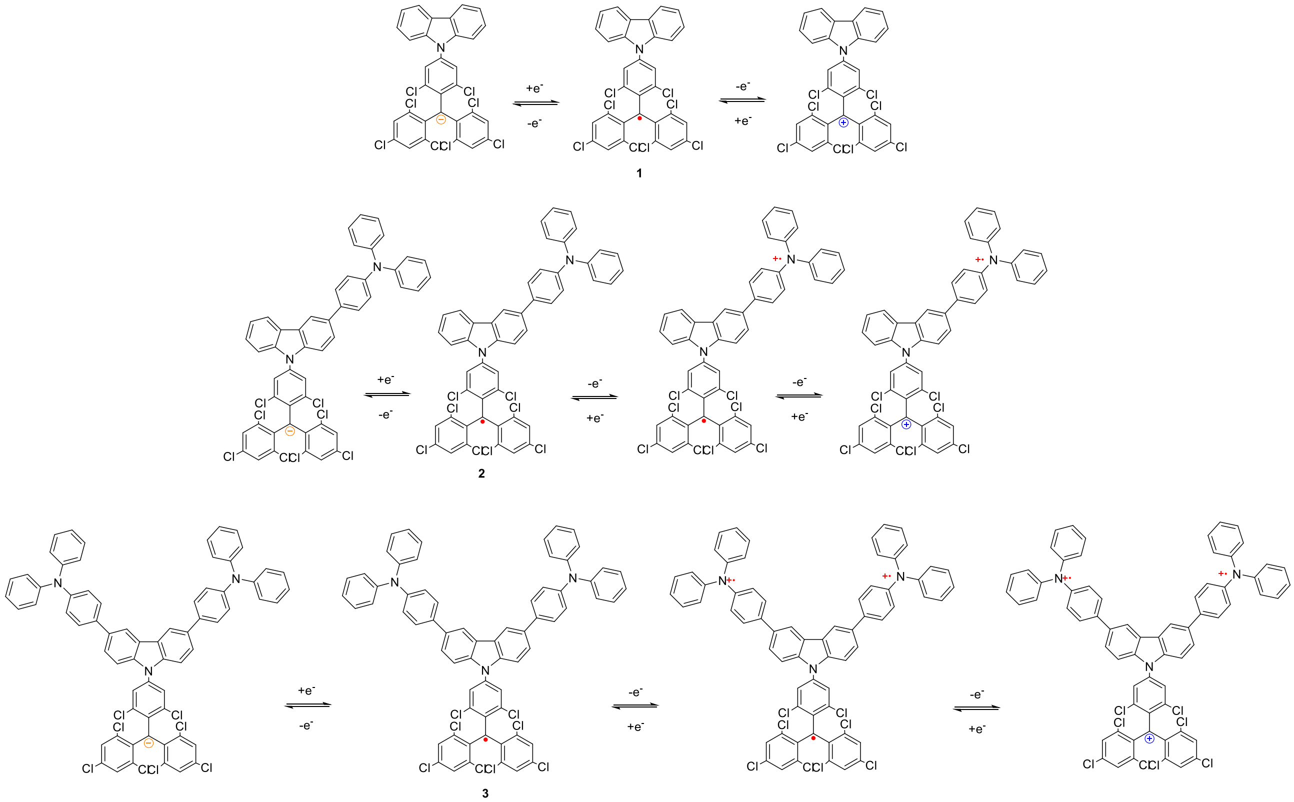

Figure 5.3. Proposed redox mechanisms for the electrochromic radicals **1-3**. The red dot denotes the carbon-centred trityl radical (neutral state). Symbols indicate the site and nature of the redox product: positive blue represents the trityl carbocation, whereas negative orange indicates the trityl carbanion, and the radical cation located on the N atom the TPA motif is represented in red.

To further corroborate the simultaneous oxidation of the two TPAs of **3,** it was chemically oxidized with $Cu(ClO_4)_2$ x $6H_2O$. This oxidant was chosen because it can precisely be weighed for accurately determining the mole ratio added relative to **3**. It also promotes single electron transfer because it is a mild oxidant. The change in absorption of **3** was monitored after the addition of known aliquots of the oxidant. Indeed, a broad NIR absorption centred at 1150 nm grew monotonically contingent on the amount of oxidant added (figure 5.4). Of worthy of noting, that the absorption change was consistent with no additional intermediates forming with upwards of 20 equivalents of oxidation. This is consistent with simultaneous formation of both arylamine radical cations within an identical potential window rather than two resolvable, sequential one-electron steps.

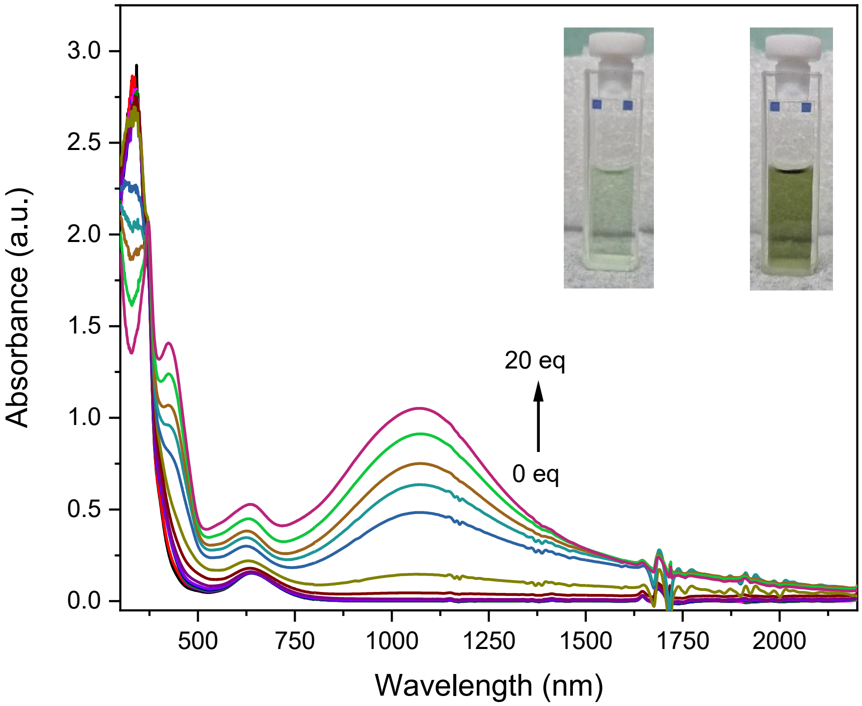

Figure 5.4. Chemical oxidation of **3** in anhydrous acetonitrile with increasing equivalents (eq) of $Cu(ClO_4)_2$ x $6H_2O$. Inset: photographs of the solution before (left) and after chemical oxidation with $Cu(ClO_4)_2$ x $6H_2O$ (20 eq, right).

5.1.2. Spectroelectrochemistry of synthesized organic radicals

Reversible broad absorption in the NIR is a requisite of electrochromes. This was evaluated by tracking the change in absorption with applied potential across the entire visible spectrum and extended into the NIR. The absorption of the neutral of **1–3** decreased with increasing applied positive potential, and it was replaced with an intense absorption in the NIR (figure 5.5). The new NIR absorptions occurred at ~816 nm for **1**, ~1139 nm for **2**, and ~1150 nm for **3**. The absorption shifts are consistent with the degree of conjugation, and hence the number of substituents. This is consistent with the redox potentials measured by cyclic voltammetry. The NIR transitions dominant the absorption, taking place in the NIR-I (750 - 1000 nm) region for **1** and the NIR-II (1000 - 1700 nm) window for **2** - **3**.[199, 200] Accordingly, the oxidized states of **2** and **3** offer addressable NIR-II wavelengths, directly accessible electrochemically for infrared electrochromic modulation.

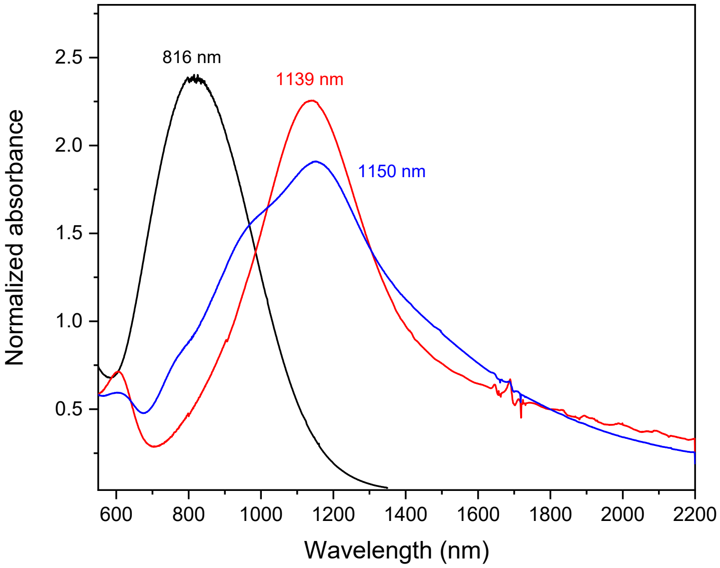

Figure 5.5. Absorption spectra of **1** (black), **2** (red), and **3** (blue) in anhydrous dichloromethane with an applied potential of 1.0 V, 0.9 V, and 0.8 V respectively.

To confirm the reversible absorption in the NIR when electrochemically switching between the neutral and the oxidized states, the NIR absorption of the given radical was monitored with applied potential for 100 cycles, showing reproducible switching and full spectral recovery at 0.0 V (figure 5.6). In all case, the original absorption spectrum of the neutral state was regenerated with open Collectively, the measurements confirm that **1 - 3** reversible switch their NIR absorption between the oxidized (ON) and neutral (OFF) states.[103] Hence, these measurements demonstrate that trityl-based radicals provide a tunable and reversible NIR electrochromic response in solution. In contrast, as discussed previously, viologen-based electrochromic systems are predominantly limited to modulation in the visible region under comparable solution-phase measurements (table 5.1).

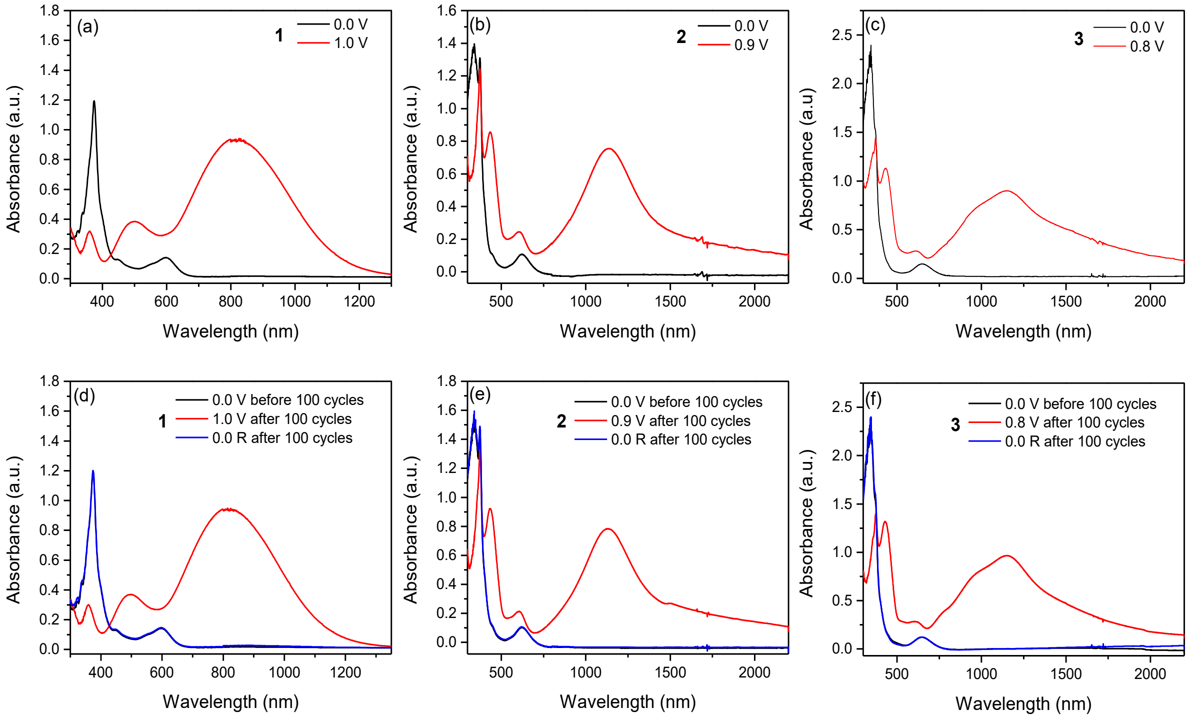

Figure 5.6. UV–Vis–NIR spectroelectrochemistry and cycling stability of **1** – **3** in anhydrous dichloromethane under controlled-potential oxidation. (a–c) Spectra at 0.0 V (black) and after anodic bias to 1.0 V (**1**), 0.9 V (**2**), and 0.8 V (**3**) (red). (d–f) Cycling tests: spectra at 0.0 V before cycling (black), after 100 oxidative cycles at the same potentials (red), and after returning to 0.0 V (blue). The near-complete recovery of the ground-state spectra indicates good spectroelectrochemical reversibility.

Table 5.1. Viologen-based ECDs in solution.[135]

EC material	**ECD type**	**Solvent**	**λ_{max} (nm)**
Phosphaviologen (thienyl-substituted)	Solution	ACN/DMF	550
Viologen–carbazole	Solution	PC	670
Viologen–triphenylamine	Solution	PC	727

Ethyl viologen/borax	Solution	PVA/Water	550
Ethyl viologen/FcNTf	Solution	–	610
Methyl viologen/GQD	Solution	PVA/water	550

A new reversible absorption band was formed in the visible region at ca. 505 nm upon applying a cathodic bias for the studied radicals (figure 5.7). Notably, these radicals exhibit a unique electrochromic response in which visible and NIR absorptions can be selectively activated depending on whether an anodic or cathodic bias is applied. This ambipolar electrochromic behavior enables bidirectional and reversible optical modulation across distinct spectral regions. In contrast to classical viologen-based electrochromic systems, which typically rely on the generation of a single-colored radical species and are largely restricted to visible modulation,[130, 135] these open-shell radicals allow electrochemical access to both visible and NIR bands. Hence, this bidirectional tunability underscores the value of these radicals as advanced electrochromic materials.

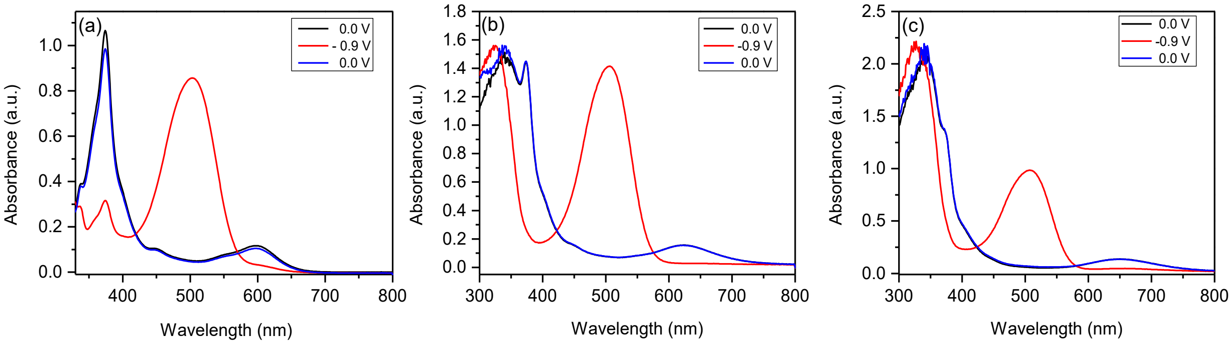

Figure 5.7. UV-Vis-NIR spectroelectrochemistry and reversibility of **1 - 3** in anhydrous dichloromethane under controlled-potential reduction. (a-c) Spectra at 0.0 V (black) and after cathodic bias. Reversibility test: spectra at 0.0 V before cathodic bias (black), after cathodic bias (red), and returning to 0.0 V (blue). The near-complete recovery of the ground-state spectra indicates good spectroelectrochemical reversibility.

5.1.3. NIR Electrochromic Performance: Contrast Ratio and Coloration Efficiency

To evaluate the suitability of the synthesized radicals as electrochromic materials, key quantitative performance parameters were analyzed, namely the optical contrast (transmittance modulation, ΔT) and the coloration efficiency (CE). These metrics are widely used to assess the performance of electrochromic materials because they quantify the magnitude of optical modulation and the efficiency with which optical density changes are generated per unit of injected charge, respectively.

The ΔT between the electrochemically off and on states at a given wavelength (transmittance modulation) was calculated. The contrast ratio was defined as:[103, 105]

$$\Delta T\ (\%) = \frac{T_{OFF}(\lambda_{max}) - T_{ON}(\lambda_{max})}{T_{OFF}\ (\lambda_{max})}\ x\ 100$$

with T_{off} (λ_{max}) being the transmittance of the neutral state and T_{on} (λ_{max}) the transmittance of the oxidized state measured at the maximum NIR absorption of the oxidized state (figure C.5.1).

The ΔT for the three radicals were higher than 80% as per table 5.2. The large voltage-addressable and reversible attenuation at well-defined NIR bands satisfies a central requirement for NIR electrochromic components.[103, 108] Notably, these values fall within or above the range typically reported for viologen-based electrochromic systems measured in solution (ΔT ≈ 40-96%).[134] Although most viologen electrochromes operate primarily in the visible region, these reported values provide a useful benchmark for evaluating electrochromic efficiency under comparable experimental conditions.

The CE for each open-shell electrochromes was measured from spectroelectrochemical measurements. Thus, absorbance at a given wavelength was continuously monitored when alternating the applied potential between the neutral and oxidized states, using symmetric time intervals per full redox cycle. The chronoamperometric current was recorded in parallel and was integrated to obtain the injected charge density per step. The charges were then normalized by the geometric area of the honeycomb working electrode ($A = 0.186\ cm^2$). The CE was calculated according to:

$$CE = \frac{\Delta O.D\ (\lambda)}{Q}$$

Where ΔO.D. (λ) is the difference in absorbance between the maximum (oxidized state) and minimum (neutral state) at the given NIR absorption maximum for a set time interval, while Q is the total injected/removed charge with the change in ΔO.D. (λ). The CE was obtained from the slope of the ΔO.D. vs Q plot (figure C.5.2).

The CE measured for radicals **1 - 3** range from 425 to 590 $cm^2\ C^{-1}$ (table 5.2), exceeding the values commonly reported for viologen-based electrochromes in solution (CE ≈ 100–350 $cm^2\ C^{-1}$).[134] Although most viologen systems operate in the visible region, this comparison highlights that the se open-shell electrochromes compared to their viologens counterparts achieve better CE values, which indicate efficient, voltage-addressable attenuation desirable for low-energy NIR electrochromic operation.[105, 108]

Table 5.2. Electrochromic Performance in DCM of TTM-Based Radical Fluorophores.

Compound	**IR band λ_{max} (nm)**	**ΔT (%)**	**CE (cm^2/C)**
1	815	88	425
2	1139	83	475
3	1150	87	590

Together, these results demonstrate that the investigated trityl-based radicals combine large optical contrast and moderate coloration efficiency while enabling tunable and reversible electrochromic modulation in the NIR and visible region, which makes them good candidates as electrochromic materials.

5.2. Materials and Methods

The electrochromes **1-3** were prepared as reported in the materials and methods section of chapter 4, where they were numbered as **2 - 4** respectively.

Electrochemical measurements

Cyclic voltammograms were measured on a multi-channel potentiostat (BioLogic VSP). Solutions of the organic radicals (10^{-3} M) were prepared in anhydrous dichloromethane with tetrabutylammonium perchlorate (0.10 M; TBAP) as the supporting electrolyte. The sames were measured in a three-electrode cell using a glassy carbon working electrode, a Pt wire counter electrode, and a silver wire pseudo-reference electrode. Ferrocene (10^{-3} M) was added as an internal standard at the end of the measurements and the potentials were calibrated to its reversible Fc/Fc^{+} couple $E°'(Fc/Fc^{+}) = 0.48$ V vs SCE in dichloromethane.[201]

Spectroelectrochemistry

Spectroelectrochemical measurements were done with the potentiostat and a combined UV-vis-NIR spectrometer (Varian Cary 5000). The measurements were done in a 1 × 1 cm quartz cuvette with an optical pathlength of 0.7 mm. A commercial ceramic honeycomb electrode (Pine Research) with 19 gold-plated low-volume wells was used as the working electrodes along with a laminated Au counter and reference electrodes. The solutions were deoxygenated by bubbling N_2 for at least 15 min**,** transferred to the cuvette, and the cell was sealed with parafilm before measuring the change in absorption with applied potential. The applied potential was stepped from 0.0 V to +1.0 V with a dwell time of 2 min before recording the resulting change in the absorption spectrum.

Chemical oxidation

Stock solution of **3** (1 mM) in anhydrous acetonitrile was used for its chemical oxidation. For the titration, 50 µL of the stock was diluted in a 1 cm quartz cuvette to giving a 25 µM sample. A solution of $Cu(ClO_4)_2$ (2.50 mM) was prepared in anhydrous acetonitrile. Aliquots (4.0 µL) corresponding between 0.2 and 20 equivalents of oxidant were added to the cuvette and the corresponding absorption spectrum measured equilibration of ca. 30 s at room temperature. Spectra were corrected for the small dilution with the oxidant at higher aliquots added, ≤ 2 vol% at the end of the titration. Identical acetonitrile aliquots were added to a separate sample in the absence of oxidant to confirm the spectral changes from the chemical oxidation rather than solvent composition.

CHAPTER 6 CONCLUSION AND FUTURE RESEARCH

This thesis exploited rational molecular design to modulate the optical, electrical, and photostability of organic compounds, bridging closed-shell crystalline polymorphs and open-shell electroactive materials. Thus, the three research objectives formulated in chapter 1 leads to the following conclusions:

1. Two crystalline polymorphs of a benzothiadiazole derivative were obtained from identical crystallization conditions via different synthetic protocols. Despite their identical molecular structure, the crystal arrangement of the polymorphs was different. Polymorph A exhibited C–H···N/S contacts and limited π overlap of the aromatic units, whereas polymorph B formed columns of extended π–π stacking and packed into a denser network, in part due to its larger Z value compared to polymorph A. These differences in supramolecular organization had a direct impact on the solid-state photophysics. Thus, the increased π-overlap and multiple intermolecular contacts in the densely packed polymorph B quenched the Φ_{fl} fourfold and produced a blue-shifted emission, accompanied by faster and multiple excited-state decay pathways. Notably, conversion from the metastable, weakly emissive polymorph B to the thermodynamically stable, highly emissive polymorph A was achieved by grinding the crystals.

Taken together, these results illustrate how subtle differences in crystal packing dictate emission in benzothiadiazole-based fluorophores. In particular, the arrangement of intermolecular contacts, directly influences the Φ_{fl} and the spectral position of emission. Beyond the specific system investigated here, these findings provide broader insight into how polymorphism can influence the design and photophysical behavior of benzothiadiazole-based fluorophores. In particular, understanding how subtle variations in crystal packing modulate emission efficiency and spectral position may prove valuable for the rational design of benzothiadiazole derivatives targeting aggregation-induced emission (AIE) or aggregation-induced emission enhancement (AIEE). More broadly, this work highlights how controlling supramolecular organization can serve as an effective strategy for tuning the solid-state optical properties of closed-shell organic fluorophores, which help in the development of advanced solid-state emitters for optoelectronic applications.

2. The electron-donor substituent strategy applied to the trityl framework proved effective for enhancing the photostability of open-shell fluorophores. In particular, the covalent attachment of electron-donating triphenylamine units to the carbazole core increased the overall degree of conjugation and promoted intramolecular charge transfer from the electron-rich periphery to the electron-deficient radical center. As a result, the emission was shifted toward the NIR region while the resistance to photodegradation was significantly improved. In addition, this electronic coupling generated a charge-transfer absorption in the red region of the visible spectrum.

Although these radicals exhibit weak fluorescence due to multiple nonradiative decay pathways, these deactivation channels contribute to the photochemical robustness of the radical species. This trade-off between emission efficiency and stability highlights an important design principle for radical-based fluorophores. Beyond the specific molecules investigated here, these findings illustrate how donor engineering can be used to control both the photophysical and photochemical behavior of open-shell molecules.

More broadly, the ability to achieve enhanced photostability while maintaining NIR optical activity may be particularly valuable for emerging technologies where optical spin polarization is required. In this context, radical-based luminophores may provide promising molecular platforms for applications in sensing and quantum computing where optical spin polarization is the key requirement.

3. Trityl radicals demonstrate the ability to electrochemically induce color switching, generating large transmittance modulation and strong voltage-addressable contrast in the NIR region. In this regard, the NIR absorption of the electrochemically oxidized radicals exhibits significant and reversible optical modulation, confirming the suitability of these open-shell systems for NIR electrochromic switching applications.

In addition, these radicals enable selective switching between visible and NIR absorption bands depending on the applied bias, highlighting a key advantage of organic radicals over traditional closed-shell electrochromic materials, like viologens. Thus, this ambipolar optical response allows independent and reversible tuning of visible and infrared optical properties through molecular design and electrochemical control.

More broadly, the ability to tune visible absorption while preserving strong NIR electrochromic modulation through donor substitution on the trityl core illustrates the versatility of this molecular platform. Such properties create new possibilities for multifunctional electrochromic systems that combine visual display capabilities with infrared modulation, potentially enabling advanced technologies such as adaptive optical displays and energy-efficient smart windows.

Limitations and Future Research

The findings in this thesis elucidate the SPR relationships that dictate the photophysical and electrochemical behavior of the examined systems; however, certain experimental limitations should be recognized.

In the polymorphism study, two crystalline polymorphs exhibiting unique emission characteristics were obtained under identical crystallization conditions but from materials prepared through different synthetic conditions. Although the structural differences between the polymorphs were clearly established, the exact factors that control their formation remain unclear. Specifically, the impact of reaction conditions on the nucleation of each polymorph was not methodically examined, resulting in an unclear mechanism governing polymorph selection. This limitation constitutes an interesting starting point for a future research project aimed at understanding the origin of the observed polymorphism.

Future research will focus on three main directions aimed at deepening the understanding and technological potential of the synthesized open-shell fluorophores.

First, further computational studies will investigate the origin of the enhanced non-radiative decay observed in the newly synthesized trityl radicals. This will be important to determine whether this increase in non-radiative processes arises from coupling with high-energy vibrational modes, setting a comparison with previously reported TTM-TPA. A detailed analysis of vibronic coupling will help clarify how the donor architecture of TPA-based radicals modulates the balance between emission efficiency and photostability.

Second, given that the synthesized radicals display ambipolar electrochromic behavior, additional spectroelectrochemical investigations in the visible region are required. These studies will evaluate how key electrochromic parameters, such as optical transmittance modulation and coloration efficiency evolve under cathodic bias. Such measurements will provide a more complete understanding of the bidirectional optical response of these materials across both the visible and NIR regions. Furthermore, the cycling stability in solution of the synthesized radicals in the visible and NIR regions should be measured by tracking the optical transmittance change at a fixed wavelength during repeated redox cycling.

Finally, future work will aim at translating these molecular properties into functional devices. In this regard, the fabrication and testing of electrochromic devices incorporating the synthesized open-shell electrochromes as active layers will be explored. Evaluating their switching stability, optical contrast, and operational durability under repeated redox cycling will be essential to assess their potential for practical applications like smart windows, and optical displays.

REFERENCES

1. Scaiano, J. C., *Photochemistry Essentials*. American Chemical Society: 2022; p -1.

2. Alfieri, M. L.; Panzella, L.; Crescenzi, O.; Napolitano, A.; d'Ischia, M., Nature-Inspired Functional Chromophores from Biomimetic o-Quinone Chemistry. *European Journal of Organic Chemistry* **2021,** *2021* (21), 2982-2989.

3. Turro, N. J., *Modern Molecular Photochemistry*. University Science Books: 1991.

4. Quenching of Fluorescence. In *Principles of Fluorescence Spectroscopy*, Lakowicz, J. R., Ed. Springer US: Boston, MA, 2006; pp 277-330.

5. Debnath, P., A Rapid and Innovative Method for Prediction of Spin Multiplicity and Spin State of Homo and Hetero Nuclear Diatomic Molecules and Ions within a Very Short Time. *IOSR Journal of Applied Chemistry* **2015,** *8*, 27-30.

6. Halstead, J. A., Teaching the Spin Selection Rule: An Inductive Approach. *Journal of Chemical Education* **2012,** *90* (1), 70-75.

7. Valeur, B. P. N. B.-S., M.;, Absorption of Ultraviolet, Visible, and Near-Infrared Radiation. In *Molecular Fluorescence*, 2012; pp 31-51.

8. Castle, K. J., High-Resolution Vibration–Rotation Spectroscopy of CO2: Understanding the Boltzmann Distribution. *Journal of Chemical Education* **2007,** *84* (3), 459.

9. Omary, M. A. P., H. H.;, Luminescence Theory. *Encyclopedia of Spectroscopy and Spectrometry* **1999**, 1186–1207.

10. Condon, E., A Theory of Intensity Distribution in Band Systems. *Physical Review* **1926,** *28* (6), 1182-1201.

11. Franck, J.; Dymond, E. G., Elementary processes of photochemical reactions. *Transactions of the Faraday Society* **1926,** *21* (February), 536-542.

12. Condon, E. U., Nuclear Motions Associated with Electron Transitions in Diatomic Molecules. *Physical Review* **1928,** *32* (6), 858-872.

13. Sauer, M., Hofkens, J. and Enderlein, J., Basic Principles of Fluorescence Spectroscopy. In *Handbook of Fluorescence Spectroscopy and Imaging*, 2011; pp 1-30.

14. Scaiano, J. C., A beginners guide to understanding the mechanisms of photochemical reactions: things you should know if light is one of your reagents. *Chem Soc Rev* **2023**.

15. Dong, H.; Zhang, C.; Liu, Y.; Yan, Y.; Hu, F.; Zhao, Y. S., Organic Microcrystal Vibronic Lasers with Full-Spectrum Tunable Output beyond the Franck-Condon Principle. *Angew Chem Int Ed Engl* **2018,** *57* (12), 3108-3112.

16. Kasha, M., Characterization of electronic transitions in complex molecules. *Discussions of the Faraday Society* **1950,** *9* (0), 14-19.

17. E., N. H., A history of luminescence from the earliest times until 1900.pdf>. *The American Philosophical Society* **1957,** *54*.

18. Matyus, L.; Szollosi, J.; Jenei, A., Steady-state fluorescence quenching applications for studying protein structure and dynamics. *J Photochem Photobiol B* **2006,** *83* (3), 223-36.

19. https://www.edinst.com/resource/what-is-a-jablonski-diagram-perrin-jablonski-diagram/. *Edinburgh Instruments Website* **2021**.

20. Lichtman, J. W.; Conchello, J.-A., Fluorescence microscopy. *Nature Methods* **2005,** *2* (12), 910-919.

21. Birks, J. B., The Rules of Organic Molecular Fluorescence. In *Research in Photobiology*, Castellani, A., Ed. Springer US: Boston, MA, 1977; pp 15-24.

22. Mao, Z.; Yang, Z.; Fan, Z.; Ubba, E.; Li, W.; Li, Y.; Zhao, J.; Yang, Z.; Aldred, M. P.; Chi, Z., The methylation effect in prolonging the pure organic room temperature phosphorescence lifetime. *Chem Sci* **2019,** *10* (1), 179-184.

23. Chang, B.; Chen, J.; Bao, J.; Sun, T.; Cheng, Z., Molecularly Engineered Room-Temperature Phosphorescence for Biomedical Application: From the Visible toward Second Near-Infrared Window. *Chem Rev* **2023,** *123* (24), 13966-14037.

24. Zhai, Y.; Li, S.; Li, J.; Liu, S.; James, T. D.; Sessler, J. L.; Chen, Z., Room temperature phosphorescence from natural wood activated by external chloride anion treatment. *Nat Commun* **2023,** *14* (1), 2614.

25. Ji, M.; Ma, X., Recent progress with the application of organic room-temperature phosphorescent materials. *Industrial Chemistry & Materials* **2023,** *1* (4), 582-594.

26. Dos Santos, J. M.; Hall, D.; Basumatary, B.; Bryden, M.; Chen, D.; Choudhary, P.; Comerford, T.; Crovini, E.; Danos, A.; De, J.; Diesing, S.; Fatahi, M.; Griffin, M.; Gupta, A. K.; Hafeez, H.; Hammerling, L.; Hanover, E.; Haug, J.; Heil, T.; Karthik, D.; Kumar, S.; Lee, O.; Li, H.; Lucas, F.; Mackenzie, C. F. R.; Mariko, A.; Matulaitis, T.; Millward, F.; Olivier, Y.; Qi, Q.; Samuel, I. D. W.; Sharma, N.; Si, C.; Spierling, L.; Sudhakar, P.; Sun, D.; Tankeleviciu Te, E.; Duarte Tonet, M.; Wang, J.; Wang, T.; Wu, S.; Xu, Y.; Zhang, L.; Zysman-Colman, E., The Golden Age of Thermally Activated Delayed Fluorescence Materials: Design and Exploitation. *Chem Rev* **2024,** *124* (24), 13736-14110.

27. Uoyama, H.; Goushi, K.; Shizu, K.; Nomura, H.; Adachi, C., Highly efficient organic light-emitting diodes from delayed fluorescence. *Nature* **2012,** *492* (7428), 234-8.

28. Endo, A.; Sato, K.; Yoshimura, K.; Kai, T.; Kawada, A.; Miyazaki, H.; Adachi, C., Efficient up-conversion of triplet excitons into a singlet state and its application for organic light emitting diodes. *Applied Physics Letters* **2011,** *98* (8).

29. Carrod, A. J.; Gray, V.; Börjesson, K., Recent advances in triplet–triplet annihilation upconversion and singlet fission, towards solar energy applications. *Energy & Environmental Science* **2022,** *15* (12), 4982-5016.

30. Zeng, L.; Huang, L.; Han, J.; Han, G., Enhancing Triplet-Triplet Annihilation Upconversion: From Molecular Design to Present Applications. *Acc Chem Res* **2022,** *55* (18), 2604-2615.

31. Shang, Y.; Hao, S.; Yang, C.; Chen, G., Enhancing Solar Cell Efficiency Using Photon Upconversion Materials. *Nanomaterials (Basel)* **2015,** *5* (4), 1782-1809.

32. Kasemthaveechok, S.; Abella, L.; Crassous, J.; Autschbach, J.; Favereau, L., Organic radicals with inversion of SOMO and HOMO energies and potential applications in optoelectronics. *Chemical Science* **2022,** *13* (34), 9833-9847.

33. Gomberg, M., AN INSTANCE OF TRIVALENT CARBON: TRIPHENYLMETHYL. *Journal of the American Chemical Society* **1900,** *22* (11), 757-771.

34. Tonnelé, C.; Casanova, D., Rationalization and tuning of doublet emission in organic radicals. *J. Mater. Chem. C* **2022,** *10*, 13826-13833.

35. Peng, Q.; Obolda, A.; Zhang, M.; Li, F., Organic Light-Emitting Diodes Using a Neutral pi Radical as Emitter: The Emission from a Doublet. *Angew Chem Int Ed Engl* **2015,** *54* (24), 7091-5.

36. He, C.; Li, Z.; Lei, Y.; Zou, W.; Suo, B., Unraveling the Emission Mechanism of Radical-Based Organic Light-Emitting Diodes. *J Phys Chem Lett* **2019,** *10* (3), 574-580.

37. Mizuno, A.; Matsuoka, R.; Mibu, T.; Kusamoto, T., Luminescent Radicals. *Chem Rev* **2024**.

38. Abella, L.; Crassous, J.; Favereau, L.; Autschbach, J., Why is the Energy of the Singly Occupied Orbital in Some Radicals below the Highest Occupied Orbital Energy? *Chemistry of Materials* **2021,** *33* (10), 3678-3691.

39. Gao, Y.; Wu, Y.; Ren, B.; Li, Y., Design of non-Aufbau organic radicals based on TTM/TTBrM core. *Organic Electronics* **2025,** *142*, 107248.

40. Obolda, A.; Hazretomar, P.; Abdulahat, M.; Ma, F.; Tuersun, A.; Ding, Z.; Hu, Z., A near-infrared luminescent organic radical with switchable emission and SOMO-HOMO inversion via a protonation/deprotonation process. *Phys Chem Chem Phys* **2025,** *27* (19), 9943-9948.

41. Hudson, J. M.; Hele, T. J. H.; Evans, E. W., Efficient light-emitting diodes from organic radicals with doublet emission. *Journal of Applied Physics* **2021,** *129* (18).

42. Sahalianov, I.; Valiev, R. R.; Ramazanov, R. R.; Baryshnikov, G., Neutral vs Charged Luminescent Radicals: Anti-Kasha Emission and the Impact of Molecular Surrounding. *J Phys Chem A* **2024,** *128* (26), 5138-5145.

43. Zhu, Y.; Zhu, Z.; Wang, S.; Kuang, Z.; Peng, Q.; Abdurahman, A., Anti-Kasha Emission in Organic Radicals: Mechanistic Insights and Experimental Caveats. *ChemPhotoChem* **2025,** *9* (8).

44. Abdurahman, A.; Hele, T. J. H.; Gu, Q.; Zhang, J.; Peng, Q.; Zhang, M.; Friend, R. H.; Li, F.; Evans, E. W., Understanding the luminescent nature of organic radicals for efficient doublet emitters and pure-red light-emitting diodes. *Nat Mater* **2020,** *19* (11), 1224-1229.

45. Dewar, M. J. S. L.-H., H C.;, The Electronic Spectra of Aromatic Molecules I: Benzenoid Hydrocarbons. *Proc. Phys. Soc. A* **1954,** *67*, 795.

46. Longuet-Higgins, H. C.; Pople, J. A., The Electronic Spectra of Aromatic Molecules IV: Excited States of Odd Alternant Hydrocarbon Radicals and Ions. *Proceedings of the Physical Society. Section A* **1955,** *68* (7), 591-600.

47. Cui, Z.; Ye, S.; Wang, L.; Guo, H.; Obolda, A.; Dong, S.; Chen, Y.; Ai, X.; Abdurahman, A.; Zhang, M.; Wang, L.; Li, F., Radical-Based Organic Light-Emitting Diodes with Maximum External Quantum Efficiency of 10.6. *J Phys Chem Lett* **2018,** *9* (22), 6644-6648.

48. Dong, S.; Xu, W.; Guo, H.; Yan, W.; Zhang, M.; Li, F., Effects of substituents on luminescent efficiency of stable triaryl methyl radicals. *Phys Chem Chem Phys* **2018,** *20* (27), 18657-18662.

49. Dong, S.; Obolda, A.; Peng, Q.; Zhang, Y.; Marder, S.; Li, F., Multicarbazolyl substituted TTM radicals: red-shift of fluorescence emission with enhanced luminescence efficiency. *Materials Chemistry Frontiers* **2017,** *1* (10), 2132-2135.

50. Gao, Y.; Xu, W.; Ma, H.; Obolda, A.; Yan, W.; Dong, S.; Zhang, M.; Li, F., Novel Luminescent Benzimidazole-Substituent Tris(2,4,6-trichlorophenyl)methyl Radicals: Photophysics, Stability, and Highly Efficient Red-Orange Electroluminescence. *Chemistry of Materials* **2017,** *29* (16), 6733-6739.

51. Cho, E.; Coropceanu, V.; Bredas, J.-L., Impact of chemical modifications on the luminescence properties of organic neutral radical emitters. *Journal of Materials Chemistry C* **2021**.

52. Velasco, D.; Castellanos, S.; López, M.; López-Calahorra, F.; Brillas, E.; Juliá, L., Red Organic Light-Emitting Radical Adducts of Carbazole and Tris(2,4,6-trichlorotriphenyl)methyl Radical That Exhibit High Thermal Stability and Electrochemical Amphotericity. *The Journal of Organic Chemistry* **2007,** *72* (20), 7523-7532.

53. Brown, A. M.; McCusker, C. E.; McCusker, J. K., Spectroelectrochemical identification of charge-transfer excited states in transition metal-based polypyridyl complexes. *Dalton Trans* **2014,** *43* (47), 17635-46.

54. Moore, B., 2nd; Sun, H.; Govind, N.; Kowalski, K.; Autschbach, J., Charge-Transfer Versus Charge-Transfer-Like Excitations Revisited. *J Chem Theory Comput* **2015,** *11* (7), 3305-20.

55. Cui, Z.; Abdurahman, A.; Ai, X.; Li, F., Stable Luminescent Radicals and Radical-Based LEDs with Doublet Emission. *CCS Chemistry* **2020,** *2* (4), 1129-1145.

56. Hicks, R. G., What's new in stable radical chemistry? *Org Biomol Chem* **2007,** *5* (9), 1321-38.

57. Griller, D.; Ingold, K. U., Persistent carbon-centered radicals. *Accounts of Chemical Research* **1976,** *9* (1), 13-19.

58. Osiecki, J. H.; Ullman, E. F., Studies of free radicals. I. .alpha.-Nitronyl nitroxides, a new class of stable radicals. *Journal of the American Chemical Society* **1968,** *90* (4), 1078-1079.

59. Cirujeda, J.; Ochando, L. E.; Amigó, J. M.; Rovira, C.; Rius, J.; Veciana, J., Structure Determination from Powder X-Ray Diffraction Data of a Hydrogen-Bonded Molecular Solid with Competing Ferromagnetic and Antiferromagnetic Interactions: The 2-(3,4-Dihydroxyphenyl)-α-Nitronyl Nitroxide Radical. *Angewandte Chemie International Edition in English* **1995,** *34* (1), 55-57.

60. Hawker, C. J.; Bosman, A. W.; Harth, E., New Polymer Synthesis by Nitroxide Mediated Living Radical Polymerizations. *Chemical Reviews* **2001,** *101* (12), 3661-3688.

61. Joseph, J.; Kalyanaraman, B.; Hyde, J. S., Trapping of Nitric Oxide by Nitronyl Nitroxides: An Electron Spin Resonance Investigation. *Biochemical and Biophysical Research Communications* **1993,** *192* (2), 926-934.

62. Hicks, R. G.; Lemaire, M. T.; Öhrström, L.; Richardson, J. F.; Thompson, L. K.; Xu, Z., Strong Supramolecular-Based Magnetic Exchange in π-Stacked Radicals. Structure and Magnetism of a Hydrogen-Bonded Verdazyl Radical:Hydroquinone Molecular Solid. *Journal of the American Chemical Society* **2001,** *123* (29), 7154-7159.

63. Power, P. P., Persistent and Stable Radicals of the Heavier Main Group Elements and Related Species. *Chemical Reviews* **2003,** *103* (3), 789-810.

64. Armet, O.; Veciana, J.; Rovira, C.; Riera, J.; Castaner, J.; Molins, E.; Rius, J.; Miravitlles, C.; Olivella, S.; Brichfeus, J., Inert carbon free radicals. 8. Polychlorotriphenylmethyl radicals: synthesis, structure, and spin-density distribution. *The Journal of Physical Chemistry* **1987,** *91* (22), 5608-5616.

65. Carilla, J.; Fajarí, L.; Juliá, L.; Riera, J.; Viadel, L., Two functionalized free radicals of the tris(2,4,6-trichlorophenyl)methyl radical series. Synthesis, stability and EPR analysis. *Tetrahedron Letters* **1994,** *35* (35), 6529-6532.

66. Carilla, J.; Fajarí, L.; Juliá, L.; Sañé, J.; Rius, J., (2,6-Dichlorophenyl)bis(2,4,6-trichlorophenyl)methyl radical. Synthesis, magnetic behaviour and crystal structure. *Tetrahedron* **1996,** *52* (20), 7013-7024.

67. Karplus, M., Vicinal Proton Coupling in Nuclear Magnetic Resonance. *Journal of the American Chemical Society* **1963,** *85* (18), 2870-2871.

68. Schreiner, K.; Berndt, A.; Baer, F., Spin density distribution and stereochemistry of triphenylmethyl radical in solution. *Molecular Physics* **1973,** *26* (4), 929-939.

69. Alcón, I.; Bromley, S. T., Structural control over spin localization in triarylmethyls. *RSC Advances* **2015,** *5* (119), 98593-98599.

70. Ballester, M.; Riera-Figueras, J.; Castaner, J.; Badfa, C.; Monso, J. M., Inert carbon free radicals. I. Perchlorodiphenylmethyl and perchlorotriphenylmethyl radical series. *Journal of the American Chemical Society* **1971,** *93* (9), 2215-2225.

71. Veciana, J.; Carilla, J.; Miravitlles, C.; Molins, E., Free radicals as clathrate hosts: crystal and molecular structure of 1:1 perchlorotriphenylmethyl radical–benzene. *Journal of the Chemical Society, Chemical Communications* **1987,** (11), 812-814.

72. Falle, H. R.; Luckhurst, G. R.; Horsfield, A.; Ballester, M., Electron Resonance Studies of Perchlorodiphenylmethyl and Perchlorotriphenylmethyl Free Radicals. *The Journal of Chemical Physics* **1969,** *50* (1), 258-264.

73. Matsuda, K.; Xiaotian, R.; Nakamura, K.; Furukori, M.; Hosokai, T.; Anraku, K.; Nakao, K.; Albrecht, K., Photostability of luminescent tris(2,4,6-trichlorophenyl)methyl radical enhanced by terminal modification of carbazole donor. *Chem Commun (Camb)* **2022,** *58* (97), 13443-13446.

74. Obolda, A.; Li, W.; Abdulahat, M.; Ma, F.; Li, B.; Ai, X.; Zhang, M.; Li, F., High-efficiency deep-red organic radical crystals and OLEDs with solid-state fluorescence and excellent photostability. *Organic Electronics* **2022,** *107.*

75. Luo, A.; Zhang, J.; Xiao, D.; Xie, G.; Xu, X.; Zhao, Q.; Sun, C.; Li, Y.; Zhang, Z.; Li, P.; Luo, S.; Xie, X.; Peng, Q.; Li, H.; Chen, R.; Chen, Q.; Tao, Y.; Huang, W., Efficient metal free organic radical scintillators. *Nat Commun* **2024,** *15* (1), 8181.

76. Green, A. P.; Buckley, A. R., Solid state concentration quenching of organic fluorophores in PMMA. *Phys Chem Chem Phys* **2015,** *17* (2), 1435-40.

77. Anne Fox M., G. E., Chen C-C., Photochemistry of Stable Free Radicals: The Photolysis of Perchlorotryphenylmethyl Radicals. *J. Am. Chem. Soc.* **1987,** *109*, 7088-7094.

78. Armet, O. V., J.; Rovira, C.; Riera, J.; Castaner, J.; Molins, E.; Rius, J.; Miravitlles, C.; Olivella, S.; Brichfeus, J.;, Inert Carbon Free Radicals. 8. Polychlorotriphenylmethyl Radicals. Synthesis, Structure, and Spin-Density Distribution. *J. Phys. Chem.* **1987,** *91*, 5608-5616.

79. Mayorga-Burrezo, P.; Jimenez, V. G.; Blasi, D.; Parella, T.; Ratera, I.; Campana, A. G.; Veciana, J., An Enantiopure Propeller-Like Trityl-Brominated Radical: Bringing Together a High Racemization Barrier and an Efficient Circularly Polarized Luminescent Magnetic Emitter. *Chemistry* **2020,** *26* (17), 3776-3781.

80. Chen, L.; Arnold, M.; Blinder, R.; Jelezko, F.; Kuehne, A. J. C., Mixed-halide triphenyl methyl radicals for site-selective functionalization and polymerization. *RSC Adv* **2021,** *11* (44), 27653-27658.

81. Liu, C. H.; Hamzehpoor, E.; Sakai-Otsuka, Y.; Jadhav, T.; Perepichka, D. F., A Pure-Red Doublet Emission with 90 % Quantum Yield: Stable, Colorless, Iodinated Triphenylmethane Solid. *Angew Chem Int Ed Engl* **2020,** *59* (51), 23030-23034.

82. Kusamoto, T.; Kimura, S., Photostable Luminescent Triarylmethyl Radicals and Their Metal Complexes: Photofunctions Unique to Open-shell Electronic States. *Chemistry Letters* **2021,** *50* (7), 1445-1459.

83. Hattori, Y.; Kusamoto, T.; Nishihara, H., Luminescence, stability, and proton response of an open-shell (3,5-dichloro-4-pyridyl)bis(2,4,6-trichlorophenyl)methyl radical. *Angew Chem Int Ed Engl* **2014,** *53* (44), 11845-8.

84. Tanushi, A.; Kimura, S.; Kusamoto, T.; Tominaga, M.; Kitagawa, Y.; Nakano, M.; Nishihara, H., NIR Emission and Acid-Induced Intramolecular Electron Transfer Derived from a SOMO–HOMO Converted Non-Aufbau Electronic Structure. *The Journal of Physical Chemistry C* **2019,** *123* (7), 4417-4423.

85. Kimura, S.; Matsuoka, R.; Kimura, S.; Nishihara, H.; Kusamoto, T., Radical-Based Coordination Polymers as a Platform for Magnetoluminescence. *J Am Chem Soc* **2021,** *143* (15), 5610-5615.

86. Li, X.; Wang, Y. L.; Chen, C.; Ren, Y. Y.; Han, Y. F., A platform for blue-luminescent carbon-centered radicals. *Nat Commun* **2022,** *13* (1), 5367.

87. Cho, H. H.; Gorgon, S.; Hung, H. C.; Huang, J. Y.; Wu, Y. R.; Li, F.; Greenham, N. C.; Evans, E. W.; Friend, R. H., Efficient and Bright Organic Radical Light-Emitting Diodes with Low Efficiency Roll-Off. *Adv Mater* **2023,** *35* (45), e2303666.

88. Cho, H. H.; Kimura, S.; Greenham, N. C.; Tani, Y.; Matsuoka, R.; Nishihara, H.; Friend, R. H.; Kusamoto, T.; Evans, E. W., Near-Infrared Light-Emitting Diodes from Organic Radicals with Charge Control. *Advanced Optical Materials* **2022**.

89. Xiaotian, R.; Ota, W.; Sato, T.; Furukori, M.; Nakayama, Y.; Hosokai, T.; Hisamura, E.; Nakamura, K.; Matsuda, K.; Nakao, K.; Monkman, A. P.; Albrecht, K., Carbazole-Dendronized Luminescent Radicals. *Angew Chem Int Ed Engl* **2023**, e202302550.

90. Gamero, V.; Velasco, D.; Latorre, S.; López-Calahorra, F.; Brillas, E.; Juliá, L., [4-(N-Carbazolyl)-2,6-dichlorophenyl]bis(2,4,6-trichlorophenyl)methyl radical an efficient red light-emitting paramagnetic molecule. *Tetrahedron Letters* **2006,** *47* (14), 2305-2309.

91. Castellanos, S.; Velasco, D.; Lopez-Calahorra, F.; Brillas, E.; Julia, L., Taking advantage of the radical character of tris(2,4,6-trichlorophenyl)methyl to synthesize new paramagnetic glassy molecular materials. *J Org Chem* **2008,** *73* (10), 3759-67.

92. Wei, Y.; An, K.; Xu, X.; Ye, Z.; Yin, X.; Cao, X.; Yang, C., Π-Radical Photosensitizer for Highly Efficient and Stable Near-Infrared Photon Upconversion. *Advanced Optical Materials* **2023**.

93. Gorgon, S.; Lv, K.; Grune, J.; Drummond, B. H.; Myers, W. K.; Londi, G.; Ricci, G.; Valverde, D.; Tonnele, C.; Murto, P.; Romanov, A. S.; Casanova, D.; Dyakonov, V.; Sperlich, A.; Beljonne, D.; Olivier, Y.; Li, F.; Friend, R. H.; Evans, E. W., Reversible spin-optical interface in luminescent organic radicals. *Nature* **2023,** *620* (7974), 538-544.

94. Englman, R.; Jortner, J., The energy gap law for non-radiative decay in large molecules. *Journal of Luminescence* **1970,** *1-2*, 134-142.

95. Bixon, M.; Jortner, J., Intramolecular Radiationless Transitions. *The Journal of Chemical Physics* **1968,** *48* (2), 715-726.

96. Liu, X.; Shi, C.; Zhao, M.; Li, F.; Zhang, J.; Jiang, Z.; Li, Q.; Yuan, A.; Yan, H., Robust Radicals Featuring B- and N-Embedded Dioxygen-Bridged Units: Synthesis, Structures, and Optical Properties. *Chemistry* **2024**, e202400927.

97. Ding, J.; Zhang, M.; Gao, Y.; Lu, C.; Zhang, M.; Li, F., A Simple Molecular Design Strategy for Luminescent Radicals to Achieve Near-Infrared Emission. *J Phys Chem Lett* **2023**, 8244-8250.

98. Anraku, K.; Matsuda, K.; Miyata, S.; Ishii, H.; Hosokai, T.; Okada, S.; Nakamura, K.; Nakao, K.; Albrecht, K., A water-soluble luminescent tris(2,4,6-trichlorophenyl)methyl radical-carbazole dyad. *J Mater Chem B* **2024,** *12* (28), 6840-6846.

99. Ghosh, P.; Alvertis, A. M.; Chowdhury, R.; Murto, P.; Gillett, A. J.; Dong, S.; Sneyd, A. J.; Cho, H. H.; Evans, E. W.; Monserrat, B.; Li, F.; Schnedermann, C.; Bronstein, H.; Friend, R. H.; Rao, A., Decoupling excitons from high-frequency vibrations in organic molecules. *Nature* **2024,** *629* (8011), 355-362.

100. Wilson, J. S.; Chawdhury, N.; Al-Mandhary, M. R.; Younus, M.; Khan, M. S.; Raithby, P. R.; Köhler, A.; Friend, R. H., The energy gap law for triplet states in Pt-containing conjugated polymers and monomers. *J Am Chem Soc* **2001,** *123* (38), 9412-7.

101. Benduhn, J.; Tvingstedt, K.; Piersimoni, F.; Ullbrich, S.; Fan, Y.; Tropiano, M.; McGarry, K. A.; Zeika, O.; Riede, M. K.; Douglas, C. J.; Barlow, S.; Marder, S. R.; Neher, D.; Spoltore, D.; Vandewal, K., Intrinsic non-radiative voltage losses in fullerene-based organic solar cells. *Nature Energy* **2017,** *2* (6), 17053.

102. Cougnard-Gregoire, A.; Merle, B. M. J.; Aslam, T.; Seddon, J. M.; Aknin, I.; Klaver, C. C. W.; Garhofer, G.; Layana, A. G.; Minnella, A. M.; Silva, R.; Delcourt, C., Blue Light Exposure: Ocular Hazards and Prevention-A Narrative Review. *Ophthalmol Ther* **2023,** *12* (2), 755-788.

103. Gu, C.; Jia, A. B.; Zhang, Y. M.; Zhang, S. X., Emerging Electrochromic Materials and Devices for Future Displays. *Chem Rev* **2022,** *122* (18), 14679-14721.

104. Wang, Z.; Zhu, H.; Zhuang, J.; Lu, Y.; Chen, Z.; Guo, W., Recent Advance in Electrochromic Materials and Devices for Display Applications. *Chempluschem* **2024,** *89* (5), e202300770.

105. Ghosh, T.; Kandpal, S.; Rani, C.; Chaudhary, A.; Kumar, R., Recipe for Fabricating Optimized Solid-State Electrochromic Devices and Its Know-How: Challenges and Future. *Advanced Optical Materials* **2023**.

106. Rai, V.; Singh, R. S.; Blackwood, D. J.; Zhili, D., A Review on Recent Advances in Electrochromic Devices: A Material Approach. *Advanced Engineering Materials* **2020,** *22* (8).

107. Deb, S. K., A novel electrophotographic system. *Appl Opt* **1969,** *8 Suppl 1*, 192-5.

108. Niu, J.; Wang, Y.; Zou, X.; Tan, Y.; Jia, C.; Weng, X.; Deng, L., Infrared electrochromic materials, devices and applications. *Applied Materials Today* **2021,** *24*.

109. Wang, Z.; Wang, X.; Cong, S.; Geng, F.; Zhao, Z., Fusing electrochromic technology with other advanced technologies: A new roadmap for future development. *Materials Science and Engineering: R: Reports* **2020,** *140*.

110. Harimoto, T.; Ishigaki, Y., Recent Advances in NIR-Switchable Multi-Redox Systems Based on Organic Molecules. *Chemistry* **2025,** *31* (3), e202403273.

111. Yu, F.; Liu, W.; Ke, S. W.; Kurmoo, M.; Zuo, J. L.; Zhang, Q., Electrochromic two-dimensional covalent organic framework with a reversible dark-to-transparent switch. *Nat Commun* **2020,** *11* (1), 5534.

112. Hao, Q.; Li, Z. J.; Bai, B.; Zhang, X.; Zhong, Y. W.; Wan, L. J.; Wang, D., A Covalent Organic Framework Film for Three-State Near-Infrared Electrochromism and a Molecular Logic Gate. *Angew Chem Int Ed Engl* **2021,** *60* (22), 12498-12503.

113. Bessinger, D.; Muggli, K.; Beetz, M.; Auras, F.; Bein, T., Fast-Switching Vis-IR Electrochromic Covalent Organic Frameworks. *J Am Chem Soc* **2021,** *143* (19), 7351-7357.

114. Shi, P.; Wang, J.; Guo, Z., A one-dimensional covalent organic framework film for near-infrared electrochromism. *Chemical Engineering Journal* **2023,** *451*.

115. Zheng, W.; Wang, B.-B.; Lai, J.-C.; Wan, C.-Z.; Lu, X.-R.; Li, C.-H.; You, X.-Z., Electrochromic properties of novel octa-pinene substituted double-decker Ln(iii) (Ln = Eu, Er, Lu) phthalocyanines with distinctive near-IR absorption. *Journal of Materials Chemistry C* **2015,** *3* (13), 3072-3080.

116. Yao, C. J.; Yao, J.; Zhong, Y. W., Metallopolymeric films based on a biscyclometalated ruthenium complex bridged by 1,3,6,8-tetra(2-pyridyl)pyrene: applications in near-infrared electrochromic windows. *Inorg Chem* **2012,** *51* (11), 6259-63.

117. Ionescu, A.; Aiello, I.; La Deda, M.; Crispini, A.; Ghedini, M.; De Santo, M. P.; Godbert, N., Near-IR Electrochromism in Electrodeposited Thin Films of Cyclometalated Complexes. *ACS Appl Mater Interfaces* **2016,** *8* (19), 12272-81.

118. Li, Z. J.; Shao, J. Y.; Zhong, Y. W., Near-Infrared and Two-Wavelength Electrochromism Based on Nanocrystalline TiO(2) Films Functionalized with Ruthenium-Amine Conjugated Complexes. *Inorg Chem* **2017,** *56* (14), 8538-8546.

119. Cui, B. B.; Zhong, Y. W.; Yao, J., Three-state near-infrared electrochromism at the molecular scale. *J Am Chem Soc* **2015,** *137* (12), 4058-61.

120. Yu, C. L.; Luo, S. C., Enhanced NIR Electrochromic Properties of Corannulene-(triphenylamine)(5) and EDOT-Derived Polymers via Electrochemical Layer-by-Layer Polymerization Compared to Copolymerization. *ACS Appl Mater Interfaces* **2025,** *17* (7), 10920-10930.

121. Zhang, Y.; Kong, L.; Zhang, Y.; Du, H.; Zhao, J.; Chen, S.; Xie, Y.; Wang, Y., Ultra-low-band gap thienoisoindigo-based ambipolar type neutral green copolymers with ProDOT and thiophene units as NIR electrochromic materials. *Organic Electronics* **2020,** *81*.

122. Kung, Y. R.; Cao, S. Y.; Hsiao, S. H., Electrosynthesis and Electrochromism of a New Crosslinked Polydithienylpyrrole with Diphenylpyrenylamine Subunits. *Polymers (Basel)* **2020,** *12* (12).

123. Simayi, R.; Murat, A.; Imerhasan, M.; Mijit, M.; Mahmut, M., Low band gap polymers based on the electrochemical polymerization of Phenazine: studies on the color changing ability in near-infrared region. *Journal of Polymer Research* **2020,** *27* (10).

124. Pinheiro, D.; Fernandes, M.; Pereira, R. F. P.; Pereira, S.; Correia, S. F. H.; Silva, M. M.; Fortunato, E.; Ferreira, R. A. S.; Gonçalves, M. C.; de Zea Bermudez, V., NIR-emitting Electrochromic Windows for Cold Climate Region Buildings. *ChemElectroChem* **2023,** *11* (3).

125. Pan, J.; Wang, Y.; Zheng, R.; Wang, M.; Wan, Z.; Jia, C.; Weng, X.; Xie, J.; Deng, L., Directly grown high-performance WO3 films by a novel one-step hydrothermal method with significantly improved stability for electrochromic applications. *Journal of Materials Chemistry A* **2019,** *7* (23), 13956-13967.

126. Shi, Y.; Sun, M.; Zhang, Y.; Cui, J.; Shu, X.; Wang, Y.; Qin, Y.; Liu, J.; Tan, H. H.; Wu, Y., Rational Design of Oxygen Deficiency-Controlled Tungsten Oxide Electrochromic Films with an Exceptional Memory Effect. *ACS Appl Mater Interfaces* **2020,** *12* (29), 32658-32665.

127. Wang, Z.; Gong, W.; Wang, X.; Chen, Z.; Chen, X.; Chen, J.; Sun, H.; Song, G.; Cong, S.; Geng, F.; Zhao, Z., Remarkable Near-Infrared Electrochromism in Tungsten Oxide Driven by Interlayer Water-Induced Battery-to-Pseudocapacitor Transition. *ACS Appl Mater Interfaces* **2020,** *12* (30), 33917-33925.

128. Corrente, G. A.; González, D. A.; Aktas, E.; Capodilupo, A. L.; Mazzone, G.; Ruighi, F.; Accorsi, G.; Imbardelli, D.; Rodriguez-Seco, C.; Martinez-Ferrero, E.; Palomares, E.; Beneduci, A., Vis–NIR Electrochromism and NIR–Green Electroluminochromism in Dual Functional Benzothiadiazole-Arylamine Mixed-Valence Compounds. *Advanced Optical Materials* **2022,** *11* (1).

129. Raj, M. R. A.; Yao, C.; Balakrishnan Muthuperumal, G.; Hu, L.; Malinge, A.; Fremont, M.; Cambe, C.; Ortiz, O.; Porlier, S.; Skene, W. G., The Dual-Role of Benzothiadiazole Fluorophores for Enabling Electrofluorochromic and Electrochromic Devices. *Chempluschem* **2024**, e202400667.

130. Shah, K. W.; Wang, S. X.; Soo, D. X. Y.; Xu, J., Viologen-Based Electrochromic Materials: From Small Molecules, Polymers and Composites to Their Applications. *Polymers (Basel)* **2019,** *11* (11).

131. Chang, M.; Chen, W.; Xue, H.; Liang, D.; Lu, X.; Zhou, G., Conjugation-extended viologens with thiophene derivative bridges: near-infrared electrochromism, electrofluorochromism, and smart window applications. *Journal of Materials Chemistry C* **2020,** *8* (45), 16129-16142.

132. Ling, H.; Su, F.; Tian, Y.; Luo, D.; Liu, Y. J.; Sun, X. W., A Highly Stable and Tunable Visible-Near-IR Electrochromic All-in-One Gel Device. *ChemPhotoChem* **2020,** *4* (5), 357-365.

133. Wu, N.; Ma, L.; Zhao, S.; Xiao, D., Novel triazine-centered viologen analogues for dual-band electrochromic devices. *Solar Energy Materials and Solar Cells* **2019,** *195*, 114-121.

134. Ambrose, B.; Krishnan, M.; Ramamurthy, K.; Kathiresan, M., Recent Advances in Molecular Engineering for Viologen-Based Electrochromic Materials: A Mini-Review. *Advanced Photonics Research* **2024,** *5* (10).

135. Madasamy, K.; Velayutham, D.; Suryanarayanan, V.; Kathiresan, M.; Ho, K.-C., Viologen-based electrochromic materials and devices. *Journal of Materials Chemistry C* **2019,** *7* (16), 4622-4637.

136. Ding, J.; Zheng, C.; Wang, L.; Lu, C.; Zhang, B.; Chen, Y.; Li, M.; Zhai, G.; Zhuang, X., Viologen-inspired functional materials: synthetic strategies and applications. *Journal of Materials Chemistry A* **2019,** *7* (41), 23337-23360.

137. Porter, W. W. V., T.P;, Isolation and Characterization of Phenyl Viologen as a Radical Cation and Neutral Molecule. *J. Org. Chem.* **2005,** *70*, 5028-5035.

138. Wałęsa-Chorab, M.; Skene, W. G., Extending the Color Retention of an Electrochromic Device by Immobilizing Color Switching and Ion-Storage Complementary Layers. *Electronic Materials* **2020,** *1* (1), 40-53.

139. Walesa-Chorab, M.; Skene, W. G., Visible-to-NIR Electrochromic Device Prepared from a Thermally Polymerizable Electroactive Organic Monomer. *ACS Appl Mater Interfaces* **2017,** *9* (25), 21524-21531.

140. Wałęsa-Chorab, M.; Muras, K.; Filiatrault, H. L.; Skene, W. G., Suitability of alkyne donor-π-donor-π-donor scaffolds for electrofluorochromic and electrochromic use. *Journal of Materials Chemistry C* **2022,** *10* (10), 3691-3703.

141. Anthony Raj, M. R.; Yao, C.; Fremont, M.; Skene, W. G., Exploiting Mixed Valence Charge Transfer for Electrochromic and Electrofluorochromic Use. *Chemistry* **2024,** *30* (42), e202401417.

142. Lerond, M.; Raj, A. M.; Wu, V.; Skene, W. G.; Cicoira, F., An intrinsically stretchable and bendable electrochromic device. *Nanotechnology* **2022,** *33* (40).

143. Hong, Y.; Lam, J. W.; Tang, B. Z., Aggregation-induced emission: phenomenon, mechanism and applications. *Chem Commun (Camb)* **2009,** (29), 4332-53.

144. Gierschner, J.; Park, S. Y., Luminescent distyrylbenzenes: tailoring molecular structure and crystalline morphology. *Journal of Materials Chemistry C* **2013,** *1* (37).

145. Huber, A.; Dubbert, J.; Scherz, T. D.; Voskuhl, J., Design Concepts for Solution and Solid-State Emitters - A Modern Viewpoint on Classical and Non-Classical Approaches. *Chemistry* **2023,** *29* (2), e202202481.

146. Neto, B. A. D.; Lapis, A. A. M.; da Silva Júnior, E. N.; Dupont, J., 2,1,3-Benzothiadiazole and Derivatives: Synthesis, Properties, Reactions, and Applications in Light Technology of Small Molecules. *European Journal of Organic Chemistry* **2013,** *2013* (2), 228-255.

147. Wang, Y.; Michinobu, T., Benzothiadiazole and its π-extended, heteroannulated derivatives: useful acceptor building blocks for high-performance donor–acceptor polymers in organic electronics. *Journal of Materials Chemistry C* **2016,** *4* (26), 6200-6214.

148. Chen, W.; Yang, Z.; Xie, Z.; Li, Y.; Yu, X.; Lu, F.; Chen, L., Benzothiadiazole functionalized D–A type covalent organic frameworks for effective photocatalytic reduction of aqueous chromium(vi). *Journal of Materials Chemistry A* **2019,** *7* (3), 998-1004.

149. Fell, V. H. K.; Findlay, N. J.; Breig, B.; Forbes, C.; Inigo, A. R.; Cameron, J.; Kanibolotsky, A. L.; Skabara, P. J., Effect of end group functionalisation of small molecules featuring the fluorene–thiophene–benzothiadiazole motif as emitters in solution-processed red and orange organic light-emitting diodes. *Journal of Materials Chemistry C* **2019,** *7* (13), 3934-3944.

150. Yang, S.-Y.; Zhang, Y.-L.; Khan, A.; Yu, Y.-J.; Kumar, S.; Jiang, Z.-Q.; Liao, L.-S., Nondoped organic light-emitting diodes with low efficiency roll-off: the combination of aggregation-induced emission, hybridized local and charge-transfer state as well as high photoluminescence efficiency. *Journal of Materials Chemistry C* **2020,** *8* (9), 3079-3087.

151. Zhang, D.; Yang, T.; Xu, H.; Miao, Y.; Chen, R.; Shinar, R.; Shinar, J.; Wang, H.; Xu, B.; Yu, J., Triphenylamine/benzothiadiazole-based compounds for non-doped orange and red fluorescent OLEDs with high efficiencies and low efficiency roll-off. *Journal of Materials Chemistry C* **2021,** *9* (14), 4921-4926.

152. Wang, X.; Ma, C.; Xie, M.; Chu, L.; Zhou, Y.; Sun, Q.; Yang, W.; Xue, S., Efficient and ultra-high luminance orange-red organic light emitting diode (OLED) based on triphenylamine-benzothiadiazole-phenoxazine hybrid molecule with hybrid local and charge-transfer (HLCT) characteristic. *Dyes and Pigments* **2024,** *229*.

153. Neto, B. A. D.; Correa, J. R.; Spencer, J., Fluorescent Benzothiadiazole Derivatives as Fluorescence Imaging Dyes: A Decade of New Generation Probes. *Chemistry* **2022,** *28* (4), e202103262.

154. Neto, B. A.; Carvalho, P. H.; Correa, J. R., Benzothiadiazole Derivatives as Fluorescence Imaging Probes: Beyond Classical Scaffolds. *Acc Chem Res* **2015,** *48* (6), 1560-9.

155. Cruz-Cabeza, A. J.; Reutzel-Edens, S. M.; Bernstein, J., Facts and fictions about polymorphism. *Chem Soc Rev* **2015,** *44* (23), 8619-35.

156. Gentili, D.; Gazzano, M.; Melucci, M.; Jones, D.; Cavallini, M., Polymorphism as an additional functionality of materials for technological applications at surfaces and interfaces. *Chem Soc Rev* **2019,** *48* (9), 2502-2517.

157. Wang, Z.; Cui, X.; Famulari, A.; Martí-Rujas, J.; Kariuki, B. M.; Guo, F., Solid-state stability of $Z' < 1$ and $Z' = 2$ polymorphs of N,N,N′,N′-tetrabenzylethylenediamine: a combined experimental and theoretical study. *CrystEngComm* **2022,** *24* (45), 7924-7931.

158. Ito, S.; Nagai, S.; Ubukata, T.; Tachikawa, T., Multi-color mechanochromic luminescence of three polymorphic crystals of a donor–acceptor-type benzothiadiazole derivative. *CrystEngComm* **2021,** *23* (34), 5899-5907.

159. Wang, C.; Li, Z., Molecular conformation and packing: their critical roles in the emission performance of mechanochromic fluorescence materials. *Materials Chemistry Frontiers* **2017,** *1* (11), 2174-2194.

160. Langis-Barsetti, S.; Maris, T.; Wuest, J. D., Molecular Organization of 2,1,3-Benzothiadiazoles in the Solid State. *J Org Chem* **2017,** *82* (10), 5034-5045.

161. Bashirov, D. A.; Sukhikh, T. S.; Kuratieva, N. V.; Chulanova, E. A.; Yushina, I. V.; Gritsan, N. P.; Konchenko, S. N.; Zibarev, A. V., Novel applications of functionalized 2,1,3-benzothiadiazoles for coordination chemistry and crystal engineering. *RSC Advances* **2014,** *4* (54).

162. Miura, Y.; Yoshioka, N., π-Stacked structure of thiadiazolo-fused benzotriazinyl radical: Crystal structure and magnetic properties. *Chemical Physics Letters* **2015,** *626*, 11-14.

163. Ams, M. R.; Trapp, N.; Schwab, A.; Milic, J. V.; Diederich, F., Chalcogen Bonding "2S-2N Squares" versus Competing Interactions: Exploring the Recognition Properties of Sulfur. *Chemistry* **2019,** *25* (1), 323-333.

164. Zhu, Y. Y.; Xia, H. Y.; Yao, L. F.; Huang, D. P.; Song, J. Y.; He, H. F.; Shen, L.; Zhao, F., High-contrast mechanochromic benzothiadiazole derivatives based on a triphenylamine or a carbazole unit. *RSC Adv* **2019,** *9* (13), 7176-7180.

165. Ishi-i, T.; Tanaka, H.; Youfu, R.; Aizawa, N.; Yasuda, T.; Kato, S.-i.; Matsumoto, T., Mechanochromic fluorescence based on a combination of acceptor and bulky donor moieties: tuning emission color and regulating emission change direction. *New Journal of Chemistry* **2019,** *43* (13), 4998-5010.

166. Ishi, I. T.; Tanaka, H.; Kichise, R.; Davin, C.; Matsuda, T.; Aizawa, N.; Park, I. S.; Yasuda, T.; Matsumoto, T., Regulation of Multicolor Fluorescence Changes Found in Donor-acceptor-type Mechanochromic Fluorescent Dyes. *Chem Asian J* **2021,** *16* (15), 2136-2145.

167. Echeverri, M.; Ruiz, C.; Gamez-Valenzuela, S.; Martin, I.; Ruiz Delgado, M. C.; Gutierrez-Puebla, E.; Monge, M. A.; Aguirre-Diaz, L. M.; Gomez-Lor, B., Untangling the Mechanochromic Properties of Benzothiadiazole-Based Luminescent Polymorphs through Supramolecular Organic Framework Topology. *J Am Chem Soc* **2020,** *142* (40), 17147-17155.

168. Hestand, N. J.; Spano, F. C., Expanded Theory of H- and J-Molecular Aggregates: The Effects of Vibronic Coupling and Intermolecular Charge Transfer. *Chem Rev* **2018,** *118* (15), 7069-7163.

169. Sodre, E. R.; Guido, B. C.; de Souza, P. E. N.; Machado, D. F. S.; Carvalho-Silva, V. H.; Chaker, J. A.; Gatto, C. C.; Correa, J. R.; Fernandes, T. A.; Neto, B. A. D., Deciphering the Dynamics of Organic Nanoaggregates with AIEE Effect and Excited States: Lipophilic Benzothiadiazole Derivatives as Selective Cell Imaging Probes. *J Org Chem* **2020,** *85* (19), 12614-12634.

170. Steed, J. W., Should solid-state molecular packing have to obey the rules of crystallographic symmetry? *CrystEngComm* **2003,** *5* (32), 169-179.

171. Bruker, S., (2020), Bruker AXS Inc., Madison, Wisconsin, USA.

172. Krause, L.; Herbst-Irmer, R.; Sheldrick, G. M.; Stalke, D., Comparison of silver and molybdenum microfocus X-ray sources for single-crystal structure determination. *J Appl Crystallogr* **2015,** *48* (Pt 1), 3-10.

173. Sheldrick, G. M., SHELXT - integrated space-group and crystal-structure determination. *Acta Crystallogr A Found Adv* **2015,** *71* (Pt 1), 3-8.

174. Sheldrick, G. M., Crystal structure refinement with SHELXL. *Acta Crystallogr C Struct Chem* **2015,** *71* (Pt 1), 3-8.

175. Dolomanov, O. V.; Bourhis, L. J.; Gildea, R. J.; Howard, J. A. K.; Puschmann, H., OLEX2: a complete structure solution, refinement and analysis program. *Journal of Applied Crystallography* **2009,** *42* (2), 339-341.

176. D. Kratzert, F., V144, https://www.xs3.uni-freiburg.de/research/finalcif.

177. Leyre, S. C.-G., E.; Joos, J. J.; Ryckaert, J.; Meuret, Y.; Poelman, D.; Smet, P. F.; Durinck, G.; Hofkens, J.; Deconinck, G.; Hanselaer, P., Absolute determination of photoluminescence quantum efficiency using an integrating sphere setup. Rev Sci Instrum 2014, 85 (12), 123115.

178. Allain, C.; Schmidt, F.; Lartia, R.; Bordeau, G.; Fiorini-Debuisschert, C.; Charra, F.; Tauc, P.; Teulade-Fichou, M. P., Vinyl-pyridinium triphenylamines: novel far-red emitters with high photostability and two-photon absorption properties for staining DNA. *Chembiochem* **2007,** *8* (4), 424-33.

179. Zadehnazari, A.; Auras, F.; Koumoulis, D.; Abbaspourrad, A., Charge transfer in triphenylamine-tetrazine covalent organic frameworks for solar-driven hydrogen peroxide production. *Nat Commun* **2025,** *17* (1), 72.

180. Zhang, Y.-S.; Fan, Y.-F.; Tao, X.-Q.; Li, G.-Y.; Deng, Q.-S.; Liu, Z.; Wang, Y.-X.; Gao, S.; Jiang, S.-D., Potential molecular qubits with long coherence time constructed using bromo-substituted trityl radicals. *Journal of Materials Chemistry C* **2024,** *12* (14), 5150-5156.

181. Nakamura, K.; Matsuda, K.; Xiaotian, R.; Furukori, M.; Miyata, S.; Hosokai, T.; Anraku, K.; Nakao, K.; Albrecht, K., Effects of halogen atom substitution on luminescent radicals: a case study on tris(2,4,6-trichlorophenyl)methyl radical-carbazole dyads. *Faraday Discuss* **2024,** *250* (0), 192-201.

182. Martin, R. L., Natural transition orbitals. *J. Chem. Phys.* **2003,** *118* (11), 4775-4777.

183. Perdew, J. P.; Burke, K.; Ernzerhof, M., Generalized Gradient Approximation Made Simple. *Physical Review Letters* **1996,** *77* (18), 3865-3868.

184. Ballester, M. R. J. C., J.; Rovira, C,; Armet, O., An Easy, High-yield Synthesis of Highly Chlorinated Mono-, Di- and Triarylmethanes. *Synthesis* **1986,** *1*, 64-66.

185. O. V. Dolomanov, L. J. B., R. J. Gildea, J. A. K. Howard & H. Puschmann, J. Appl. Cryst. 2009, 42, 339-341.

186. Leyre, S.; Coutino-Gonzalez, E.; Joos, J. J.; Ryckaert, J.; Meuret, Y.; Poelman, D.; Smet, P. F.; Durinck, G.; Hofkens, J.; Deconinck, G.; Hanselaer, P., Absolute determination of photoluminescence quantum efficiency using an integrating sphere setup. *Rev Sci Instrum* **2014,** *85* (12), 123115.

187. Frisch, M. J.; Trucks, G. W.; Schlegel, H. B.; Scuseria, G. E.; Robb, M. A.; Cheeseman, J. R.; Scalmani, G.; Barone, V.; Petersson, G. A.; Nakatsuji, H.; Li, X.; Caricato, M.; Marenich, A. V.; Bloino, J.; Janesko, B. G.; Gomperts, R.; Mennucci, B.; Hratchian, H. P.; Ortiz, J. V.; Izmaylov, A. F.; Sonnenberg, J. L.; Williams; Ding, F.; Lipparini, F.; Egidi, F.; Goings, J.; Peng, B.; Petrone, A.; Henderson, T.; Ranasinghe, D.; Zakrzewski, V. G.; Gao, J.; Rega, N.; Zheng, G.; Liang, W.; Hada, M.; Ehara, M.; Toyota, K.; Fukuda, R.; Hasegawa, J.; Ishida, M.; Nakajima, T.; Honda, Y.; Kitao, O.; Nakai, H.; Vreven, T.; Throssell, K.; Montgomery Jr., J. A.; Peralta, J. E.; Ogliaro, F.; Bearpark, M. J.; Heyd, J. J.; Brothers, E. N.; Kudin, K. N.; Staroverov, V. N.; Keith, T. A.; Kobayashi, R.; Normand, J.; Raghavachari, K.; Rendell, A. P.; Burant, J. C.; Iyengar, S. S.; Tomasi, J.; Cossi, M.; Millam, J. M.; Klene, M.; Adamo, C.; Cammi, R.; Ochterski, J. W.; Martin, R. L.; Morokuma, K.; Farkas, O.; Foresman, J. B.; Fox, D. J., *Gaussian 16 Rev. C.01*. Wallingford, CT: 2016.

188. Casida, M. E., Time-Dependent Density Functional Response Theory for Molecules. In *Recent Advances in Density Functional Methods*, Chong, D. P., Ed. World Scientific: Singapore, 1995; Vol. 1, pp 155-192.

189. Dennington, R. D.; Keith, T. A.; Millam, J. M. *GaussView, Version 6.0.16*, 6.0.16; Semichem, Inc.: Shawnee Mission, KS, 2016.

190. Chen, Z. X.; Li, Y.; Huang, F., Persistent and Stable Organic Radicals: Design, Synthesis, and Applications. *Chem* **2021,** *7* (2), 288-332.

191. Murto, P.; Bronstein, H., Electro-optical π-radicals: design advances, applications and future perspectives. *Journal of Materials Chemistry C* **2022,** *10* (19), 7368-7403.

192. Perera, K.; Wu, W.; Jenkins, K. A.; Espenship, M. F.; Zeller, M.; You, L.; Ahmed, M.; Lang, K.; Liu, G.; Chaudhary, J.; Abtahi, A.; Forbes, D.; Laskin, J.; Savoie, B. M.; Mei, J., Degradation Pathways of Conjugated Radical Cations. *Chemistry of Materials* **2023,** *35* (21), 9135-9149.

193. Chen, F.; Fu, X.; Zhang, J.; Wan, X., Near-infrared and multicolored electrochromism of solution processable triphenylamine-anthraquinone imide hybrid systems. *Electrochimica Acta* **2013,** *99*, 211-218.

194. Zhuang, Y.-C.; Hsiao, S.-H., Visible and Near-Infrared Electrochromic Polyamides and Polyimides Featuring a Phenothiazine-Triphenylamine Star-Shaped Architecture. *ACS Applied Polymer Materials* **2025**.

195. Nad, S.; Jana, R.; Datta, A.; Malik, S., Fully organic electroactive monomers for electrochromic behaviors having high coloration efficiency and long cycle stability towards flexible Solid-State electrochromic device. *Journal of Electroanalytical Chemistry* **2022,** *918*.

196. Zhang, J.; Liu, G.; Wang, X.-Y.; Yu, G.-A.; Yin, J.; Liu, S.-H., Multistate near-infrared electrochromism and electron transfer in different oligotriphenylamine systems. *Dyes and Pigments* **2017,** *143*, 416-426.

197. Satyanarayana, A. N. V.; Halder, S.; Samanta, P. K.; Chakraborty, C.; Chatterjee, T., Design and synthesis of triphenylamine-substituted vinyl sulphide and its derivatives for fully transparent-to-black electrochromism. *Chem Commun (Camb)* **2025**.

198. Nad, S.; Malik, S., Design, Synthesis, and Electrochromic Behaviors of Donor-Acceptor-Donor type Triphenylamine-iso-Naphthalenediimide Derivatives. *ChemElectroChem* **2020,** *7* (19), 4144-4152.

199. Wiley, L.; Cavanaugh, R.; Follansbee, J.; Burrell, D.; Grimming, R.; Pimpinella, R.; Voss, J.; Furxhi, O.; Driggers, R., Comparison of reflective band (Vis, NIR, SWIR, eSWIR) performance in daytime reduced illumination conditions. *Appl Opt* **2023,** *62* (31), 8316-8326.

200. Kenry; Duan, Y.; Liu, B., Recent Advances of Optical Imaging in the Second Near-Infrared Window. *Adv Mater* **2018,** *30* (47), e1802394.

201. Connelly, N. G.; Geiger, W. E., Chemical redox agents for organometallic chemistry. *Chem. Rev.* **1996,** *96* (2), 877-910.

APPENDIX A supporting information chapter 3

Excitation spectra

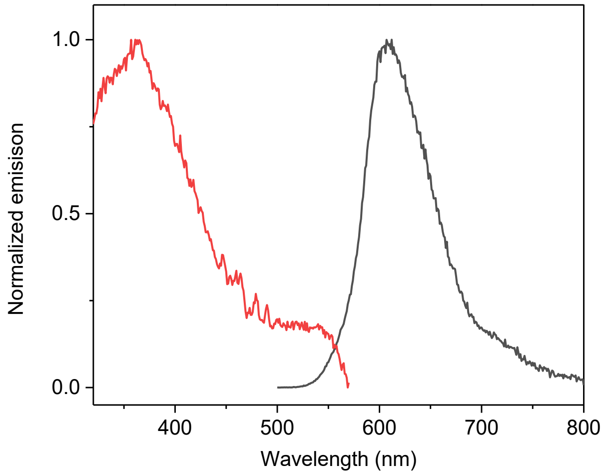

Figure A.3.1. Excitation (red) and emission (black) spectra of crystals of Polymorph A.

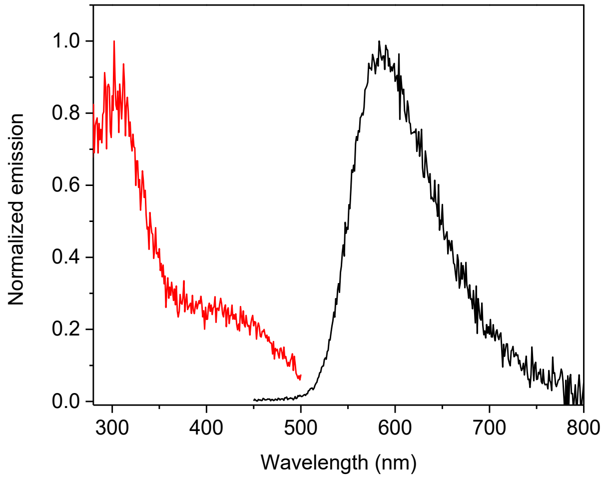

Figure A.3.2. Excitation (red) and emission (black) spectra of crystals of Polymorph B.

Time Resolved Emission Spectra

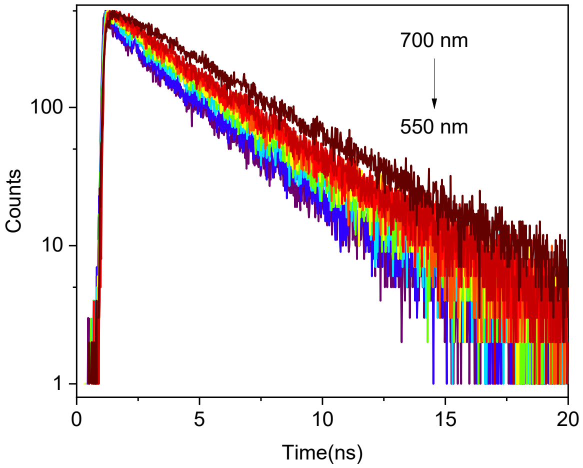

Figure A.3.3. Time-resolved photoluminescence decays of Polymorph A measured at different wavelengths (10 nm intervals).

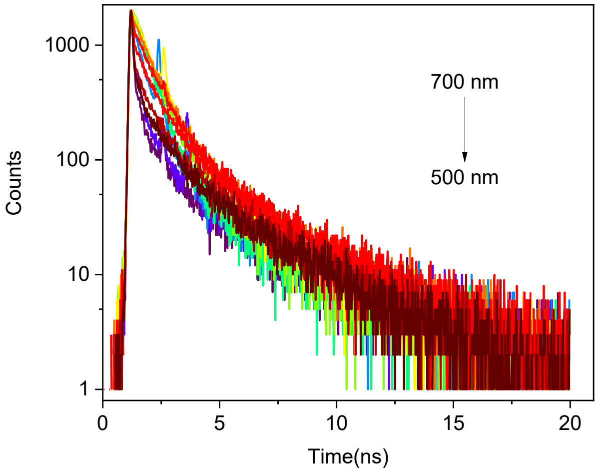

Figure A.3.4. Time-resolved photoluminescence decays of Polymorph B measured at different wavelengths (10 nm intervals).

Solution lifetime

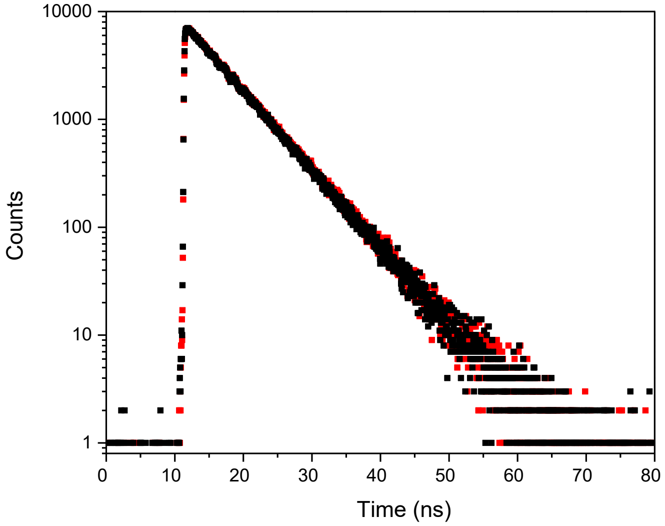

Figure A.3.5. Time-resolved emission decays fitted monoexponentially with $\tau = 6.01$ ns for polymorphs A (red) and B (black).

Table A.3.1. Single-crystal diffraction data of Polymorphs A and B.

	Polymorph A	Polymorph B
Empirical formula	$C_{24}H_{16}BrN_3S$	$C_{24}H_{16}BrN_3S$
CCDC number	2486816	2486817
Formula weight	458.37	458.37
Temperature [K]	150	150
Crystal system	orthorhombic	orthorhombic
Space group (number)	$Pbca$ (61)	$Pna2_1$ (33)
a [Å]	10.1597(2)	10.9741(5)
b [Å]	16.5771(3)	73.932(4)
c [Å]	23.4674(4)	7.3151(4)
α [°]	90	90
β [°]	90	90
γ [°]	90	90
Volume [$Å^3$]	3952.34(13)	5935.0(5)
Z	8	12
ρ_{calc} [gcm^{-3}]	1.541	1.539
μ [mm^{-1}]	2.600	2.622
F(000)	1856	2784
Crystal size [mm^3]	0.047×0.24×0.33	0.04×0.1×0.2
Crystal colour	clear light orange	clear light orange
Crystal shape	plate	plate
Radiation	Ga K_α (λ=1.34139 Å)	Ga K_α (λ=1.34139 Å)
2θ range [°]	9.28 to 116.17 (0.79 Å)	2.08 to 121.39 (0.77 Å)
Index ranges	$-12 \le h \le 12$ $-20 \le k \le 20$ $-29 \le l \le 29$	$-11 \le h \le 14$ $-93 \le k \le 95$ $-8 \le l \le 9$
Reflections collected	48936	75406
Independent reflections	4171 R_{int} = 0.0304 R_{sigma} = 0.0154	12770 R_{int} = 0.0440 R_{sigma} = 0.0337
Completeness to θ = 53.594°	99.7	99.7
Data / Restraints / Parameters	4171 / 0 / 262	12770 / 1 / 785
Goodness-of-fit on F^2	1.079	1.074
Final R indexes [$I \ge 2\sigma(I)$]	R_1 = 0.0295 wR_2 = 0.0830	R_1 = 0.0248 wR_2 = 0.0630
Final R indexes [all data]	R_1 = 0.0319 wR_2 = 0.0848	R_1 = 0.0260 wR_2 = 0.0635
Largest peak/hole [$eÅ^{-3}$]	0.41/−0.49	0.41/−0.34
Flack Parameter	N/A	0.067(13)

Empirical formula	$C_{24}H_{16}BrN_3S$	$C_{24}H_{16}BrN_3S$
Formula weight	458.37	458.37
Temperature [K]	150	150
Crystal system	orthorhombic	orthorhombic
Space group (number)	$Pbca$ (61)	$Pna2_1$ (33)
a [Å]	10.1597(2)	10.9741(5)
b [Å]	16.5771(3)	73.932(4)
c [Å]	23.4674(4)	7.3151(4)
α [°]	90	90
β [°]	90	90
γ [°]	90	90
Volume [Å^3]	3952.34(13)	5935.0(5)
Z	8	12
ρ_{calc} [gcm^{-3}]	1.541	1.539
μ [mm^{-1}]	2.600	2.622
F(000)	1856	2784
Crystal size [mm^3]	0.047×0.24×0.33	0.04×0.1×0.2
Crystal colour	clear light orange	clear light orange
Crystal shape	plate	plate
Radiation	Ga K_α (λ=1.34139 Å)	Ga K_α (λ=1.34139 Å)
2θ range [°]	9.28 to 116.17 (0.79 Å)	2.08 to 121.39 (0.77 Å)
Index ranges	$-12 \le h \le 12$ $-20 \le k \le 20$ $-29 \le l \le 29$	$-11 \le h \le 14$ $-93 \le k \le 95$ $-8 \le l \le 9$
Reflections collected	48936	75406
Independent reflections	4171 R_{int} = 0.0304 R_{sigma} = 0.0154	12770 R_{int} = 0.0440 R_{sigma} = 0.0337
Completeness to θ = 53.594°	99.7	99.7
Data / Restraints / Parameters	4171 / 0 / 262	12770 / 1 / 785
Goodness-of-fit on F^2	1.079	1.074
Final R indexes [I≥2σ(I)]	R_1 = 0.0295 wR_2 = 0.0830	R_1 = 0.0248 wR_2 = 0.0630
Final R indexes [all data]	R_1 = 0.0319 wR_2 = 0.0848	R_1 = 0.0260 wR_2 = 0.0635
Largest peak/hole [eÅ^{-3}]	0.41/−0.49	0.41/−0.34
Flack Parameter	N/A	0.067(13)

Table A.3.2. 2D fingerprint plot values for Polymorphs A and B

Interactions	Polymorph A	Polymorph B
H···H/H···H	36.9 %	41.3 %
C···H/H···C	26.7 %	23.7 %
N···H/H···N	8.3 %	10.4 %
S···H/H···S	3.7 %	5.0 %
S···N/N···S	0.0 %	1.5 %

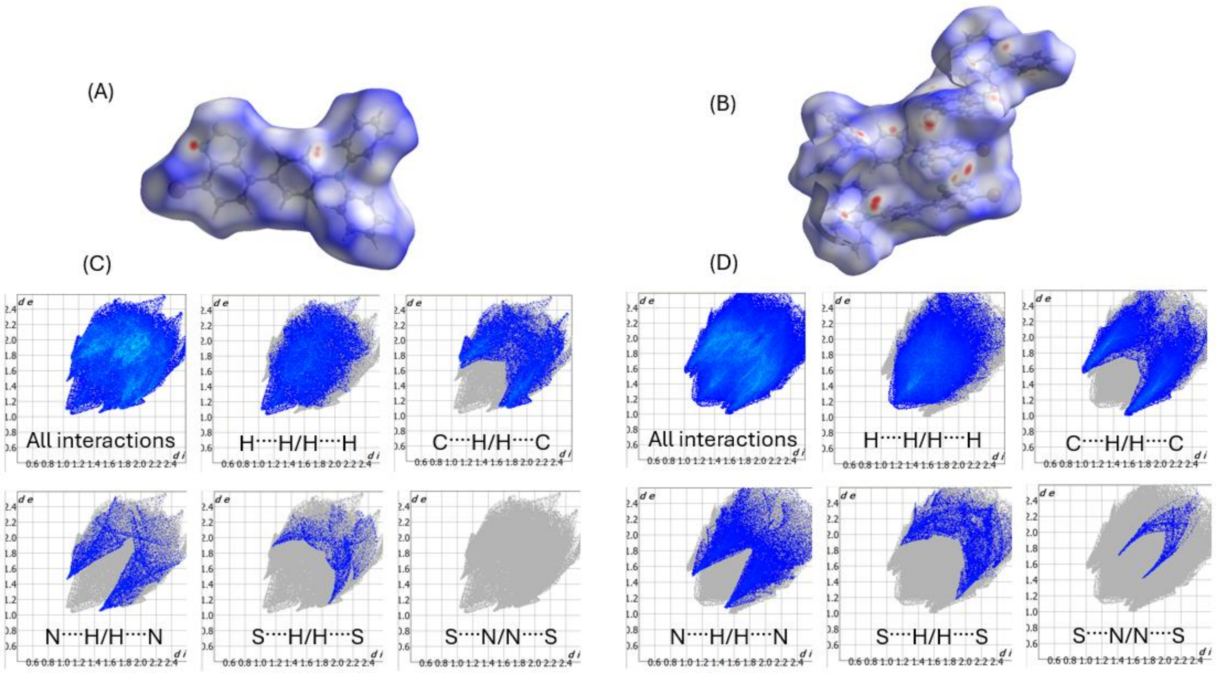

Figure A.3.6. d_{norm} maps and 2D fingerprint plots graphs for polymorph A (a, c) and polymorph B (b, d)

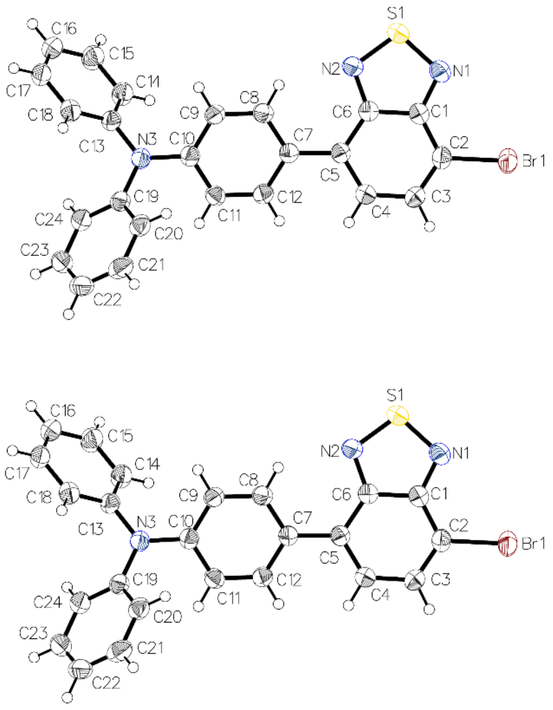

Figure A.3.7. Thermal atomic displacement ellipsoid plot for the independent molecule in Polymorph A with atom label numbers. Ellipsoids are drawn at the 50% probability level and hydrogen atoms are shown as spheres of arbitrary size.

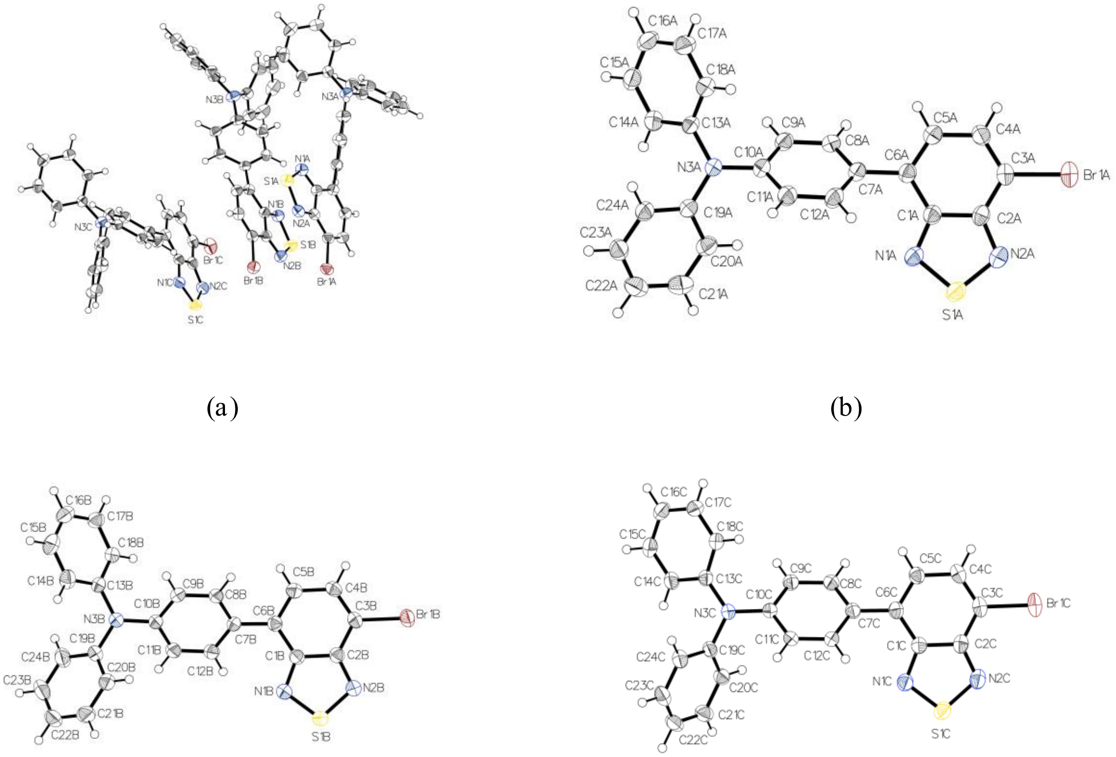

(a) (b)

(c) (d)

Figure A.3.8. Thermal atomic displacement ellipsoid plots with atom label numbers for Polymorph B. View of the asymmetric unit with the 3 independent molecules. (b,c,d) (a). Separate views of the three individual molecules of the asymmetric unit. In all views, ellipsoids are drawn at the 50% probability level and hydrogen atoms are shown as spheres of arbitrary size.

Single-crystal X-ray diffraction after recrystallization

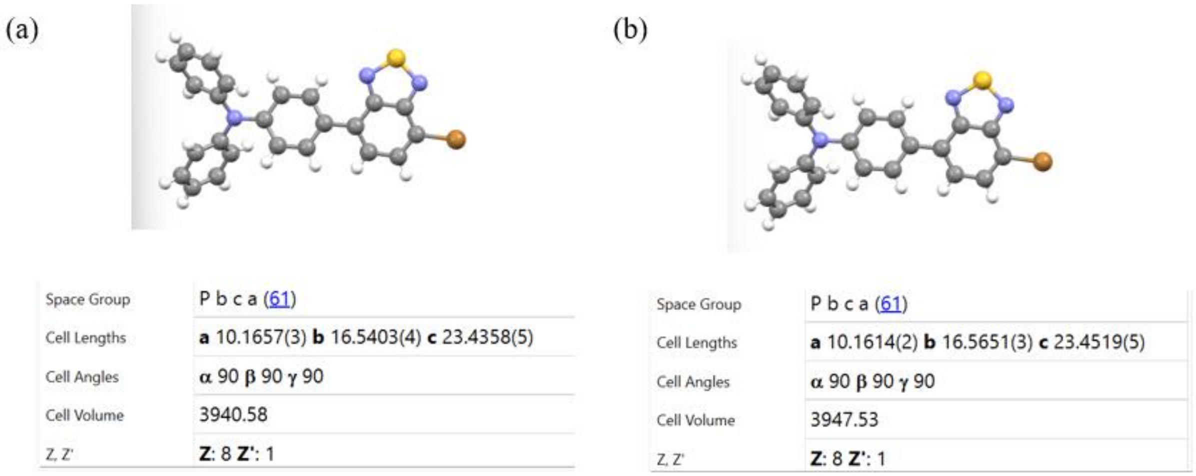

(a)

Space Group	P b c a (61)
Cell Lengths	**a** 10.1657(3) **b** 16.5403(4) **c** 23.4358(5)
Cell Angles	α 90 β 90 γ 90
Cell Volume	3940.58
Z, Z'	**Z**: 8 **Z'**: 1

(b)

Space Group	P b c a (61)
Cell Lengths	**a** 10.1614(2) **b** 16.5651(3) **c** 23.4519(5)
Cell Angles	α 90 β 90 γ 90
Cell Volume	3947.53
Z, Z'	**Z**: 8 **Z'**: 1

Figure A.3.9. Unit cell data of the recrystallized crystals after grounding initial crystals of Polymorph A (a) and polymorph B (b) giving new crystals of Polymorph A only. Figures generated using Mercury.

NMR Spectra

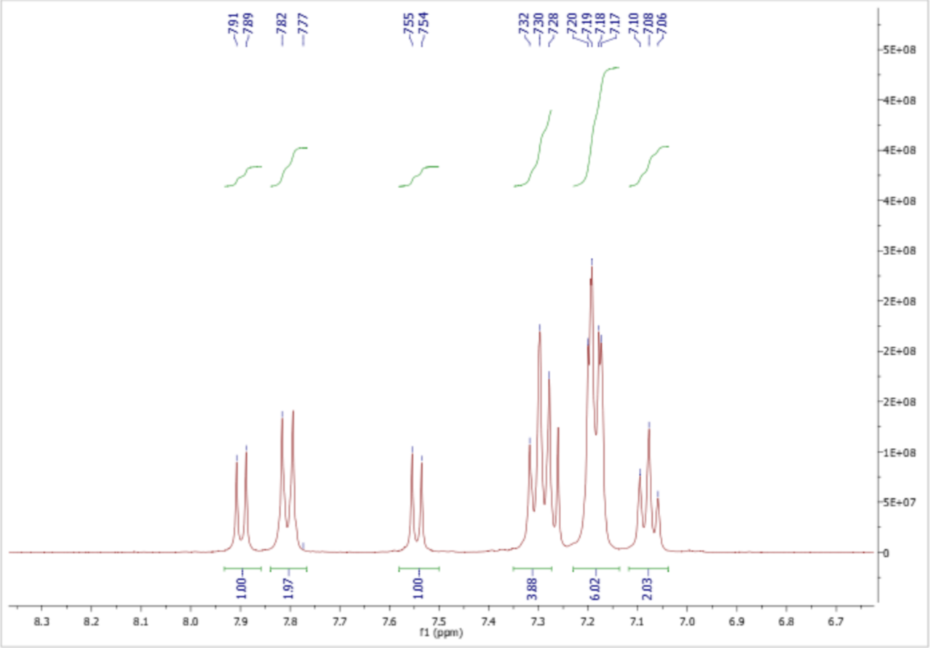

Figure A.3.10. ^{1}H NMR spectrum of Polymorph A measured in $CDCl_3$.

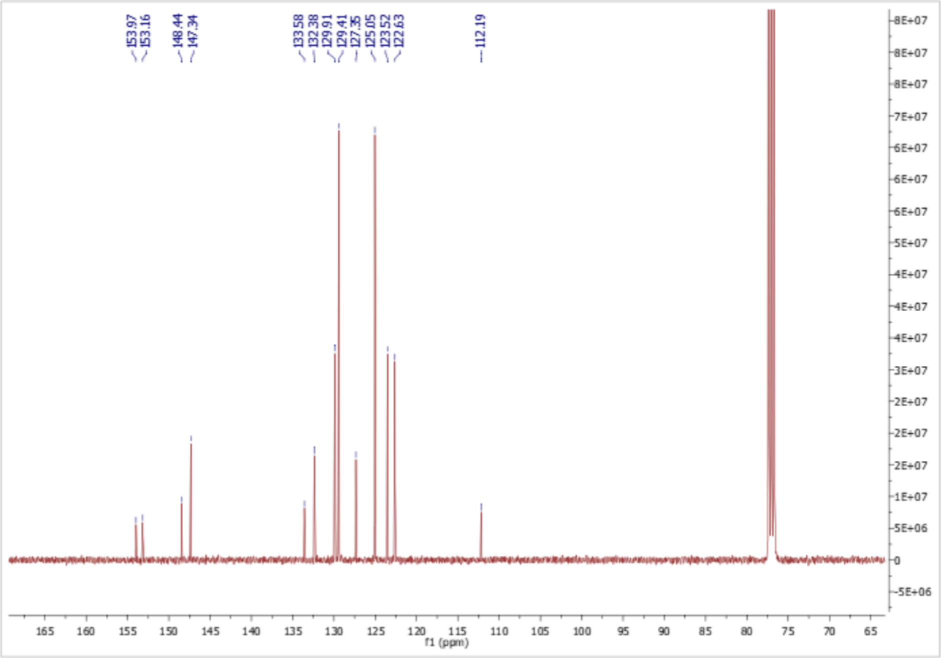

Figure A.3.11. ^{13}C NMR spectrum of Polymorph A measured in CDCl$_3$.

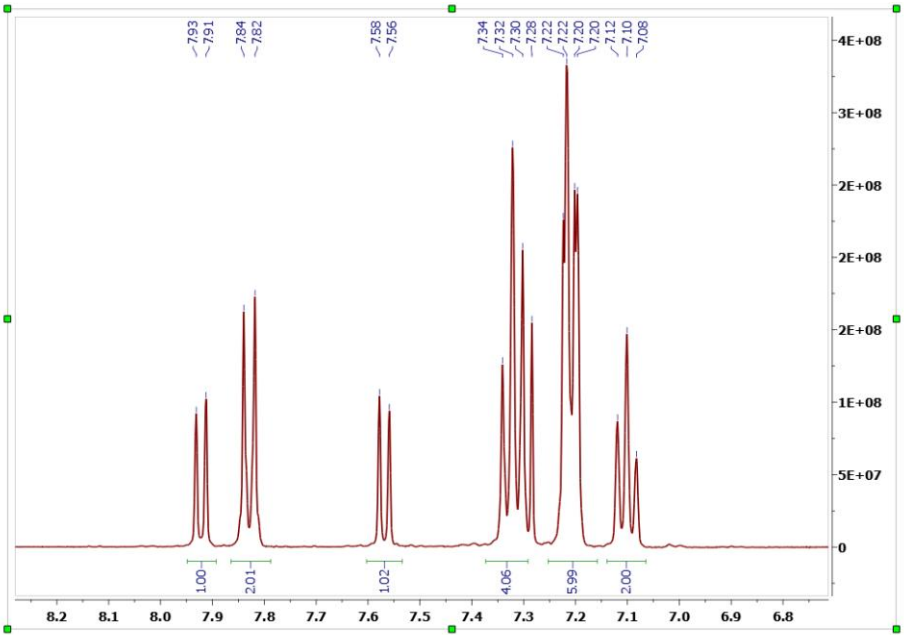

Figure A.3.12. ^{1}H NMR spectrum of Polymorph B measured in CDCl$_3$.

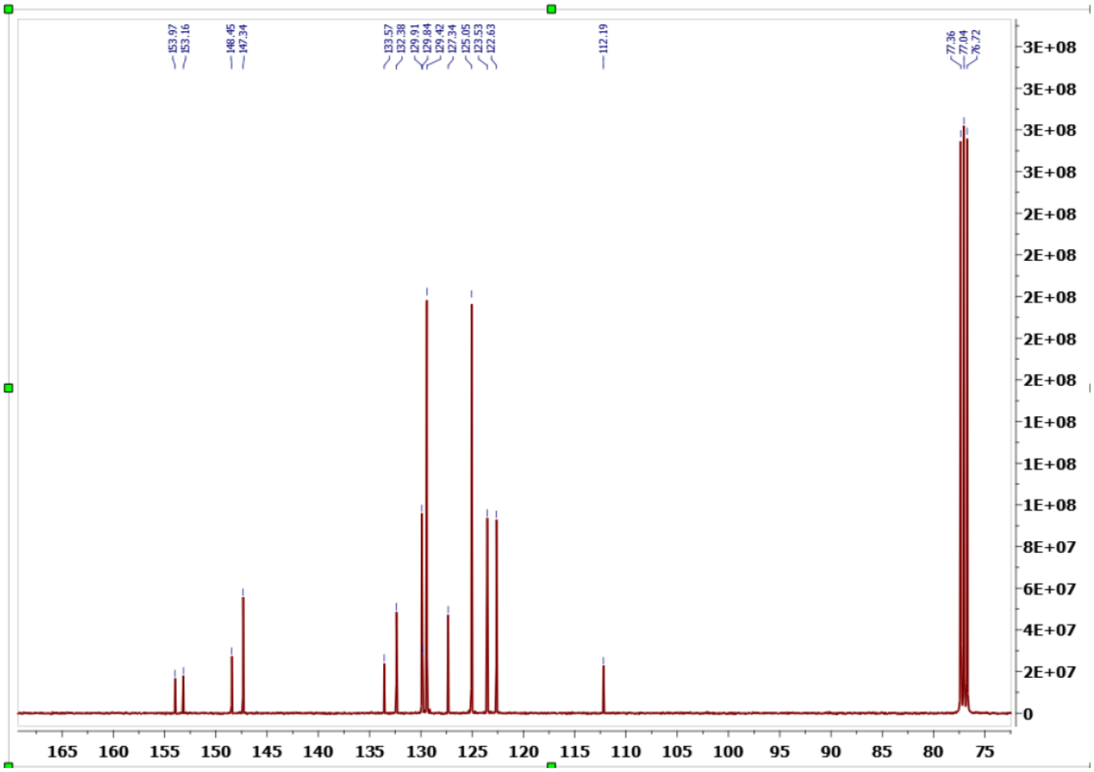

Figure A.3.13. ^{13}C NMR spectrum of Polymorph B measured in $CDCl_3$.

Mass Spectrometry

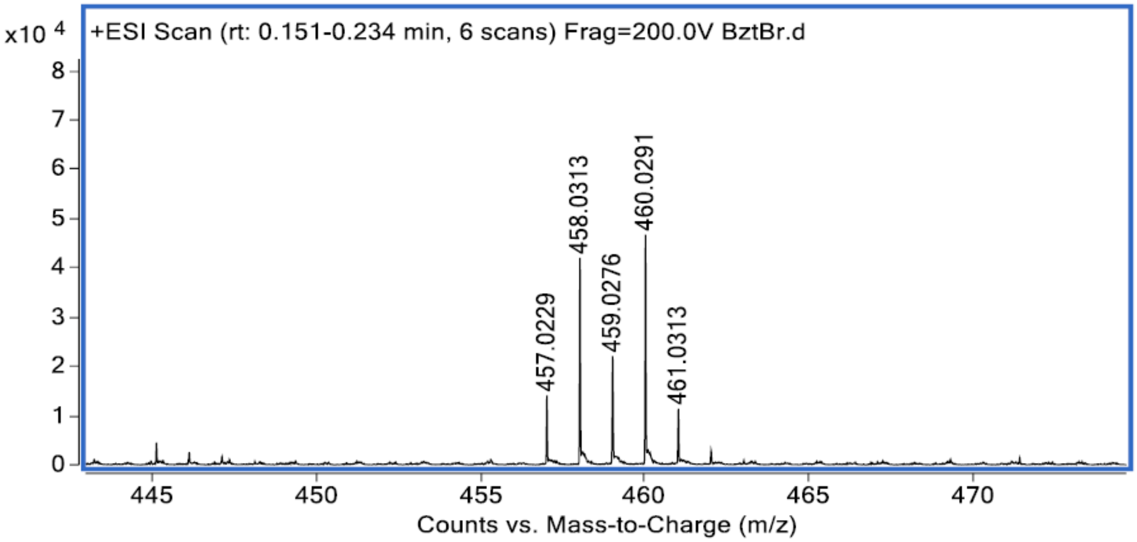

Ion	Formula	Expe. m/z	Calc. m/z	Diff (ppm)
[M+H]+	C24 H16 Br N3 S	458.0313	458.0321	-1.8

Figure A.3.14. High-resolution mass spectrometry of Polymorph A.

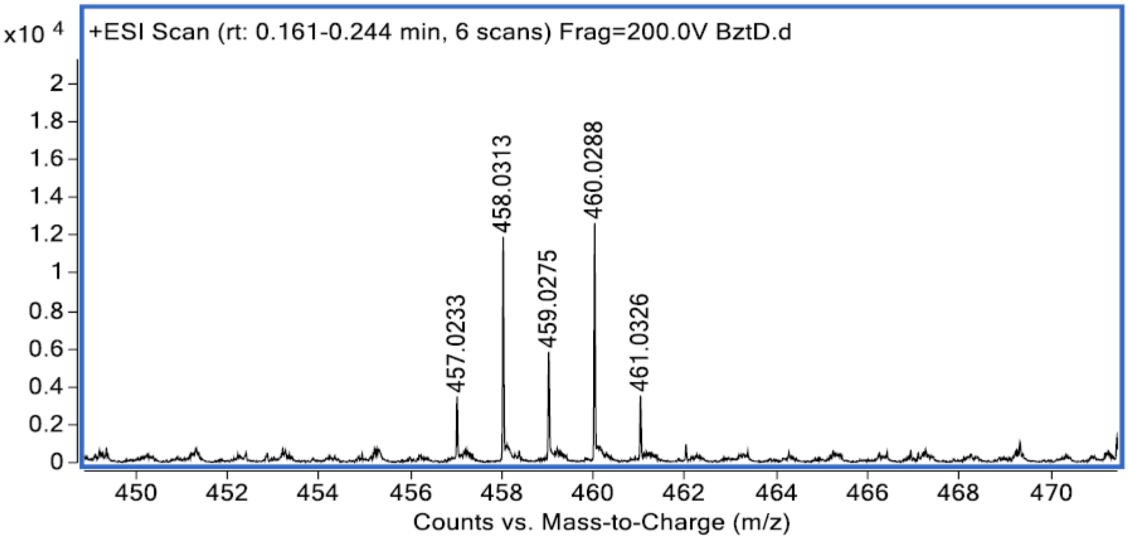

Ion	Formula	Expe. m/z	Calc. m/z	Diff (ppm)
[M+H]+	C24 H16 Br N3 S	458.0313	458.0321	-1.8

Figure A.3.15. High-resolution mass spectrometry of Polymorph B.

Purity Analysis

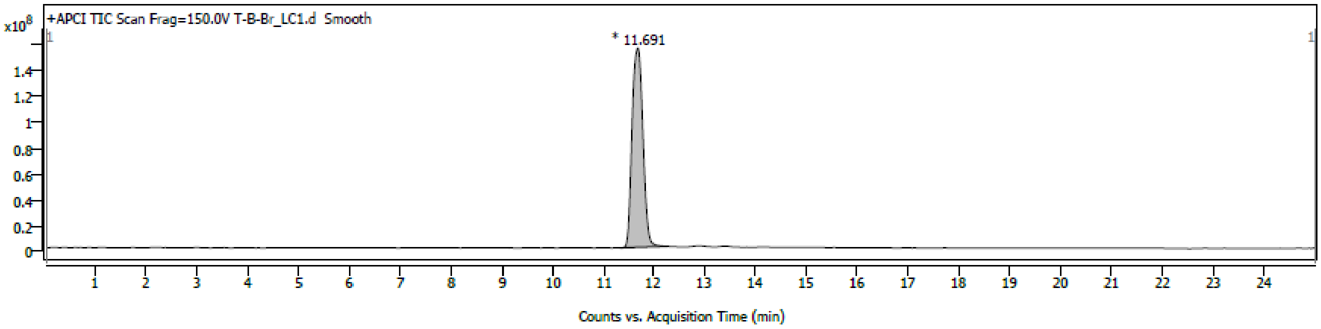

Chromatogram Peaks

RT	Area	Area Sum %
11.7	2321540662	100.00

Figure A.3.16. LC purity chromatogram of Polymorph A.

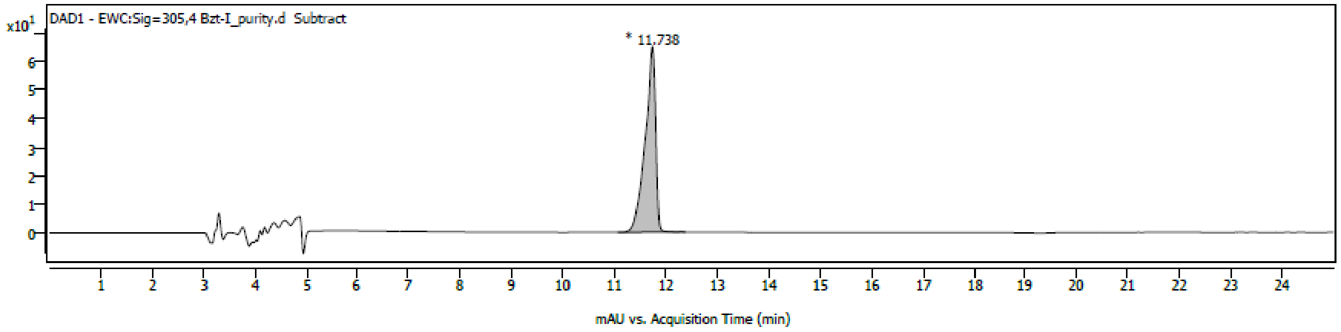

Chromatogram Peaks

RT	Area	Area Sum %
11.7	926	100.00

Figure A.3.17. LC purity chromatogram of Polymorph B.

APPENDIX B supporting information chapter 4

EPR spectra

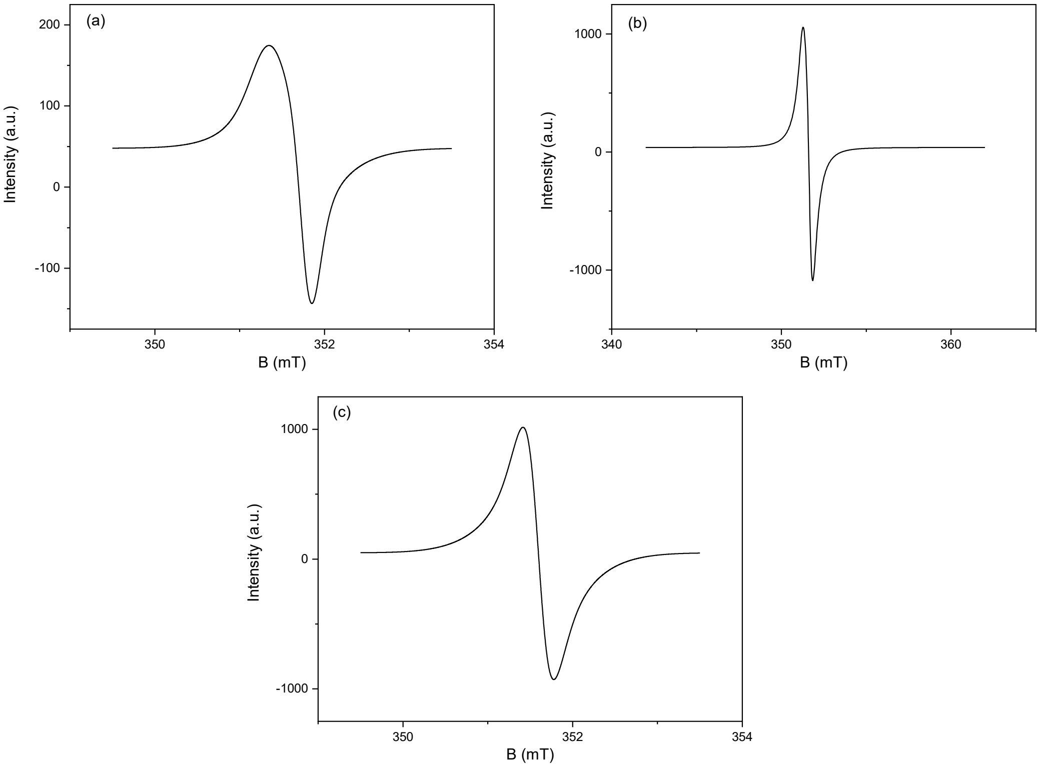

Figure B.4.1. EPR spectra of 2 (a) g = 2.00598, 351.6889 mT; 3 (b) g = 2.00653, 351.5925 mT; 4 (c) g = 2.00674, 351.5561 mT in powder at room temperature.

Single-crystal X-ray diffraction

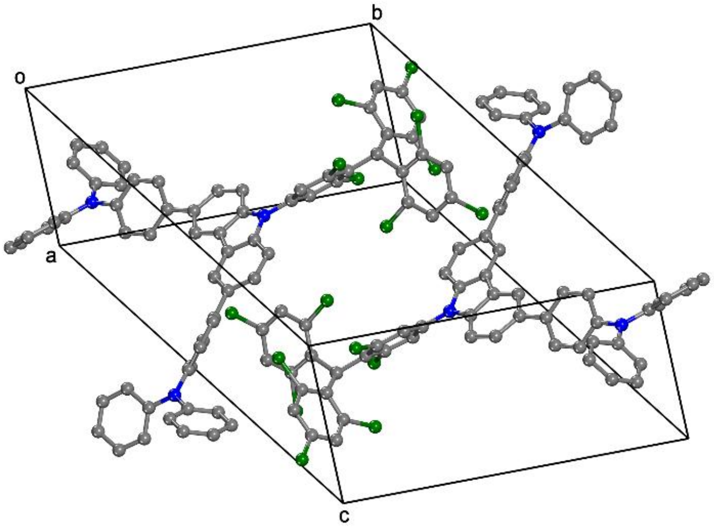

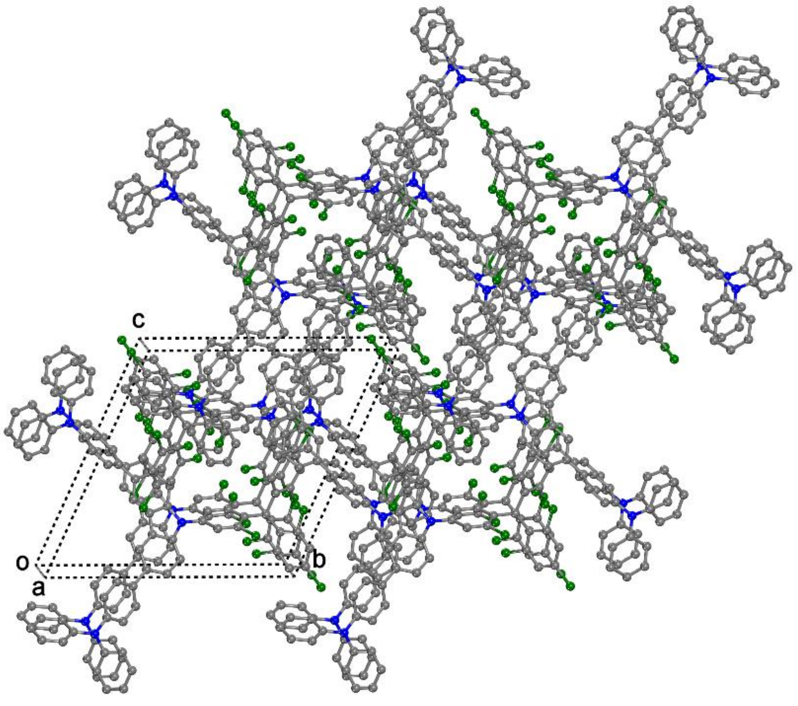

Figure B.4.2. Top: Two molecules of **10** in the unit cell. Bottom: 2×2×2 supercell showing the extended packing and steric environment around the trityl core. Color code: C (gray), N (blue), Cl (green)**;** H atoms omitted for clarity**.** Unit-cell axes (a, b, c) are indicated. Hydrogen atoms have been omitted for clarity.

Table B.4.1. Crystallographic details of 10.

Empirical formula	$C_{67}H_{41}Cl_8N_3$
Formula weight	1171.63
Temperature [K]	150
Crystal system	triclinic
Space group (number)	$P\overline{1}$ (2)
a [Å]	12.2425(7)
b [Å]	16.9386(8)
c [Å]	17.3910(8)
α [°]	61.633(3)
β [°]	71.863(3)
γ [°]	71.001(3)
Volume [Å^3]	2946.8(3)
Z	2
ρ_{calc} [gcm^{-3}]	1.320
μ [mm^{-1}]	2.544
F(000)	1200
Crystal size [mm^3]	0.03×0.09×0.11
Crystal colour	clear light green
Crystal shape	plate
Radiation	Ga K_α (λ=1.34139 Å)
2θ range [°]	5.12 to 110.03 (0.82 Å)
Index ranges	$-14 \le h \le 14$ $-20 \le k \le 20$ $-21 \le l \le 21$
Reflections collected	52355
Independent reflections	11197 $R_{int} = 0.0802$ $R_{sigma} = 0.0634$
Completeness to θ = 53.594°	99.8 %
Data / Restraints / Parameters	11197 / 0 / 703
Goodness-of-fit on F^2	1.097
Final R indexes [$I\geq2\sigma(I)$]	$R_1 = 0.0945$ $wR_2 = 0.2719$
Final R indexes [all data]	$R_1 = 0.1235$ $wR_2 = 0.3037$

Largest peak/hole [eÅ^{-3}]	0.88/–0.88

Table B.4.2. Hydrogen bonds for **10**.

D–H···A [Å]	**d(D–H) [Å]**	**d(H···A) [Å]**	**d(D···A) [Å]**	**<(DHA) [°]**
C34–H34···Cl4$^{\#1}$	0.95	2.99	3.927(5)	171.4
C52–H52···Cl7$^{\#1}$	0.95	2.91	3.684(6)	139.6
C57–H57···Cl8$^{\#2}$	0.95	2.83	3.692(6)	151.8

Symmetry transformations used to generate equivalent atoms: #1: -1+X, 1+Y, +Z;   #2: 1-X, 1-Y, 2-Z;

Absorption, Excitation and Emission spectra

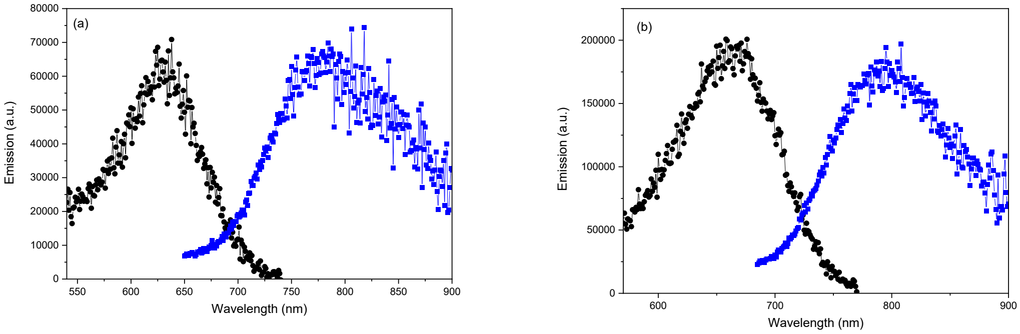

Figure B.4.3. Excitation (black circles) and emission (blue squares) spectra of **3** (a) and **4** (b) in cyclohexane at room temperature.

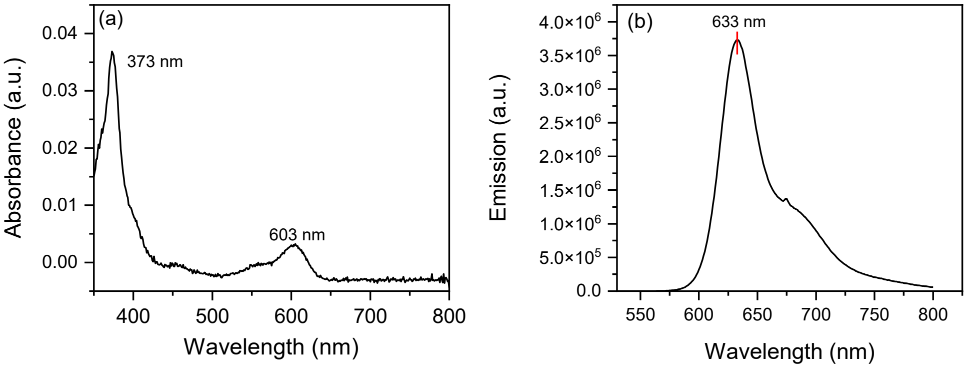

Figure B.4.4. Absorption (a) and emission (b) spectra of 2 in cyclohexane.

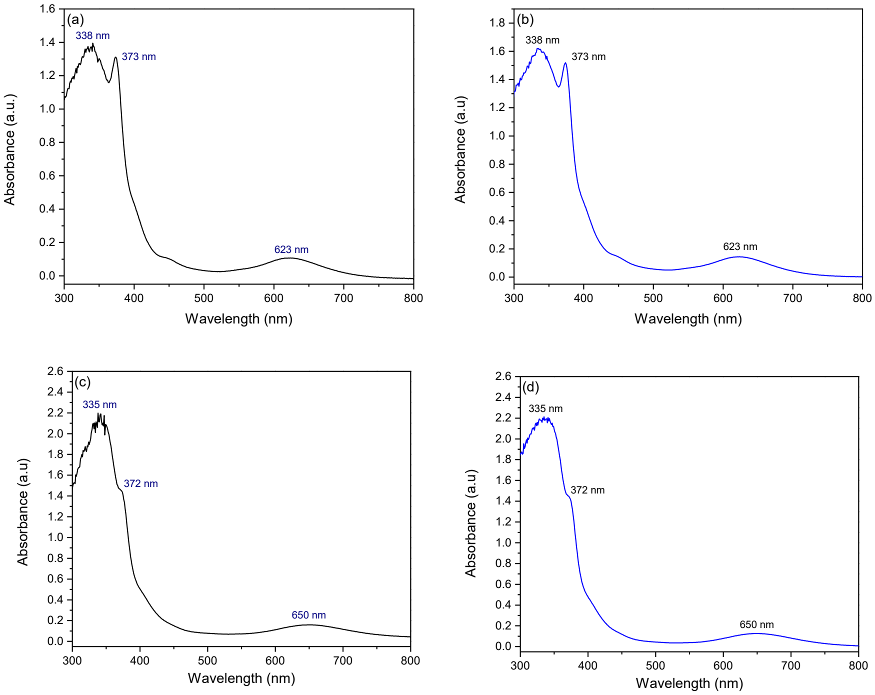

Figure B.4.5. Absorption spectra of **3** (a, b) and **4** (c,d) in dichloromethane. Freshly prepared solutions (black) and same solutions after four months stored outside the glovebox under ambient conditions (blue).

Fluorescence lifetime

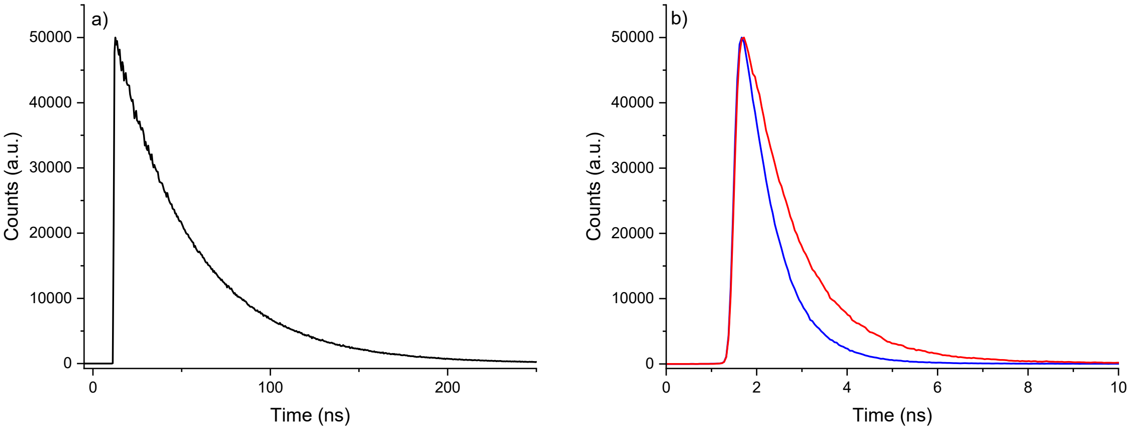

Figure B.4.6. Time-resolved photoluminescence decays of 2 (a), **3** (b, blue) and **4** (red) in cyclohexane at room temperature.

Theoretical Calculations

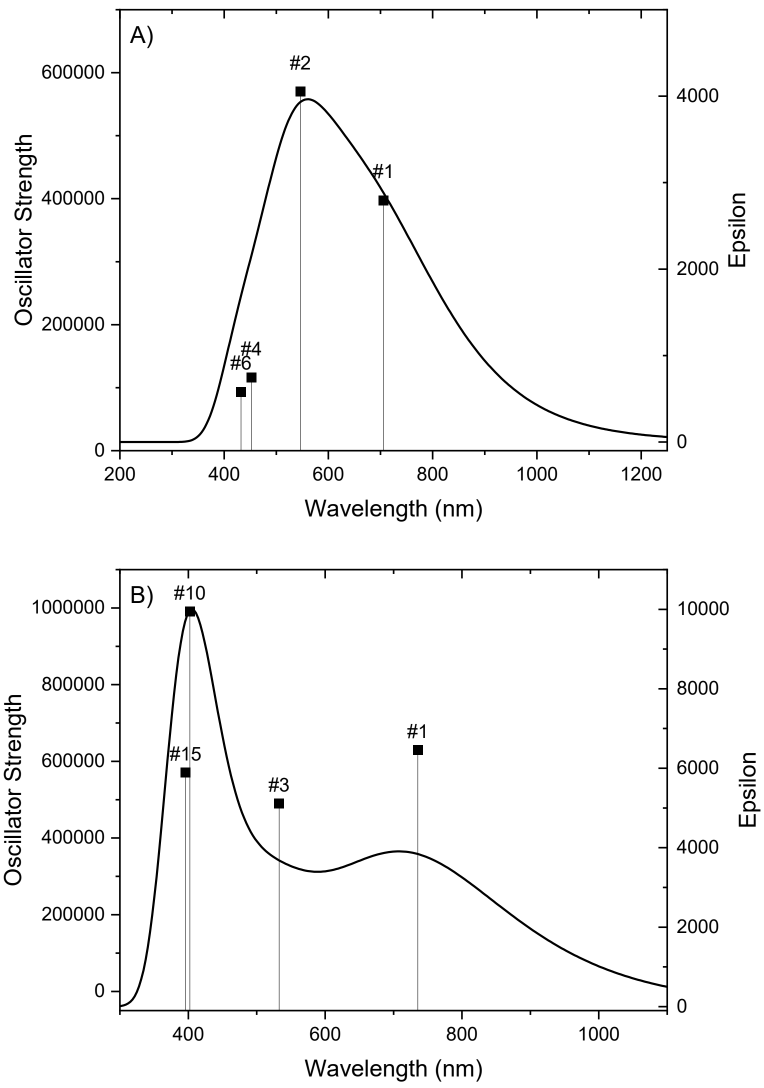

Figure B.4.7. Calculated absorption spectrum (solid line) and corresponding electronic transition number (symbols) for **3** (A) and **4** (B) in chloroform with the PBE0 functional by TD-DFT.

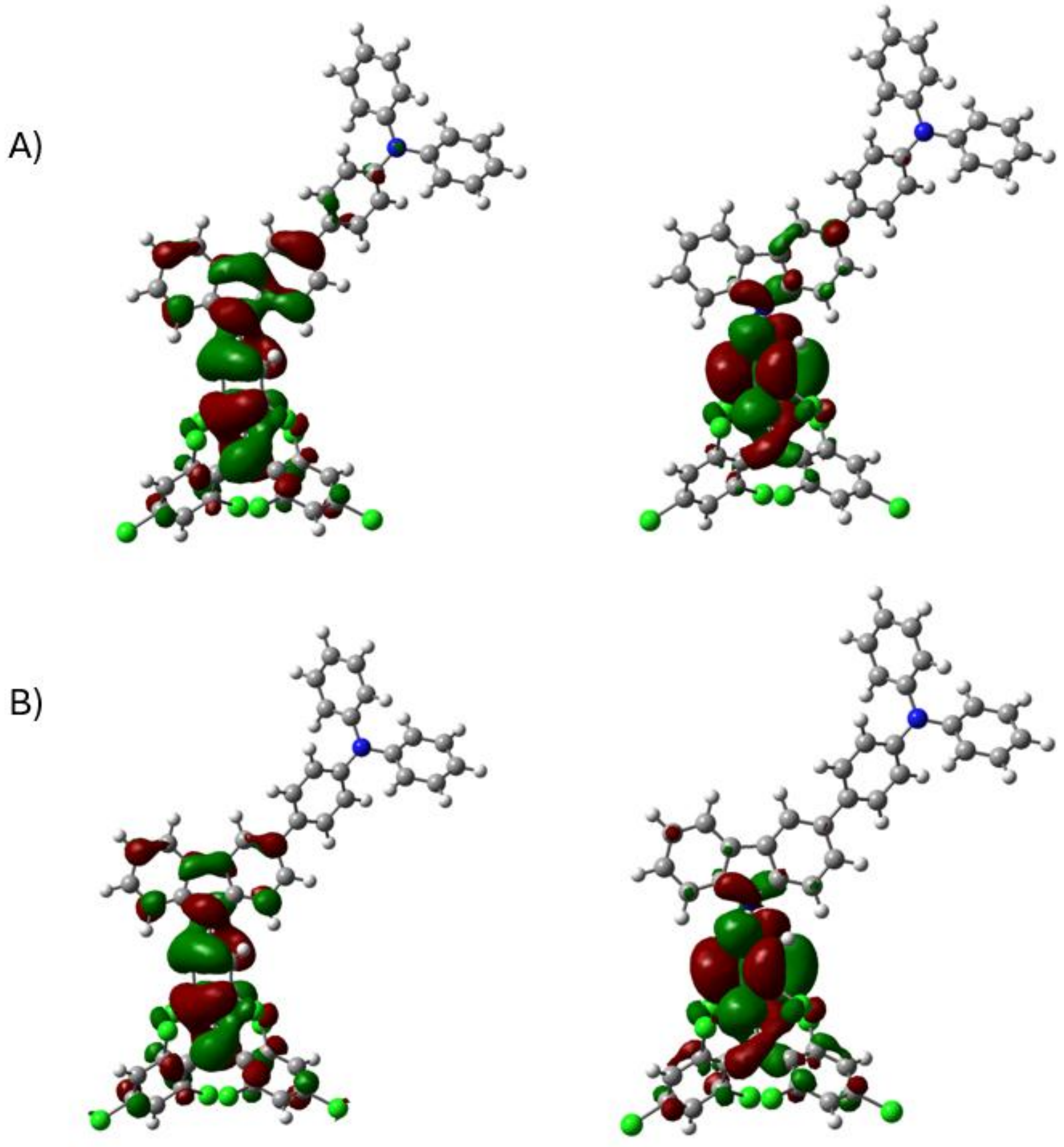

Figure B.4.8. Singly occupied (left) and lowest unoccupied (right) orbitals calculated from the natural transition orbital analysis for a given energy transition by TD-DFT of the 3 in cyclohexane: A) α-spin of transition #1; B) α-spin of transition #2.

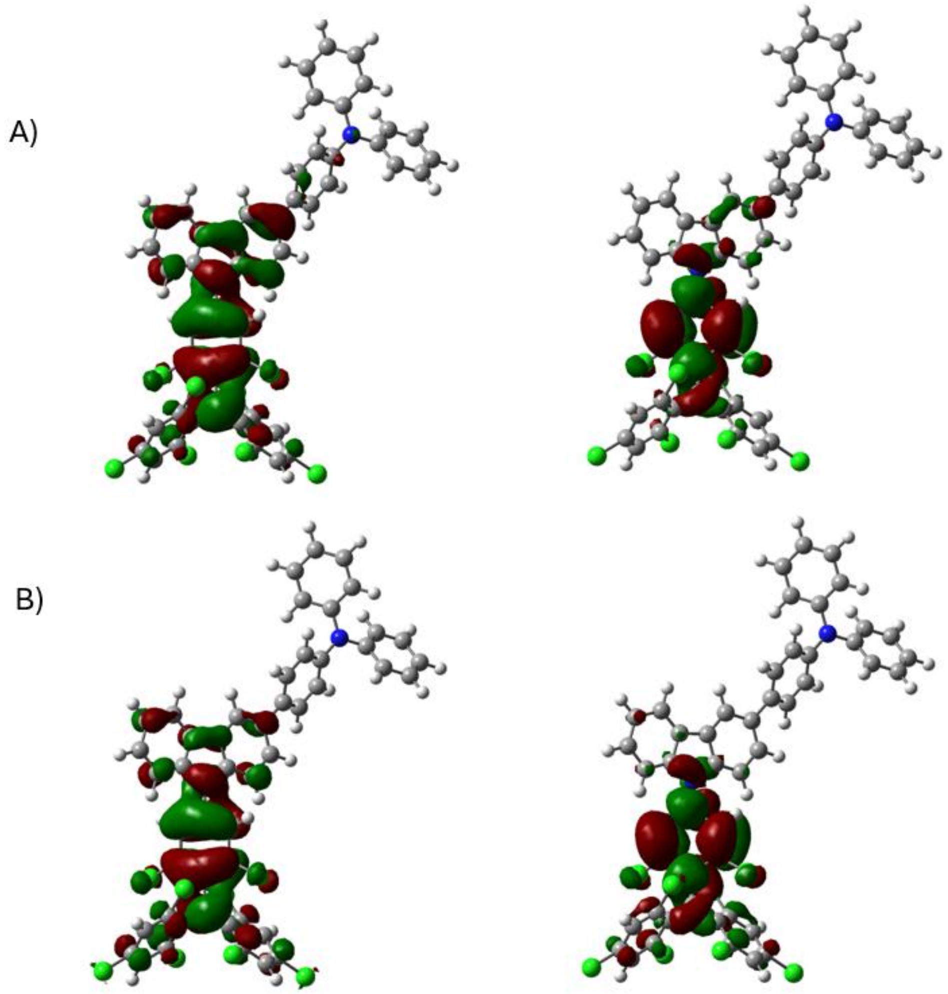

Figure B.4.9. Singly occupied (left) and lowest unoccupied (right) orbitals calculated from the natural transition orbital analysis for a given energy transition by TD-DFT of the 3 in toluene: A) α-spin of transition #1; B) α-spin of transition #2.

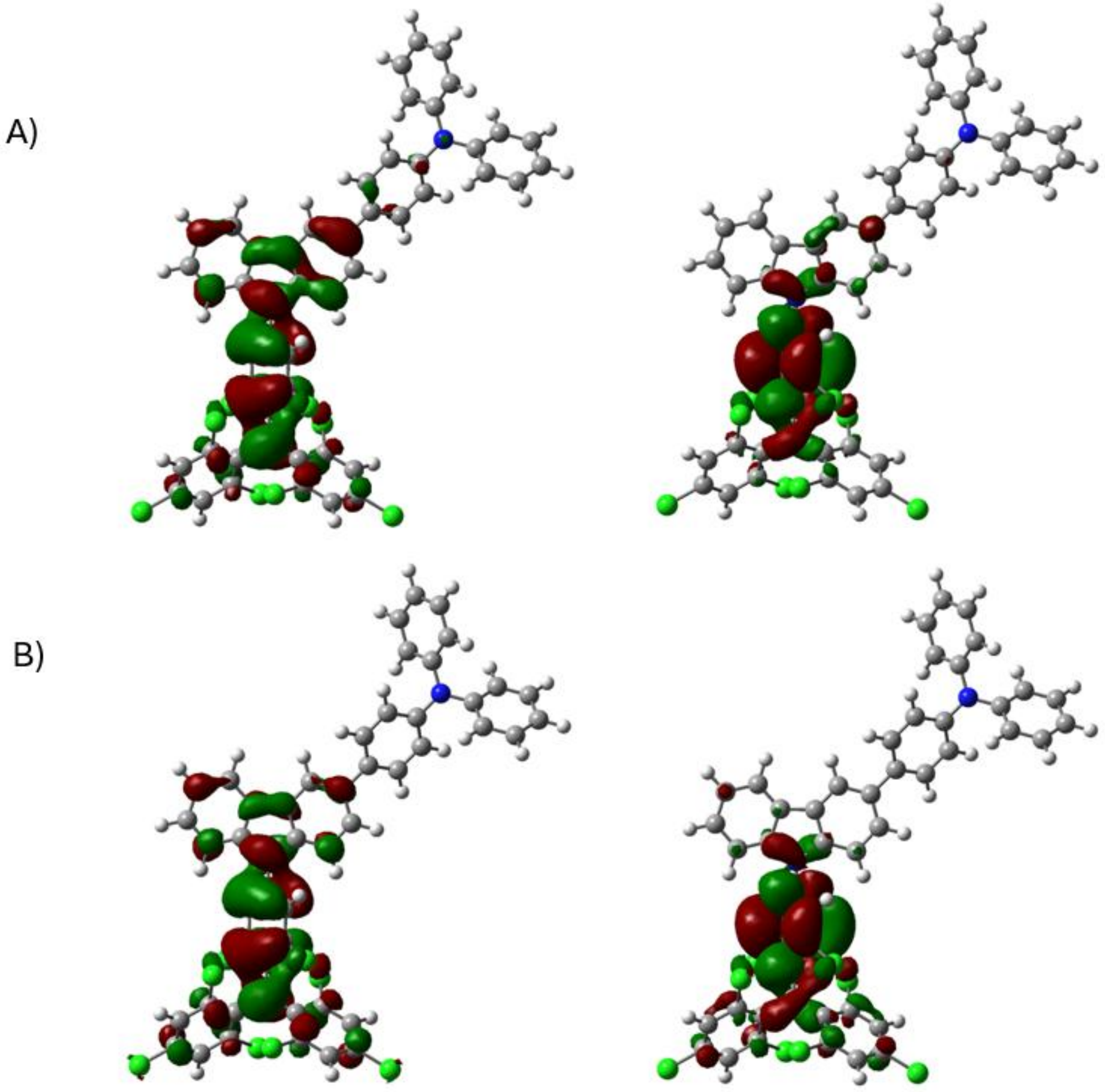

Figure B.4.10. Singly occupied (left) and lowest unoccupied (right) orbitals calculated from the natural transition orbital analysis for a given energy transition by TD-DFT of the 3 in chloroform: A) α-spin of transition #1; B) α-spin of transition #2.

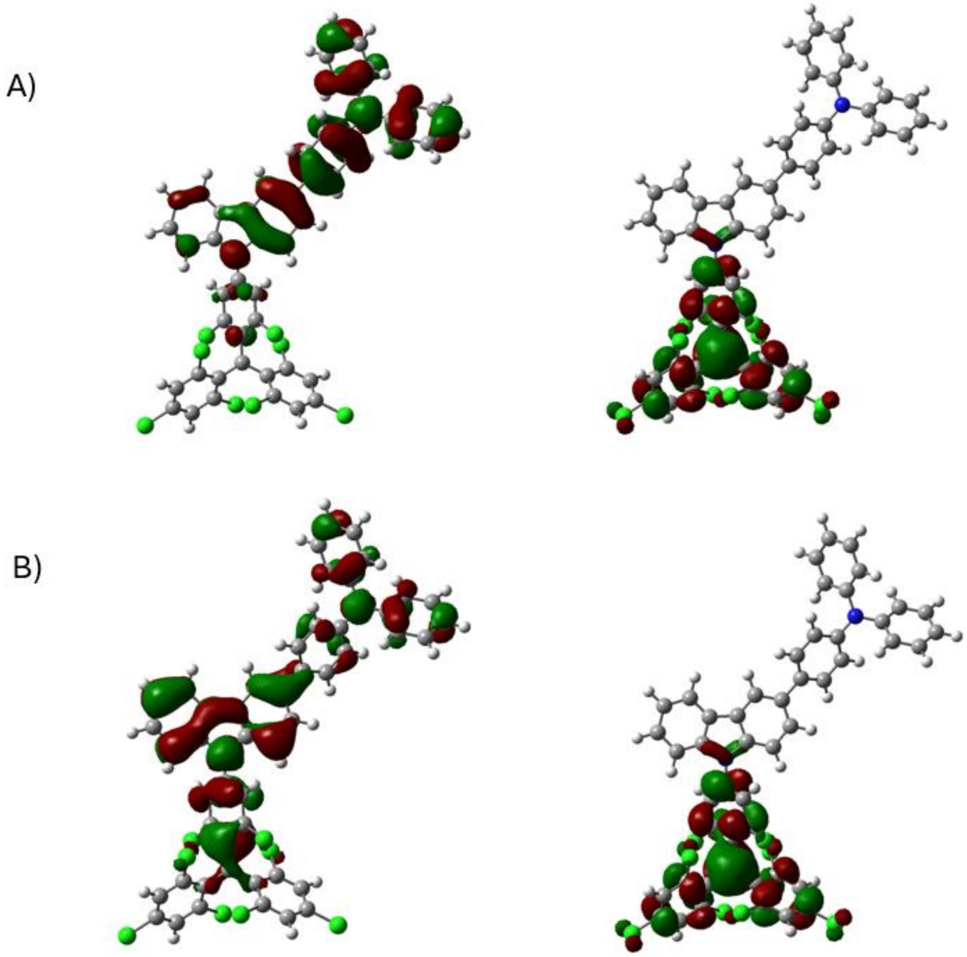

Figure B.4.11. Highest occupied (left) and lowest unoccupied (right) orbitals calculated from the natural transition orbital analysis for a given energy transition by TD-DFT of the 3 in cyclohexane: A) β-spin of transition #1; B) β-spin of transition #2.

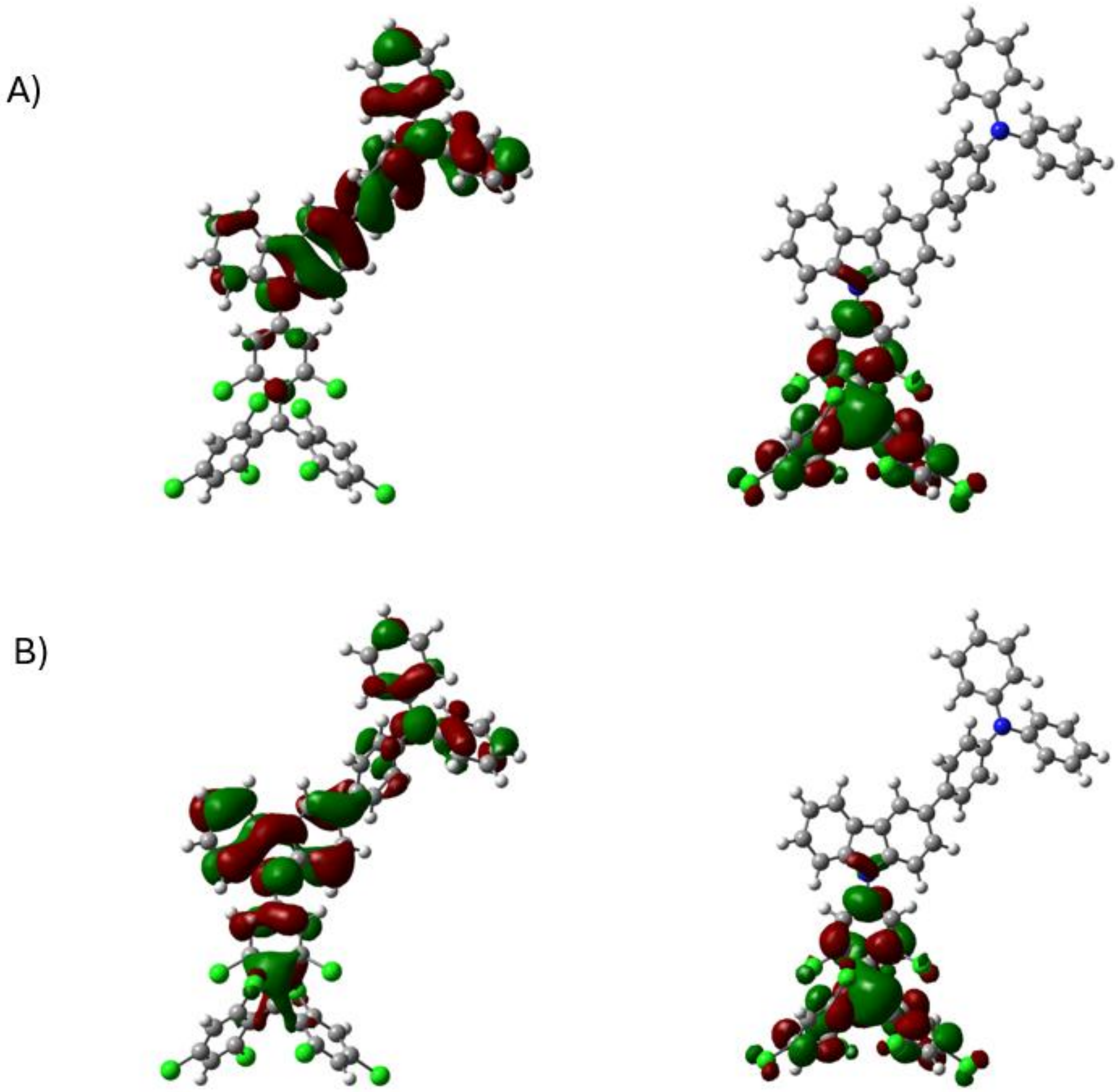

Figure B.4.12. Highest occupied (left) and lowest unoccupied (right) orbitals calculated from the natural transition orbital analysis for a given energy transition by TD-DFT of the 3 in toluene: A) β-spin of transition #1; B) β-spin of transition #2.

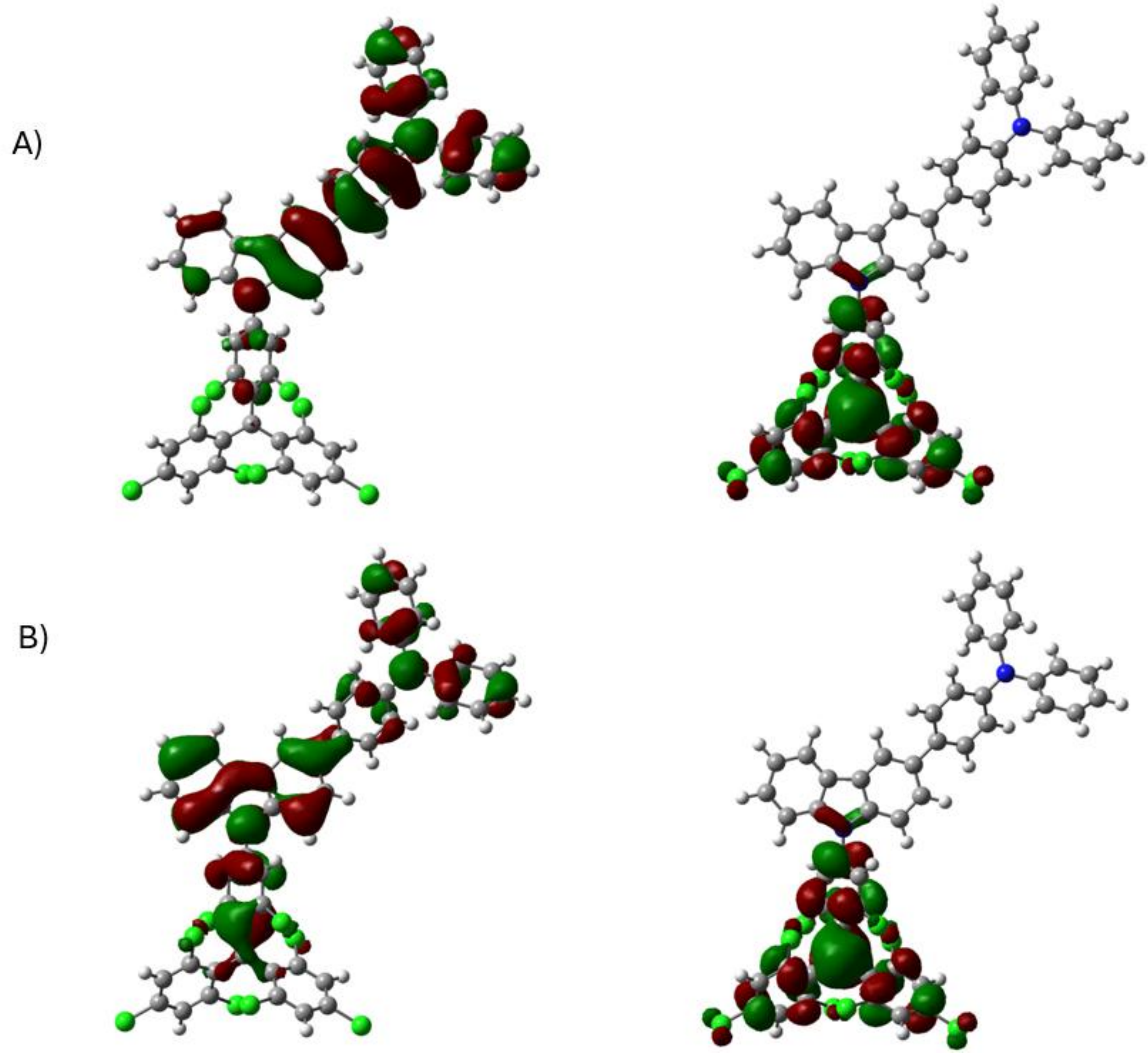

Figure B.4.13. Highest occupied (left) and lowest unoccupied (right) orbitals calculated from the natural transition orbital analysis for a given energy transition by TD-DFT of the 3 in chloroform: A) β-spin of transition #1; B) β-spin of transition #2.

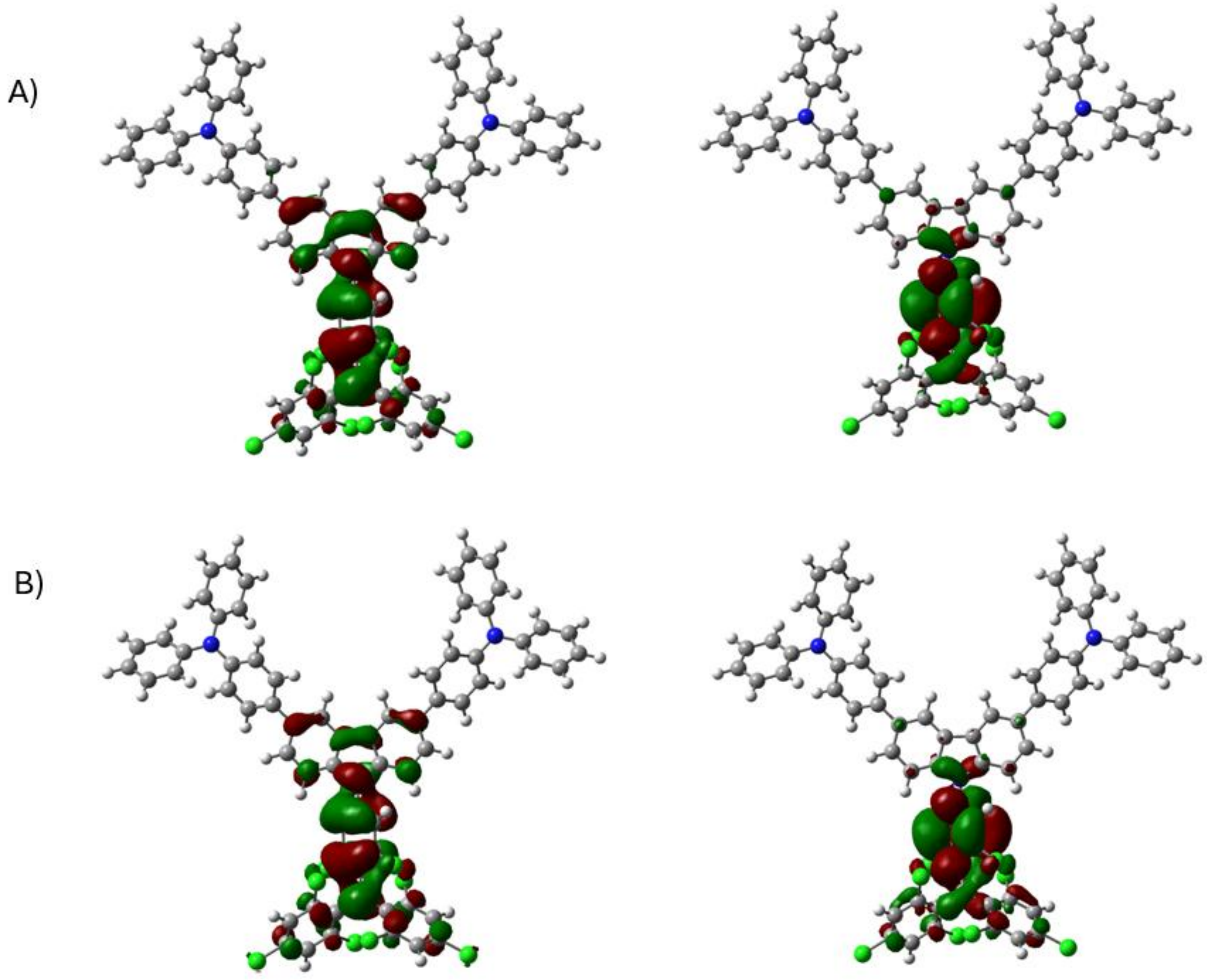

Figure B.4.14. Singly occupied (left) and lowest unoccupied (right) orbitals calculated from the natural transition orbital analysis for a given energy transition by TD-DFT of the 4 in cyclohexane: A) α-spin of transition #1; B) α-spin of transition #2.

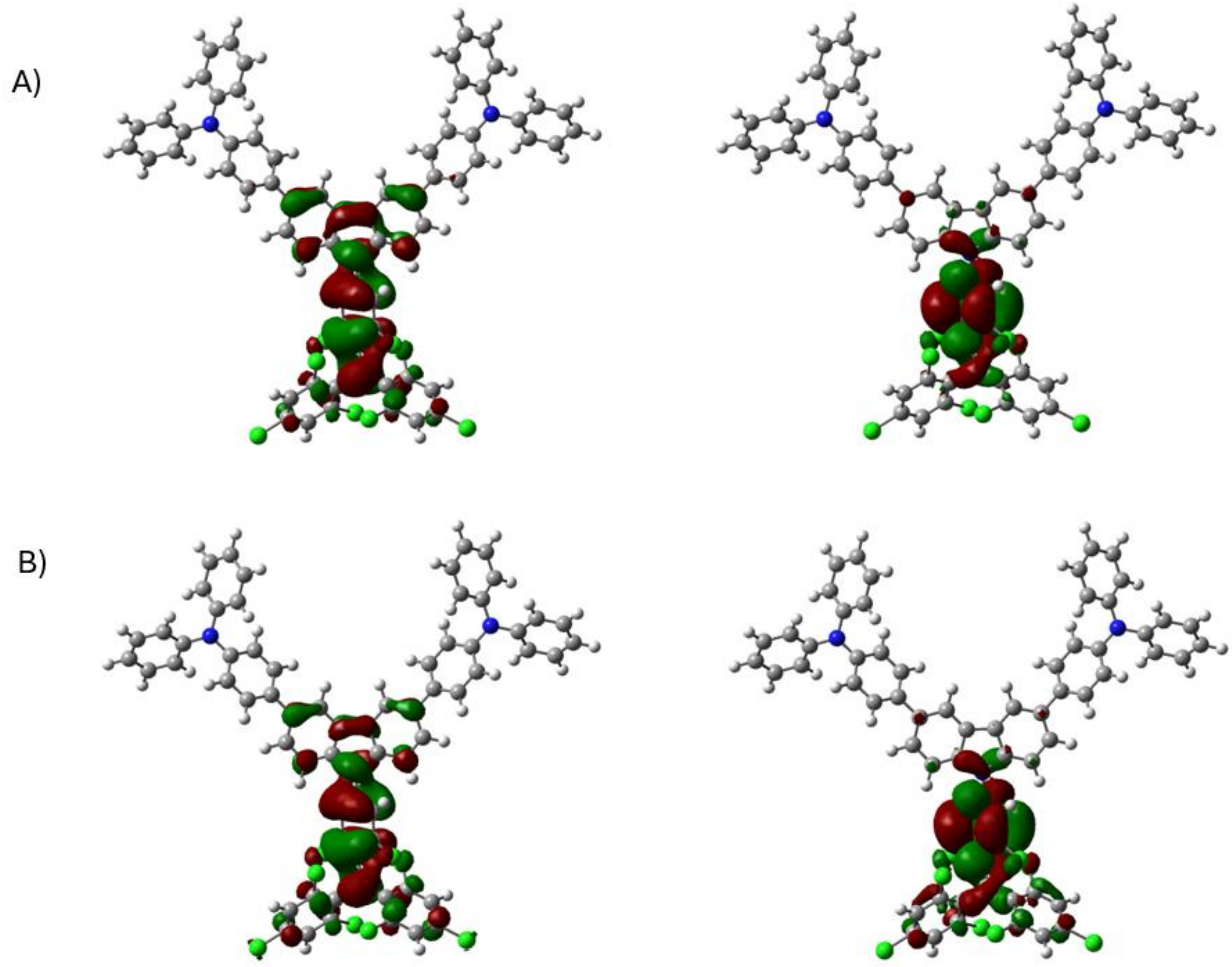

Figure B.4.15. Singly occupied (left) and lowest unoccupied (right) orbitals calculated from the natural transition orbital analysis for a given energy transition by TD-DFT of the radical 4 in toluene: A) α-spin of transition #1; B) α-spin of transition #2.

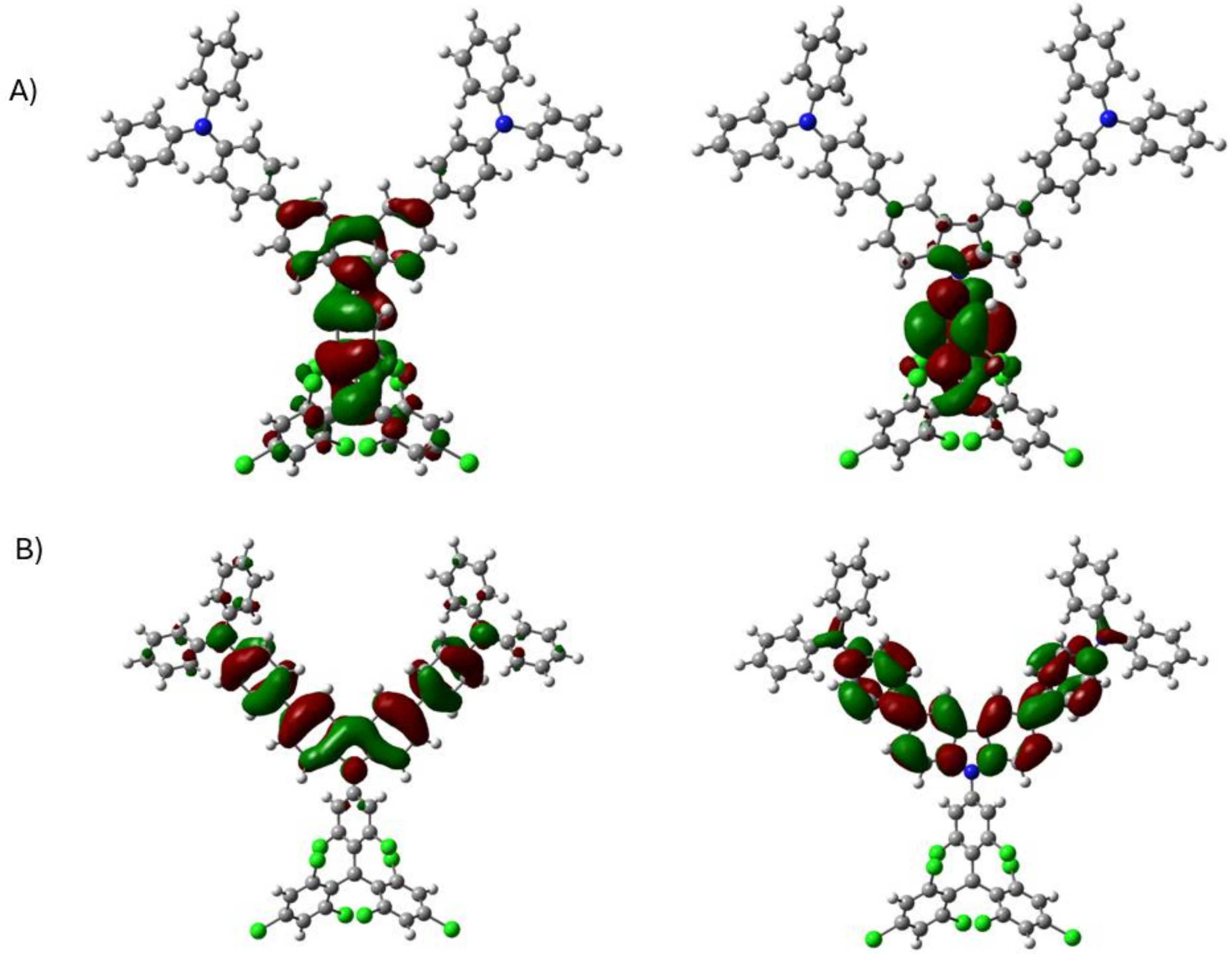

Figure B.4.16. Singly occupied (left) and lowest unoccupied (right) orbitals calculated from the natural transition orbital analysis for a given energy transition by TD-DFT of the 4 in chloroform: A) α-spin of transition #1; B) α-spin of transition #2.

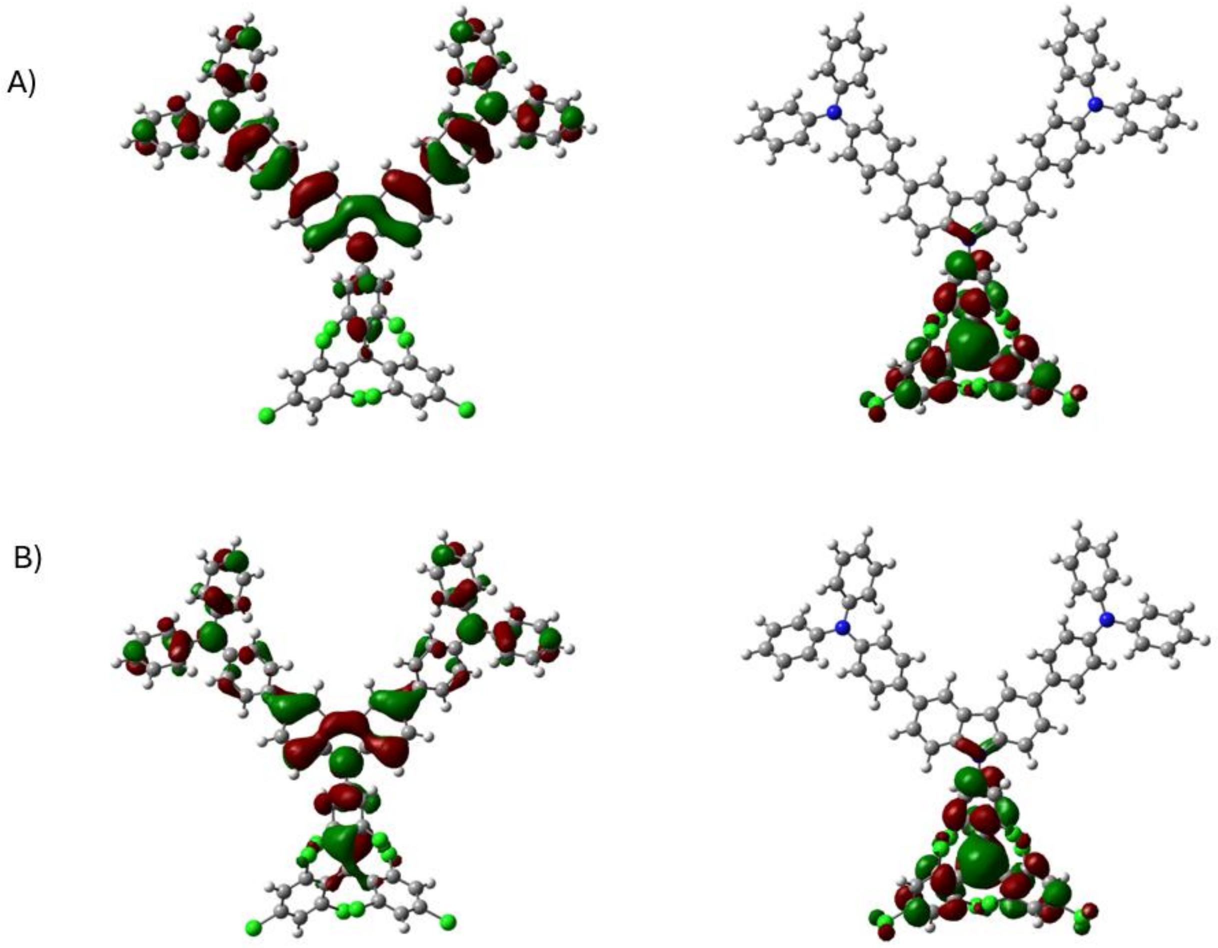

Figure B.4.17. Highest occupied (left) and lowest unoccupied (right) orbitals calculated from the natural transition orbital analysis for a given energy transition by TD-DFT of the 4 in cyclohexane: A) β-spin of transition #1; B) β-spin of transition #2.

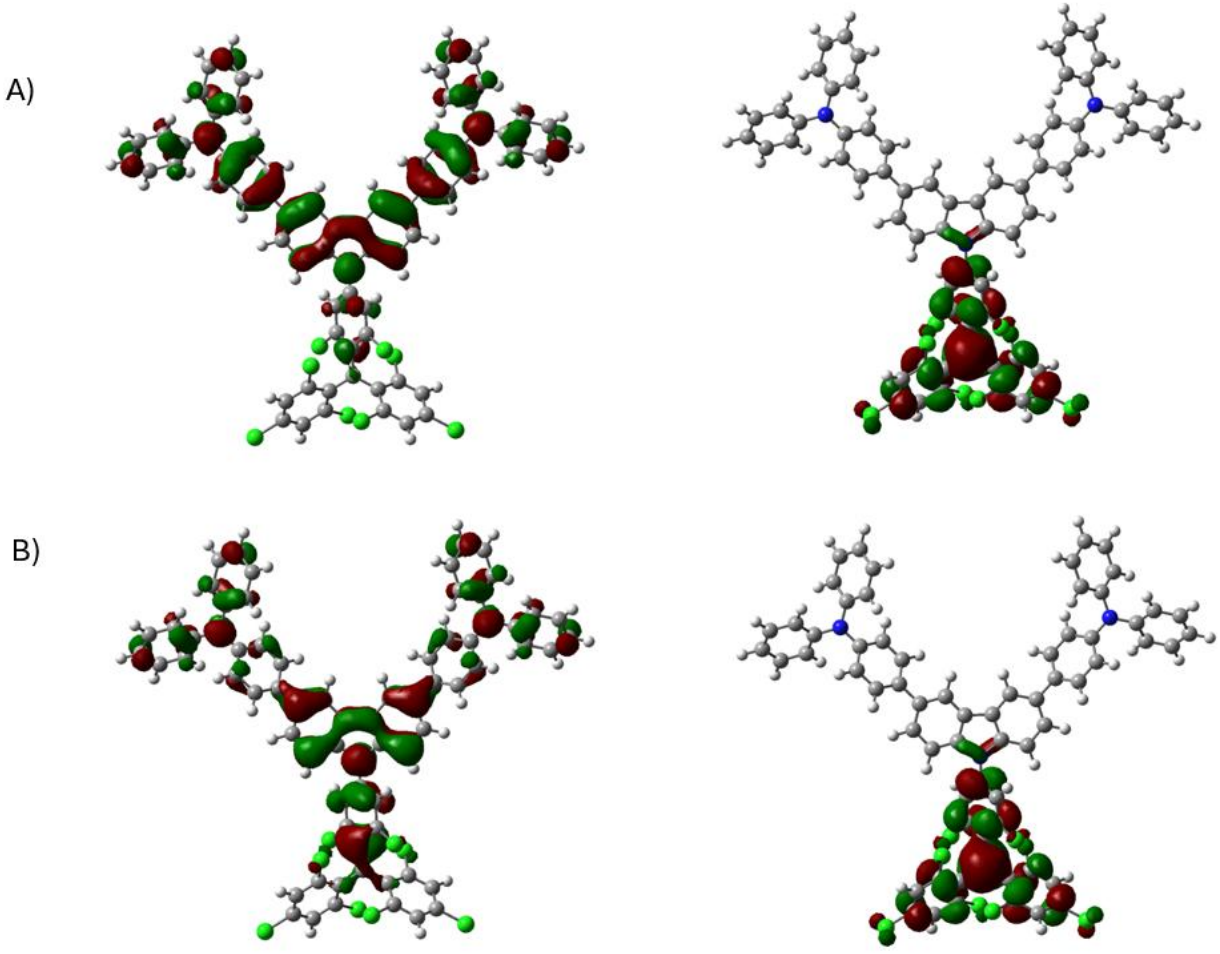

Figure B.4.18. Highest occupied (left) and lowest unoccupied (right) orbitals calculated from the natural transition orbital analysis for a given energy transition by TD-DFT of the 4 in toluene: A) β-spin of transition #1; B) β-spin of transition #2.

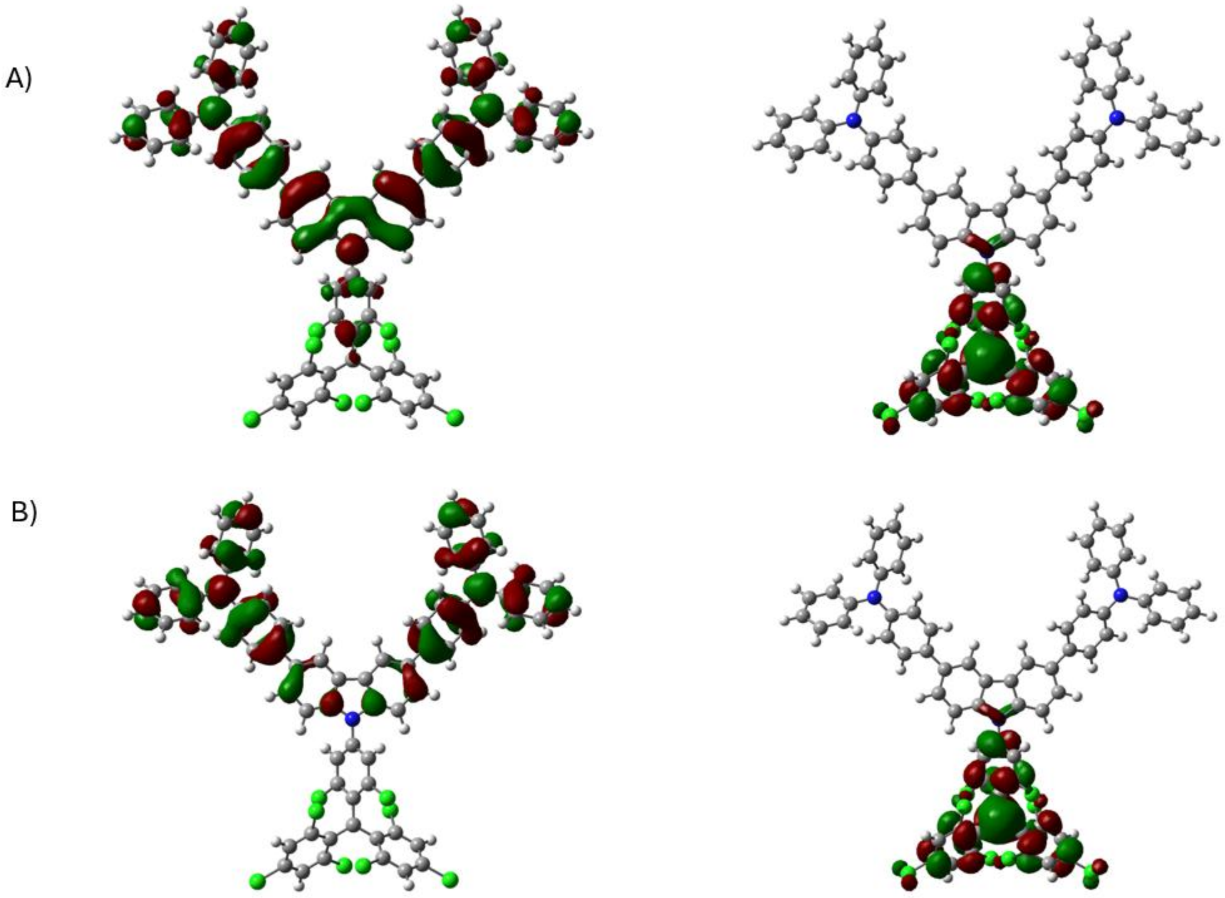

Figure B.4.19. Highest occupied (left) and lowest unoccupied (right) orbitals calculated from the natural transition orbital analysis for a given energy transition by TD-DFT of the 4 in chloroform: A) β-spin of transition #1; B) β-spin of transition #2.

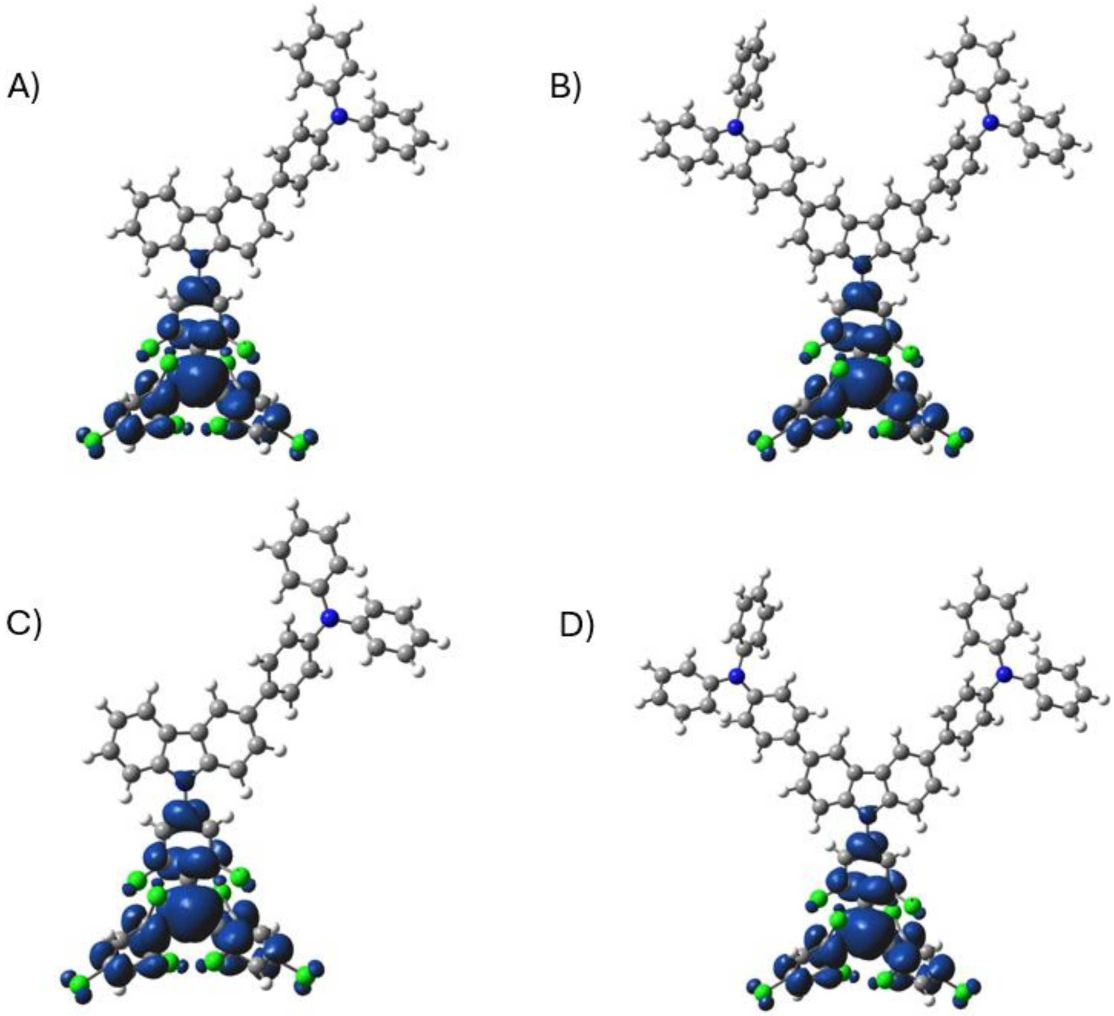

Figure B.4.20. Electron spin density of 3 (A,C in toluene and chloroform respectively) and radical 4 (B,D in toluene and chloroform respectively) drawing at density=0.0004.

NMR Spectra

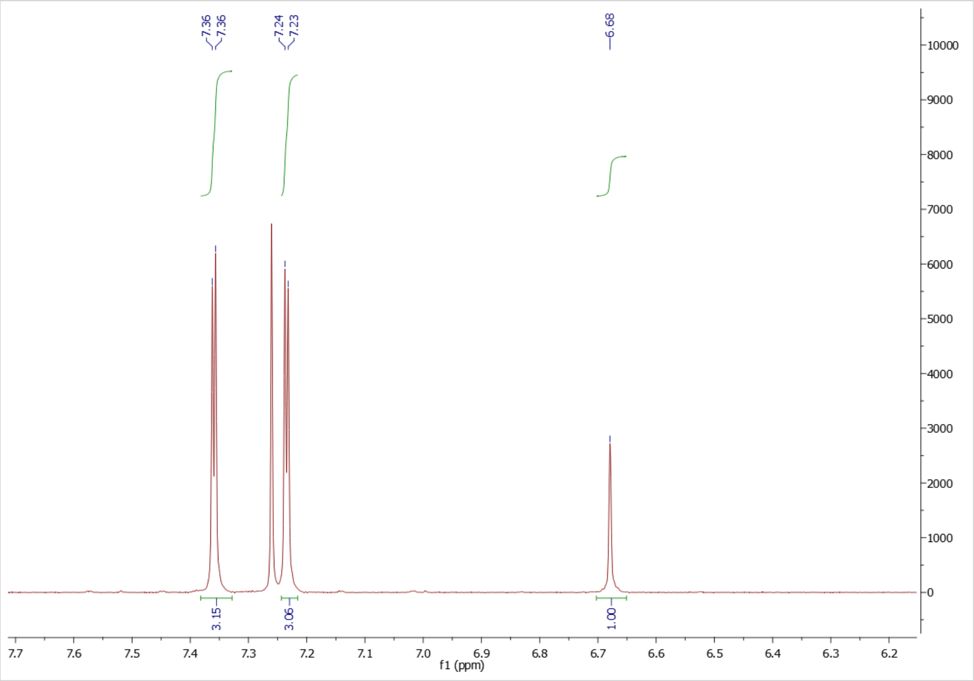

Figure B.4.21. ^{1}H NMR spectrum of 6 measured in $CDCl_3$.

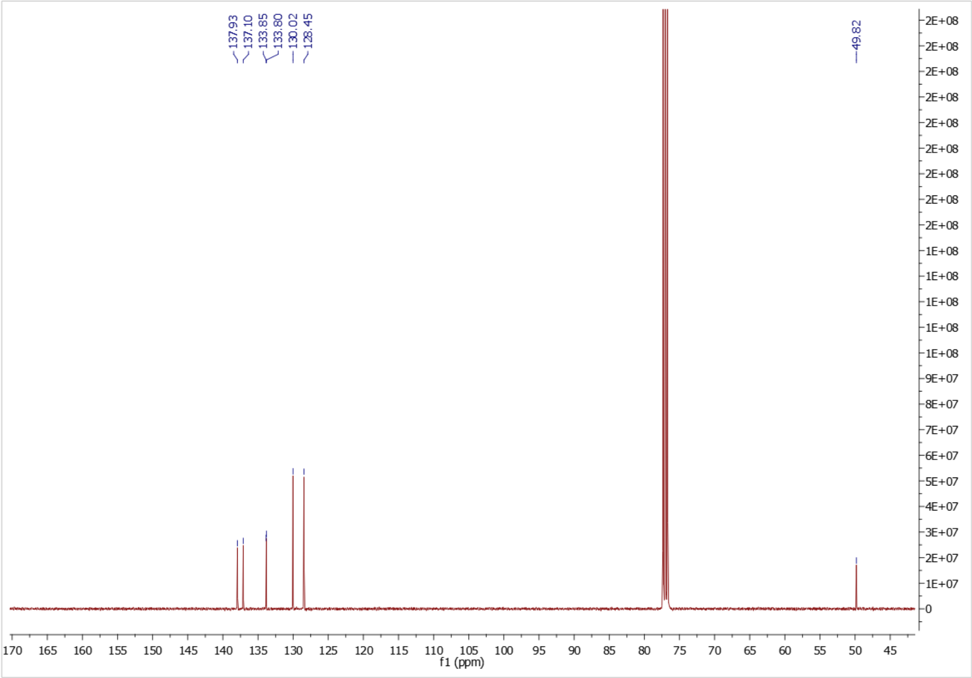

Figure B.4.22. ^{13}C NMR spectrum of 6 measured in $CDCl_3$.

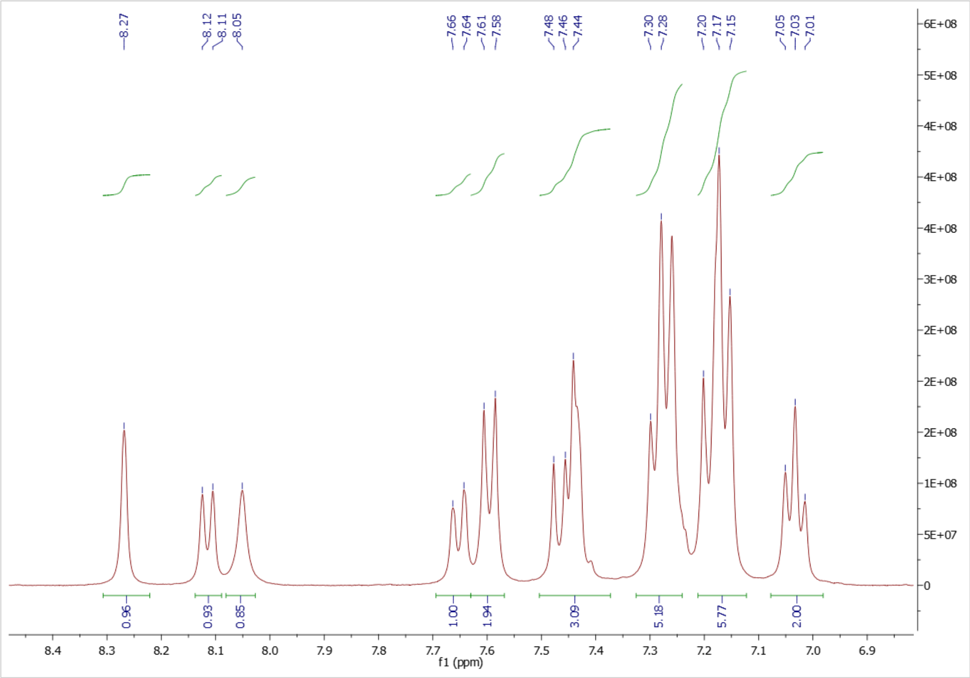

Figure B.4.23. ^{1}H NMR spectrum of 7 measured in $CDCl_3$.

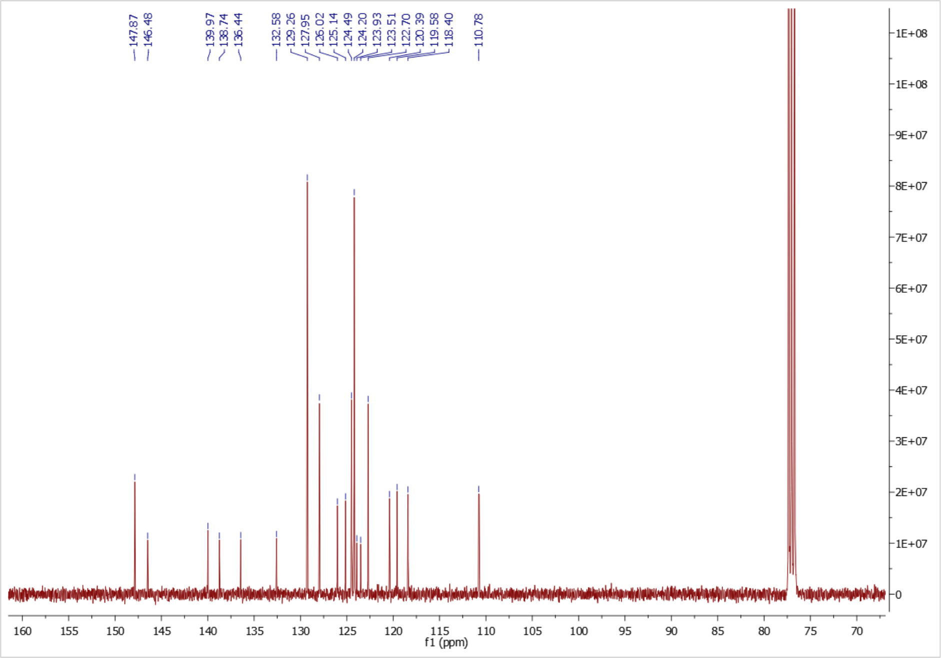

Figure B.4.24. ^{13}C NMR spectrum of 7 measured in CDCl$_3$.

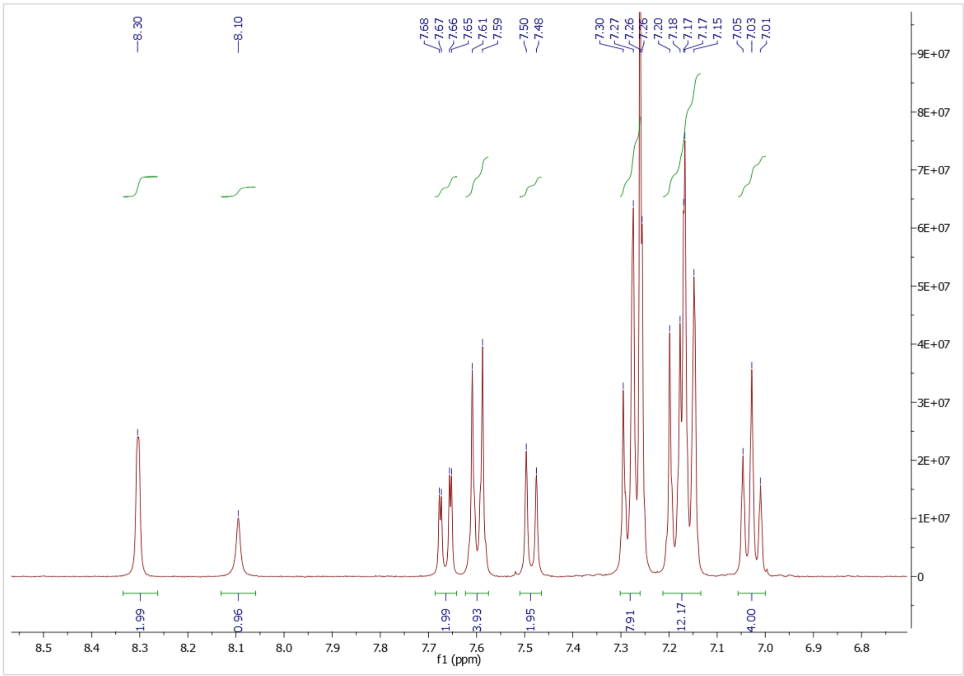

Figure B.4.25. ^{1}H NMR spectrum of 8 measured in CDCl$_3$.

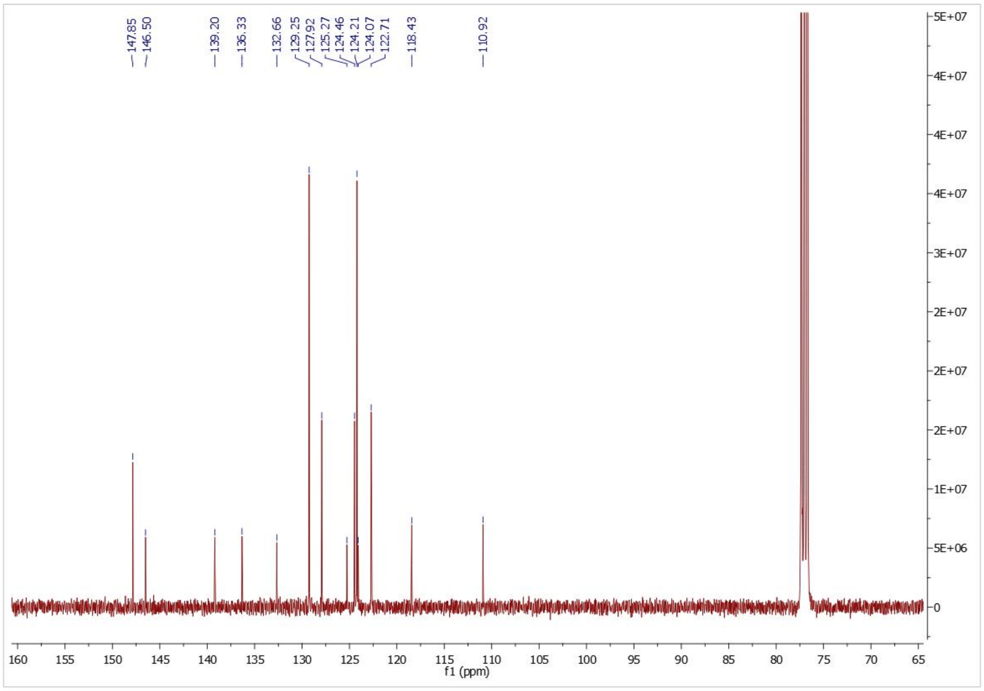

Figure B.4.26. ^{13}C NMR spectrum of 8 measured in $CDCl_3$.

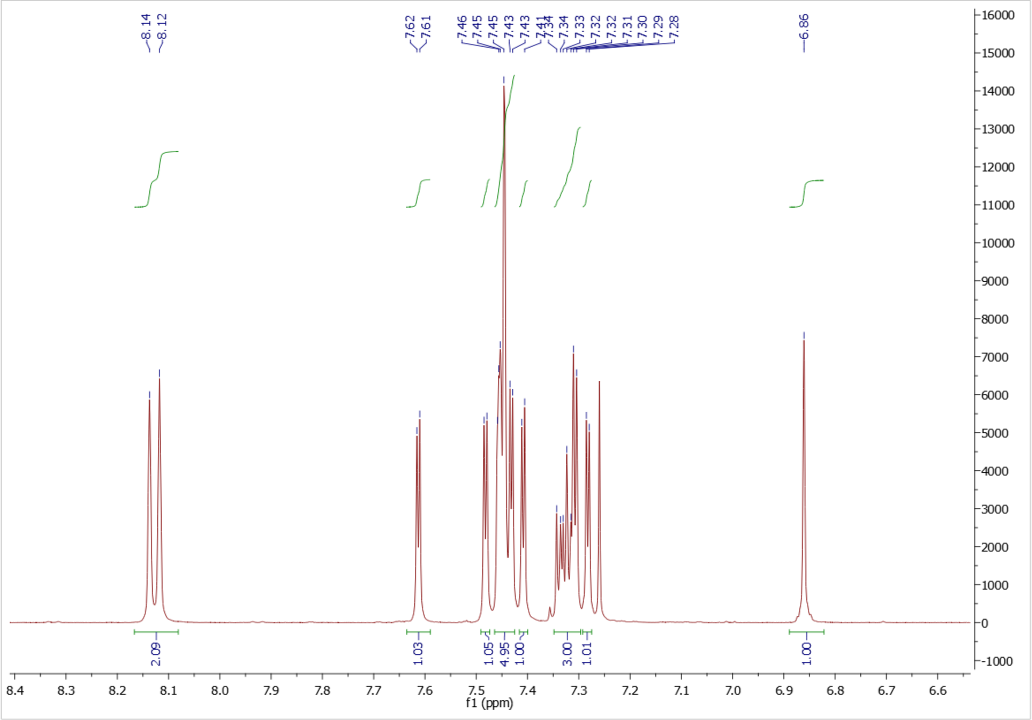

Figure B.4.27. ^{1}H NMR spectrum of 11 measured in $CDCl_3$.

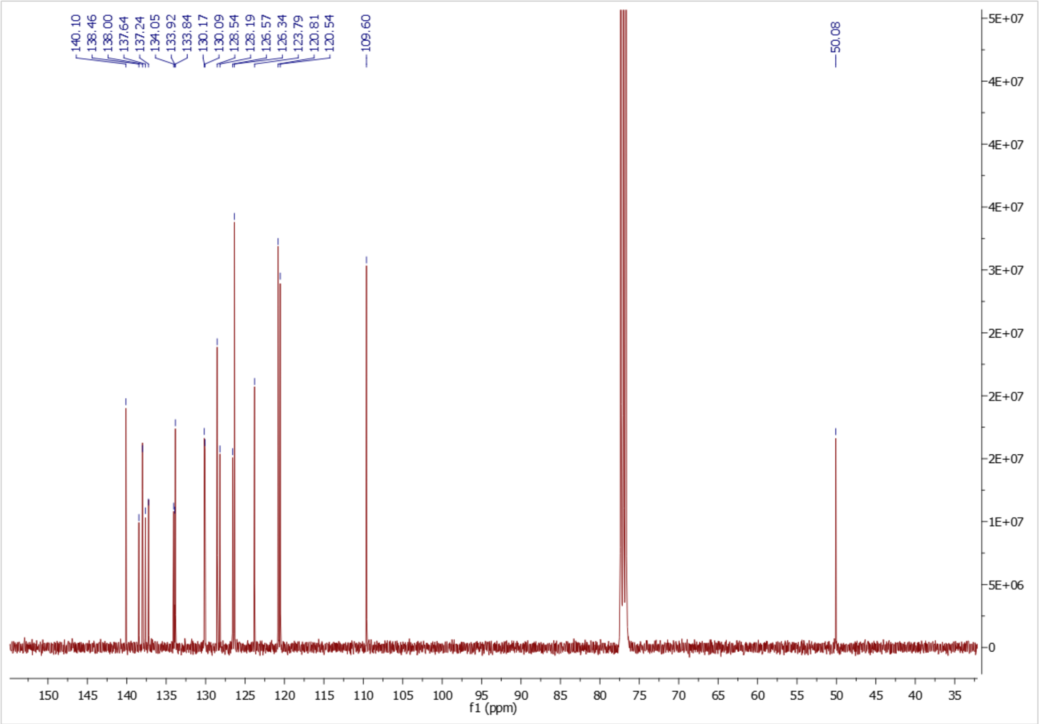

Figure B.4.28. ^{13}C NMR spectrum of 11 measured in $CDCl_3$.

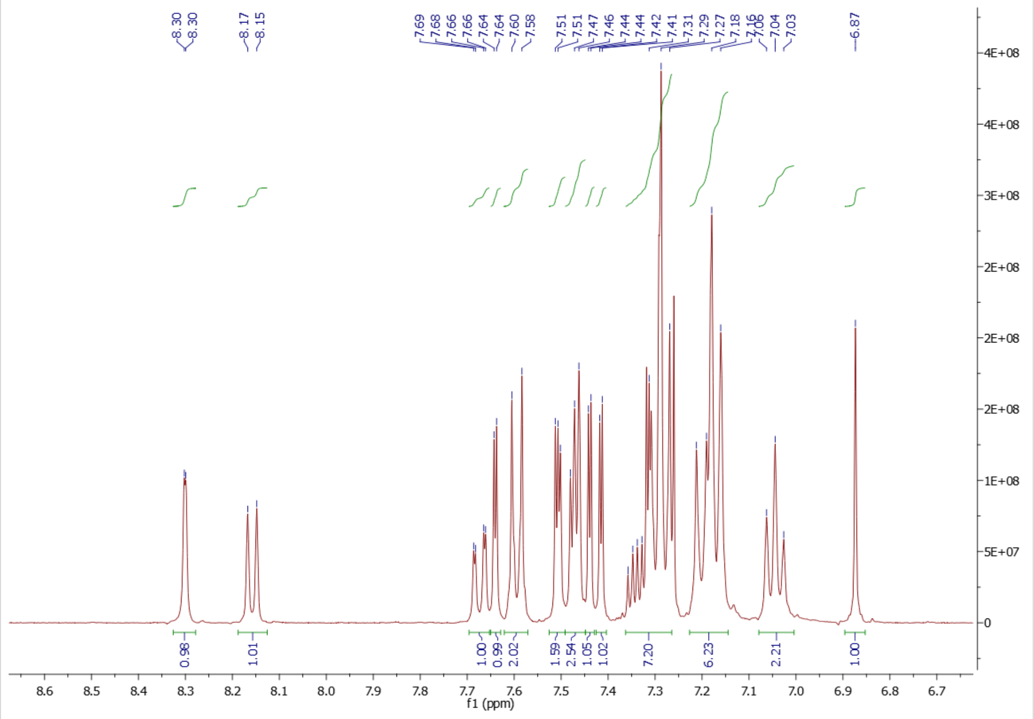

Figure B.4.29. ^{1}H NMR spectrum of 9 measured in $CDCl_3$.

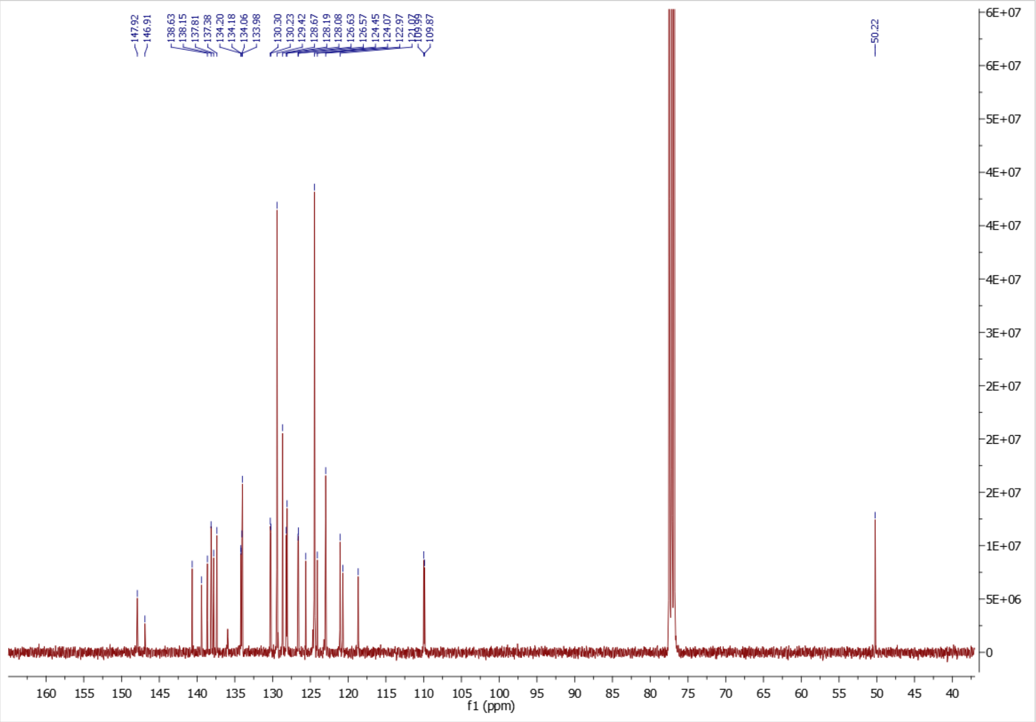

Figure B.4.30. ^{13}C NMR spectrum of 9 measured in $CDCl_3$.

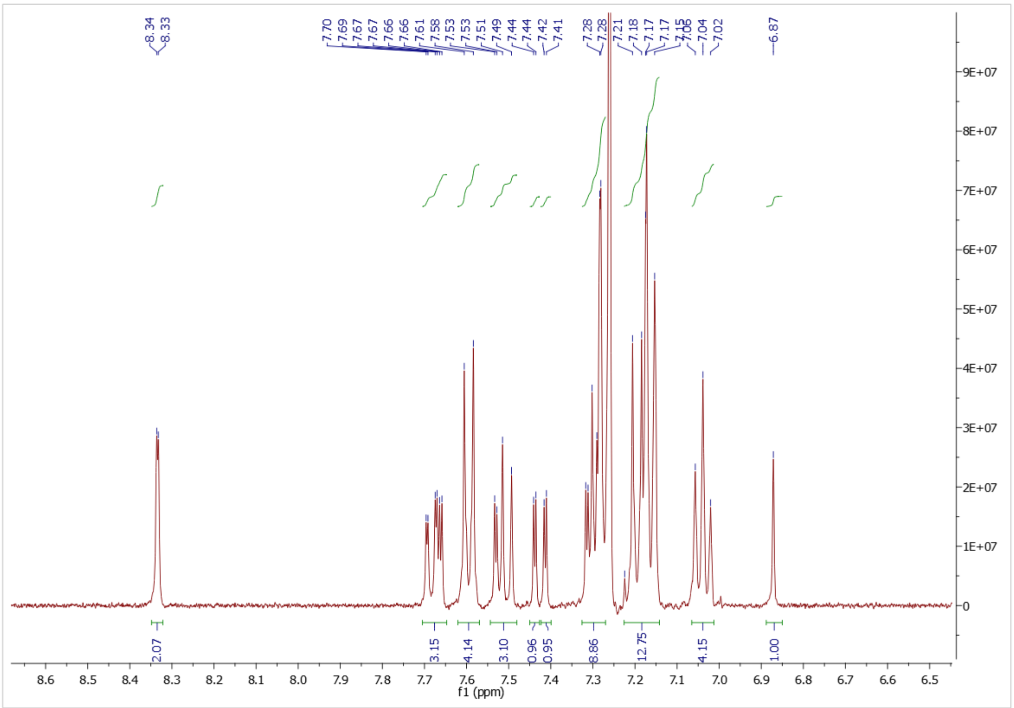

Figure B.4.31. ^{1}H NMR spectrum of 10 measured in $CDCl_3$.

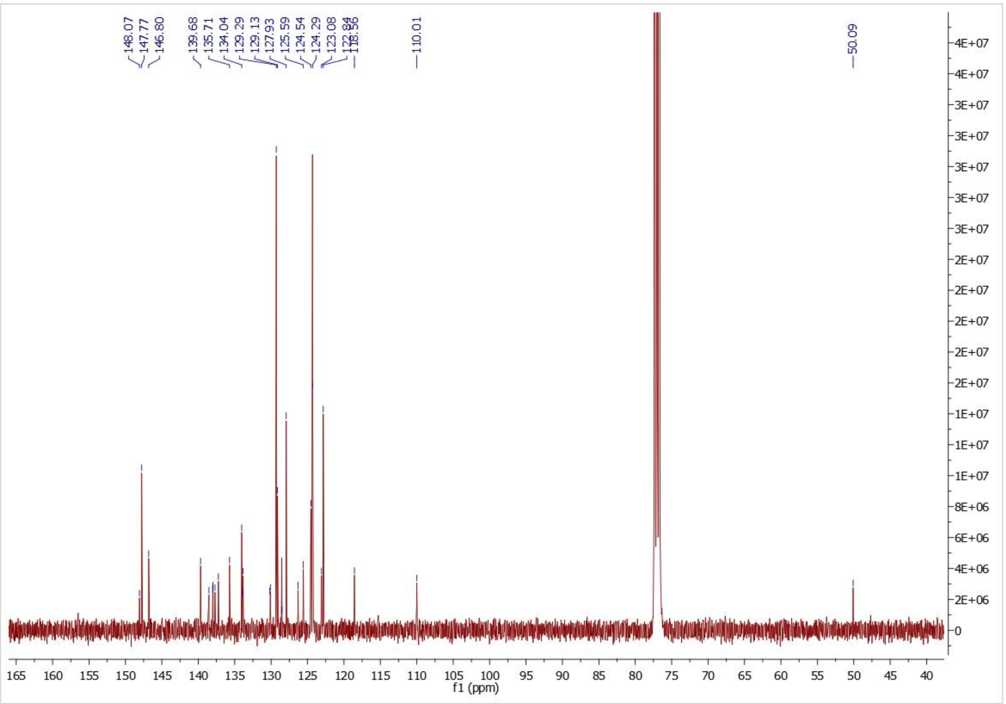

Figure B.4.32. ^{13}C NMR spectrum of 10 measured in $CDCl_3$.

Mass Spectrometry

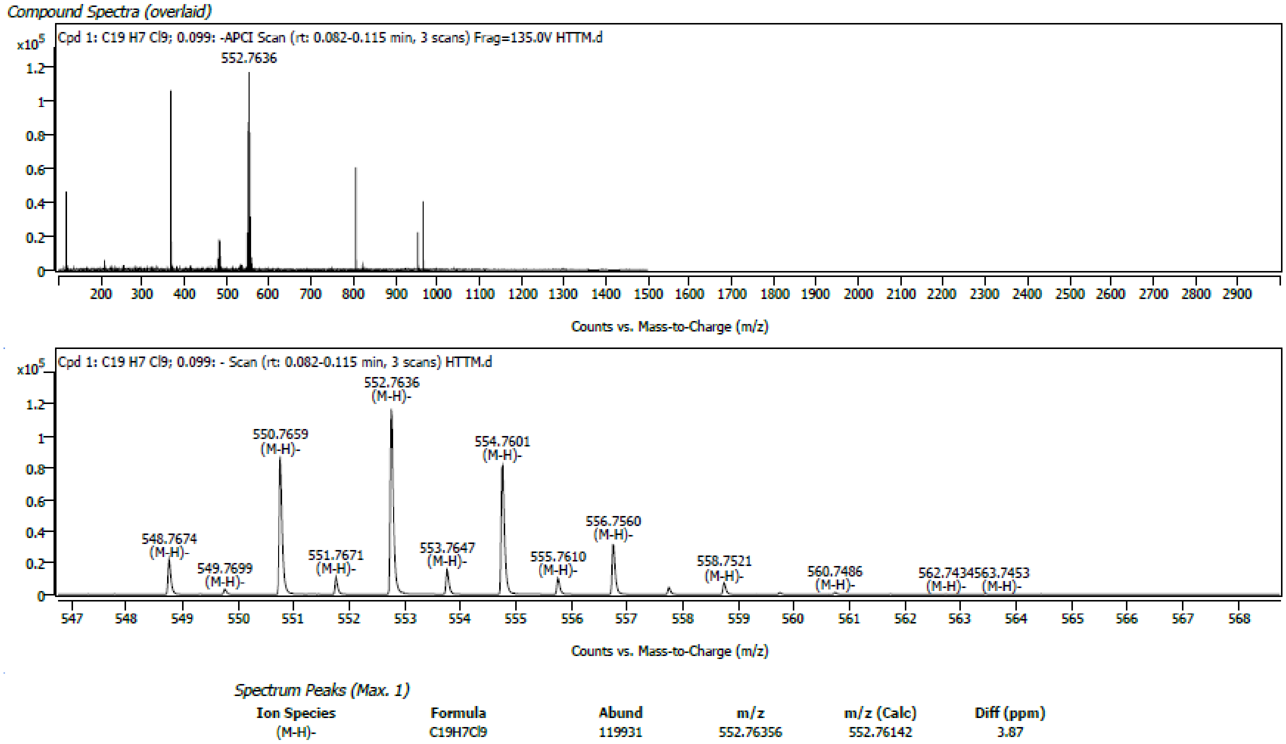

Spectrum Peaks (Max. 1)

Ion Species	Formula	Abund	m/z	m/z (Calc)	Diff (ppm)
(M-H)-	C19H7Cl9	119931	552.76356	552.76142	3.87

Figure B.4.33. High resolution mass spectrometry of 6.

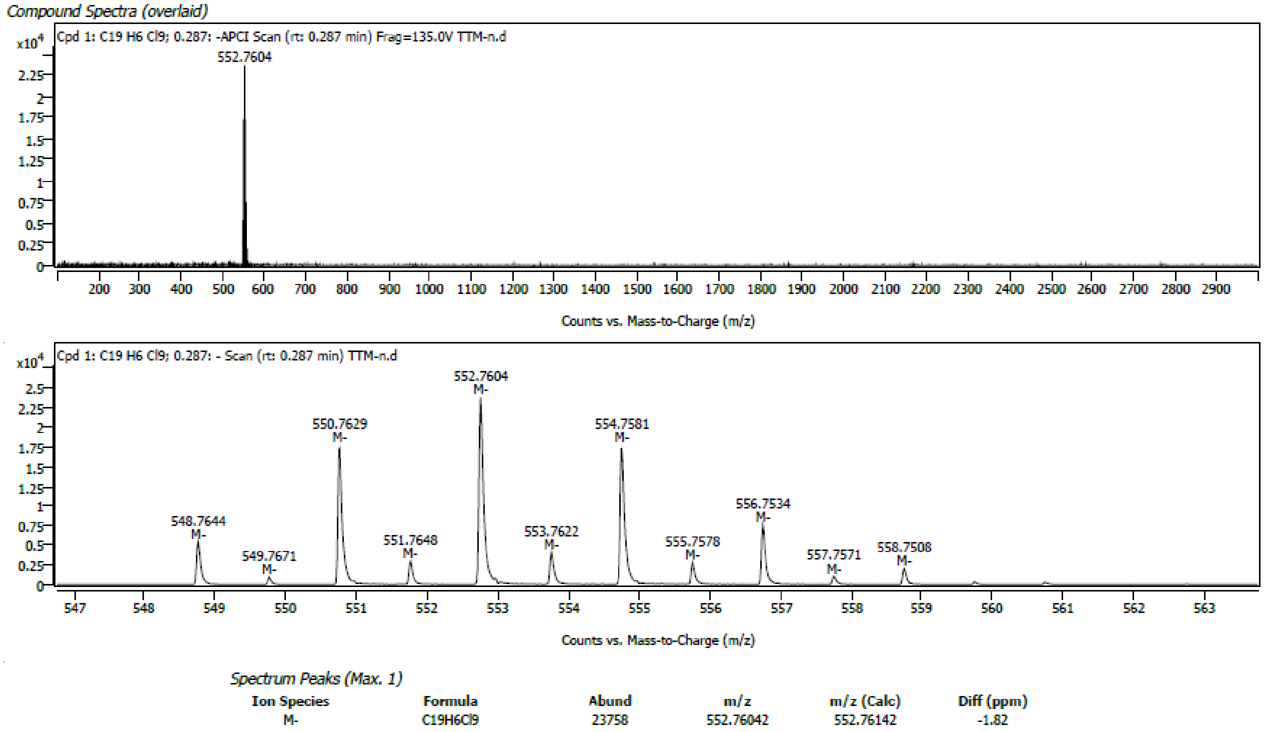

Spectrum Peaks (Max. 1)

Ion Species	Formula	Abund	m/z	m/z (Calc)	Diff (ppm)
M-	C19H6Cl9	23758	552.76042	552.76142	-1.82

Figure B.4.34. High resolution mass spectrometry of 1.

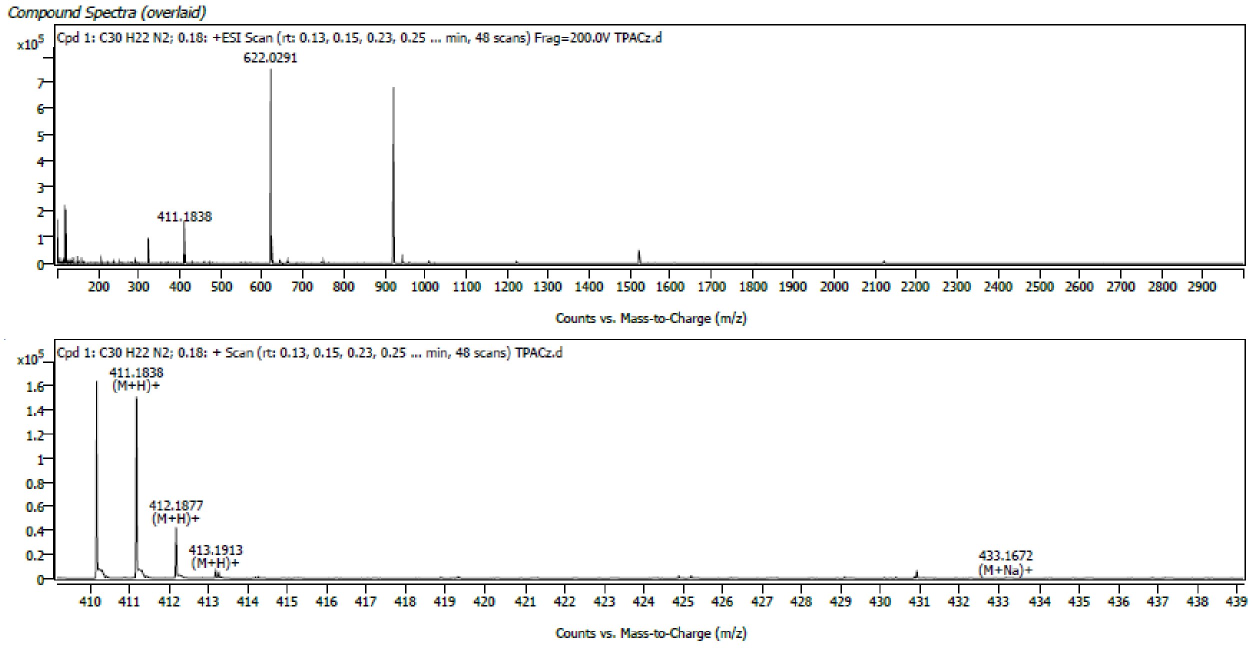

Spectrum Peaks (Max. 1)

Ion Species	Formula	Abund	m/z	m/z (Calc)	Diff (ppm)	Diff (mDa)
(M+H)+	C30H22N2	153990	411.18382	411.18558	-4.28	-1.76

Figure B.4.35. High resolution mass spectrometry of 7.

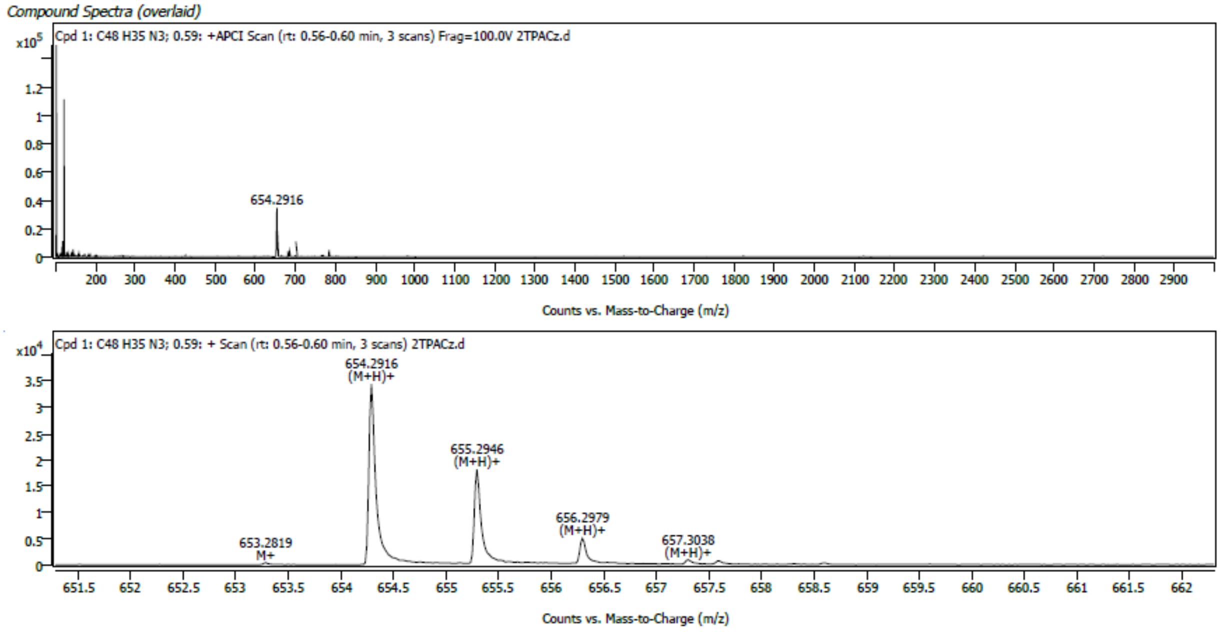

Spectrum Peaks (Max. 1)

Ion Species	Formula	Abund	m/z	m/z (Calc)	Diff (ppm)	Diff (mDa)
(M+H)+	C48H35N3	34413	654.29164	654.29037	1.93	1.26

Figure B.4.36. High resolution mass spectrometry of 8.

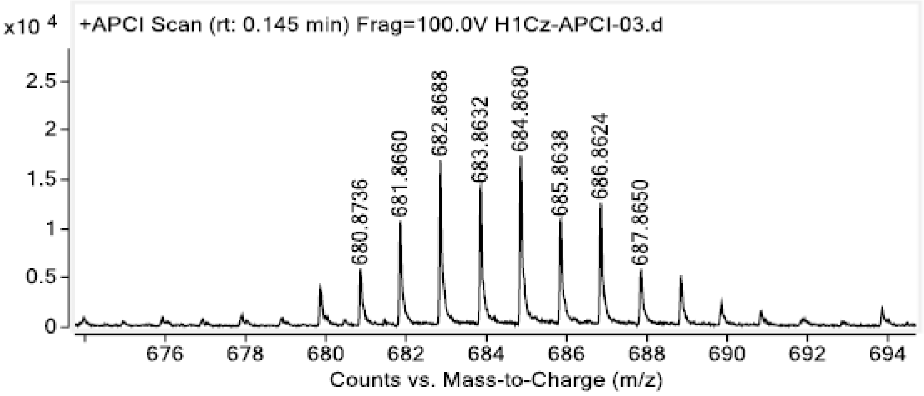

Ion	Formula	Expe. m/z	Calc. m/z	Diff (ppm)	Diff (mDa)
[M]+	C31 H15 Cl8 N	680.8736	680.8707	4.23	2.88

Figure B.4.37. High resolution mass spectrometry of 11.

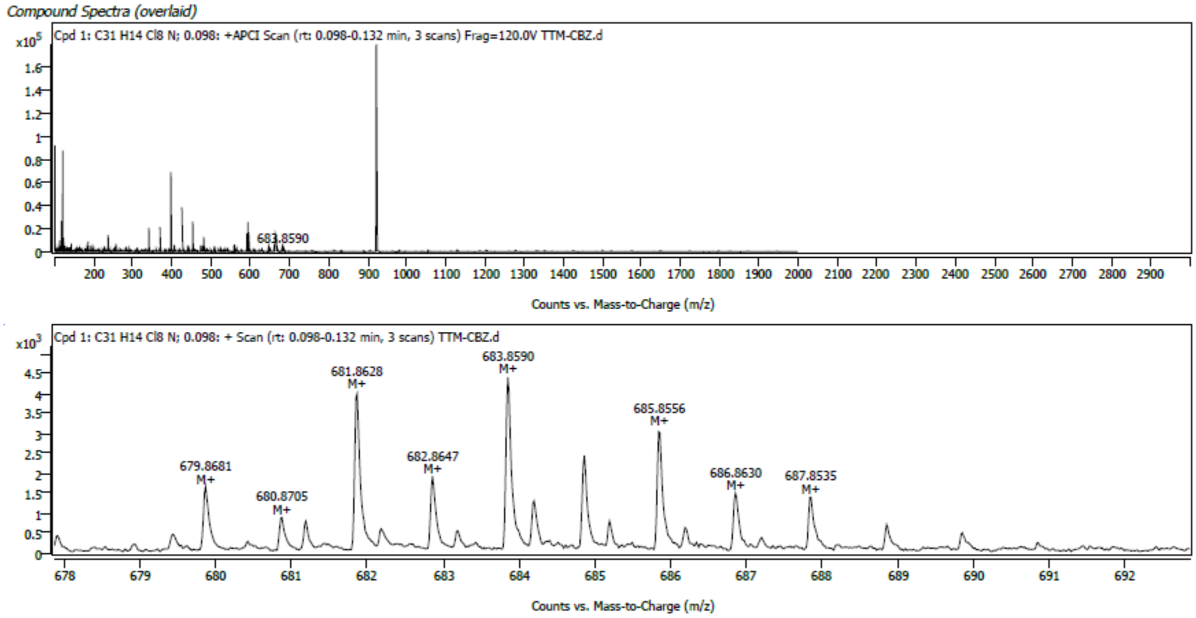

Spectrum Peaks (Max. 1)

Ion Species	Formula	Abund	m/z	m/z (Calc)	Diff (ppm)
M+	C31H14Cl8N	4429	683.85905	683.85746	2.33

Figure B.4.38. High resolution mass spectrometry of 2.

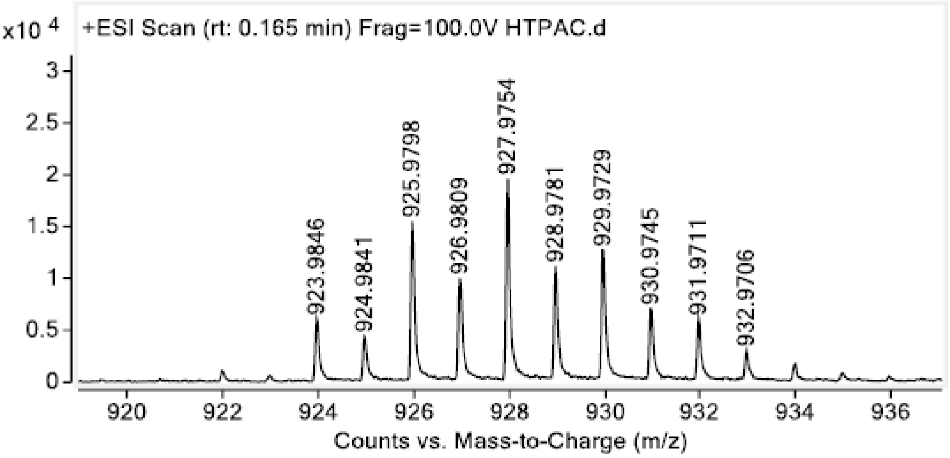

Ion	Formula	Expe. m/z	Calc. m/z	Diff (ppm)	Diff (mDa)
[M+H]+	C49 H28 Cl8 N2	924.9841	924.9833	0.81	0.75

Figure B.4.39. High resolution mass spectrometry of 9.

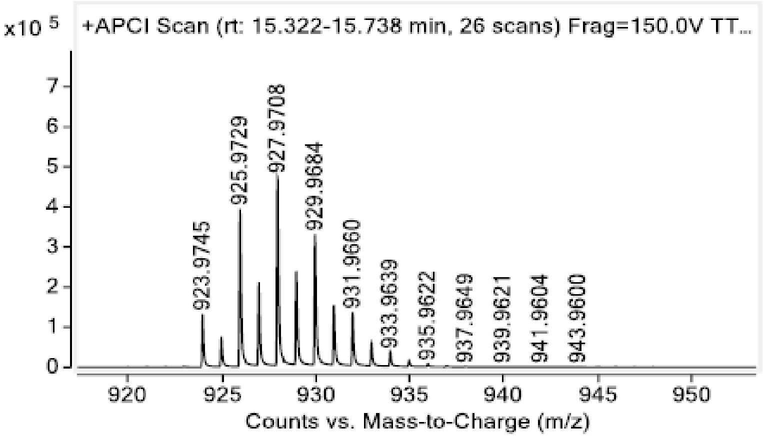

Ion	Formula	Expe. m/z	Calc. m/z	Diff (ppm)	Diff (mDa)
[M+H]+	C49 H27 Cl8 N2	923.9745	923.9755	-1.11	-1.02

Figure B.4.40. High resolution mass spectrometry of 3.

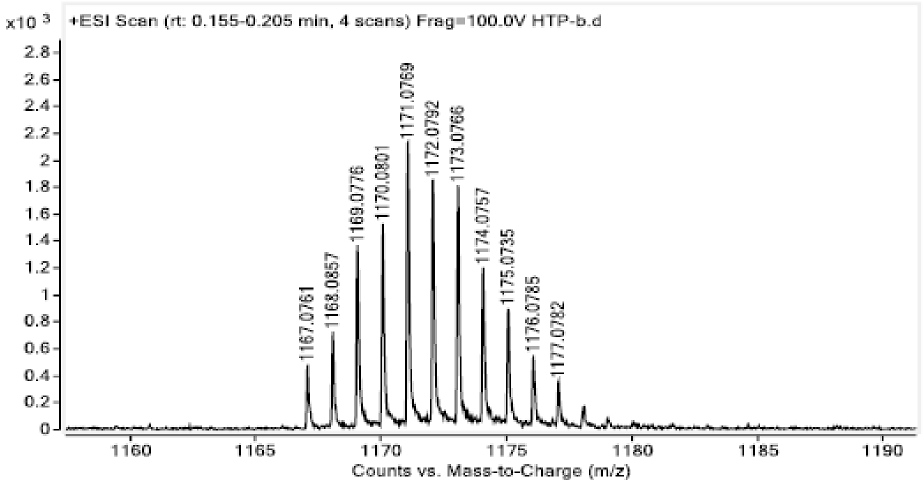

Ion	Formula	Expe. m/z	Calc. m/z	Diff (ppm)	Diff (mDa)
[M+H]+	C67H41Cl8N3	1168.0857	1168.0881	-2.09	-2.45

Figure B.4.41. High resolution mass spectrometry of 10.

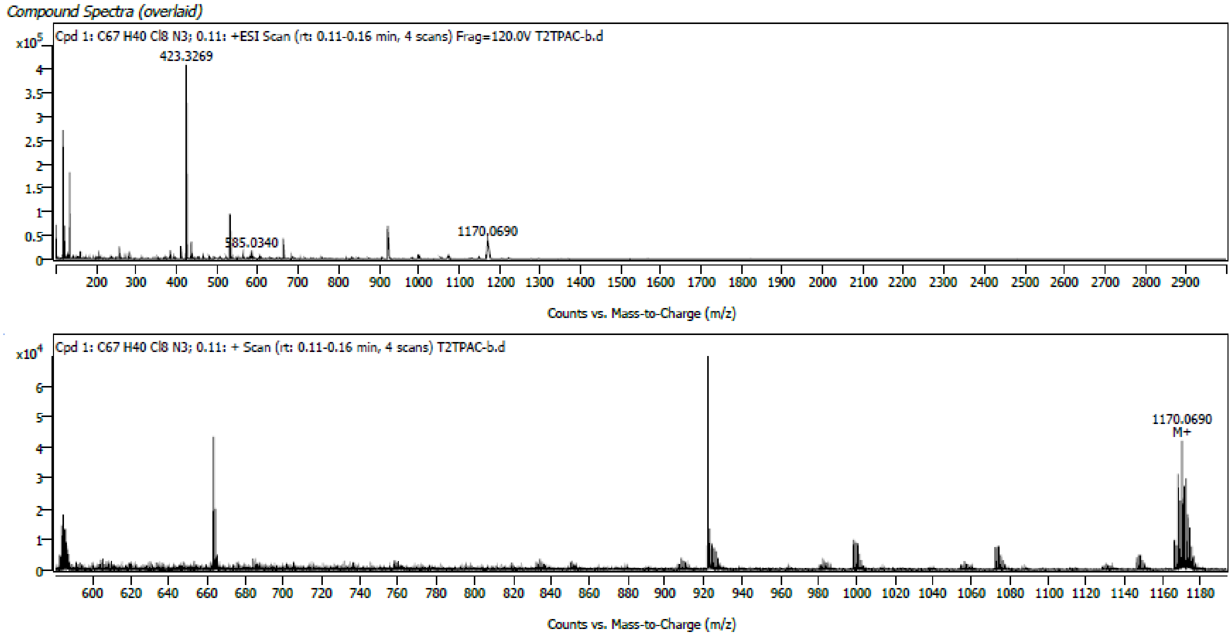

Spectrum Peaks (Max. 1)

Ion Species	Formula	Abund	m/z	m/z (Calc)	Diff (ppm)	Diff (mDa)
M+	C67H40Cl8N3	42329	1170.06903	1170.06850	0.46	0.53

Figure B.4.42. High resolution mass spectrometry of 4.

Purity Analysis

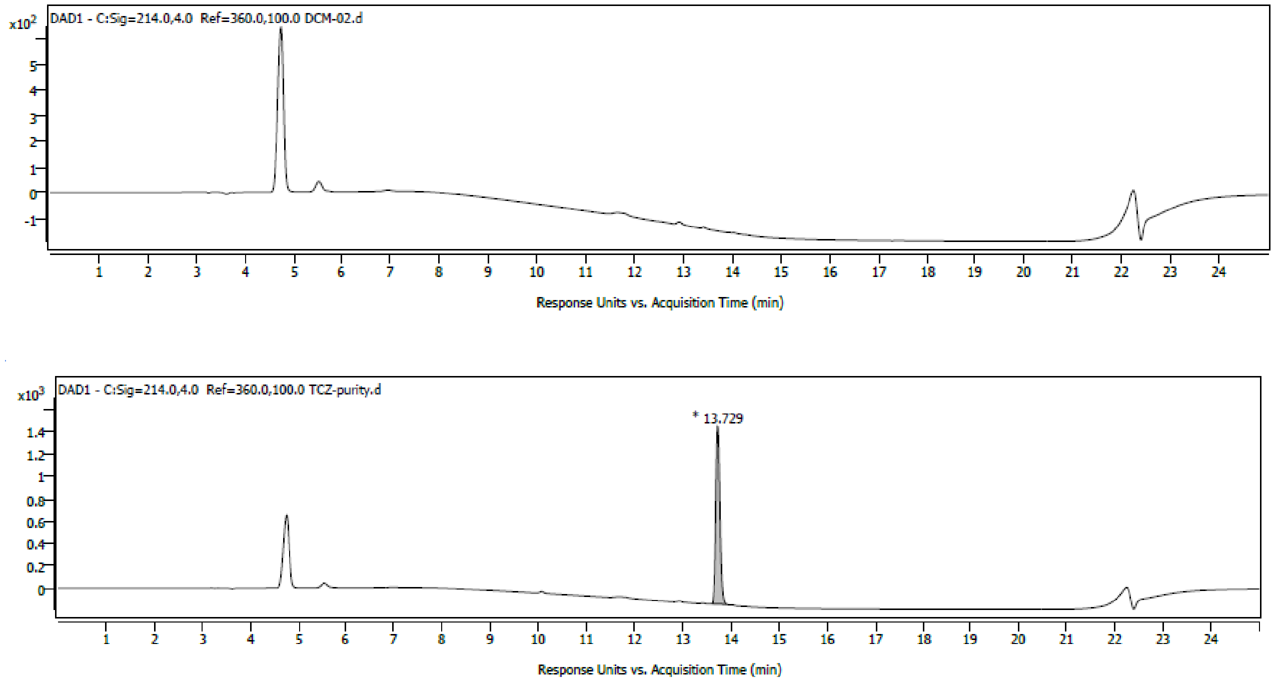

Chromatogram Peaks

RT	Area	Area Sum %
13.7	9425	100.00

Figure B.4.43. LC purity chromatogram 2. Method: ZORBAX SB-Aq (4.6 × 100 mm, 1.8 µm); gradient 50-95% B in 25 min (A = H_2O + 0.1% formic acid; B = ACN/IPA 1:9); ESI(+)-TOF; DAD 214 nm (ref 360 nm). Residue at ~5 min is from blank (above chromatogram) assigned to the solvent/matrix peak and it is excluded from the purity. Analyte elutes at ~13.7 min.

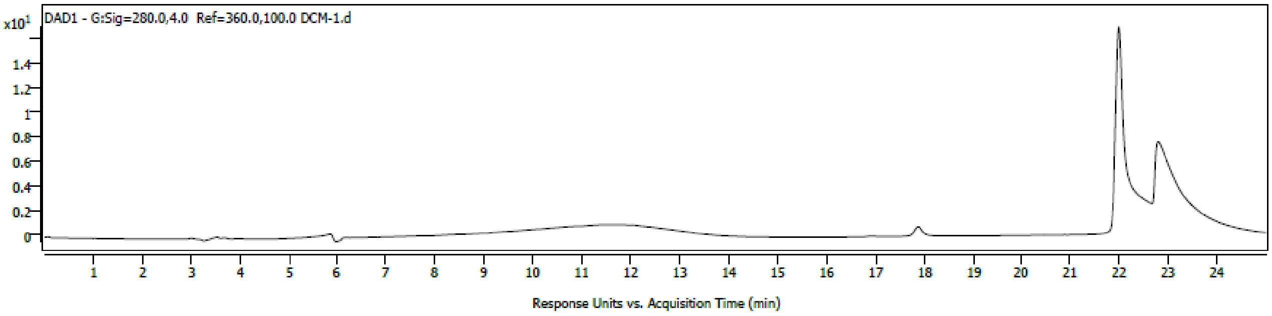

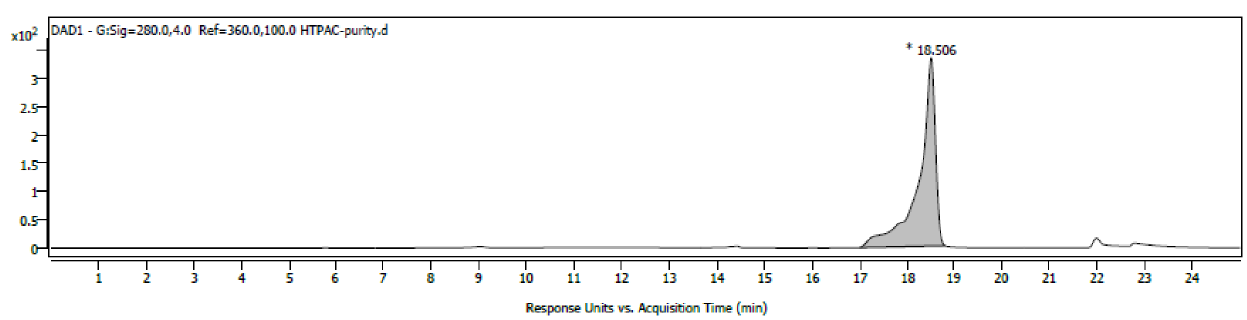

Chromatogram Peaks

RT	Area	Area Sum %
18.5	7922	100.00

Figure B.4.44. LC purity chromatogram 9. Method: ZORBAX SB-Aq (4.6 × 100 mm, 1.8 µm); gradient 50-95% B in 25 min (A = H_2O; B = ACN/IPA 1:9); ESI(+)-TOF; DAD 280 nm (ref 360 nm). Single analyte peak at ~18.5 min.

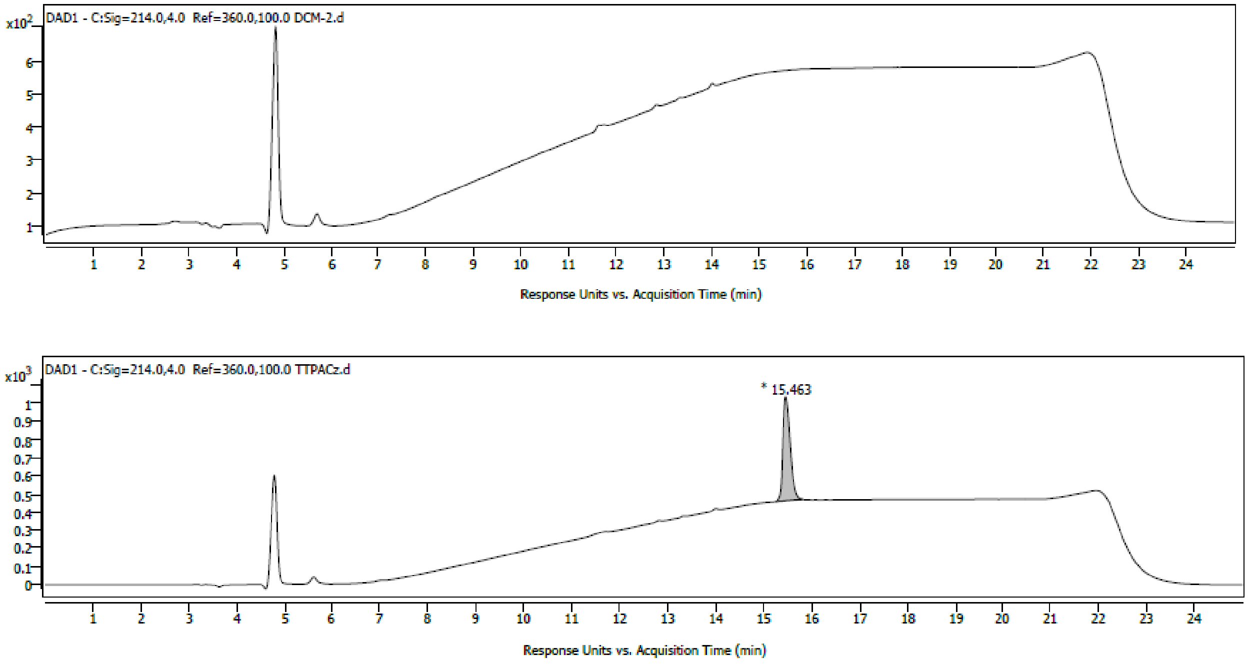

Chromatogram Peaks

RT	Area	Area Sum %
15.5	6106	100.00

Figure B.4.45. LC purity chromatogram 3. Method: ZORBAX SB-Aq (4.6 × 100 mm, 1.8 µm); gradient 50-95% B in 25 min (A = H_2O + 0.1% formic acid; B = ACN/IPA 1:9); APCI(+)-TOF; DAD 214/210 nm (ref 360 nm). Peak at ~5 min is from blank (above chromatogram) and it is assigned to a solvent/matrix peak and it is excluded from the purity. Analyte elutes at ~15.5 min.

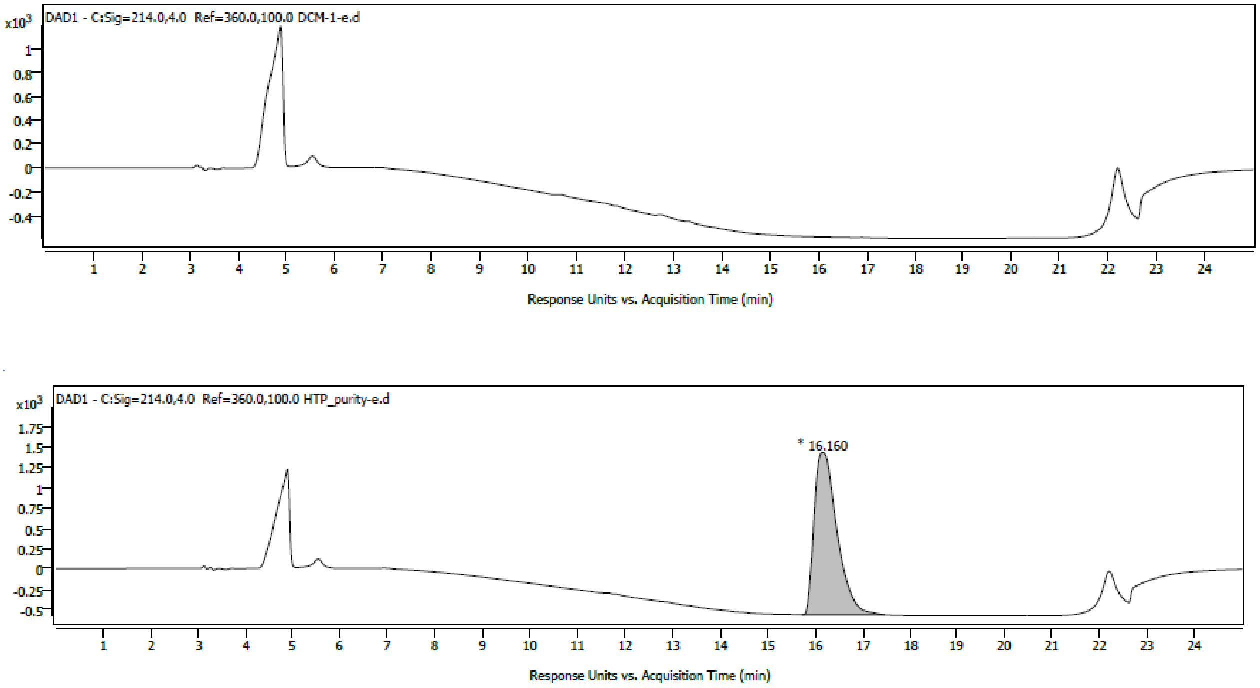

Chromatogram Peaks

RT	Area	Area Sum %
16.2	66942	100.00

Figure B.4.46. LC purity chromatogram 10. Method: ZORBAX SB-Aq (4.6 × 100 mm, 1.8 µm); gradient 50-95% B over 25 min (A = H_2O; B = ACN/IPA 1:9); ESI(+)-TOF; DAD 280 nm (ref. 360 nm. Peak at ~5 min is from blank (above chromatogram) and it is assigned to a solvent/matrix peak and it is excluded from the purity. Analyte elutes at ~16.2 min.

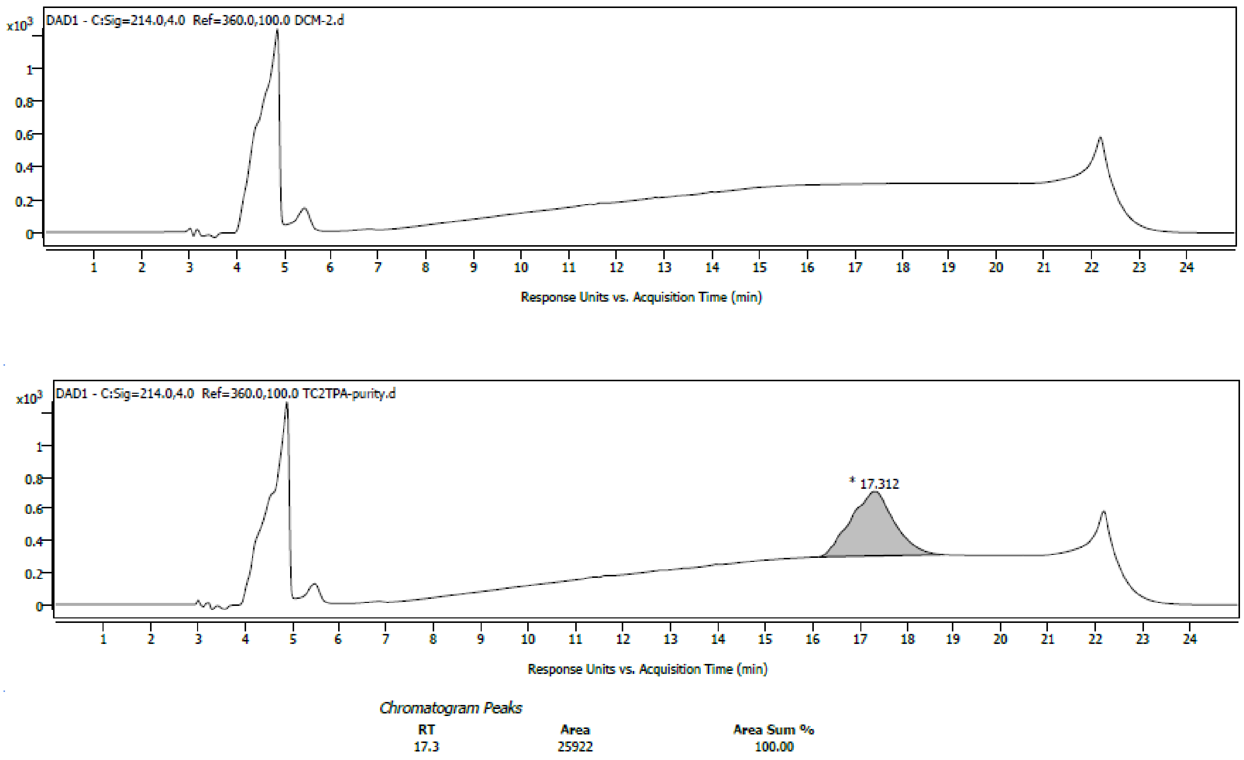

Chromatogram Peaks

RT	Area	Area Sum %
17.3	25922	100.00

Figure B.4.47. LC purity chromatogram 4. Method: ZORBAX SB-Aq (4.6 × 100 mm, 1.8 µm); gradient 50-95% B over 25 min (A = H_2O; B = ACN/IPA 1:9); APCI(+)-TOF; DAD 214/210 nm (ref. 360 nm). Peak at ~5 min is from blank (above chromatogram) and it is assigned to a solvent/matrix peak and it is excluded from the purity. Analyte peak elutes at 17.3 min.

APPENDIX C supporting information chapter 5

Electrochemistry

Table C.5.1. Electrochemical half-wave potentials ($E_{1/2}$) of **1**–**3**.

Compound	$E_{1/2}^{ox}$(TPA)	$E_{1/2}^{ox}$(Radical)	$E_{1/2}^{Red}$((Radical)
1	-	0.92 V	-0.64 V
2	0.98 V	1.18V	-0.46 V
3	0.92 V	1.18 V	-0.51 V

Transmission

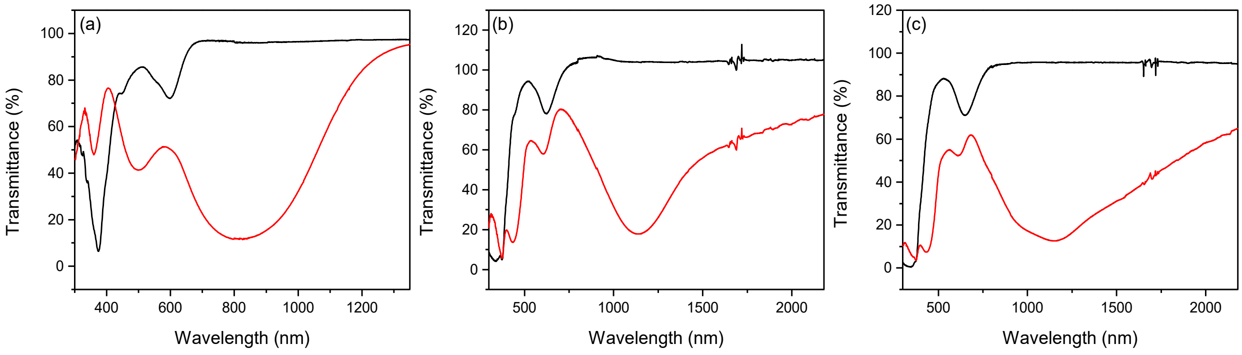

Figure C.5.1. Transmission spectra of **1** (a), **2** (b), and **3** (c) in anhydrous dichloromethane in the neutral (black) and oxidized state (red): 1.0 V for **1**, 0.9 V for **2**, and 0.8 V for **3**.

Coloration efficiency (CE)

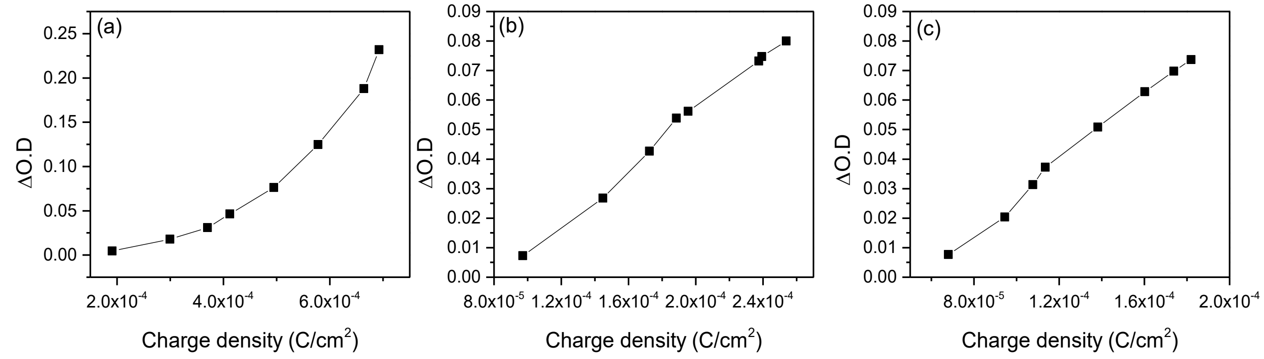

Figure C.5.2. Coloration efficiency for **1-3** in anhydrous dichloromethane. Plots show the optical density change (ΔO.D) at the compound's NIR band maximum versus charge density (Q/A) obtained under controlled-potential steps. a) 1.0 V to 0.0 V monitored at 816 nm for **1.** b) 0.9 V to 0.0 V at 1139 nm for **2**. c) 0.8 V to 0.0 V at 1150 nm for **3.** The CE was taken as the slope of ΔO.D vs Q/A in the mid linear regime.